Computational modeling of material behavior on different scales based on continuum mechanics

von der Fakultät Maschinenbau der Technischen Universität Dortmund zur Verleihung
der Lehrbefugnis (Venia Legendi) für das Fach Kontinuumsmechanische
Materialmodellierung angenomme Habilitationsschrift

von J.-Prof. Dr.-Ing. Swantje Bargmann

Referenten:	Prof. Dr. rer. nat. B. Svendsen Prof. Dr.-Ing. S. Diebels

Tag der Einreichung:	25.11.2010
Vollzug des Habilitationsverfahrens:	14.12.2011

Preface

The research presented in this thesis has been carried out during the years 2008-2010, first being a PostDoc at the Division of Material and Computational Mechanics at Chalmers University of Technology in Gothenburg, Sweden (supported by VR - Swedish Research Council), then being employed at the Institute of Mechanics at University of Dortmund, Germany. The work presented in Chapter 6 was done while I visited the Centre for Research in Computational and Applied Mechanics, University of Cape Town (supported by Heinrich Hertz foundation). The work presented in Chapter 7 was done while I visited the Institute of Low Temperature Science at Hokkaido University in Sapporo, Japan (supported by DFG - German Science Foundation). All support is gratefully acknowledged.

The exceptionally pleasant and open working atmosphere at the Division of Material and Computational Mechanics has had a great impact on the motivation for the present work, wherefore I would like to thank Professors Magnus Ekh, Kenneth Runesson, Ragnar Larsson and Fredrik Larsson. The hospitality of Professor Daya Reddy at University of Cape Town and of Professor Ralf Greve at Hokkaido University is gratefully acknowledged as well. I always felt very welcome abroad.

I would like to express my appreciation to Professor Bob Svendsen for the invaluable guidance, his continuous support and the freedom to follow different fields of research. Moreover, I thank Professor Stefan Diebels for kindly accepting to be correferee of this thesis and the interest in my work.

Moreover, I would like to express my gratitude to my fellow colleagues at the Institute of Mechanics, TU Dortmund. The discussions I have had with them have been fruitful, inspirational and have facilitated my research. In addition, I benefited from engineers, mathematicians and physicists who had impact on this work during research stays, conferences and personal discussions, for example.

Last but not least, I would like to thank all those who have contributed in one way or another in their very personal ways.

Dortmund, December 2011 Swantje Bargmann

Contents

Zusammenfassung

Die Modellierung und Simulation von Materialverhalten ist seit Jahrzehnten wichtiger Bestandteil ingenieurwissenschaftlicher Forschung. Sowohl innovative Ingenieurmaterialien (wie z.B. Leichtbaustoffe) als auch klassische Werkstoffe (z.B. Metalle) verlangen bei ihrer Entwicklung bzw. bei der Ermittlung ihrer mechanischen Eigenschaften ein stark verzahntes Wissen des Ingenieurs. In dem multidisziplinären Forschungsfeld sind Materialwissenschaftler, Ingenieure, Mathematiker und Physiker aktiv und profitieren von interdisziplinären Ansätzen.

Modellierung inelastischen Werkstoffverhaltens von Metallen

In vielen ingenieurwissenschaftlichen Anwendungen wie z.B. Umformprozessen spielt die Deformation von metallischen Materialien eine wichtige Rolle. Metalle verhalten sich bis zu einer kritischen Spannung linear-elastisch. Bei größeren Deformationen sinkt die Steigung der Spannungs-Dehnungskurve und schließlich beginnt das Material sich plastisch zu verfestigen.

Das Werkstoffverhalten ist abhängig von mehreren Phänomenen auf verschiedenen Skalen, wie z.B. der Mikroebene. Ein gutes Beispiel hierfür sind polykristalline metallische Werkstoffe. In deren Fall hat man festgestellt, dass die zugrunde liegende Mikrostruktur, z.B. die Kornmikrostruktur, eine große Rolle spielt. Relevante Aspekte hierbei sind die Abhängigkeit des Materialverhaltens von der Korngröße oder von der Interaktion zwischen Versetzungen und Korngrenzen. Wenn das umzuformende Metallstück ungefähr die gleiche Größe hat wie die Kristalle, aus denen es besteht, dann ist die Spannungs-Dehnungskurve im plastischen Bereich stark von der Korngröße abhängig. Dieses Verhalten nennt man Größeneffekt.

Im Gegensatz zur herkömmlichen Kristallplastizität werden die genannten Aspekte von den Ansätzen der erweiterten Kristallplastizität bzw. der Gradientenkristallplastizität berücksichtigt. Bei der Anwendung solcher Modelle und deren Umsetzung in die numerische Simulation ergeben sich mehrere Herausforderungen. Nicht zuletzt gehören dazu die Analyse der entsprechenden gekoppelten Anfangs-Randwertprobleme und die Entwicklung von effektiven numerischen Lösungsstrategien für diese Probleme.

In den Kapiteln 2–6 werden erweiterte Kristallplastizitätstheorien betrachtet. Dabei werden große Deformationen berücksichtigt, basierend auf nicht-linearer Kontinuumsmechanik.

Die resultierenden mathematischen Gleichungen sind hochgradig nicht-linear und miteinander gekoppelt, so dass ein effizienter numerischer Algorithmus benötigt wird.

Modellierung und Simulation von Polareis in der Antarktis

Inlandeisflächen und Gletscher spielen für das Erdklima eine sehr wichtige Rolle. Rund 90% des irdischen Eises und damit 75% der weltweiten Süßwasserreserven sind in der bis zu 4500m dicken Eisdecke der Antarktis enthalten. Das antarktische Inlandeis ist die größte einzelne Eismasse der Erde. Fast der gesamte Kontinent ist durch das ca. 12 Millionen km^2 große Eisschild der Antarktis bedeckt.

Eis in natürlichen Landeismassen, wie z.B. polaren Eisflächen oder Gletschern, besteht aus Milliarden individuellen hexagonalen Eiskristallen, so genannten “ice Ih”. Diese haben typischerweise einen Durchmesser von wenigen Millimetern oder Zentimetern. Diese Größenskala steht im Kontrast zu der Größe der Masse, die üblicherweise zwischen mehreren Hundert Metern bis zu Tausende von Kilometern rangiert. Es ist seit langem bekannt, dass obwohl die Verteilung der kristallographischen Achsen an der Oberfläche von Eisflächen zufällig ist und das Materialverhalten somit dort als isotrop angesehen werden kann, sich dieses Verhalten an tieferen Stellen verändert. In der Tiefe beginnen die Kristalle, sich zu verschiedenen Typen von anisotropen Gebilden mit bevorzugten kristallographischen Achsen zu entwickeln.

In Kapitel 7 wird ein Computermodell für den anisotropen Eisfluss basierend auf den Felddaten der EPICA (European Project for Ice Coring in Antarctica) Eisbohrungen an der Kohnen Station vorgestellt. Die Kohnen Station ist die einzige deutsche polare Forschungsstation in der Antarktis und liegt im Dronning Maud Land. Hauptziel des EPICA an der Kohnen Station ist die Rekonstruktion des antarktischen Klimas in den letzten hunderttausend Jahren mittels Tiefeisbohrungen. Aufgrund dieser Bohrungen sind Daten über die Anisotropie des Eises sowie über den Eisfluss vorhanden.

Physikalisch gesehen ist Eis ein kristalliner Festkörper, d.h. natürliches terrestrisches Eis setzt sich aus Milliarden Eiskristallen zusammen. An der Oberfläche von Eisflächen bzw. in kleinen Eismassen ist die Verteilung der kristallographischen Achsen zufällig. Das makroskopische Materialverhalten von Eis kann in diesen Fällen folglich vereinfachend als isotrop angenommen werden. Bei dicken Eisschichten verändert sich dieses Verhalten jedoch in der Tiefe, d.h. die Kristalle richten sich mit bevorzugter kristallographischer Achse aus. Diese Anisotropie bewirkt unter Last eine im Vergleich zu isotropen Oberflächeneis eine bis zu zehnfach schnellere Deformation. Daher müssen für dicke Eisschichten anisotrope Materialgesetze formuliert werden.

Das zugrunde liegende Modell, das so genannte continuum-mechanical, anisotropic flow model based on an anisotropic flow enhancement factor model (kurz: CAFFE-Modell), erfüllt alle grundlegenden Prinzipien der klassischen Kontinuumsmechanik und berücksichtigt die Anisotropie des Eis. Die Gewebebildung wird mittels einer Massenbilanz, die mehrere

Rekristallisationseffekte beinhaltet, modelliert. Rekristallisation ist der Abbau von Kristallgitterfehlern durch Neubildung des Gefüges. Die Polygonisierung, d.h. die Rekristallisation durch Partikelrotation, ist eine stetige dynamische Rekristallisierung und wird im CAFFE-Modell durch den Orientierungsfluss beschrieben. Letzterer wird als diffusiver Prozess modelliert. Hierbei wird eine Verallgemeinerung des so genannten Fickschen Diffusionsgesetz angesetzt.

Modellierung von Lösungsdurchdringung in Polymeren: case II Diffusion

Klassische Diffusion ("case I Diffusion") wird üblicherweise mit Hilfe des Fickschen Gesetzes modelliert. Im Fall von glasigen Polymeren in Umgebung der Glasübergangstemperatur list dies jedoch nicht möglich. Wenn eine Lösung mit niedrigem Molekulargewicht in der Nähe der Glasübergangstemperatur in ein sprödes Polymer diffundiert, durchläuft das Polymer einen Phasenwechsel von Glas zu Gummi. Dieser Diffusionsvorgang wird nach Alfrey et al. [11] als "case II Diffusion" bezeichnet. Im Gegensatz zur klassischen Diffusion ist im Fall der case II Diffusion die Massenaufnahme der Lösung durch das Polymer nicht proportional zur Wurzel aus der Zeit, sondern linear in der Zeit. Zusätzlich teilt eine scharfe Front das Polymer in zwei Regionen. Vor der Front, wo das Polymer spröde ist, ist die Konzentration der Lösung deutlich geringer als hinter der Front.

Ein typisches Beispielsystem ist Polymethylmethacrylat (PMMA) und Methanol. Die Werkstoffmodellierung von Polymeren, in denen case II Diffusion stattfindet, ist insbesondere in der pharmazeutischen und der Automobilindustrie von Interesse. In der Literatur existieren viele verschiedene Modellansätze, die unterschiedliche charakteristische Merkmale der case II Diffusion beschreiben können. Es existiert zur Zeit jedoch noch kein Ansatz, der alle Eigenschaften abbilden kann. In Kapitel 8 werden bestehende Modelle besprochen, miteinander verglichen, sowie Vor- und Nachteile aufgelistet.

Modellierung von nicht-klassischer Diffusion in weiteren biologischen und physikalischen Vorgängen

Neben der case II Diffusion in Polymeren existieren weitere biologische und physikalische Prozesse, in denen nicht-klassische (d.h. nicht-Ficksche) Diffusion statt findet. Einige dieser Fälle werden in Kapitel 9 genauer betrachtet. Der Fokus liegt dabei auf der Untersuchung von Wellen- und Schockausbreitungsphänomenen. Unter anderem wird ein modifiziertes SIR Modell für Epidemien betrachtet. Mit Hilfe dieses Modells kann die Seuchenausbreitung und -übertragung durch Individuen simuliert werden. Die Bevölkerungsgruppe wird in diesem Zusammenhang in potentielle Empfänger (S), Infizierte (I) und Genesende (R) unterteilt. Die Verbreitung der Krankheit wird dabei mittels eines nicht-klassischen Diffusionsgesetz modelliert.

This thesis consists of an introduction and 9 chapters presenting different results on computational modeling of material behavior. These results have been submitted to scientific journals for international publication. In order to illustrate connections, extend explanations and avoid unnecessary repetitions, the original papers are slightly modified wherever it is beneficial. An overview of the research undertaken is given in the introduction, i.e. Chapter 1. This thesis is based on the following papers:

Chapter 2	S. Bargmann, M. Ekh, K. Runesson, B. Svendsen [22] Modeling of polycrystals with gradient crystal plasticity - a comparison of strategies Philosophical Magazine 90(10), 1263-1288, 2010
Chapter 3	S. Bargmann, M. Ekh, B. Svendsen, K. Runesson [23] Computational modeling of gradient hardening in polycrystals Technische Mechanik, 30(4), 316-323, 2010
Chapter 4	M. Ekh, S. Bargmann, M. Grymer [84] Influence of grain boundary conditions on modeling of size-dependence in polycrystals Acta Mechanica 218(1–2), 103–113, 2011
Chapter 5	S. Bargmann, B. Svendsen, M. Ekh [35] An extended crystal plasticity model for latent hardening in polycrystals Computational Mechanics 48, 631–645, 2011
Chapter 6	S. Bargmann, B. D. Reddy [26] Modeling of polycrystals using a gradient crystal plasticity theory that includes dissipative microstresses European Journal of Mechanics - A/Solids, 30 (5), 719–730, 2011
Chapter 7	S. Bargmann, H. Seddik, R. Greve [27] Computational modeling of the flow of anisotropic polar ice at the EDML deep-drilling site, Antarctica International Journal for Numerical and Analytical Methods in Geomechanics, accepted for publication, 2011
Chapter 8	S. Bargmann, A. T. McBride, P. Steinmann [25] Models of solvent penetration in glassy polymers with an emphasis on case II diffusion. A comparative review Applied Mechanics Reviews, 64(1), 2011
Chapter 9	S. Bargmann, P. M. Jordan [24] Non-Fickian reaction-diffusion models in biological and physical sciences partly published in A second-sound based, hyperbolic SIR model for high-diffusivity spread, Physics Letters A 375 (5), 898–907, 2011 partly to be submitted

The papers were prepared in collaboration with co-authors.

The author of this thesis took part in planning the papers ([22, 23, 35, 25, 26, 24, 27, 84]), took part in developing the theory ([22, 23, 35, 24, 26]), took part in outlining the theory [22, 23, 35, 25, 24, 26, 27, 84], did the numerical implementation ([22, 23, 35, 26, 27]), carried out the numerical simulations ([22, 23, 35, 26, 27]), carried out parts of the numerical simulations ([84]), for example.

1. Introduction - The big picture

Modern technology craves for new engineering materials when it comes to the design of new products. Computational modeling and simulation is regarded as one of the key technologies in this sector. Further, modeling and simulation of material behavior have been important parts of engineering research during the last decades. Hereby, computational methods play an important role. Usually this is due to the complex equations at hand and/or the complex structure to be studied.

The development of innovative engineering materials (such as light construction materials, polymers, graphene, modern ceramics, for examples) as well as the development of classical materials (e.g. metals, alloys, carbon, wood, glass, ice) requires deep knowledge of this issue. In addition to the development of new engineering materials, the progress in technology has led to the discovery and investigation of unknown physical phenomena in classical materials, especially at smaller scales. One powerful modeling approach when it comes to the investigation of solids is the theory of continuum mechanics. Ever since it has been developed (see e.g. [119, 133, 202]), a lot of fields have been discovered where the classical theory of continuum mechanics forms a very good basis but needs to be enhanced in order to be capable of modeling all the different phenomena that exist in nature. One widely used possibility of extending classical continuum mechanics are gradient theories which have been studied in and applied to a variety of material modeling areas. Gradient theories take into account the gradient of the primary variable(s). In this thesis, they are investigated in the context of the computational modeling of crystal plasticity (Chapters 2-6) and in the context of case II diffusion in polymers (Chapter 8).

A material's existing or emergent mesostructure often influences the behavior of many materials of engineering interest (such as e.g., metals, alloys, granular materials, composites, liquid crystals, polycrystals). Such a mesostructure can be dominated by e.g., phases in multiphase materials, phase transitions, microcracks, voids, dislocation substructures, inclusions, or texture. Examples of mechanical engineering interest are e.g., the material response of polycrystals having a preferred crystalline lattice orientation of the grains, granular materials (e.g., sand) depending on the arrangement of the particles, or the remaining stability of materials already incorporating microcracks. In geomechanics, the anisotropy of polar ice strongly influences the deformation process of the ice. Its anisotropy is characterized by the distribution of the ice crystals.

The fact that materials with microstructure are widely spread in nature, engineering or biomechanical applications, leads to a thorough research in the field of computational modeling. Approaches to the modeling of such materials often result in coupled- and multifield models in which the microstructure and/or processes associated with its emergence and development (e.g., damage and order parameter fields, director fields) are idealized as additional fields in the material. The progress in computer sciences has made it possible to solve these rather large resulting system of coupled and often highly nonlinear equations. To date, there exists no unified efficient agreement/approach on how to involve the different underlying microstructures in a continuum mechanical model.

This thesis starts considering models on the mesoscale (Chapters 2-6). In particular, it is looked at inelastic material behavior in crystalline metals. The mesoscopic level is fully resolved. Next, in Chapter 7, a so-called mesoscopic continuum approach is applied to the modeling of anisotropic flow of polar ice. The terminology "mesoscopic continuum theory" arises from the fact that it contains more information than a pure macroscopic continuum theory. On the other hand, neither the microscopic nor mesoscopic level are resolved. In addition to the general macroscopic field quantities which depend on position and time, a mesoscopic field is introduced which depends on a mesoscopic variable. Some of the macroscopic quantities are then defined in terms of the mesoscopic fields. This is a clear advantage in comparison to ordinary continuum mechanical theories as the additional information from the mesoscopic level is not lost. However, the underlying mesostructure is only modeled phenomenologically. Thus, less information on the material's microstructure is known than in case of pure mesoscopic theory. Finally, in Chapter 9 a continuum mechanics approach is discussed. It is enhanced in the way that the Fick's classical law of diffusion is replaced by a non-classical flux law.

At a first glance, the choice of materials and phenomena looked at in this contribution may look a bit incoherent. However, the mathematical structure of some the governing equations is similar. Also, this shows the power and the ability of continuum mechanics. Fick's law, for example, plays a role in the modeling of ice (Chapter 7), polymers (Chapter 8) and in the reaction-diffusion models in Chapter 9. Moreover, metals as well as ice are polycrystalline materials and in both cases discussed in this thesis the underlying crystalline microstructure cannot be neglected.

In general, the mathematical models consists of partial differential equations which are too complex to be solved analytically. Thus, computer simulations approximate the solutions. They have become an important and powerful tool in the understanding of existing materials and the development and prediction of new materials. Even though the models introduced and discussed in this thesis are set up for different applications, they all have in common that they are continuum mechanics approaches (enhanced in one way or the other) and that they have a profound thermodynamical basis. Moreover, with the exception of Chapter 9, the underlying microtructure plays a distinct role in the models. On the implementation side, all models are implemented in self-written codes. Computational methods play an important role for solving modeling problems in engineering sciences. Usually this is due to the complex structure of the equations at hand. This thesis aims at establishing mathematical models and discusses their numerical treatment. The finite element method is already widely accepted in the field of structural solid mechanics and enjoys a growing significance in thermal analyses. It is used as the underlying discretization method in Chapters 2–6. Chapter 7 discusses a continuum mechanics approach for polar ice which is modeled as a Non-Newtonian fluid. In the field of fluid mechanics, the

Finite Volume Method is the most important discretization method and, consequently, is applied to the governing equation in Chapter 7.

In addition, theories on e.g. the micro- or the atomistic scale as well as to multiscale theories have been developed. When considering different scales, the question on how to bridge those scales pops up immediately. This is usually done via homogenization methods. The analysis and application of computational homogenization methods goes beyond the scope of this thesis and is therefore not part of it. Nevertheless, physical phenomena at the meso- and macro-scale are studied in different materials, modeled and discussed in this work. Besides coupling different scales, phenomena can be coupled in the sense of multi-field problems. Multifield theories model the interaction between various processes. In Chapter 8, models coupling (non-classical) mass diffusion and mechanics are discussed.

1.1. Modeling inelastic material behavior of metals: gradient crystal plasticity

In many engineering applications such as forming processes, the deformation of metallic materials plays a key role. Metals are polycrystalline materials. It is well-known that the macroscopic behavior of a polycrystalline material is influenced by the size and morphology of the grains, the volume fraction of different phases, and subgrain processes, for example. If the metal is approximately of the same size as the crystal grain size, the slope of the stress–strain curve depends on the grain size and the grain orientations in the plastic region. During elastic deformation, the crystal lattice deforms. On the contrary, plastic behavior arises from slipping of the crystal lattice. The slipping takes place along preferred slip directions and is irreversible. Physically, the grain boundaries cause size-dependent material behavior since the directions of the slip planes change at the grain boundaries. The material behavior depends on various phenomena on different scales in polycrystals. The underlying microstructure of the grains plays an important role. An important aspect is the dependence on the grain size of the macroscopic material response arising from the interaction between slips and grain boundaries.

In the last ten to fifteen years, there has been a veritable explosion of work on the investigation of the effects of decreasing system size and increasing influence of the material microstructure on what has traditionally been considered to be “bulk” system behavior alone. On the technological side, this has been driven for example by innovation in the form of miniaturization. Already during the manufacture of miniaturized systems, great care has to be taken in order to avoid unwanted size effects due to the manufacturing method chosen (e.g. Janssen et al. [148]).

One size effect in metals is known as the Hall–Petch effect, i.e. the influence of the grain size on the macroscopic stress-strain characteristics. It is one of the important unresolved issues in computational material modeling. Hall [127] and Petch [213] independently studied different behaviors of steel, but eventually obtained the same result. While Hall

[127] focused on factors influencing the mechanical properties of mild steels, Petch [213] studied brittle failure of steels. Nevertheless, Petch's results from 1953 are in excellent agreement with the ones of Hall which had been published two years earlier. The fact that the (current) flow stress $\sigma(\epsilon)$ depends on the mean grain size d became known as the Hall–Petch effect:

$$\sigma_{\mathrm{y}}(\epsilon) = \sigma_{\mathrm{y},0}(\epsilon) + \frac{k(\epsilon)}{\sqrt{d}}. \tag{1.1.1}$$

Both parameters, $\sigma_{\mathrm{y},0}$ and k, may depend on the strain level ϵ due to hardening of the material. Further experimental proofs for size dependent material behavior in crystals can be found in Armstrong et al. [14], Brown and Ham [47], De Guzmjan et al. [73], Ebeling and Ashby [81], Fleck et al. [96], Hutchinson [143], Ma and Clarke [181], Stelmashenko et al. [242], Stölkens and Evans [243], for example. More recent data is published by e.g. Al–Rub [10], Dimiduk et al. [75], Espinosa et al. [90], Gruber et al. [116], Hemker and Sharpe [129], Kals and Eckstein [155], Motz et al. [190], Nicola et al. [199], Nix et al. [200], Xiang and Vlassak [280].

Crystal plasticity theories are of special interest in the class of materials with plastic behavior since the deformation is mainly determined by the deformation of the underlying grains, e.g. the microstructure. In order to include micro-effects in a macroscopic model, a complete scale separation is often assumed. Unfortunately, conventional models of crystal plasticity do not contain intrinsic material length-scales and are, thus, not capable of capturing macroscopic size-dependent effects. Consequently, extended crystal plasticity theories including plastic strain gradients are developed in order to overcome this drawback of ordinary crystal plasticity theories. The existing approaches have different origins (e.g., discrete dislocation theories, continuum dislocation approaches) and, of course, varying strengths and weaknesses. In this thesis, the focus is on continuum models.

Aifantis [8] is the first to propose a plasticity theories enhanced by the consideration of the plastic strain gradient. Subsequently, several extended continuum theories (also referred to as gradient crystal plasticity theories or strain gradient theories) are proposed, including those of e.g. Acharya [1], Bargmann et al. [35], Bayley et al. [37, 38], Borg [45], Cermelli and Gurtin [53], Clayton et al. [56], Cuitino and Ortiz [68], Dai and Parks [70], Ekh et al. [85], Evers et al. [92, 93], Fleck et al. [96], Gao et al. [104], Han et al. [128], Lele and Anand [171, 172], Levkovitch and Svendsen [173], Kuroda and Tvergaard [165, 166, 167], Menzel and Steinmann [186], Nicola et al. [198], Ohno and Okumura [203], Shizawa and Zbib [236], Shu and Fleck [237], Svendsen [247].

Other approaches, being based on statistical mechanics, are suggested by e.g. Akasheh et al. [9], Groma et al. [114, 115], Limkumnerd and van der Giessen [176], Lubarda et al. [179], or Yefimov and van der Giessen [282, 283]. The latter group combines statistical mechanics and discrete dislocation methods. Discrete dislocation theories are also introduced by Bassani et al. [36], Bittencourt et al. [43], Cleveringa et al. [57], van der Giessen and Needleman [262], and Shu et al. [238].

The extended continuum mechanics theories listed above can be split into physically based (e.g. [3, 37, 38, 93, 92, 167]) and thermodynamically based (e.g. [35, 26, 53, 56, 85, 121, 118, 171, 172, 173, 198, 247]). Despite the large amount of models, there only exist few classifications or analyses of the common features and major differences. With it, the important question of when (and how) to choose which of these theories remains unanswered. In Kassner et al. [157], modeling the Hall–Petch effect is termed one of the important unresolved mesoscale issues and challenges. Thus, the investigation, comparison and unification of different models is carried out in Chapter 2. Three gradient crystal plasticity strategies are compared and their computational modeling behavior is discussed.

Ekh et al. [85] propose a simple, but very effective, gradient crystal plasticity model. Originally, it is formulated accounting for self-hardening only, i.e. the influence of one slip system on another is neglected. The experiments of Franciosi and Zaoui [100] show that two active slip systems exhibit latent hardening. As a first step towards the more sophisticated model accounting for latent hardening (cf. Chapter 5), latent hardening is added to the model of [85] in Chapter 3.

Chapter 6 investigates thermodynamically consistent dissipative hardening in gradient crystal plasticity. A viscoplastic model which accounts for constitutive dependences on the slip, the slip gradient as well as the slip rate gradient is presented. The resulting theory includes three different types of hardening. Standard isotropic hardening is incorporated as well as energetic hardening driven by the slip gradient. In addition, as a third type, dissipative hardening associated with plastic strain rate gradients is worked in.

The models discussed in this thesis are higher order gradient theories which need additional boundary conditions (and additional governing equations). The two most common micro boundary conditions are called micro-hard (also: micro-clamped) and micro-free. The micro-hard condition assumes the plastic slip γ_α to be zero on the grain boundaries, the micro-free condition sets the micro-stress $\kappa_{\Gamma,\alpha}$ zero on the grain boundaries. In Chapter 4 a more general and more complex type of boundary conditions which incorporates the micro-hard and micro-free conditions as limiting cases is suggested. One main feature is that they take the crystallographic misorientation of adjacent grains into account such that for a large misorientation the resistance against dislocation motion is large (with a large grain boundary energy), whereas for a low misorientation the resistance is small.

Gradient theories include the micro-effects in the macroscopic modeling by assuming a complete scale separation. The macroscopic deformation gradient is imposed on the representative volume element (RVE) by solving the mechanical governing equation on the whole RVE with Dirichlet boundary conditions.

In the following, large deformation theories are discussed and the field equations are highly coupled. Thus, a numerically efficient solution algorithm is needed. The algorithms applied in Chapters 2–6 are based on the dual mixed finite element method suggested by Svedberg et al. [245], rendering a coupled two-field problem. The coupling effect is fully taken into account as the system of equations is solved monolithically. The resulting system of equations is solved using a three-level iteration strategy based on a generalized form of domain decomposition, whereby each grain constitutes a subdomain. Due to the fact that each grain can be considered independently (with prescribed boundary conditions), the algorithms are suitable for parallelization.

1.2. Modeling anisotropic polar ice: a mesoscopic continuum approach

About 98% of the Earth's southernmost continent Antarctica are covered by ice with an average ice thickness of 1.6 km. With this, it has about 70% of the world's fresh water and it is by far the largest single land ice body at the moment. In addition, the ice contains an abundance of historic climate information. Researchers hope to obtain full documentation of the climatic and atmospheric records archived in the Antarctic ice and to reconstruct large parts of the climate history by analyzing the ice particles. Therefore, deep drilling sites are installed in Antarctica. It is the focus of Chapter 7 to model the flow of Antarctic ice. As it is the case for the gradient crystal plasticity discussed above, the ice is modeled with a continuum mechanics approach. Moreover, ice is also a crystalline material and its microstructure influences the macroscopic deformation behavior.

Usually natural ice consists of a vast number of small individual hexagonal crystallites with random orientation and can therefore be regarded as isotropic. However, this is not the case for thick ice masses [20, 108]. At the surface the distribution of the crystallographic axes is mainly random. Deeper into the ice, fabrics with preferred directions develop [208]. Moreover, one is dealing with two different length scales: the diameter of crystal which is usually of the unit millimeters to centimeters and the size of the ice masses which can be up to thousands of kilometers. The modeling approach is based on the continuum-mechanical, anisotropic flow model based on an anisotropic flow enhancement factor introduced by [216, 217]. Thereby, the anisotropic response of the polycrystalline ice is modeled with the help of a generalization of Glen's flow law. Then, the evolution of the ice fabrics is studied. As opposed to the gradient crystal plasticity approach, the microstructure is not fully resolved. The model is set up for large polar ice masses, i.e. a large system is to be simulated. Consequently, it is extremely important that the underlying governing equations result in an efficient computational model. Therefore, a mesoscopic continuum theory is chosen for the modeling approach. Hereby, the microstructure of the ice is taken into account phenomenologically.

1.3. Modeling solvent penetration in polymers: case II diffusion

For most engineering applications, Fick's law accurately describes diffusive processes. One of the applications where it miserably fails is in glassy polymers near the glass transition temperature. In the vicinity of the glass transition temperature, when a low molecular weight solvent diffuses into a glassy polymer, the latter is caused to undergo a rubber-glass phase transition. The diffusive process follows non-Fickian behavior. Whereas the classical Fickian diffusion is referred to as case I diffusion, diffusion in glassy polymers is known as non-Fickian “case II diffusion”. A typical system undergoing case II diffusion is polymethylmethacrylate (PMMA) and methanol, for example.

Modeling polymers which undergo case II diffusion is of particular interest in pharmaceutical and automotive industries, for example. Due to the importance of diffusion in many industrial and biological processes, a complete examination from a variety of perspectives and techniques is necessary.

The diffusion of a low-molecular weight solvent within a glassy polymeric solid can exhibit significant deviations from classical Fickian diffusion. The diffusion of the solvent particles is initially restrained by the tightly knit polymeric network. The pressure exerted by the solvent causes the polymer network to rearrange to accommodate the solvent. This rearrangement of the polymer chains takes a finite amount of time and manifests itself as a viscoelastic response at the scale of the polymeric solid. Concurrently, the presence of the solvent increases the rate of polymer relaxation. The polymeric solid is observed to undergo a glass–rubber transition with a sharp front separating the two regions propagating through the polymeric solid at a finite speed. In the swollen rubber-like region behind the front the concentration gradient of the solvent is negligible. In the glass-like region ahead of the front the solvent concentration drops rapidly. A small Fickian precursor is often observed directly ahead of the front. The mass uptake of the solvent by the polymer is linear in time; this is in strong contrast to classical diffusion where the mass uptake is proportional to the square-root of time. This non-classical type of diffusion was coined case II diffusion by Alfrey et al. [11] who were the first to document it. Extensive descriptions of the key features, models and experimental observations of case II type diffusion exist in the literature.

In Chapter 8, the existing literature on modeling approaches accounting for solvent penetration in glassy polymers is carefully reviewed and compared. Unifications are made wherever possible.

1.4. Modeling non-Fickian reaction-diffusion in biological and physical sciences

Modeling of case II diffusion in polymers necessitates a non-Fickian flux law. Further non-Fickian models in biological and physical sciences are studied in Chapter 9. The purpose is to investigate wave propagation under nonlinear growth laws and assuming the inertia-type II flux relation, where the main focus is on traveling wave and shock phenomena. The derivation and analysis of traveling wave solutions has been, and remains, an important approach in the study of nonlinear wave phenomena. This is primarily due to the fact that in the case of many nonlinear partial differential equations, a traveling wave solution is the only type solution that can be obtained using analytical methods. Over the years, the number of known traveling wave solutions has steadily increased.

Among others, a modified SIR epidemic dynamics model is considered. The SIR model is used in simulations of epidemic diseases for the description of the transmission of communicable diseases through individuals, i.e. it describes the spread of an epidemic outbreak through a population. In this context, the population is divided into susceptible (S), infected (I) and recovered (R) persons.

2. Modeling of polycrystals with gradient crystal plasticity - A comparison of strategies

In Svendsen and Bargmann [249] different gradient crystal plasticity strategies are analyzed in a thermodynamic context. Selected models for extended, gradient, or "higher-order" crystal plasticity are studied in the context of a unified formulation and generalization via the application of a recently developed rate variational approach to the formulation of continuum thermodynamic models for history-dependent, inelastic systems. The investigation includes models which were not originally formulated in a thermodynamic or "work-conjugate" fashion, such as e.g. Bayley et al. [37, 38] or Evers et al. [93, 92]. The approach is based on the formulation of rate potentials for each model whose form is determined by (i) energetic processes via the free energy, (ii) kinetic processes via the dissipation potential, and (iii) the form of the evolution relations for the internal-variable-like quantities upon which the free energy and dissipation potential depend. For the case of extended crystal plasticity, these latter quantities include for example the inelastic local deformation, or dislocation densities. The stationarity conditions of the corresponding rate functional then yield volumetric and surficial balance-like field relations determining in the current context for example the form of momentum balance or that of the generalized glide-system flow rule. With the help of this approach, thermodynamically-consistent forms of specific models for extended crystal plasticity are derived.

In addition to the thermodynamic investigations of Svendsen and Bargmann [249], different gradient crystal plasticity strategies are implemented and compared in this chapter. For the numerical implementation, a dual-mixed finite element formulation which is suitable for parallelization is applied.

2.1. Introduction

In the literature, different models have been developed in order to capture size dependence effects in crystals. These include thermodynamic approaches like [85, 122, 124, 171, 172, 173, 174, 244, 246, 247, 271] as well as dislocation-field-theory-based approaches like Bayley et al. [38] and Evers et al. [92]. Despite the large amount of models, there only exist few classifications or analyses of the common features and major differences. Examples which discuss similarities between Cosserat, strain gradient crystal plasticity and the statistical theory of dislocations in the case of single slip are the works of Forest and Sedláček [98, 99]. A nonlocal plasticity theory is compared with a discrete dislocation model in [36] and [43]. Numerical results are presented for single slip in a two-dimensional composite material subject to plane strain simple shear. A boundary value problem for a single crystal undergoing small deformations is discussed for a phase field dislocation theory and Gurtin's theory (cf. [122]) in [142]. This contribution aims at comparing the three models presented in Ekh et al. [85], Evers et al. [92] and a combination of Ekh et al. [85] and Lele and Anand [171].

The first model to be investigated in this contribution is the one introduced by Evers et al. [92] and continued by Bayley et al. [38]. As opposed to the two models mentioned below, it does not originate from a thermodynamic setting. Rather, it is based on physical considerations involving dislocation densities. An extended slip law, which also accounts for statistically stored dislocation densities, is introduced as well. Besides the mechanical displacements, the model of Geers and co-workers is based on the fields of geometrically necessary and statistically stored dislocation densities, which are used to affect crystallographic slip resistance in an extended slip law.

The second model is the one introduced in Ekh et al. [85], which is an extension of the model for isotropic plasticity proposed by Svedberg and Runesson [244]. In Ekh et al. [85], a formulation is proposed which models the size effect by assuming that the hardening stress in the yield function depends on both the associated hardening strain (equal to the accumulated plastic slip) and its Hessian along the slip direction similarly to models for isotropic plasticity originally proposed by Aifantis [8]. Similar formulations can be found in Gurtin [122] and Liebe and Steinmann [174]. The thermodynamic setting of Liebe and Steinmann [174] and Ekh et al. [85] is identical. However, in contrast to [174], where the gradient hardening is isotropic, Ekh et al. [85] obtain anisotropic hardening by restricting the gradient effect to each slip direction. Note that a similar strategy, also thermodynamically based, is followed by Vrech and Etse [271] for small strains. Gurtin's formulation [122] is motivated from a so-called microforce balance instead of introducing the gradient hardening in the free energy.

As a third model, the model of Ekh et al. [85] is in this chapter extended by an idea of Lele and Anand [171]. The approach of Lele and Anand [171] is formulated for small strains and isotropic materials, with a similar approach to the one of Ekh et al. [85]. Their idea is to introduce a slip rate with a similar structure to the one of [85]; however, including an additional higher-order dissipative term. Thus, as a third model, the model of Ekh et al. [85] extended by this particular term is investigated.

The main issue of this chapter is the comparison of the three models using a dual mixed finite element algorithm. For all investigated models, it has been shown in previous publications that they are all capable of handling advanced modeling of the hardening. However, no direct comparison has been possible so far, since the discretization approaches and examples presented differ strongly. Such a comparison is desirable in order to further develop micromechanical models capturing size effects in polycrystals. We therefore choose to investigate all three models in the context of anisotropic polycrystals undergoing large deformations.

This chapter is organized as follows. In Section 2.2, the general underlying mathematical framework is introduced. The basic kinematic and constitutive issues and relations of crystal plasticity relevant for all three models are revised. In a second step, in Section 2.3 the three different models are presented. Having then all constitutive and governing equations at hand, we outline the dual mixed finite element algorithm in Section 2.4. Subsequently, a two-dimensional polycrystal is investigated as a numerical example in Section 2.5. The chapter ends with a discussion of the different models.

2.2. Basic deformation and stress measures

In this section the basic kinematics needed in the following are reiterated in order to introduce the notation used in this contribution.

A solid body B is considered to be a collection of physical particles. Let $\boldsymbol{X}$ denote the fixed position of a particular particle in the undeformed and stress-free configuration $\mathcal{B}_0$, the region the body B occupies at the initial time t_0. Its boundary is denoted by $\partial\mathcal{B}_0$. $\boldsymbol{X}$ and $\mathcal{B}_0$ are called the particle's material position and the material configuration, respectively. The body B deforms under the action of applied body forces and tractions and prescribed displacements. All fields on $\mathcal{B}_0$ are assumed to be continuous and at least once continuously differentiable with respect to all elements of the state space $\mathbb{S}$ and in case of time-dependence additionally with respect to time t. Moreover, in this thesis, $\mathcal{B}_0$ does not contain singular surfaces. This assumption is justified because the modeling of material instabilities in materials with microstructure and internal lengthscales in this thesis results in "diffuse" rather than "sharp" interfaces between homogeneous regions in $\mathcal{B}_0$.
The deformation of the reference configuration $\mathcal{B}_0$ of the solid body is described by the time-dependent vector field of the nonlinear spatial deformation map

$$\boldsymbol{\varphi} : \mathcal{B}_0 \times \mathbb{R}_+ \rightarrow \mathcal{B}_t \quad \text{with} \quad \boldsymbol{\varphi}(\boldsymbol{X}, t) := \boldsymbol{x}, \tag{2.2.1}$$

where $\boldsymbol{x}$ denotes the spatial position of the particle $\boldsymbol{X}$ in the deformed (spatial) configuration $\mathcal{B}_t$ at time t. As usual, the vector field $\boldsymbol{\varphi}$ is assumed to be unique, continuously differentiable and to have a continuous inverse, i.e., $\boldsymbol{\varphi}$ is required to be a diffeomorphism.

The deformation gradient $\boldsymbol{F}$ is defined by

$$\boldsymbol{F} : \mathcal{T}\mathcal{B}_0 \rightarrow \mathcal{T}\mathcal{B}_t \quad \text{with} \quad \boldsymbol{F} := \nabla_{\mathrm{r}}\boldsymbol{\varphi}(\boldsymbol{X}, t). \tag{2.2.2}$$

In large strain plasticity, the main assumption is the classical multiplicative split of the deformation gradient $\boldsymbol{F}$ into an elastic $\boldsymbol{F}_{\mathrm{E}}$ and a plastic part $\boldsymbol{F}_{\mathrm{P}}$ (Lee [168]):

$$\boldsymbol{F} = \boldsymbol{F}_{\mathrm{E}} \cdot \boldsymbol{F}_{\mathrm{P}}. \tag{2.2.3}$$

The plastic part $\boldsymbol{F}_\text{P}$ describes the deformation from the tangent space $\mathcal{T}\mathcal{B}_0$ to the intermediate tangent space $\mathcal{T}\bar{\mathcal{B}}$. It is assumed to arise due to inelastic slip in the preferred crystal planes. The elastic contribution $\boldsymbol{F}_\text{E}$ accounts for lattice distortion and rotation. This leads to the following relations for the deformation measures

$$\boldsymbol{C}_\text{E} := [\boldsymbol{F}_\text{E}]^t \cdot \boldsymbol{F}_\text{E}, \quad \boldsymbol{E}_\text{E} := \frac{1}{2}[\boldsymbol{C}_\text{E} - \boldsymbol{I}], \tag{2.2.4}$$

where the right Cauchy–Green tensor in the intermediate configuration $\bar{\mathcal{B}}$ is denoted by $\bar{\boldsymbol{C}}_\text{E}$ and $\boldsymbol{E}_\text{E}$ is the Green–Lagrange strain.

Next, recall the stress measures of interest. The 1st Piola–Kirchhoff stress, $\boldsymbol{P}$, and the 2$^\text{nd}$ Piola–Kirchhoff stress, $\boldsymbol{S}_\text{E}$ on the intermediate configuration $\bar{\mathcal{B}}$, are defined as:

$$\boldsymbol{P} := \boldsymbol{\tau} \cdot \boldsymbol{f}^t = \boldsymbol{F}_\text{E} \cdot \boldsymbol{S}_\text{E} \cdot [\boldsymbol{f}_\text{P}]^t, \quad \boldsymbol{S}_\text{E} := \boldsymbol{f}_\text{E} \cdot \boldsymbol{\tau} \cdot [\boldsymbol{f}_\text{E}]^t, \tag{2.2.5}$$

with the notation $\boldsymbol{f}^x := [\boldsymbol{F}^x]^{-1}$ and $\boldsymbol{\tau}$ being the Kirchhoff stress. Moreover, the Mandel stress, $\boldsymbol{M}_\text{E}$, on the intermediate configuration $\bar{\mathcal{B}}$, is introduced

$$\boldsymbol{M}_\text{E} := [\boldsymbol{F}_\text{E}]^t \cdot \boldsymbol{\tau} \cdot [\boldsymbol{f}_\text{E}]^t = \boldsymbol{C}_\text{E} \cdot \boldsymbol{S}_\text{E}. \tag{2.2.6}$$

As usual, the model formulation in the context of crystal plasticity is based on the slip-system geometry for each slip-system α: the slip direction $\boldsymbol{s}_\alpha$ and the slip plane normal $\boldsymbol{n}_\alpha$ which are two orthonormal vectors in the reference configuration $\mathcal{B}_0$. For the sake of simplicity, it is assumed that the intermediate configuration is isoclinic such that all slip-systems $(\bar{\boldsymbol{s}}_\alpha, \bar{\boldsymbol{n}}_\alpha)$ are fixed in $\bar{\mathcal{B}}$ and known a priori from the given crystal structure. Consequently, the slip direction and the slip plane normal do not change between the reference and the intermediate configuration, i.e., $(\boldsymbol{s}_\alpha, \boldsymbol{n}_\alpha) = (\bar{\boldsymbol{s}}_\alpha, \bar{\boldsymbol{n}}_\alpha)$. Therefore, the bars are omitted from now on. Then, following Rice [226], the evolution of the plastic deformation is given by the form

$$\boldsymbol{L}_\text{P} = \dot{\boldsymbol{F}}_\text{P} \cdot \boldsymbol{f}_\text{P} = \sum_\alpha \dot{\gamma}_\alpha [\boldsymbol{s}_\alpha \otimes \boldsymbol{n}_\alpha], \tag{2.2.7}$$

with $\boldsymbol{L}_\text{P}$ denoting the plastic velocity gradient tensor. The resolved shear (Schmid) stress τ_α, associated with the slip-system $(\boldsymbol{s}_\alpha, \boldsymbol{n}_\alpha)$, is defined as

$$\tau_\alpha := \boldsymbol{s}_\alpha \cdot \boldsymbol{M}_\text{E} \cdot \boldsymbol{n}_\alpha = \boldsymbol{M}_\text{E} : [\boldsymbol{s}_\alpha \otimes \boldsymbol{n}_\alpha] \,. \tag{2.2.8}$$

If γ_α is interpreted as the slip-system shear, it can be positive or negative and increase or decrease, in which case $\dot{\gamma}_\alpha \, \boldsymbol{s}_\alpha = |\dot{\gamma}_\alpha| \; \text{sign}(\dot{\gamma}_\alpha) \, \boldsymbol{s}_\alpha = \pm \, |\dot{\gamma}_\alpha| \, \boldsymbol{s}_\alpha$. This motivates to consider both $\boldsymbol{s}_\alpha$ and $-\boldsymbol{s}_\alpha$ as different slip directions. Henceforth, this idea is followed. $\gamma_\alpha \geq 0$ can then be interpreted as the accumulated slip-system shear and it is always positive and monotonically-increasing, i.e., $\dot{\gamma}_\alpha \geq 0$ for all $\alpha = 1, \ldots, n$. Of course, from the computational point of view, one has to deal with the expense of doubling the number of slip directions/systems.

2.3. Constitutive models

The St. Venant–Kirchhoff law for the elastic behavior is assumed for all three models. Thus the second Piola–Kirchhoff stress $\boldsymbol{S}_{\mathrm{E}}$ on the intermediate configuration is given by

$$\boldsymbol{S}_{\mathrm{E}} = \lambda \boldsymbol{I} : \boldsymbol{E}_{\mathrm{E}} + 2\mu \boldsymbol{E}_{\mathrm{E}}, \tag{2.3.1}$$

where λ and μ are the Lamé parameters pertinent to small elastic deformations.

2.3.1. Model I

As a first model, the one developed by Evers et al. [92], see also [38], is summarized. It is motivated from physical dislocation densities and evolution equations for these. During plastic deformation, two types of dislocations occur: edge and screw dislocations, see Figure 2.1. For modeling purposes, a further categorization was established: One type, the so-called statistically stored dislocations (SSD) accumulate by a random trapping process. The elastic distortion of the crystal's lattice is not compatible with a deformation which is derivable from a continuously differentiable displacement field. This leads to the presence of the second type of dislocations that are called geometrically necessary dislocations (GNDs) which, in other words, are stored due to the locally heterogeneous plastic shear strain. They are introduced to preserve lattice compatibility.

Evers et al. [92] present a model which quantifies for the densities of geometrically necessary dislocations (GNDs) and statistically stored dislocations (SSDs). Only edge dislocation densities are considered as done in [38][1]. In addition, they assume that all dislocations of interest lie in the slip planes.

The density of GNDs $\rho_\alpha^{\mathrm{GND}}$ is associated with certain spatial gradients of plastic shear and it can be calculated directly by geometry considerations once the active slip-systems have been defined. Only edge dislocation densities are considered, thus

$$\rho_\alpha^{\mathrm{GND}} = \rho_\alpha^{\mathrm{GND}_0} - \frac{1}{b} \nabla_{\mathrm{r}} \gamma_\alpha \cdot \boldsymbol{s}_\alpha, \tag{2.3.2}$$

where b is magnitude of the Burger's vector and $\rho_\alpha^{\mathrm{GND}_0}$ denotes the initial GND density.

Following Ashby [16], gradients of the slip in direction normal to slip plane, i.e., in direction of $\boldsymbol{n}_\alpha$, do not affect the crystal lattice. In other words, those gradients do not result in the formation of GNDs. Moreover, as stated by Evers et al. [92], Eq. (2.3.2) "leads to a dislocation density [...] depending on the direction of the plastic gradients in relation to the crystallographic orientation, all independent of the mechanism that actually caused the strain gradient."

---

[1] The model introduced in [92] is formulated for edge and screw dislocation densities. However, the numerical example presented in [92] is restricted to self-hardening and double slip where only edge dislocations are considered.

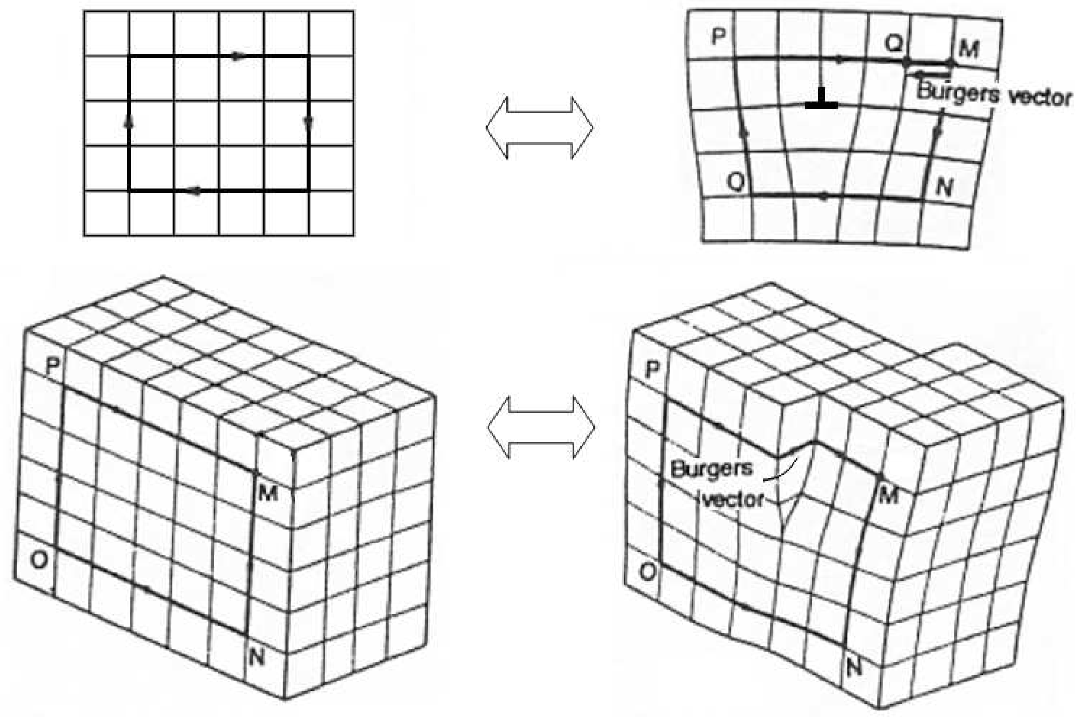

Figure 2.1.: Illustration of edge (top) respectively screw (bottom) dislocations. Picture credit: Wikipedia

Note that, if screw locations are considered as well, an additional term taking those into account is necessary to include. However, there is no such simple relation for SSD densities $\rho_\alpha^{\mathrm{SSD}}$ as the physical processes of the statistically storage of dislocations is complex. Evers et al. apply a generalization of the rate equation proposed by Essmann and Mughrabi [91]:

$$\dot{\rho}_\alpha^{\mathrm{SSD}} = \frac{1}{b}\left[\frac{1}{L_\alpha} - 2y_c\rho_\alpha^{\mathrm{SSD}}\right]|\dot{\gamma}_\alpha|. \tag{2.3.3}$$

The SSD density is initialized by $\rho_\alpha^{\mathrm{SSD}}(t=0) = \rho^{\mathrm{SSD}_0} > 0$ and stays positive. The rate equation (2.3.3) consists of one term taking the accumulation and a second term taking the annihilation rates of the SSD densities into account, i.e., $1/L_\alpha$ respectively $2y_c\rho_\alpha^{\mathrm{SSD}}$. The latter is controlled by the critical annihilation length, i.e., the constant y_c. The average dislocation segment length of statistically stored dislocations L_α is determined by the current dislocation state and can be expressed as

$$L_\alpha = \frac{K}{\sqrt{\sum_\beta H_{\alpha\beta}|\rho_\alpha^{\mathrm{SSD}}| + \sum_\beta H_{\alpha\beta}|\rho_\alpha^{\mathrm{GND}}|}}. \tag{2.3.4}$$

The interaction coefficients $H_{\alpha\beta}$ account for the mutual immobilization between dislocations of different slip-systems. Following the way of Evers et al. [92], $H_{\alpha\beta} = h_0 \ \ \forall\alpha,\beta$

is chosen with h_0 being the constant immobilization coefficient. The evolution relation for the slip-system shear γ_α is given by a power law

$$\dot{\gamma}_\alpha = \dot{\gamma}_0 \left[\frac{|\tau_\alpha^{\text{eff}}|}{s_\alpha} \right]^m , \tag{2.3.5}$$

relating the slip rates $\dot{\gamma}_\alpha$ to the effective shear stress τ_α^{eff} and the slip-system strength s_α. The plastic shear rate $\dot{\gamma}_0$ and the rate sensitivity parameter m are constant material parameters and assumed to be the same for all slip-systems α. The power-law form allows one to characterize nearly rate-independent behavior (for very large values of m). The slip rate is influenced by back stresses on the slip-systems α. As mentioned in the Introduction, the back stress relations are derived through physical arguments. The effective shear stress τ_α^{eff} is defined as

$$\tau_\alpha^{\text{eff}} = \tau_\alpha - \bar{\boldsymbol{\tau}}^b : [\boldsymbol{s}_\alpha \otimes \boldsymbol{n}_\alpha] \, . \tag{2.3.6}$$

where $\bar{\boldsymbol{\tau}}^b$ is the global back-stress tensor. In case of pure edge dislocations it can be expressed as the symmetric tensor

$$\bar{\boldsymbol{\tau}}^b = \sum_\alpha \tau_\alpha^e \left[[\boldsymbol{s}_\alpha \otimes \boldsymbol{n}_\alpha] + [\boldsymbol{s}_\alpha \otimes \boldsymbol{n}_\alpha]^t \right] . \tag{2.3.7}$$

A global back-stress tensor $\sum_\alpha \tau_\alpha^e [\boldsymbol{s}_\alpha \otimes \boldsymbol{n}_\alpha]$ would pull back and push forward in the same way the elastic Mandel stress $\boldsymbol{M}_\text{E}$ does.

The projection of the global back-stress tensor $\boldsymbol{\tau_b}$, e.g. as in Eq. (2.3.6), results in depending resolved back-stresses $\tau_\alpha^b = \boldsymbol{\tau_b} : [\boldsymbol{s}_\alpha \otimes \boldsymbol{n}_\alpha]$. Dependent in such a way that the effect of a shear stress on slip-system α has the largest effect on that same slip-system and a smaller effect on the other slip-systems, see [92]. The resulting shear stress τ_α^e

$$\tau_\alpha^e = \frac{\mu b R^2}{8\,[1-\nu]} \nabla_\text{r} \rho_\alpha^{\text{GND}} \cdot \boldsymbol{s}_\alpha \tag{2.3.8}$$

develops independently. The circular region around a material point $\boldsymbol{X}$ with radius R accounts for the geometrically necessary dislocations contributing to the shear stress on slip-system α. Moreover, μ is the shear modulus and ν is Poisson's ratio. The slip-system strength s_α reads

$$s_\alpha = c\mu b \sqrt{\sum_\beta a_0 |\rho_\beta^{\text{SSD}}| + \sum_\beta a_0 |\rho_\beta^{\text{GND}}|}, \tag{2.3.9}$$

where c is a constant material parameter. In particular, it is a function of the SSD and GND densities.

2.3.2. Model II

As a second model, the approach introduced by Ekh et al. [85] which is summarized below is investigated. In contrast to model I, it is embedded in a thermodynamic framework.

Moreover, it is simpler with respect to hardening, but still showed realistic simulation results in [85]. The free energy Ψ_0 per unit intermediate volume is introduced as a function of the intermediate Green–Lagrange strain $\boldsymbol{E}_{\mathrm{E}}$, the slip-system shears γ_α and its gradient $\boldsymbol{\nabla}_{\mathbf{r}}\gamma_\alpha$:

$$\begin{aligned}\Psi_0(\boldsymbol{E}_{\mathrm{E}},\{\gamma_\alpha\},\{\boldsymbol{\nabla}_{\mathbf{r}}\gamma_\alpha\}) = {} & \frac{\lambda}{2}\left[\mathrm{tr}\boldsymbol{E}_{\mathrm{E}}\right]^2+\mu\mathrm{tr}\left((\boldsymbol{E}_{\mathrm{E}})^2\right) \\ & +\frac{1}{2}\sum_\alpha H^{1}_\alpha\gamma_\alpha^2+\frac{1}{2}\sum_\alpha l_\alpha^2\boldsymbol{\nabla}_{\mathbf{r}}\gamma_\alpha\cdot\left[H^g_\alpha\boldsymbol{s}_\alpha\otimes\boldsymbol{s}_\alpha\right]\cdot\boldsymbol{\nabla}_{\mathbf{r}}\gamma_\alpha.\end{aligned} \tag{2.3.10}$$

It is additively decomposed in a hyperelastic contribution following the St. Venant model and a hardening contribution. This leads to the following constitutive state equation for elastic response in terms of the second Piola–Kirchhoff stress tensor $\bar{\boldsymbol{S}}_{\mathrm{E}}$

$$\boldsymbol{S}_{\mathrm{E}} := \frac{\partial\Psi_0}{\partial\boldsymbol{E}_{\mathrm{E}}} = \lambda\boldsymbol{I}:\boldsymbol{E}_{\mathrm{E}}+2\mu\boldsymbol{E}_{\mathrm{E}}. \tag{2.3.11}$$

Consequently, the elastic response is the same as in model I. However, in model II, it stems from a free energy acting as a potential.

The hardening contribution to the free energy can be decomposed further into contributions from local and gradient hardening, respectively. The corresponding hardening moduli, H^l_α and H^g_α, are chosen as constant and positive semi-definite measures associated with each slip-system α. As to the necessary constant internal lengthscale, $\boldsymbol{H}^g_\alpha l^2_\alpha$ is treated as a material parameter without any physical interpretation. The chosen expression for local hardening represents vanishing latent hardening, which is a non-physical simplification. By choosing $\boldsymbol{H}^g_\alpha = H^g_\alpha\boldsymbol{s}_\alpha\otimes\boldsymbol{s}_\alpha$, Ekh et al. [85] induce crystallographic hardening.

This leads to the following hardening stresses κ_α which are defined in such a way that they can be derived from the free energy via

$$\begin{aligned}\kappa_\alpha &:= \frac{\partial\Psi_0}{\partial\gamma_\alpha}-\mathrm{Div}\left(\frac{\partial\Psi_0}{\partial(\boldsymbol{\nabla}_{\mathbf{r}}\gamma_\alpha)}\right) \quad \text{in } \mathcal{B}_{0,\,\mathrm{grain}},\ \alpha=1,2,...,n_{\mathrm{slip}} \\ \kappa^{(b)}_\alpha &:= \boldsymbol{N}\cdot\frac{\partial\Psi_0}{\partial(\boldsymbol{\nabla}_{\mathbf{r}}\gamma_\alpha)} \quad \text{on } \partial\mathcal{B}_{0,\,\mathrm{grain}},\ \alpha=1,2,...,n_{\mathrm{slip}}.\end{aligned} \tag{2.3.12}$$

Here, $\boldsymbol{N}$ is the outward unit normal to the boundary $\partial\mathcal{B}_{0,\,\mathrm{grain}}$ and the superscript "b" denotes "boundary". It is noted that the hardening stresses κ_α are composed of local as well as gradient contributions, whereas the gradient tractions $\kappa^{(b)}_\alpha$ on the boundary $\partial\mathcal{B}_{0,\,\mathrm{grain}}$ represent the gradient effect only. In particular, for the free energy function stated in Eq. (2.3.10), this leads to

$$\begin{aligned}\kappa_\alpha &= H^l_\alpha\gamma_\alpha-\mathrm{Div}(l^2_\alpha\boldsymbol{H}^g_\alpha\cdot\boldsymbol{\nabla}_{\mathbf{r}}\gamma_\alpha) \\ &= H^l_\alpha\gamma_\alpha-l^2_\alpha H^g_\alpha\left[\boldsymbol{s}_\alpha\otimes\boldsymbol{s}_\alpha\right]:\left[\boldsymbol{\nabla}_{\mathbf{r}}\otimes\boldsymbol{\nabla}_{\mathbf{r}}\right]\gamma_\alpha, \qquad (2.3.13) \\ \kappa^{(\mathrm{b})}_\alpha &= \boldsymbol{N}\cdot l^2_\alpha\boldsymbol{H}^g_\alpha\cdot\boldsymbol{\nabla}_{\mathbf{r}}\gamma_\alpha. \qquad (2.3.14)\end{aligned}$$

Clearly, the extension of a regular local hardening is represented by the additional gradient term $l_\alpha^2 \boldsymbol{H}_\alpha^g : [\boldsymbol{\nabla}_\mathbf{r} \otimes \boldsymbol{\nabla}_\mathbf{r}]\gamma_\alpha$.

The evolution of the plastic slip γ_α is assumed to follow a viscoplastic power law

$$\dot{\gamma}_\alpha = \frac{1}{t_*}\left[\frac{< \tau_\alpha - Y_\alpha - \kappa_\alpha >}{C_0}\right]^m , \tag{2.3.15}$$

with $< x > := 1/2[x + |x|]$ denoting the Macaulay brackets. The material parameter C_0 is constant and the same for all slip-systems and Y_α and t_* denote the initial yield stress and the relaxation time, respectively. Furthermore, the relaxation time t_* is equal for all slip-systems α, but could easily be generalized to be slip-system dependent. The Schmid stress τ_α is defined in Eq. (2.2.8). Note the special case of rate-independent plasticity is retrieved in the limit when $t_*(C_0)^m \to 0$. Moreover, nearly rate-independent behavior can be retrieved for large rate sensitivity parameters m as well.

2.3.3. Model III

Following Gurtin [124], Lele and Anand [171] propose a thermodynamic-consistent small-deformation strain-gradient theory for isotropic viscoplastic materials similar to the large-deformation model II (which is formulated for anisotropic materials). As in the case of model II, the free energy is split additively into an elastic and a plastic contribution and the latter depends on the slip-system shear gradient $\boldsymbol{\nabla}_\mathbf{r}\gamma_\alpha$. Moreover, the free energy Ψ_0 acts an potential for what they call the energetic microstress $\boldsymbol{\xi}_\alpha^{\text{en}}$ - in a similar way to the gradient hardening stress κ_α of Ekh et al. [85]. In addition to the approach of Ekh et al. [85], they introduce a further length scale, the constant dissipative lengthscale l_d, corresponding to dissipative effects associated with the slip rate gradient $\boldsymbol{\nabla}_\mathbf{r}\dot{\gamma}_\alpha$. Since promising results are presented in [171] for the case of small deformation and isotropy, the flow rule of the large deformation, anisotropic model II is extended in the spirit of Anand, Gurtin and Lele and the following expression as the flow rule of model III is proposed

$$\dot{\gamma}_\alpha = \frac{1}{t_*}\left[\frac{< \tau_\alpha - Y_\alpha - \kappa_\alpha >}{C_0}\right]^m + l_d^2\, {}^0s_\alpha \text{Div}\left(\left[\frac{d_\alpha}{{}^0d}\right]^q \frac{\boldsymbol{\nabla}_\mathbf{r}\dot{\gamma}_\alpha \cdot \boldsymbol{s}_\alpha}{d_\alpha}\boldsymbol{s}_\alpha\right). \tag{2.3.16}$$

Hence, the last term in Eq. (2.3.16), i.e.,

$$l_d^2\, {}^0s_\alpha \text{Div}\left(\left[\frac{d_\alpha}{{}^0d}\right]^q \frac{\nabla_\text{r}\dot{\gamma}_\alpha \cdot \boldsymbol{s}_\alpha}{d_\alpha}\boldsymbol{s}_\alpha\right) \tag{2.3.17}$$

is nonstandard. Interest in such a higher-order dissipative term has arisen only recently, see e.g. the works of [101], [124], and the very recent [171]. Hence, it is of great interest to obtain further results on its effect. Here, the scalar ${}^0s_\alpha = s_\alpha(t = 0) > 0$ represents the initial flow resistance, see also Eq. (2.3.9). Furthermore, ${}^0d$ is a reference rate and d_α denotes the scalar non-negative effective flow-rate

$$d_\alpha := \sqrt{|\dot{\gamma}_\alpha|^2 + l_d^2|\nabla_\text{r}\dot{\gamma}_\alpha|^2}\ . \tag{2.3.18}$$

2.3.4. Model comparison

Here it is appropriate to point out the similarities of the three models. Taking another look at the rate equations of the slip-system shear of model I and II, i.e., Eqs. (2.3.5) and (2.3.15), highlights the differences of those two approaches. The rate equation of model I is rewritten by inserting the effective shear stress relations (2.3.6)-(2.3.8) into the flow rule of model I (Eq. (2.3.5)) first. Subsequently, the GND density $\rho_\alpha^{\mathrm{GND}}$ is substituted by relation (2.3.2). Consequently, one obtains:

$$\begin{aligned}\dot{\gamma}_\alpha &= \dot{\gamma}_0 \left[\frac{|\tau_\alpha + \frac{\mu R^2}{8[1-\nu]} \left[\sum_\beta \nabla_{\mathrm{r}} \left[\nabla_{\mathrm{r}} \gamma_\beta \cdot \boldsymbol{s}_\beta \right] \cdot \boldsymbol{s}_\beta P_{\beta\alpha} \right] |}{s_\alpha} \right]^m \\ &= \dot{\gamma}_0 \left[\frac{|\tau_\alpha + \frac{\mu R^2}{8[1-\nu]} \left[\sum_\beta P_{\beta\alpha} \left[\boldsymbol{s}_\beta \otimes \boldsymbol{s}_\beta \right] : \left[\boldsymbol{\nabla}_{\mathbf{r}} \otimes \boldsymbol{\nabla}_{\mathbf{r}} \right] \gamma_\beta \right] |}{s_\alpha} \right]^m , \end{aligned} \tag{2.3.19}$$

where the scalar quantity is defined $P_{\beta\alpha} = \left[[\boldsymbol{s}_\beta \otimes \boldsymbol{n}_\beta] + [\boldsymbol{s}_\beta \otimes \boldsymbol{n}_\beta]^t \right] : [\boldsymbol{s}_\alpha \otimes \boldsymbol{n}_\alpha]$ which accounts for latent hardening. Analogously, inserting the hardening stress relation (2.3.12) into the flow rule of model II, i.e., Eq. (2.3.15), yields

$$\dot{\gamma}_\alpha = \frac{1}{t_*} \left[\frac{< \tau_\alpha - Y_\alpha - H_\alpha^l \gamma_\alpha + l_\alpha^2 H_\alpha^g \left[\boldsymbol{s}_\alpha \otimes \boldsymbol{s}_\alpha \right] : \left[\boldsymbol{\nabla}_{\mathbf{r}} \otimes \boldsymbol{\nabla}_{\mathbf{r}} \right] \gamma_\alpha >}{C_0} \right]^m . \tag{2.3.20}$$

Clearly, in both cases, the rate equations contain terms depending on the second spatial derivatives of the slips, i.e., $[\boldsymbol{\nabla}_{\mathbf{r}} \otimes \boldsymbol{\nabla}_{\mathbf{r}}]\gamma_\alpha$. These terms influence the effective resolved stress driving the glide-system dislocation motion.[2]

Evers et al. [92] use the absolute signs in the numerator whereas Ekh et al. [85] employ the Macaulay brackets. Therefore, the rate of the plastic slip can be equal to zero in case of model II as opposed to model I where it is always positive. Thus, in case of model I the slip systems are activated viscously at the stress of s_α. On the other hand, model II discretely activates the slip systems at the yield stress Y_α.

One can easily identify what is called the reference plastic strain rate $\dot{\gamma}_0$ in Evers et al. [92] with the inverse of the relaxation time t_* in Ekh et al. [85]. Moreover, the material parameter C_0 of model II has the unit of a stress and plays the same role the slip-system strength s_α does in the slip-system rate equation of model I. However, C_0 is chosen to be constant and the same for all slip-systems α. On the contrary, the slip-system strength differs for slip-systems and depends on the SSD and GND densities and consequently is an implicit function of the slip-system shear as well, i.e., $s_\alpha = s_\alpha(\rho^{\mathrm{SSD}}, \rho^{\mathrm{GND}}; \gamma)$. Anticipating the material parameters stated in Table 2.1 reveals that in the simplest case possible,

---

[2] Different stress terms and their relations are compared in [98] - with the main focus on linking the phenomenological Cosserat theory, the statistical theory of dislocations and strain gradient crystal plasticity.

i.e., no slip and no GND density at initial time $t = 0$, both are of approximately the same magnitude (1 [MPa] vs. 3.7 [MPa] for C_0 respectively ${}^0s_\alpha = s_\alpha(t = 0) = c\mu b\sqrt{a_0\rho_\alpha^{\mathrm{SSD}_0}}$).

While model I accounts for local hardening via the fact that the denominator, the slip-system strength s_α, depends a.o. on the square root of the SSD densities ρ^{SSD}, Ekh et al. [85] include a local hardening contribution in the free energy function Ψ_0 and therefore in the hardening stresses κ_α - which is part of the numerator. Furthermore, both approaches account for gradient hardening in a similar, but not the same way, via directional gradients of the slip-system shear along the given slip directions via $\boldsymbol{\nabla}_{\mathbf{r}}\gamma_\alpha \cdot \boldsymbol{s}_\alpha$.

Lele and Anand's approach [171] is based on the so-called microforce balance representing a viscoplastic yield condition

$$\tau_\alpha + \mathrm{Div}\left(\boldsymbol{\xi}_\alpha^{\mathrm{en}} + \boldsymbol{\xi}_\alpha^{\mathrm{diss}}\right) = f_\alpha\left(\gamma_\alpha, \dot{\gamma}_\alpha\right), \tag{2.3.21}$$

see also Gurtin and Anand [124]. Here, $\boldsymbol{\xi}_\alpha^{\mathrm{en}}$ and $\boldsymbol{\xi}_\alpha^{\mathrm{diss}}$ are referred to as the energetic and the dissipative microstress, respectively, and they expend power over the slip-rate gradient $\nabla_{\mathrm{r}}\dot{\gamma}_\alpha$. What is here denoted by a function f is referred to as a scalar microscopic stress in [171] which expends power over the slip-rate $\dot{\gamma}_\alpha$. In case of model III, the energetic and the dissipative microstress are given by the relations

$$\begin{aligned}
\boldsymbol{\xi}_\alpha^{\mathrm{en}} &= l_\alpha^2 H_\alpha^g \boldsymbol{s}_\alpha \left[\boldsymbol{s}_\alpha \cdot \nabla_{\mathrm{r}}\gamma_\alpha\right] \\
\boldsymbol{\xi}_\alpha^{\mathrm{diss}} &= l_d^2\, {}^0s_\alpha \left[\frac{d_\alpha}{{}^0d}\right]^q \frac{\nabla_{\mathrm{r}}\dot{\gamma}_\alpha \cdot \boldsymbol{s}_\alpha}{d_\alpha}\boldsymbol{s}_\alpha.
\end{aligned} \tag{2.3.22}$$

Moreover,

$$f_\alpha\left(\gamma_\alpha, \dot{\gamma}_\alpha\right) = \left[t_*\dot{\gamma}_\alpha\right]^{1/m} C_0 + Y_\alpha + H_\alpha^l \gamma_\alpha. \tag{2.3.23}$$

Clearly, the energetic microstress $\boldsymbol{\xi}_\alpha^{\mathrm{en}}$ and the dissipative microstress $\boldsymbol{\xi}_\alpha^{\mathrm{diss}}$ are tangent to the corresponding slip plane α. If plastic loading is obtained in case of model II, i.e., if $\tau_\alpha - Y_\alpha - \kappa_\alpha > 0$, the microforce balance is obtained with

$$\begin{aligned}
\boldsymbol{\xi}_\alpha^{\mathrm{en}} &= l_\alpha^2 H_\alpha^g \boldsymbol{s}_\alpha \left[\boldsymbol{s}_\alpha \cdot \nabla_{\mathrm{r}}\gamma_\alpha\right], \\
\boldsymbol{\xi}_\alpha^{\mathrm{diss}} &= \mathbf{0}, \\
f_\alpha\left(\gamma_\alpha, \dot{\gamma}_\alpha\right) &= \left[t_*\dot{\gamma}_\alpha\right]^{1/m} C_0 + Y_\alpha + H_\alpha^l \gamma_\alpha.
\end{aligned} \tag{2.3.24}$$

3

---

[3] As Macaulay brackets have been used in the formulation of the flow rule for model II and III, the microforces are determinate because microclamped respectively microfree grain boundary conditions (cf. Eq. (2.4.6)) are assumed. In case of an elastically deforming grain with a plastically deforming neighboring grain, the microforces at its grain boundary might be indeterminate - e.g. if continuity conditions are assumed at the grain boundary.

In a similar way, in the case of plastic loading $\tau_\alpha^{\text{eff}} > 0$, the rate equation (2.3.5) of model I could be interpreted as a generalized microforce balance with the following choices:

$$\begin{aligned}\boldsymbol{\xi}_\alpha^{\text{en}} &= \frac{\mu R^2}{8\,[1-\nu]} \sum_\beta P_{\beta\alpha} \boldsymbol{s}_\beta \left[\boldsymbol{s}_\beta \cdot \nabla_{\text{r}} \gamma_\beta\right], \\ \boldsymbol{\xi}_\alpha^{\text{diss}} &= \mathbf{0}, \\ f_\alpha\left(\gamma_\alpha, \dot{\gamma}_\alpha, \nabla_{\text{r}} \gamma_\alpha\right) &= \left[\frac{\dot{\gamma}_\alpha}{\dot{\gamma}_0}\right]^{1/m} s_\alpha. \qquad (2.3.25)\end{aligned}$$

A more generalized comparison is chosen at this point, because the slip strength s_α depends on the slip rate $\dot{\gamma}_\alpha$ as well as on the slip gradient $\nabla_{\text{r}}\gamma_\alpha$. Moreover, in the thermodynamic setting of Lele and Anand [171], the energetic microstresses $\boldsymbol{\xi}_\alpha^{\text{en}}$ are determined in terms of the free energy acting as a potential.

2.4. Numerical framework

2.4.1. Governing equations: strong and weak formulation

The mechanical problem is governed by the quasi-static balance of momentum

$$\mathbf{0} = \text{Div}\boldsymbol{P} + \boldsymbol{b}_v, \qquad (2.4.1)$$

with $\boldsymbol{b}_v$ representing the volume forces.

For the slip problem, the following procedure is applied to all three models: In the spirit of Svedberg and Runesson [245], an auxiliary scalar field g_α is introduced for the directional gradient of the slip-system shear γ_α along the given slip direction $\boldsymbol{s}_\alpha$,

$$g_\alpha := \boldsymbol{\nabla}_{\mathbf{r}} \gamma_\alpha \cdot \boldsymbol{s}_\alpha. \qquad (2.4.2)$$

Moreover, following Svedberg and Runesson [245], the slip-system shear γ_α and the scalar g_α are approximated independently in $\mathcal{B}_{0,\,\text{grain}}$ using a so-called dual mixed space-variational format of the gradient equation $g_\alpha - \nabla_{\text{r}}\gamma_\alpha \cdot \boldsymbol{s}_\alpha = 0$, which is a global equation in space. In particular, a three-level Newton–Raphson iteration scheme will be applied, see Section 2.4.2, in which it is possible to choose the FE-approximation of the gradient g_α as $\mathcal{P}_q$ (piecewise polynomial of order q), whereas the FE-approximation of the slip γ_α is chosen as $\mathcal{P}_{q-1}$.

The first roots finite element method in general go back to the 1940s and its earnest triumphant progress started in the 1950s. It is based on the idea that the domain under consideration can be decomposed into a finite number (n_{el}) of disjoint subsets

$$\mathcal{B} = \bigcup_{e=1}^{n_{\text{el}}} \mathcal{B}^e, \qquad \mathcal{B}^i \cap \mathcal{B}^j = \emptyset \text{ for } i \neq j. \qquad (2.4.3)$$

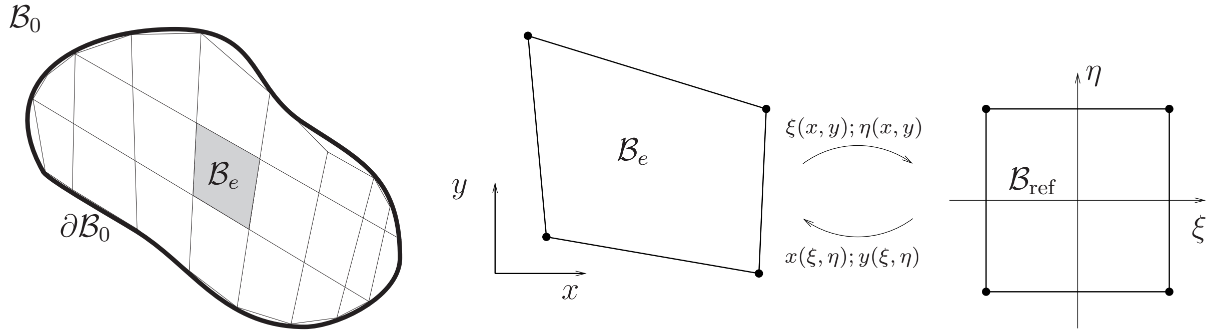

Figure 2.2.: Spatial discretization of a body B: The domain $\mathcal{B}_0$ is subdivided into a finite number of subdomains $\mathcal{B}_e$. Each element $\mathcal{B}_e$ is transferred onto the spatial reference element $\mathcal{B}_{\mathrm{ref}}$.

Today, the finite element method is one of the most powerful numerical methods for solving mathematical models describing engineering problems.

To obtain a finite element formulation, Eqs. (2.4.1) and (2.4.2) are rephrased in a weak form. This is obtained by multiplying with test functions $\delta\boldsymbol{u} \in \mathbb{U}^0$ respectively $\delta g_\alpha \in \mathbb{G}$ and integrating over the undeformed domain $\mathcal{B}_0$. In standard fashion, $\mathbb{U}^0$, a suitable space of test functions, contains those displacements in $\mathbb{U}$ that vanish on the Dirichlet part of the boundary (with prescribed displacements), $\partial\mathcal{B}_{0,\mathrm{D}}$. Moreover, $\mathbb{G}$ denotes a suitable space of test functions for the gradient problem. Thus, the standard variational formats read: Find $\boldsymbol{u} \in \mathbb{U}$ that solves[4]

$$\int\limits_{\mathcal{B}_0} \boldsymbol{P}(\boldsymbol{F}, \boldsymbol{F}_{\mathrm{P}}) : \boldsymbol{H}[\delta\boldsymbol{u}]\,\mathrm{d}V_0 = l(\delta\boldsymbol{u}) \quad \forall\delta\boldsymbol{u} \in \mathbb{U}^0 \tag{2.4.4}$$

and find $g_\alpha \in \mathbb{G}$ that solve

$$\int\limits_{\mathcal{B}_{0,\,\mathrm{grain}}} g_\alpha \delta g_\alpha \,\mathrm{d}V_0 + \int\limits_{\mathcal{B}_{0,\,\mathrm{grain}}} \gamma_\alpha \mathrm{Div}(\boldsymbol{s}_\alpha \delta g_\alpha)\,\mathrm{d}V_0 = \int\limits_{\partial\mathcal{B}_{0,\,\mathrm{grain}}} [\boldsymbol{N}\cdot\boldsymbol{s}_\alpha]\gamma_\alpha \delta g_\alpha \,\mathrm{d}S_0 \quad \forall\delta g_\alpha \in \mathbb{G}. \tag{2.4.5}$$

The linear functional $l(\delta\boldsymbol{u})$ represents the applied load in the interior and the Neumann part of the boundary of $\mathcal{B}_0$ (with prescribed boundary tractions), $\partial\mathcal{B}_{0,\mathrm{N}}$. At a later point, the intergrain conditions (either as boundary conditions on each individual grain or as connectivity conditions that couple the gradient effect in neighboring grains) are incorporated. “Micro-hard” boundary conditions are assumed, i.e.,

$$\gamma_\alpha = 0 \quad \text{on } \partial\mathcal{B}_{0,\,\mathrm{grain}}. \tag{2.4.6}$$

In both cases, the boundary term in Eq. (2.4.5) vanishes, thus Eq. (2.4.5) is simplified as

$$\int\limits_{\mathcal{B}_{0,\,\mathrm{grain}}} g_\alpha \delta g_\alpha \,\mathrm{d}V_0 + \int\limits_{\mathcal{B}_{0,\,\mathrm{grain}}} \gamma_\alpha \mathrm{Div}(\boldsymbol{s}_\alpha \delta g_\alpha)\,\mathrm{d}V_0 = 0. \tag{2.4.7}$$

---

[4] $\boldsymbol{H}[\bullet] = \bullet \otimes \boldsymbol{\nabla}$ is the gradient operator

Subsequently, the variational forms in Eqs. (2.4.4) and (2.4.7) are discretized in space with the help of the finite element method. The pertinent FE–spaces are chosen as follows: Both $\mathbb{U}_h \subset \mathbb{U}$ and $\mathbb{G}_h \subset \mathbb{G}$ are chosen as $\mathcal{P}_1$ (on triangular elements in 2D). In this way, it is achieved that $\boldsymbol{\nabla} g_\alpha$ becomes constant in each triangular element and represents the value at the Gauss point in the centroid.

Remark: For a quite detailed description of the finite element discretization, the reader is referred to [85], in which the exact FE-approximations, the matrix formulation of the finite element problem, the algorithmic iteration matrices and tool boxes describing the flow of the algorithm are given.

2.4.2. Three-level Newton–Raphson iteration strategy

The basic solution strategy is Newton–Raphson iterations on three levels. Global FE–solutions of the balance of momentum and gradient equations will yield the displacement field $\boldsymbol{u}(\boldsymbol{X})$ and the gradient field $g_\alpha(\boldsymbol{X})$ at $t = t_n$. A grain–structure is considered. Each grain igr occupies the domain $\mathcal{B}_\square^{igr}$ with the grain boundary $\partial\mathcal{B}_\square^{igr}$ for $igr = 1, 2, ..., n_{GR}$ (=total number of grains). Hence, $\mathcal{B}_\square = \bigcup\limits_{igr} \mathcal{B}_\square^{igr}$. There exist different model assumptions on “geometric constraints” on the grain structure, which infer restrictions on the displacement $\boldsymbol{u}$. It is highly desirable to have a displacement field as unconstrained as possible. Therefore, only the displacements at the grain-structure (RVE) boundary are prescribed. As part of this strategy, we solve for the displacements on the grain boundaries in an outer iteration loop called “grain boundary iteration loop”. Then, in the “inner grain iteration loop”, updated values of displacements $\boldsymbol{u}$ and gradients g_α within each grain are computed. During the “inner grain iteration loop”, the displacements on the grain boundaries are kept fixed, given the updated values from the “grain boundary iteration loop”. Therefore, the resulting algorithm is suitable for parallelization.

Furthermore, a third iteration loop is carried out. The purpose of this “local iteration loop” is to find updated values for the slip γ_α (and in case of model I also for the SSD density $\rho_\alpha^{\mathrm{SSD}}$) in each Gauss point, given values of $\boldsymbol{u}$ and $\underline{g}$ (as provided from the outer loop).

Both $\gamma_\alpha \in \mathbb{K}_\gamma$ and $\rho_\alpha^{\mathrm{SSD}} \in \mathbb{K}_\rho$ are approximated piecewise constant in the finite element formulation. I.e., $\mathbb{K}_{\gamma,h} \subset \mathbb{K}_\gamma$ and $\mathbb{K}_{\rho,h} \subset \mathbb{K}_\rho$ are chosen as $\mathcal{P}_0$, thus representing the simplest possible approximations. Consequently, the slip γ_α as well as the SSD density $\rho_\alpha^{\mathrm{SSD}}$ also become constant in each triangular element and represent the value at the Gauss point in the centroid.

As mentioned above, see Section 2.4.1, the intergrain conditions are assumed to be micro-hard, i.e., there is no explicit coupling of slip gradients across the grain boundaries. Consequently, we do not have to solve for the gradients g_α during the “grain boundary iteration loop”. In the grain iteration loop, the fully discretized system of equations, based on the weak formulations (2.4.4) and (2.4.7), are coupled. Furthermore, in the inner iteration loop of model I, the rate equations (2.3.5) and (2.3.3) are coupled. In both cases the coupled system is solved monolithically.

2.4.3. Time integration

Although the governing equations (2.4.1) and (2.4.2) are not time-dependent, on the "local iteration loop" level the model contains evolution equations which have to be discretized in time. The state at $t = t_{n-1}$ is assumed to be known for a given time history of the pertinent loading. The purpose is to compute all the relevant variables at $t = t_n$ from the evolution equations. Thus, the fully implicit backward Euler scheme is applied to Eqs. (2.2.7), (2.3.3), (2.3.5), (2.3.15) and (2.3.16). For example, in case of the velocity gradient $\boldsymbol{L}_\mathrm{P} = \dot{\boldsymbol{F}}_\mathrm{P} \cdot \boldsymbol{f}_\mathrm{P}$, i.e., Eq. (2.2.7), this leads to

$$\boldsymbol{I} - {}^{n-1}\boldsymbol{F}_\mathrm{P} \cdot {}^{n}\boldsymbol{f}_\mathrm{P} - \sum_\alpha \Delta t \dot{\gamma}_\alpha [\boldsymbol{s}_\alpha \otimes \boldsymbol{m}_\alpha] = \boldsymbol{0}. \tag{2.4.8}$$

Here, $\Delta t = [t_n - t_{n-1}]$ denotes the current time step and we initialize ${}^{0}\boldsymbol{f}_\mathrm{P} = \boldsymbol{I}$ and ${}^{0}\gamma_\alpha = 0$.

Furthermore, the slip-system shear rate equations have to discretized in time for all three models. For the sake of comprehensibility, we leave the spatial discretization aside for this moment. Therefore, the semi-discrete formulations of Eqs. (2.3.5), (2.3.15) and (2.3.16) read:

$$\begin{aligned}
&\text{model I}\\
&0 = \frac{1}{\dot{\gamma}_0}\Delta\gamma_\alpha - \Delta t \left[\frac{|\tau_\alpha^\mathrm{eff}|}{s_\alpha}\right]^m,\\
&\text{model II}\\
&0 = t_* \Delta\gamma_\alpha - \Delta t \left[\frac{< \tau_\alpha - Y_\alpha - \kappa_\alpha >}{C_0}\right]^m,\\
&\text{model III}\\
&0 = t_* \Delta\gamma_\alpha - \Delta t \left[\frac{< \tau_\alpha - Y_\alpha - \kappa_\alpha >}{C_0}\right]^m - l_d^2\, {}^{0}s_\alpha \mathrm{Div}\left(\left[\frac{d_\alpha}{{}^{0}d}\right]^q \frac{\Delta g_\alpha}{d_\alpha} \cdot \boldsymbol{s}_\alpha\right).
\end{aligned} \tag{2.4.9}$$

In case of the rate equation of model III, it is used $\nabla_\mathrm{r}\dot{\gamma}_\alpha \cdot \boldsymbol{s}_\alpha = \dot{g}_\alpha$.

2.5. Numerical example: macro-scale simple shear

2.5.1. Set-up of the model

The grain-structure, occupying the square domain $\mathcal{B}_\square$ in 2D with boundary $\partial\mathcal{B}_\square$, as shown in Figure 2.3, is considered. Dirichlet boundary conditions on $\partial\mathcal{B}_{\square,\mathrm{D}}$ are chosen that correspond to a prescribed macro-scale deformation gradient $\boldsymbol{F}_\mathrm{macro} = \boldsymbol{I} + \boldsymbol{H}_\mathrm{macro}$ (where the subscript "macro" indicates a macro–scale quantity). Hence, the boundary conditions for the mechanical problem are

$$\boldsymbol{u}(\boldsymbol{X}) = \boldsymbol{H}_\mathrm{macro} \cdot \boldsymbol{X}, \quad \boldsymbol{X} \in \partial\mathcal{B}_\square. \tag{2.5.1}$$

As a consequence, the appropriate spaces of displacements for the sub–scale are defined as

$$\mathbb{U}(\boldsymbol{H}_{\text{macro}}) = \{\boldsymbol{u} |\ \ \boldsymbol{u} = \boldsymbol{H}_{\text{macro}} \cdot \boldsymbol{X} \quad \text{for } \boldsymbol{X} \in \partial\mathcal{B}_{\square}\}. \tag{2.5.2}$$

The grain-structure consists of 4 grains, see Figure 2.3, and is discretized by 1990 elements (1384 nodes).

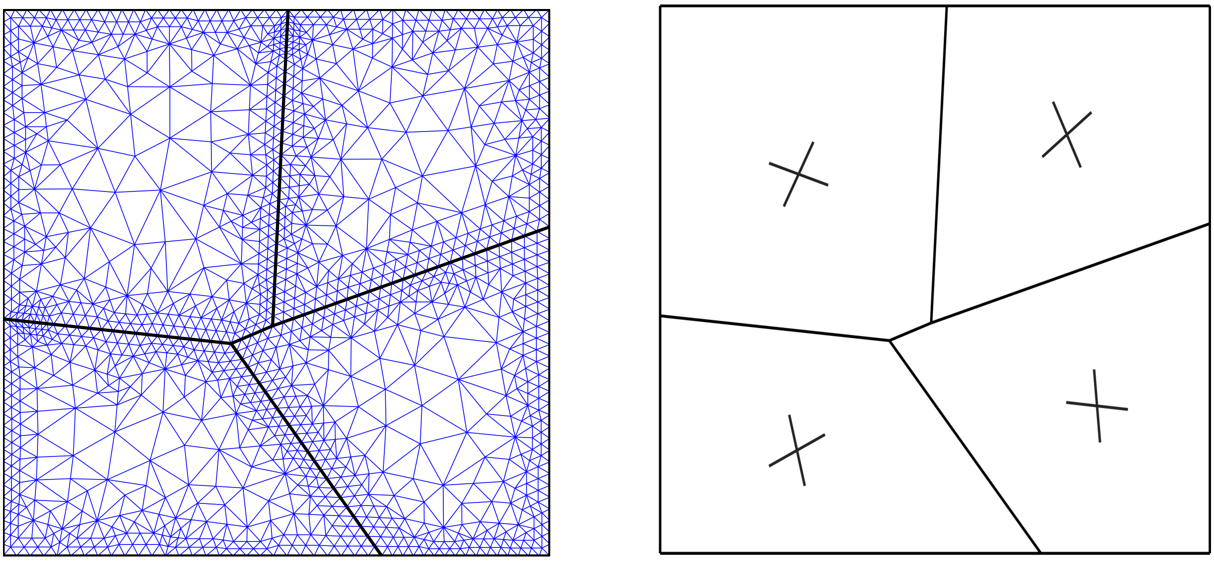

Figure 2.3.: Left: Discretization and grain geometry used during simulations. The square grain-structure consists of 4 grains and the thick black lines represent the grain boundaries. The grains are discretized with 726 (upper left grain), 620 (upper right), 630 (lower left), and 614 (lower right) elements, respectively. The mesh is refined near the grain boundaries. The side length L of the grain-structure is varied during simulations in order to capture the size effects.
Right: Schematic sketch of slip plane directions $\boldsymbol{s}_\alpha$. Double slip is assumed and slip plane directions are randomly distributed.

So far, nothing has been said about the number of slip-systems. Henceforth, the numerical study is limited to double slip in order reduce computation time. From the modeling point of view this means $\alpha = 4$, as explained at the end of Section 2.2. The directions $\boldsymbol{s}_\alpha$ of the slips are randomly distributed, see Figure 2.3. Values of the material parameters are listed in Table 2.1.

Plane strain is assumed. In particular, the standard representative example of simple shear on the macro-scale is considered in order to highlight the major characteristics of the different models. Simple shear is defined by $\boldsymbol{F}_{\text{macro}} = \boldsymbol{I} + \bar{\gamma}\boldsymbol{e}_1 \otimes \boldsymbol{e}_2$, where $\bar{\gamma}$ is the macroscopic shear deformation. Computations are carried out in monotonic loading with $\bar{\gamma}_{\max} = 0.15$ with the constant loading rate of 0.03 [1/s].

Remark (Material parameters): The slip rate equation of model I, i.e., Eq. (2.3.5), is defined in terms of the reference plastic strain rate $\dot{\gamma}_0$ and the slip resistance s_α. In

Parameter	Symbol	Value				
Young's modulus	E	$2 \cdot 10^5$	[MPa]			
Poisson's ratio	ν	0.3				
local hardening modulus	H^l_α	10^4	[MPa]	resp.	0	[MPa]
gradient hardening modulus	H^g_α	$4 \cdot 10^7$	[MPa]			
internal length scale	l_α	10^{-2}	[mm]			
initial yield stress	Y_α	10^3	[MPa]	resp.	0	[MPa]
relaxation time	t_*	10^4	[s]			
material constant	C_0	1	[MPa]			
material constant	c	0.3				
reference plastic strain rate	$\dot{\gamma}_0$	0.0001	[s^{-1}]			
rate sensitivity parameter	m	1		resp.	0.02	
strain rate sensitivity parameter	q	1				
magnitude of Burger's vector	b	0.256	[nm]			
immobilization coefficient	h_0	1				
interaction coefficient	a_0	0.06				
radius GND evaluation region	R	10^{-1}	[mm]			
critical annihilation length	y_c	1.6	[nm]			
initial SSD density	ρ^{SSD_0}	$7 \cdot 10^{12}$	[m^{-2}]			
initial GND density	ρ^{GND_0}	0	[m^{-2}]			
material constant	K	25				
initial slip resistance	${}^0s_\alpha = s_\alpha(t=0)$	3.7	[MPa]			
dissipative length scale	l_d	0.06	[μm]	resp.	0	[μm]
reference rate	${}^0d$	0.0001	[s^{-1}]			

Table 2.1.: Material parameters. The data is taken from [85], [91], [92] and [171]. Some of the values are adjusted in such a way that comparison between the models is possible, see also the remark on this aspect. During simulations some of the parameters are varied in order to study their influence in the material behavior.

contrast, the slip rate equations of model II and III, i.e., Eqs. (2.3.15) and (2.3.16), are expressed in terms of the relaxation time t_* and the constant C_0. In order to derive comparable results, one has to take care that $1/[t_* C_0^m] \approx \dot{\gamma}_0 / s_\alpha^m(t=0)$.
In addition, the fraction $\mu R / [8\,[1-\nu]]$ in Eq. (2.3.19) (model I) plays a similar role as $l_\alpha^2 H_\alpha^g$ in Eq. (2.3.20) (model II).
As to the choice of the yield stress, a constant value of Y_α is chosen in model II, whereas the yield stress of model I is strain-rate dependent and incorporated indirectly via s_α.

2.5.2. Discussion of results

First, model I is examined. Figure 2.4 shows a size effect for fixed material parameters but for increasing side length L of the grain-structure. The plot shows a representation of the plastic strain field in terms of "effective" effective shear strain $\gamma_{\text{eff}} := \sqrt{\gamma_1^2 + \gamma_2^2 + \gamma_3^2 + \gamma_4^2}$. Since the (absolute) size of the boundary layers with large gradient effects should be approximately the same regardless of the actual size of the grains, the boundary layers will appear thinner when the grain size increases (see Figure 2.4).

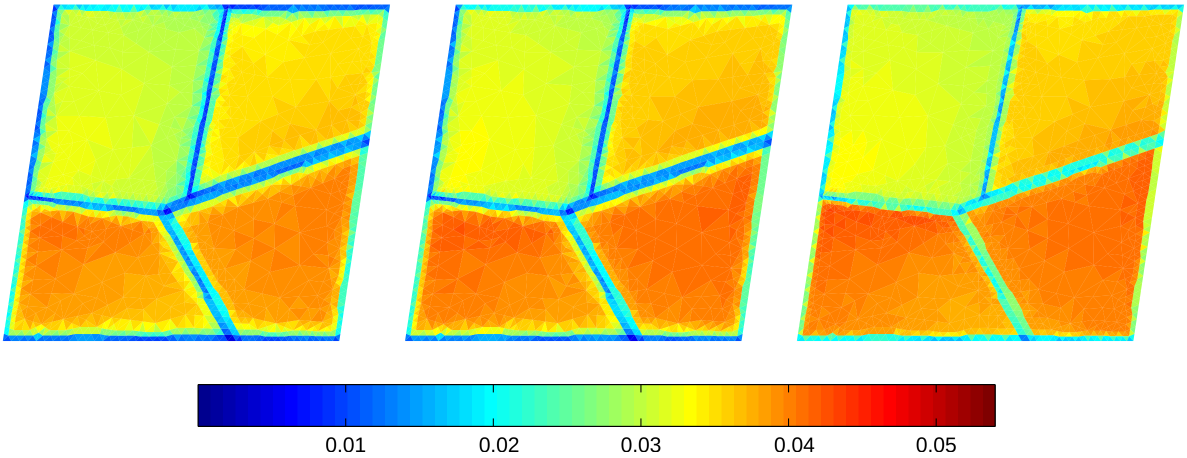

Figure 2.4.: Model I, Evers et al. [92]. Effective hardening strain $\gamma_{\text{eff}} := \sqrt{\gamma_1^2 + \gamma_2^2 + \gamma_3^2 + \gamma_4^2}$. From left to right the solutions for grain-structure side lengths $L = 4$ μm, $L = 8$ μm, and $L = 16$ μm are depicted. The evolution of the slip-system shear is given in Eq. (2.3.5). Computations are carried out in monotonic loading with a maximum macroscopic shear deformation $\bar{\gamma}_{\max} = 0.15$. The displacement field inside the grain-structure is unconstrained. The slip resistance s_α is computed according to Eq. (2.3.9), the rate sensitivity parameter reads $m = 1$.

The macroscopic stress-strain response in terms of the nominal shear stress component $\bar{P}_{12}$ versus the macroscopic shear $\bar{\gamma}$ is shown in Figure 2.5. As expected, stiffer response in the hardening regime can be seen for smaller grain size. This observation is in agreement with the findings of Bayley et al. [38] and Evers et al. [92]. The size-dependence of the stress-strain response is due the existence of the slip gradient in the numerator of Eq. (2.3.19). As already reported by Evers et al. [92], a size dependence for both densities can be found. Figure 2.6 exemplarily shows the distribution of the GND density ρ_{GND} for two sample lengths. On the left $L = 4$ μm is depicted and on the right the distribution for a grain-structure with length $L = 16$ μm is plotted. In agreement with the results of [92, 171], the GND density ρ_{GND} mainly develops near the grain boundaries. Moreover, the significant difference between the results for the two lengths is also observed. This is due to the fact that the distance between the grain middle and the boundary is much smaller in the case of $L = 4$ μm - the boundary being the place where the plastic slip is blocked and therefore GNDs develop. On the contrary, the SSD density ρ_{SSD} remains small near the grain boundaries, see Figure 2.7. Furthermore, the order of magnitude of the GND and the SSD densities are roughly the same. For the sake of brevity and as we mainly aim at comparing different approaches, the figures of this finding for the other examples simulated with model I are omitted. Instead it is referred to the discussion in Evers et al. [92].

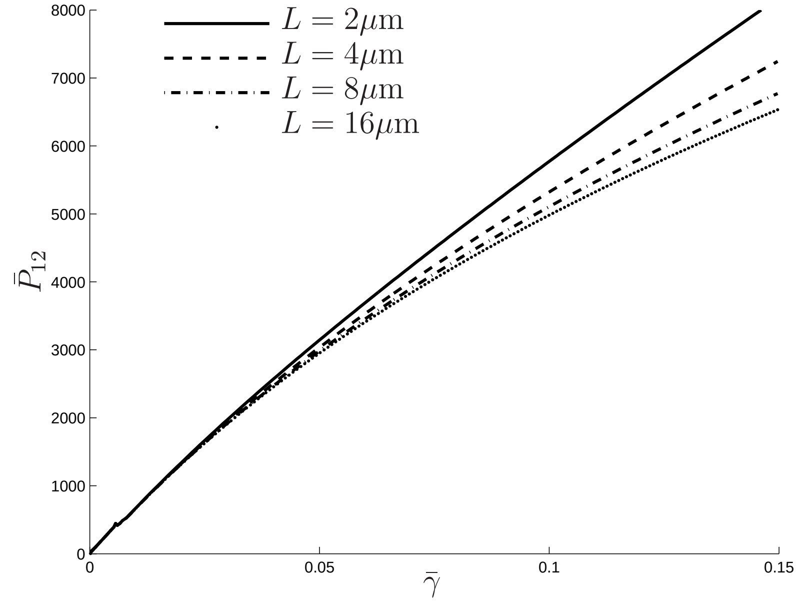

Figure 2.5.: Model I, Evers et al. [92]. Macroscopic stress–strain response ($\bar{P}_{12}$ vs. $\bar{\gamma}$) showing the size dependence on the amount of hardening. Under the assumption of increasing slip resistance s_α according to Eq. (2.3.9) and $m = 1$.

One of the differences between model I and II is the use of the absolute signs respectively Macauley brackets. We ran simulations in which we applied Macauley brackets to Eq. (2.3.5). Due to the fact that load is applied only in one direction, there is no difference for this particular numerical example. However, if loading directions change during the simulation, there should be an impact.

In order to examine the effect of gradient hardening only, simulations are carried out with a constant slip resistance $s_\alpha = C_0 = 1$ [MPa]. In other words, local hardening is omitted. The results are depicted in Figures 2.8 and 2.9. Due to the gradient contribution, the stress-strain response still depends on the grain-structure side length L. However, the material response is significantly softer than in Figure 2.5.

In [92], the rate sensitivity parameter $m = 20$ is used, which is significantly lower than our choice. Therefore, simulations with a rate sensitivity parameter of $m = 5$ are run as

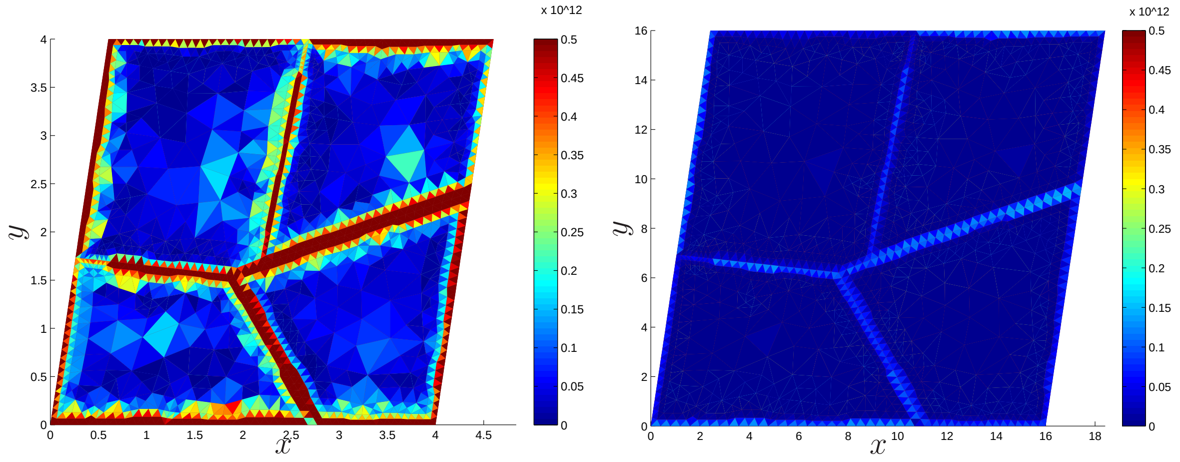

Figure 2.6.: Model I, Evers et al. [92]. Slip-system 1 GND densities are plotted for two samples lengths after applying 15% shear. One the left the distribution of the GND density ρ_{GND} for a grain structure with $L = 4\ \mu$m and on the right with $L = 16\ \mu$m can be seen. A size-dependence is found for the density distribution. Under the assumption of increasing slip resistance s_α according to Eq. (2.3.9) and $m = 1$. The sign of the ρ_{GND} is ignored in this plot. The results are in qualitative accordance to Evers et al. [92].

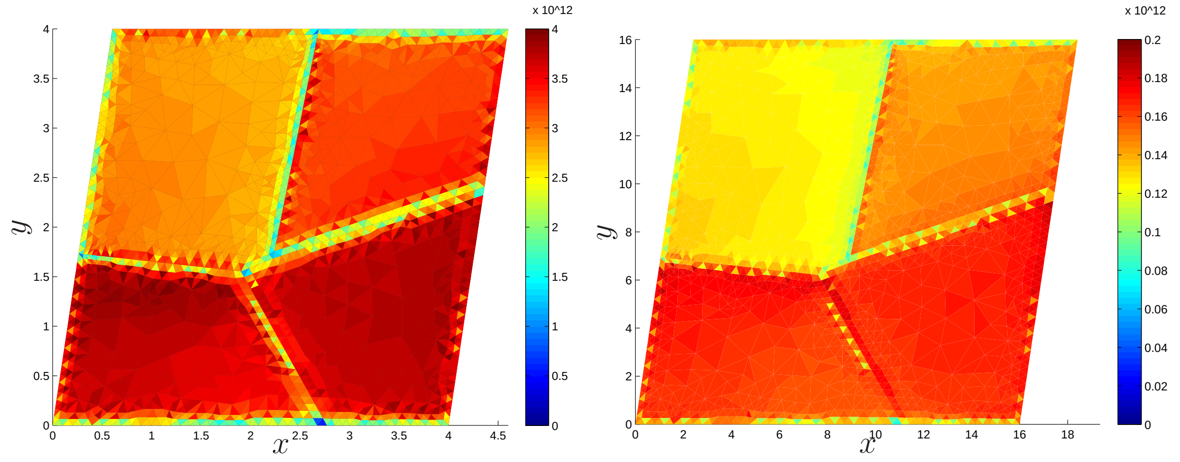

Figure 2.7.: Model I, Evers et al. [92]. Slip-system 1 SSD densities are illustrated for two samples lengths after applying 15% shear. One the left the distribution of the SSD density ρ_{SSD} for a grain structure with $L = 4\ \mu$m and on the right with $L = 16\ \mu$m can be seen. ρ_{SSD} decreases towards the boundary. Under the assumption of increasing slip resistance s_α according to Eq. (2.3.9) and $m = 1$. The results are in accordance to Evers et al. [92].

well in order to investigate its influence, see Figure 2.10. The higher the rate sensitivity parameter m, the softer responds the material.

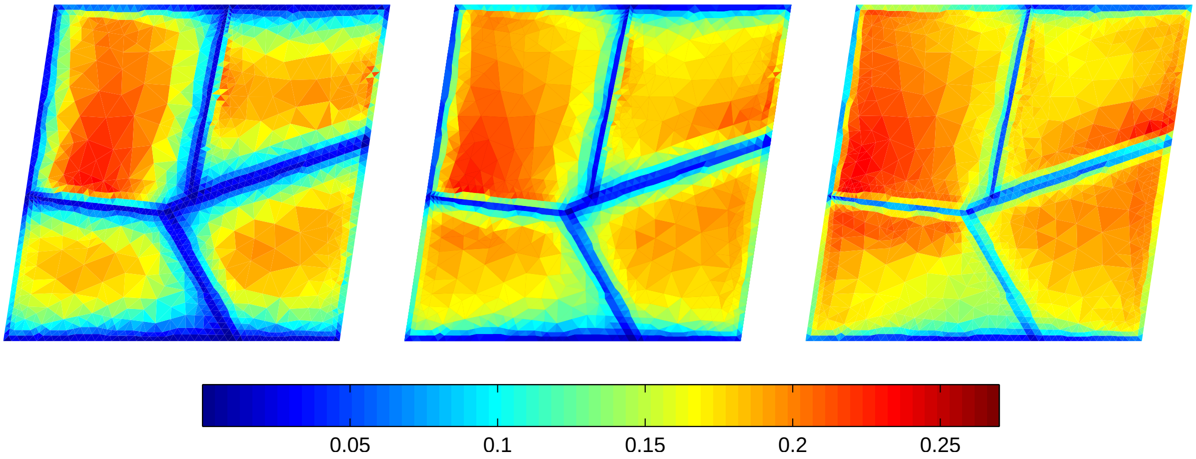

Figure 2.8.: Model I, Evers et al. [92]. Effective hardening strain $\gamma_{\text{eff}} := \sqrt{\sum_\alpha \gamma_\alpha}$. From left to right the accumulated plastic strain field for grain-structure side lengths $L = 4$ μm, $L = 8$ μm, and $L = 16$ μm are depicted. The evolution of the slip-system shear is given in Eq. (2.3.5). Computations are carried out in monotonic loading with a maximum macroscopic shear deformation $\bar{\gamma}_{\max} = 0.15$. The displacement field inside the grain-structure is unconstrained. The slip resistance s_α is assumed to be constant with $s_\alpha = C_0 = 1$ [MPa] and $m = 1$.

Now, model II is studied. In all simulations of model II, the rate sensitivity parameter $m = 1$ is used. Figure 2.11 presents the distribution of the effective plastic slip γ_{eff} according to Eq. (2.3.15) with an initial yield stress $Y_\alpha = 10^3$ [MPa] for different grain-structure side lengths. The macroscopic stress-strain response is shown in Figure 2.12. The results are qualitatively similar to those reported in Ekh et al. [85].

As in the case of model I, the size-dependent stress-strain response is due to the gradient effect. Although both models reach a similar macroscopic stress $\bar{P}_{12}$ at 15 % shear, the effective slip-system shear of model I is smaller (cf. Figures 2.4 and 2.11). For the chosen parameter values less plastic strain develops. Thus, model I accommodates more shear elastically than model II.

In order to investigate the influence of the initial yield stress Y_α and the local hardening module H^l_α (which contributes to the hardening stresses κ_α) in model II, those parameters are neglected one after the other. Figures 2.13 and 2.14 illustrate the solution with initial yield stress $Y_\alpha = 0$ [MPa] and the local hardening module $H^l_\alpha = 10^4$ [MPa] for all

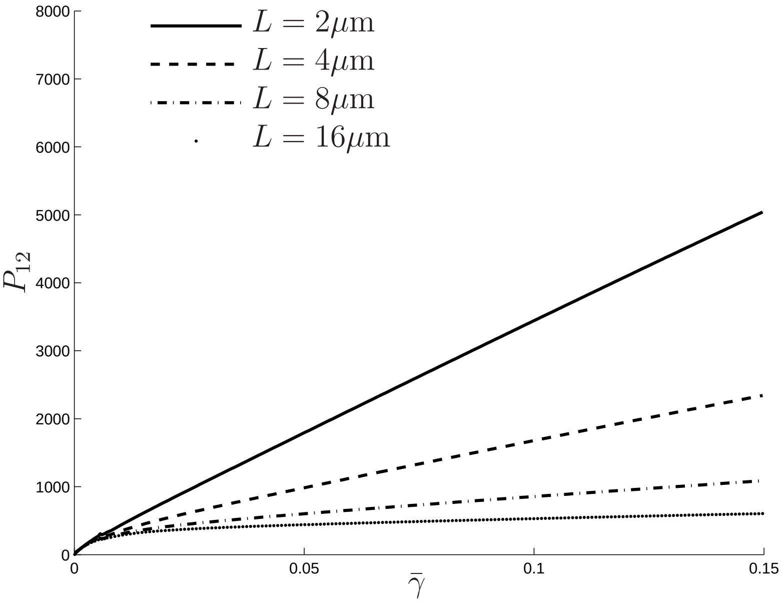

Figure 2.9.: Model I, Evers et al. [92]. Macroscopic stress–strain response ($\bar{P}_{12}$ vs. $\bar{\gamma}$) showing the size dependence on the amount of hardening. $m = 1$. Constant slip resistance $s_\alpha = C_0 = 1$ [MPa] presumed, i.e., no local contribution to the hardening exists. The grain-structure still shows a size-dependent response.

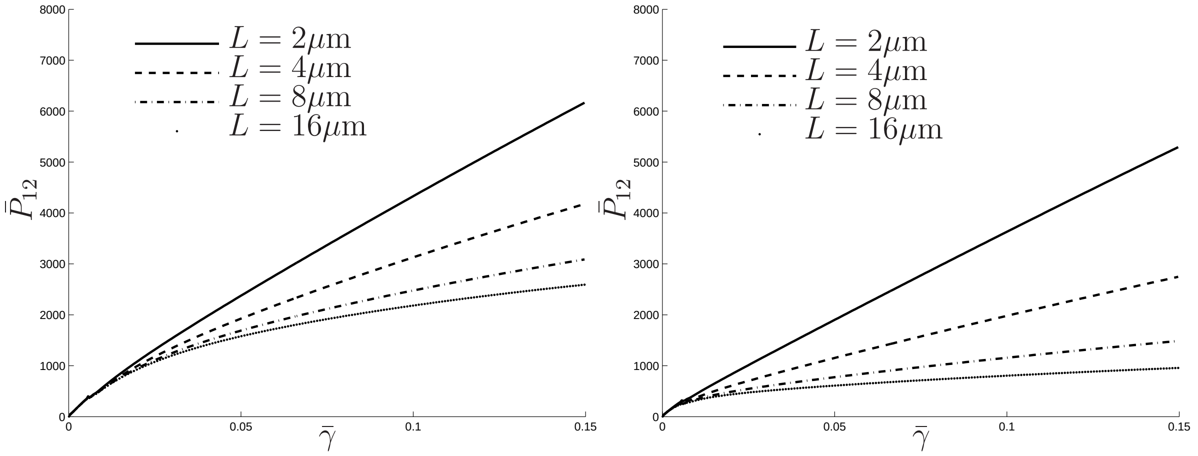

Figure 2.10.: Model I, Evers et al. [92]. Macroscopic stress–strain response ($\bar{P}_{12}$ vs. $\bar{\gamma}$) showing the size dependence on the amount of hardening. Local hardening is admitted. The rate sensitivity parameter m is raised to $m = 5$ (left) and $m = 20$ (right). The higher the rate sensitivity parameter m, the softer responds the material.

slip-systems $\alpha = 1, \ldots, 4$. As expected, the plots of the effective hardening strain γ_{eff} (Figure 2.13) and the macroscopic stress-strain response (Figure 2.14) reveal that the initial yield stress $Y_\alpha = 10^3$ [MPa] leads to plastic yielding from the beginning of the deformation.

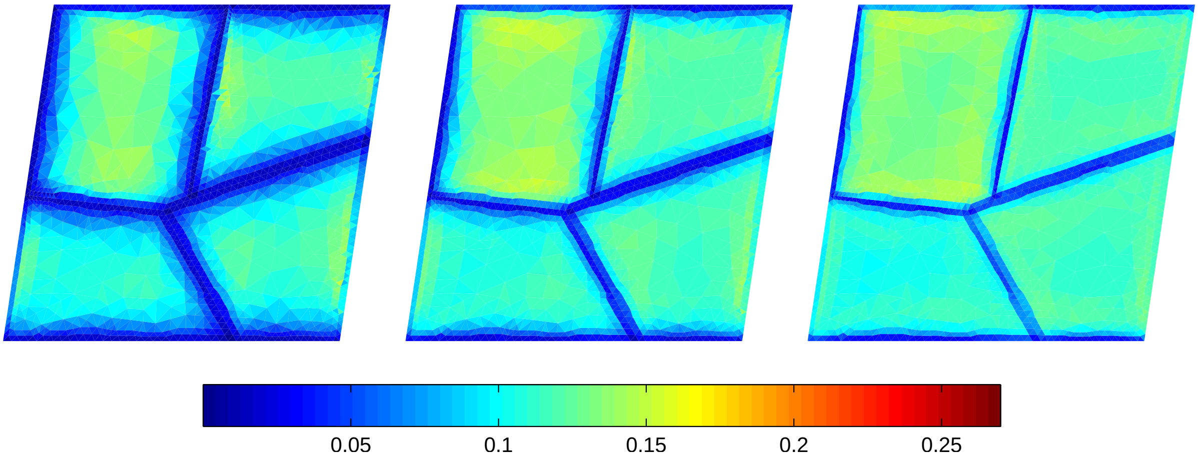

Figure 2.11.: Model II, Ekh et al. [85]. Effective hardening strain $\gamma_{\text{eff}} = \sqrt{\sum_\alpha \gamma_\alpha}$. From left to right the accumulated plastic strain field for grain-structure side lengths $L = 4$ μm, $L = 8$ μm, and $L = 16$ μm are depicted. The evolution of the slip-system shear γ_α is given in Eq. (2.3.15) - with an initial yield stress $Y_\alpha = 10^3$ [MPa] and a local hardening module $H^l_\alpha = 10^4$ [MPa] for all slip-systems $\alpha = 1, \ldots, 4$. The rate sensitivity parameter is set at $m = 1$. The displacement field inside the grain-structure is unconstrained. Since the (absolute) size of the boundary layers with large gradient effects is approximately the same regardless of the actual size of the grains, the boundary layers appear thinner as the grain size increases.

Subsequently, the local hardening module is additionally chosen to be zero, i.e., $H^l_\alpha = 0$ [MPa] for all slip-systems $\alpha = 1, \ldots, 4$ and $Y_\alpha = 0$ [MPa]. It is observed that a material with a vanishing local hardening module H^l_α still shows a size-dependent stiffness response, see Figures 2.15 and 2.16. The general stiffness of the material decreases considerably, though. As already mentioned in Section 2.3.4, model II includes the local hardening contribution in the hardening stress κ_α and, thus, in the numerator, whereas model I takes it into account via the slip-system strength s_α and, therefore, in the denominator. The comparison of Figures 2.5 and 2.9 versus 2.14 and 2.16 underlines that, nevertheless, both models have a similar local hardening response. Figures 2.5 and 2.14 include local hardening, whereas Figures 2.9 and 2.16 neglect this contribution - leading to a significant decrease of the material's stiffness. Moreover, the cases studied in Figures 2.8 and 2.9

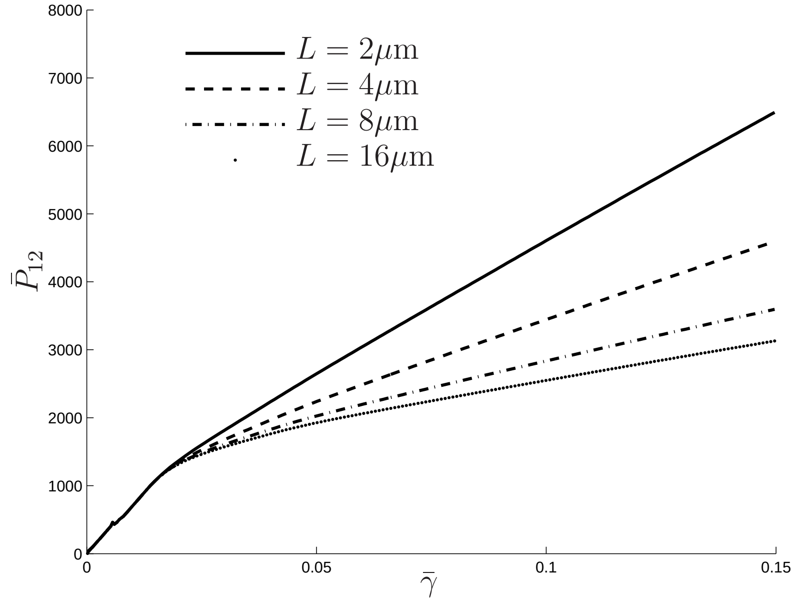

Figure 2.12.: Model II, Ekh et al. [85]. Initial yield stress $Y_\alpha = 10^3$ [MPa], local hardening module $H^l_\alpha = 10^4$ [MPa] for all slip-systems $\alpha = 1, \ldots, 4$, $m = 1$.. Macroscopic stress–strain response ($\bar{P}_{12}$ vs. $\bar{\gamma}$) showing the size dependence on the amount of hardening.

respectively 2.15 and 2.16 show the influence of latent hardening. In this special case, the only difference between the two slip laws of model I and II is that latent hardening is included in the gradient hardening of model I.

In all three cases, the macroscopic stress–strain response is grain-structure size dependent. However, there is no size-dependence in the initial yield limit, see Figures 2.12, 2.14 and 2.16. This contradicts the well-known Hall-–Petch relation which states that the yield limit is in fact size dependent.

Model II corresponds to what Anand, Lele and Gurtin [124, 171] call the case of gradient energetics respectively energetic hardening. Combining model II with what they refer to as “dissipative strengthening” leads to model III. The results for model III are pointed out in Figures 2.17 - 2.19. As stated by Lele and Anand [171], the divergence term in the flow rule (2.3.16) leads to a size-dependent initial yield limit, see Figure 2.19. However, for the parameters chosen in this example of large deformations, Figure 2.19 shows that the effect unfortunately is not strong as in the example of [171]. However, in [171] in all the simulations in which the nonstandard higher-order dissipative term was considered, the energetic hardening and standard isotropic hardening were set at zero. In our example, a higher value for the dissipative lengthscale l_d would have been desirable in order to receive a considerable side-length dependent yield stress for the case that local hardening is admitted (Figure 2.18).

As stated in Lele and Anand [171], the model “possesses a mathematically attractive structure, our experience with numerical experiments which use these constitutive equa-

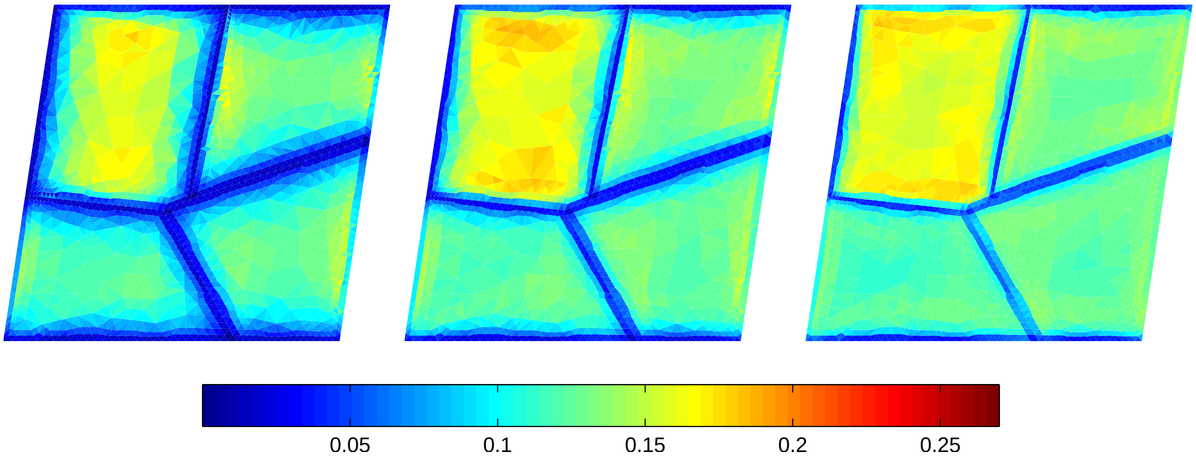

Figure 2.13.: Model II, Ekh et al. [85]. Effective hardening strain $\gamma_{\text{eff}} = \sqrt{\sum_\alpha \gamma_\alpha}$. The accumulated plastic strain field for grain-structure side lengths $L = 4$ μm, $L = 8$ μm, and $L = 16$ μm (from left to right) are depicted. The evolution of the slip-system shear γ_α is given in Eq. (2.3.15) - with an initial yield stress $Y_\alpha = 0$ [MPa] and a local hardening module $H^l_\alpha = 10^4$ [MPa] for all slip-systems $\alpha = 1, \ldots, 4$. Rate sensitivity parameter $m = 1$. The displacement field inside the grain-structure is unconstrained. It is observed that the non-existence of the initial yield stress Y_α leads to plastic yielding from the beginning of the deformation, see Figure 2.11 for comparison.

tions is that they are too tightly coupled". A completely different numerical approach was applied in this contribution[5] , nevertheless and unfortunately, for larger l_d the code did not converge.

2.6. Conclusion

Three different frameworks for including gradient hardening into crystal plasticity models were studied. Model I is physically based and has already proven to be capable of handling advanced modeling of hardening. As compared to this model, the purpose of model II is to be simple, e.g. with respect to the hardening, but still able to show realistic simulation

---

[5] Lele and Anand implemented the theory by writing a nine-node quadratic user-element subroutine for the commercial finite element package ABAQUS/Standard.

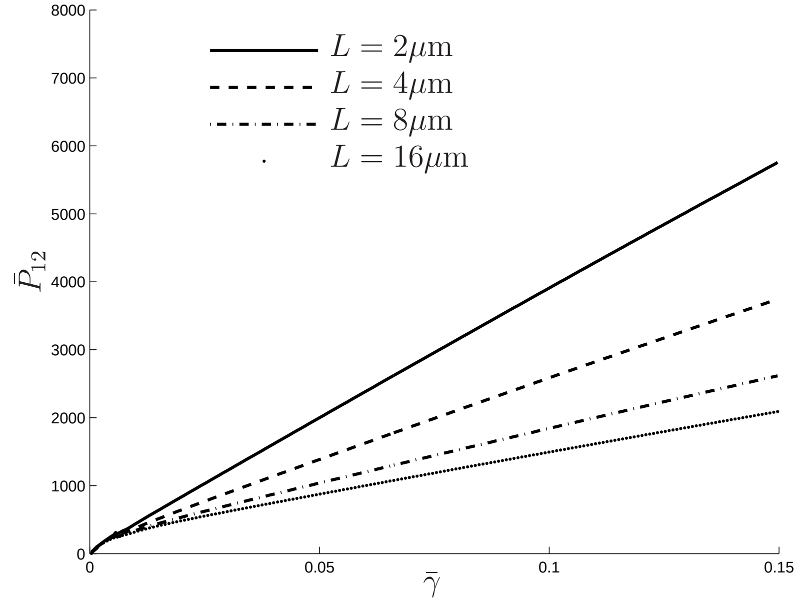

Figure 2.14.: Model II, Ekh et al. [85]. Initial yield stress $Y_\alpha = 0$ [MPa], local hardening module $H^l_\alpha = 10^4$ [MPa] for all slip-systems $\alpha = 1, \ldots, 4$, $m = 1$. Macroscopic stress–strain response ($\bar{P}_{12}$ vs. $\bar{\gamma}$) showing the size dependence on the amount of hardening and the influence of the initial yield stress Y_α, see Figure 2.12 for comparison.

results. Moreover, it is formulated in a thermodynamic setting - as is model III. In both cases, the inelastic part of the free energy was assumed to include contributions from the gradient of hardening along each slip direction.

One can clearly see the different behavior depending on the model assumptions. Model I is capable of mapping more effects than model II, such as latent hardening. However, it is also much more complex which leads to higher computation time. Model III is a first step towards mapping the Hall–Petch relation, i.e. the square-root dependence of the yield strength on the grain-size. Unfortunately, numerical convergence problems so far limit the advantage of the mathematically attractive structure. By investigating the meaning and the influence of some of the parameters of the strain gradient crystal plasticity models discussed above, this contribution presents a step towards the enhancement of such theories.

Moreover, an efficient discretization scheme suitable for parallelization has been suggested. The arising coupled boundary value problems were discretized with finite elements in space and the backward Euler in time. A dual mixed approach with displacements and gradient hardening variables as degrees of freedom is used. Such an approach is attractive since any crystal plasticity code (for the local problem) can be used by simply modifying the current yield stress due to the given gradient hardening variables in the nodes. The dual mixed finite element algorithm renders a coupled two-field problem which is solved monolithically. In particular, an algorithm suitable for parallelization was presented,

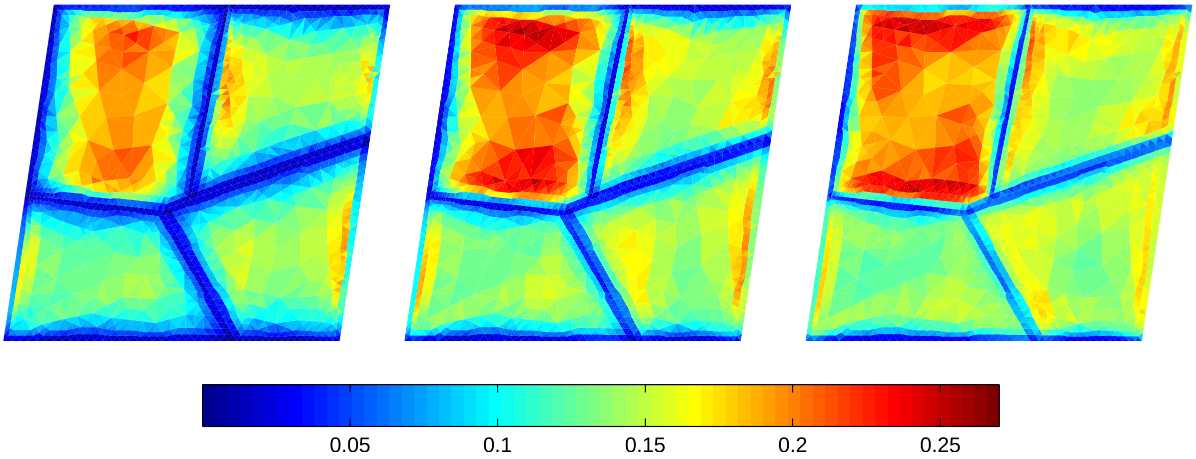

Figure 2.15.: Model II, Ekh et al. [85]. Effective hardening strain $\gamma_{\text{eff}} = \sqrt{\sum_\alpha \gamma_\alpha}$. From left to right the solutions for RVE side lengths $L = 4$ μm, $L = 8$ μm, and $L = 16$ μm are depicted. The evolution of the slip-system shear γ_α is given in Eq. (2.3.15) - with an initial yield stress $Y_\alpha = 0$ [MPa] and a local hardening module $H^l_\alpha = 0$ [MPa] for all slip-systems $\alpha = 1, \ldots, 4$. $m = 1$. The displacement field inside the grain-structure is unconstrained. Neglecting the local hardening module H^l_α leads to significantly more slip inside the grain-structure, see Figures 2.11 and 2.13 for comparison.

where each grain is treated as a subproblem. A fast solution algorithm opens up for a variety of applications, since the resulting finite element problems tend to be rather large. Possible applications are concurrent multiscale modeling, or three dimensional models, for example.

In conclusion, the presented models and the numerical strategy are all suitable for handling, e.g., more advanced modeling of the hardening. Nevertheless, work remains to be done with respect to both, the modeling (e.g. an accurate prediction of the Hall–Petch effect) and the numerical implementation (regarding e.g. the nonstandard higher order dissipative term).

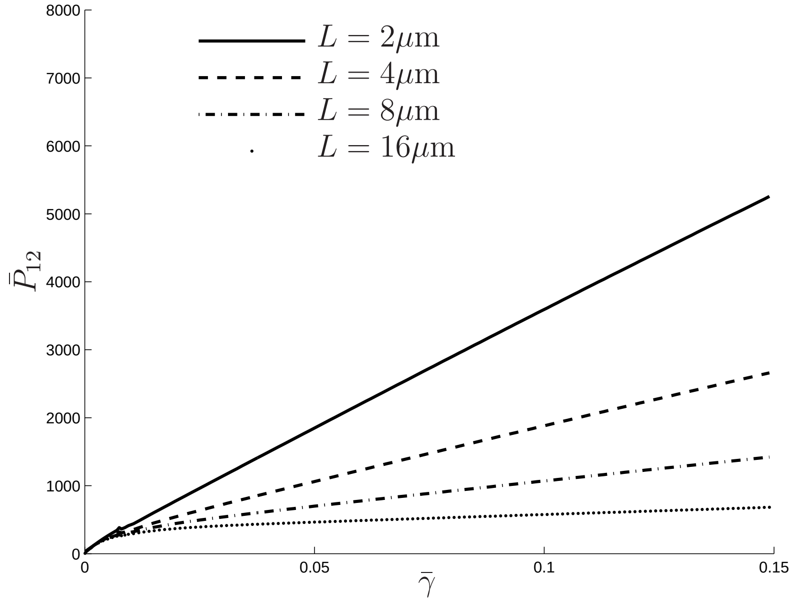

Figure 2.16.: Model II, Ekh et al. [85]. Initial yield stress $Y_\alpha = 0$ [MPa], local hardening moduli $H^l_\alpha = 0$ [MPa] for all slip-systems $\alpha = 1, \ldots, 4$. Macroscopic stress–strain response ($\bar{P}_{12}$ vs. $\bar{\gamma}$) showing the size dependence on the amount of hardening in case of vanishing local hardening moduli H^l_α. Again, it can be stated that smaller the grain-structure size the stiffer is the material's response. However, it can clearly be seen that $H^l_\alpha = 0$ [MPa] leads to a significant decrease in the stiffness for all lengths L. $m = 1$.

Appendix: Thermodynamic considerations

As mentioned above, there exists a thermodynamic setting for model II and III. First, the ideas of Ekh et al. [85] (model II) are presented and a short derivation for the definition of the hardening stresses κ_α, i.e., Eq. (2.3.12), is given. Second, the considerations of Lele and Anand [171], see also Gurtin and Anand [124], are summarized.

In rational thermodynamics the second law imposes restrictions on constitutive equations. Whereas there exists a unified opinion about the balance laws, this is not the case for the second law of thermodynamics. Exploitations of the entropy inequality are based on distinctive mathematical procedures with the help of which conditions for a given class of constitutive material behaviors are derived in order to be compatible with the entropy inequality. Probably the best-known principle is that of Clausius and Duhem in the framework established by Coleman and Noll [61].

The thermodynamic formulation of field and constitutive relations are ultimately formulated in the context of the total energy balance. Isothermal and quasi-static conditions are considered. In this case, the total energy balance reads

$$\mathrm{D}_t \int_{\mathcal{B}_0} \Psi_0 \,\mathrm{d}V + \int_{\mathcal{B}_0} \mathcal{D}_0 \,\mathrm{d}V + \int_{\mathcal{B}_0} W_{\text{int}} \,\mathrm{d}V = 0 \tag{2.6.1}$$

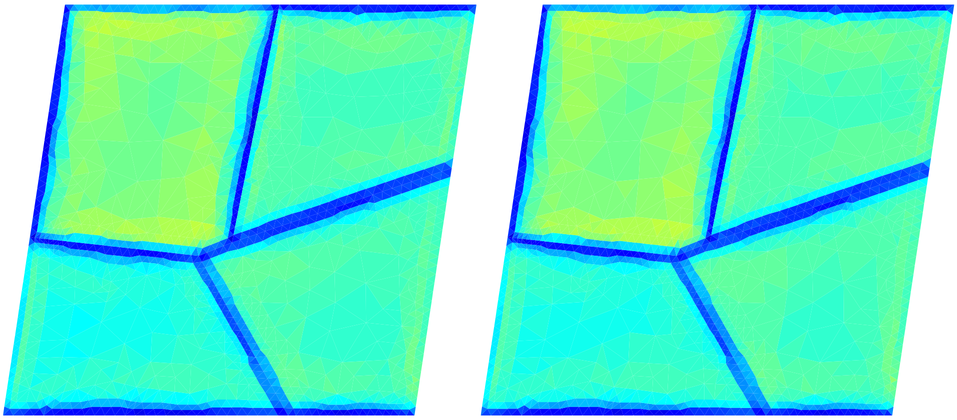

Figure 2.17.: Model III. Effective hardening strain $\gamma_{\text{eff}} = \sqrt{\sum_\alpha \gamma_\alpha}$. Left the accumulated plastic strain field according to model III with $l_d = 0$ μm for a grain-structure side length 16 μm is depicted. On the right, the accumulated plastic strain field according with $l_d = 0.06$ μm is shown. Computations are carried out in monotonic loading with a maximum macroscopic shear deformation $\bar{\gamma}_{\max} = 0.15$. The evolution of the slip-system shear γ_α is given in Eq. (2.3.16) - with an initial yield stress $Y_\alpha = 10^3$ [MPa] and a local hardening module $H^l_\alpha = 10^4$ [MPa] for all slip-systems $\alpha = 1, \ldots, 4$. The influence of the divergence term is very small, compare Figures 2.18 and 2.19. The displacement field inside the grain-structure is unconstrained and $m = 1$..

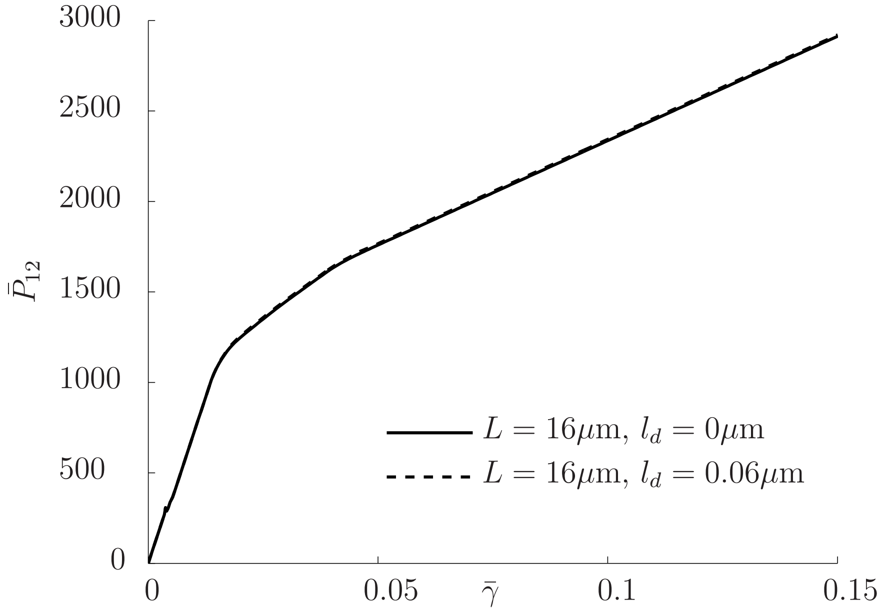

Figure 2.18.: Model III. Initial yield stress $Y_\alpha = 10^3$ [MPa], local hardening module $H^l_\alpha = 10^4$ [MPa] for all slip-systems $\alpha = 1, \ldots, 4$, $m = 1$. Macroscopic stress–strain response ($\bar{P}_{12}$ vs. $\bar{\gamma}$). Unfortunately, the influence of the divergence term can hardly been seen in this example.

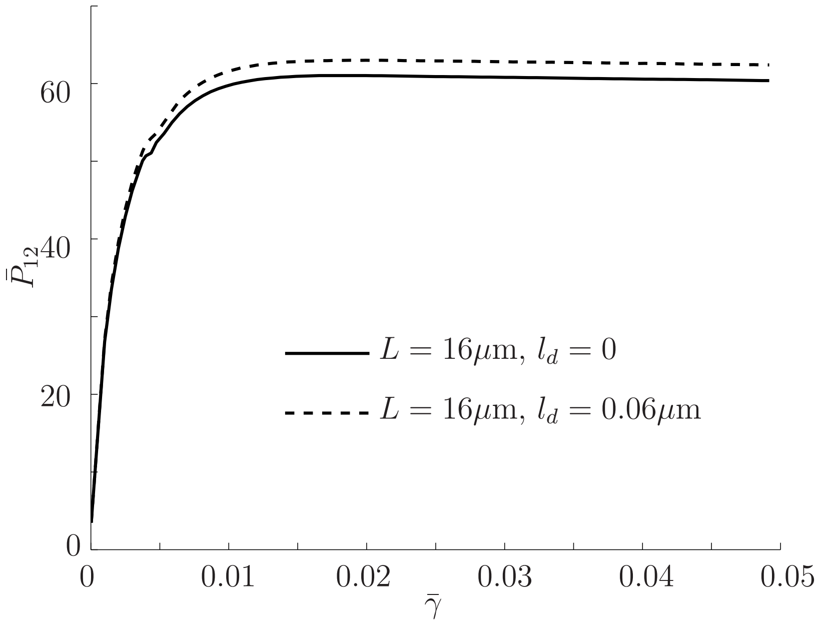

Figure 2.19.: Model III. Initial yield stress $Y_\alpha = 0$ [MPa], local hardening module $H^l_\alpha = 0$ [MPa] for all slip-systems $\alpha = 1, \ldots, 4$. Macroscopic stress–strain response ($\bar{P}_{12}$ vs. $\bar{\gamma}$) showing the influence of the divergence term. Since the influence is governed by the dissipative length scale l_d, this material parameter has been varied. $m = 1$. Note that strain is only plotted up to 0.05%.

Here, Ψ_0 is the free energy per unit undeformed volume, $\mathcal{D}_0$ the dissipation power and W_{int} stems from the rate of mechanical work supply. Although the balance equation is stated with respect to integrals over the entire material domain $\mathcal{B}_0$ respectively its entire boundary, it also has to hold for arbitrary bounded and connected parts of the body.

Considerations of Ekh et al. [85, 245]

The free energy Ψ_0 (per unit undeformed volume), in the material configuration $\mathcal{B}_0$, is proposed as a function of the deformation gradient $\boldsymbol{F}$ and a set of internal variables, which are here taken as $\boldsymbol{F}_{\text{P}}$ and the set of slip-system shears $\{\gamma_\alpha\}_{\alpha=1}^{n_{\text{slip}}}$. In addition, the free energy Ψ_0 is assumed to depend on the set $\{\boldsymbol{\nabla}_{\mathbf{r}}\gamma_\alpha\}_{\alpha=1}^{n_{\text{slip}}}$, where $\boldsymbol{\nabla}_{\mathbf{r}}$ is the gradient in the reference configuration $\mathcal{B}_0$. Thus, gradient effects (under isothermal conditions) are included and the scalar variables γ_α represent isotropic hardening on the n_{slip} slip-systems. From the principle of (spatial) objectivity, we may conclude that a possible parametrization of the free energy Ψ_0 is given by

$$\Psi_0(\boldsymbol{F}, \boldsymbol{F}_{\text{P}}, \{\gamma_\alpha\}, \{\boldsymbol{\nabla}_{\mathbf{r}}\gamma_\alpha\}) = \Psi_0(\bar{\boldsymbol{E}}_{\text{E}}, \{\gamma_\alpha\}, \{\boldsymbol{\nabla}_{\mathbf{r}}\gamma_\alpha\}). \tag{2.6.2}$$

Moreover, the the rate of mechanical work supply reads $W_{\text{int}} := \int\limits_{\mathcal{B}_0} \boldsymbol{P} : \dot{\boldsymbol{F}} \, \mathrm{d}V$. For thermodynamical consistency, it is indispensable that the dissipation is strictly non-negative, corresponding to the second law of thermodynamics. Thus, the fulfillment of the (reduced) dissipation inequality

$$\int\limits_{\mathcal{B}_0} \mathcal{D}_0 \, \mathrm{d}V = \int\limits_{\mathcal{B}_0} \left[\boldsymbol{M}_\mathrm{E} : \boldsymbol{L}_\mathrm{P} - \sum_\alpha \frac{\partial \Psi_0}{\partial \gamma_\alpha} \dot{\gamma}_\alpha - \sum_\alpha \frac{\partial \Psi_0}{\partial (\boldsymbol{\nabla}_\mathbf{r} \gamma_\alpha)} \cdot \boldsymbol{\nabla}_\mathbf{r} \dot{\gamma}_\alpha \right] \mathrm{d}V \geq 0 \qquad (2.6.3)$$

is an absolutely essential modeling-feature. Upon integrating the last term by parts and using Gauss' theorem, Eq. (2.6.3) is rewritten as

$$\int\limits_{\mathcal{B}_0} \left[\boldsymbol{M}_\mathrm{E} : \boldsymbol{L}_\mathrm{P} - \sum_\alpha \kappa_\alpha \dot{\gamma}_\alpha \right] \mathrm{d}V - \int\limits_{\partial \mathcal{B}_0} \sum_\alpha \kappa_\alpha^{(b)} \dot{\gamma}_\alpha \, \mathrm{d}A \geq 0. \qquad (2.6.4)$$

This leads to the definition of the auxiliary dissipative hardening stresses as stated in Eq. (2.3.12). It is noted that the hardening stresses κ_α may be composed of local as well as gradient contributions, whereas the gradient tractions $\kappa_\alpha^{(b)}$ on the boundary $\partial \mathcal{B}_{0,\,\mathrm{grain}}$ represent the gradient effect only.

Note that a more restrictive formulation than Eq. (2.6.3) is obtained, if it is required that the local dissipation contributions are non-negative pointwise, i.e., if $\mathcal{D}_0 \geq 0$ for all $\boldsymbol{X} \in \mathcal{B}_0$ and $\mathcal{D}_0^{(\mathrm{b})} \geq 0$ for all $\boldsymbol{X} \in \partial \mathcal{B}_0$.

Considerations of Anand, Lele and Gurtin [124, 171]

Anand, Lele and Gurtin [124, 171] apply a special kind of virtual work principle in conjunction with arguments of classical thermodynamics. Key idea is the assumption that each evolution of the body is associated with macroscopic and microscopic forces. The latter depends on a scalar microscopic force f_α whose working accompanies slip on slip-system α and a vector microscopic stress $\boldsymbol{\xi}_\alpha$ whose working accompanies slip gradients on α. This leads to a different choice of an internal energy

$$\begin{aligned} W_\mathrm{int} \;&:=\; \int\limits_{\mathcal{B}_0} \boldsymbol{S}_\mathrm{E} : \dot{\boldsymbol{E}}_\mathrm{E} + \sum_\alpha \left[f_\alpha \dot{\gamma}_\alpha + \boldsymbol{\xi}_\alpha \cdot \boldsymbol{\nabla}_\mathbf{r} \dot{\gamma}_\alpha \right] \mathrm{d}V \\ &=\; \int\limits_{\mathcal{B}_0} \boldsymbol{P} : \dot{\boldsymbol{F}} + \sum_\alpha \left[\mathrm{Div} \left(\boldsymbol{\xi}_\alpha \right) \dot{\gamma}_\alpha + \boldsymbol{\xi}_\alpha \cdot \boldsymbol{\nabla}_\mathbf{r} \dot{\gamma}_\alpha \right] \mathrm{d}V, \end{aligned} \qquad (2.6.5)$$

with $\boldsymbol{S}_\mathrm{E}$ expanding power over the Green–Lagrange strain $\dot{\boldsymbol{E}}_\mathrm{E}$. It is worth noting that, here, the work conjugacy of the scalar microscopic force f_α and the slip rate $\dot{\gamma}_\alpha$, respectively the microscopic stress $\boldsymbol{\xi}_\alpha$ and the slip rate gradient $\boldsymbol{\nabla}_\mathbf{r} \dot{\gamma}_\alpha$, is assumed first. Then the existence of a free energy function

$$\Psi_0(\boldsymbol{F}, \boldsymbol{F}_\mathrm{P}, \{\gamma_\alpha\}, \{\boldsymbol{\nabla}_\mathbf{r} \gamma_\alpha\}) = \Psi_0(\boldsymbol{E}_\mathrm{E}, \{\boldsymbol{\nabla}_\mathbf{r} \gamma_\alpha\}). \qquad (2.6.6)$$

is established. This is in contrast to the procedure described in Section 2.6, where first a free energy function depending on the slip-system shear γ_α and its gradient $\boldsymbol{\nabla}_{\mathbf{r}}\gamma_\alpha$ is assigned which then, as a consequence, leads to the definition of microscopic hardening stresses κ_α, i.e., Eq. (2.3.12). Moreover, the free energy function of Anand, Lele and Gurtin [124, 171] does not depend on the slip-system shear γ_α, only on its gradient.

Therefore, the counterpart of dissipation inequality (2.6.3) reads

$$\int\limits_{\mathcal{B}_0} \left[\boldsymbol{M}_{\mathrm{E}} : \boldsymbol{L}_{\mathrm{P}} + \sum_\alpha \left[\mathrm{Div}\left(\boldsymbol{\xi}_\alpha\right) \dot{\gamma}_\alpha + \boldsymbol{\xi}_\alpha \cdot \boldsymbol{\nabla}_{\mathbf{r}} \dot{\gamma}_\alpha \right] \right] \mathrm{d}V \geq 0. \tag{2.6.7}$$

The strategy of Anand, Lele and Gurtin leads to the microforce balance, i.e., Eq. (2.3.21), where an additive decomposition of the microstress $\boldsymbol{\xi}_\alpha$ into an energetic and a dissipative component is admitted

$$\boldsymbol{\xi}_\alpha = \boldsymbol{\xi}_\alpha^{\mathrm{en}} + \boldsymbol{\xi}_\alpha^{\mathrm{diss}}. \tag{2.6.8}$$

The energetic microscopic stress for slip-system α, i.e., $\boldsymbol{\xi}_\alpha^{\mathrm{en}}$, is given by

$$\boldsymbol{\xi}_\alpha^{\mathrm{en}} := \frac{\partial \Psi_0}{\partial(\boldsymbol{\nabla}_{\mathbf{r}}\gamma_\alpha)}. \tag{2.6.9}$$

Then, the dissipation takes the form

$$\sum_\alpha \left[f_\alpha \dot{\gamma}_\alpha + \boldsymbol{\xi}_\alpha^{\mathrm{diss}} \cdot \boldsymbol{\nabla}_{\mathbf{r}} \dot{\gamma}_\alpha \right] \mathrm{d}V \geq 0. \tag{2.6.10}$$

Inequality (2.6.10) imposes restrictions on the constitutive equations for f_α and $\boldsymbol{\xi}_\alpha^{\mathrm{diss}}$ for which a constitutive dependence on the slip rate $\dot{\gamma}_\alpha$ and the slip rate gradient $\boldsymbol{\nabla}_{\mathbf{r}}\dot{\gamma}_\alpha$ is suggested, cf. Gurtin and Anand[124] and Lele and Anand [171].

In addition, since the microscopic stress $\boldsymbol{\xi}_\alpha^{\mathrm{diss}}$ characterizes dissipative microscopic forces associated with the evolution of dislocations on the αth slip plane, and because the motion of such dislocations is tangent to this plane, it sometimes is required that dissipative microscopic stress $\boldsymbol{\xi}_\alpha^{\mathrm{diss}}$ is tangential, cf. e.g. Gurtin and Anand [124].

3. Extending the model of Ekh et al. [85] to latent hardening

In Chapter 2, among others, the gradient hardening crystal plasticity model of Ekh et al. [85] is discussed. Originally, this model is formulated for self-hardening only. As mentioned already in Ekh et al. [85], the model allows for an extension to latent hardening and this is what is done in this Chapter.

Latent hardening refers to the effect that during plastic deformation in one slip system, the hardening of other slip systems are activated. This activation of multiple slip has two primary influences on the evolution of the latent hardening ratios. Firstly, regardless of the form of the self-hardening moduli, the effective latent hardening decreases with an increase in the slip system activity. It is defined by the number and intensity of active secondary systems. Secondly, multiple slip can lead to a rapid increase in the rate of hardening as compared to single slip.

A free energy is stated which includes contributions from the gradient of hardening along each slip direction. This leads to hardening stresses depending on the second derivative of the plastic slip. The numerical implementation is carried out with the help of a dual-mixed finite element method, as described in Section 2.4. Hereby, the displacements and the plastic slips projected on the slip directions are the degrees of freedom. The resulting system of equations is highly nonlinear and strongly coupled. The numerical results show that the macroscopic strength increases with decreasing grain size as a result of gradient hardening: Moreover, latent hardening further enhances the strengthening gradient effect.

3.1. Mathematical model

For simplicity, attention is restricted here to isothermal processes. As stated in the introduction, the model is thermodynamically based. Moreover, we postulate the existence of a potential: the volume-specific free energy density Ψ. Following Ekh et al. [85], it can be decomposed additively into an elastic and a hardening contribution, i.e. Ψ_{E} and Ψ_{h} respectively,

$$\Psi(\boldsymbol{F}, \boldsymbol{F}_{\mathrm{P}}, \boldsymbol{\gamma}, \nabla_{\mathrm{r}}\boldsymbol{\gamma}) = \Psi_{\mathrm{E}}(\boldsymbol{E}_{\mathrm{E}}(\boldsymbol{F}, \boldsymbol{F}_{\mathrm{P}})) + \Psi_{\mathrm{h}}(\boldsymbol{\gamma}, \nabla_{\mathrm{r}}\boldsymbol{\gamma}) \ . \tag{3.1.1}$$

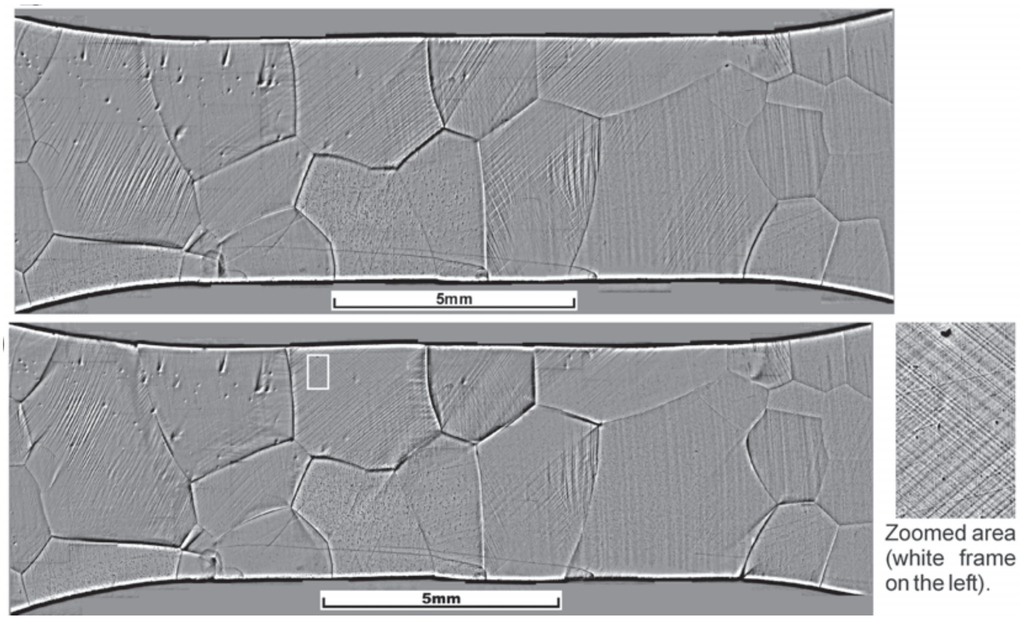

Figure 3.1.: Two samples of Fe-3%Si after deformation in a tensile test. The specimen have been strained up to 1.5% (top) and 4%. The slip directions $\boldsymbol{s}_\alpha$ (and the slip bands) can clearly been seen. Thus, the material behaves strongly anisotropic. Picture credit: Henning and Vehoff [130]

In particular, in order to include latent hardening effects, it reads

$$\begin{aligned}\Psi(\boldsymbol{F},\boldsymbol{F}_{\mathrm{P}},\boldsymbol{\gamma},\boldsymbol{\nabla}_{\mathrm{r}}\boldsymbol{\gamma}) = {} & \underbrace{\frac{\lambda}{2}\left[\mathrm{tr}\boldsymbol{E}_{\mathrm{E}}\right]^2 + \mu\boldsymbol{E}_{\mathrm{E}} : \boldsymbol{E}_{\mathrm{E}}}_{:=\Psi_{\mathrm{E}}} \\ & \underbrace{+\frac{1}{2}\sum_{\alpha,\beta} H^{l}_{\alpha\beta}\gamma_\alpha\gamma_\beta + \frac{1}{2}\sum_{\alpha,\beta} l_\alpha H^{g}_{\alpha\beta} l_\beta \left[\boldsymbol{\nabla}_{\mathrm{r}}\gamma_\alpha\cdot\boldsymbol{s}_\alpha\right]\left[\boldsymbol{\nabla}_{\mathrm{r}}\gamma_\beta\cdot\boldsymbol{s}_\beta\right]}_{:=\psi_{\mathrm{h}}}.\end{aligned} \tag{3.1.2}$$

Here, $H^{\mathrm{l}}_{\alpha\beta}$ denotes the local hardening modulus and l_α and l_β are internal length scales. Moreover, the counterpart for the gradient contribution, i.e. $\boldsymbol{H}^g$, accounts for latent hardening effects as well:

$$H^g_{\alpha\beta} := [\boldsymbol{s}_\alpha\cdot\boldsymbol{s}_\beta] h_{\alpha\beta} H^g_0, \tag{3.1.3}$$

with H^g_0 being a material constant, the gradient hardening modulus. Note that $H^g_0 \neq H^l_0$, i.e. the gradient hardening matrix is not related to the usual interaction matrix for classical hardening. $h_{\alpha\beta}$ are coefficients of the matrix $\boldsymbol{H}^g$ - the diagonal terms are related to self-hardening of the slip systems α, whereas the off-diagonal elements induce latent hardening between the slip systems α and β. This choice is motivated by the idea that the amount of latent hardening is influenced by the angle between the two slip systems α and β. Here, the angle between the two slip systems refers to the smaller of the two angles which exist between the slip directions $\boldsymbol{s}_\alpha$ and $\boldsymbol{s}_\beta$. For a maximum alignment of two slip directions, i.e. if $\boldsymbol{s}_\alpha \approx \boldsymbol{s}_\beta$, the influence on the newly activated slip system is rather large since $\boldsymbol{s}_\alpha \cdot \boldsymbol{s}_\beta = 1$. In case of orthogonal slip directions, the other slip system is not activated: $\boldsymbol{s}_\alpha \perp \boldsymbol{s}_\beta \Rightarrow \boldsymbol{s}_\alpha \cdot \boldsymbol{s}_\beta = 0$. $\boldsymbol{s}_\alpha$ and $\boldsymbol{s}_\beta$ are the slip direction of the active and of the newly activated slip system β, respectively.

Clearly, the volume-specific free energy density ψ is convex in all arguments, i.e. the elastic Green strain $\boldsymbol{E}_\mathrm{E}$, the slip $\boldsymbol{\gamma}$ and the slip gradient $\boldsymbol{\nabla}_\mathrm{r}\boldsymbol{\gamma}$, respectively. The elastic part of the free energy density Ψ_E depends on the elastic Green strain $\boldsymbol{E}_\mathrm{E}$ as defined in Eq. (2.2.4). The local elastic deformation $\boldsymbol{F}_\mathrm{E}$ and the rate of the inelastic plastic deformation $\boldsymbol{F}_\mathrm{P}$ are represented by

$$\boldsymbol{F}_\mathrm{E} := \boldsymbol{F} \cdot \boldsymbol{F}_\mathrm{P}^{-1} \qquad \text{and} \qquad \dot{\boldsymbol{F}}_\mathrm{P} = \sum_\alpha \dot{\gamma}_\alpha \, \boldsymbol{s}_\alpha \otimes \boldsymbol{F}_\mathrm{P}^\mathrm{T} \cdot \boldsymbol{n}_\alpha, \tag{3.1.4}$$

as usual. Further, $\boldsymbol{\gamma} := (\gamma_1, \ldots, \gamma_\mathfrak{g})$ represent the amount of shear deformation in the slip-systems. In the context of crystal plasticity, the model formulation is based on the slip-system geometry as described by two unit vectors, i.e. the slip direction $\boldsymbol{s}_\alpha$ and slip-plane normal $\boldsymbol{n}_\alpha$. It is well known that often two or more crystallographically equivalent systems contribute to the plastic deformation. Therefore, $\mathfrak{a} \leq \mathfrak{g}$ represent the number of active glide systems. A glide system is referred to as being passive or latent if $\dot{\gamma}_\alpha = 0$, and active if $\dot{\gamma}_\alpha \neq 0$.

Since we neglect in this chapter the effects of any processes involving a change in or evolution of either the glide direction $\boldsymbol{s}_\alpha$ or the glide-system orientation $\boldsymbol{n}_\alpha$ (e.g., texture development), these referential unit vectors are assumed constant with respect to the reference placement. A quite common idea is to consider both $\boldsymbol{s}_\alpha$ and $-\boldsymbol{s}_\alpha$ as glide directions which will be pursued in this contribution as well (see also Ortiz and Repetto [204]). Consequently, $\gamma_\alpha \geq 0$ can then be interpreted as the accumulated slip-system shear, in which case it is always positive and monotonically increasing, i.e., $\dot{\gamma}_\alpha \geq 0$ for all slip systems $\alpha = 1, \ldots, \mathfrak{g}$.

The hardening contribution to the free energy can be decomposed further into contributions from local and gradient hardening, respectively. By including a dependence on the slip gradient $\boldsymbol{\nabla}_\mathrm{r}\gamma_\alpha$, microscopic material lengthscale-dependence is introduced. The corresponding hardening moduli, $H^l_{\alpha\beta}$ and $H^g_{\alpha\beta}$, are chosen as constant and positive semi-definite measures associated with each slip-system α, β. By choosing[1]

$$\Psi_\mathrm{h} = \frac{1}{2} \sum_{\alpha,\beta} H^\mathrm{l}_{\alpha\beta} \gamma_\alpha^2 + \frac{1}{2} \sum_{\alpha,\beta} l_\alpha H^g_{\alpha\beta} l_\beta \left[\boldsymbol{\nabla}_\mathrm{r}\gamma_\alpha \cdot \boldsymbol{s}_\alpha\right] \left[\boldsymbol{\nabla}_\mathrm{r}\gamma_\beta \cdot \boldsymbol{s}_\beta\right],$$

we induce crystallographic hardening and account for latent hardening via the local hardening contribution as well as the gradient hardening term.

---

[1] [85] chose $\Psi_\mathrm{h} = \frac{1}{2} \sum_\alpha H^\mathrm{l}_\alpha \gamma_\alpha^2 + \frac{1}{2} \sum_\alpha l_\alpha^2 H^g_\alpha \left[\boldsymbol{\nabla}_\mathrm{r}\gamma_\alpha \cdot \boldsymbol{s}_\alpha\right] \left[\boldsymbol{\nabla}_\mathrm{r}\gamma_\alpha \cdot \boldsymbol{s}_\alpha\right]$ which accounts for crystallographic but not for latent hardening. The later is a non-physical simplification. The same assumption is made by [271] in case of a small deformation theory.

The hardening stresses κ_α as defined in Eq. (2.3.12) are composed of local as well as gradient contributions, whereas the gradient tractions $\kappa_\alpha^{(b)}$ on the grain boundary $\partial\mathcal{B}_{0,\,\mathrm{grain}}$ represent the gradient effect only. In particular, for the free energy function stated in Eq. $(3.1.2)_1$, this leads to

$$\begin{aligned}
\kappa_\alpha &= \sum_\beta H^l_{\alpha\beta}\gamma_\beta - \mathrm{Div}(l_\alpha \sum_\beta H^g_{\alpha\beta} l_\beta \left[\boldsymbol{\nabla}_\mathrm{r}\gamma_\beta \cdot \boldsymbol{s}_\beta\right] \boldsymbol{s}_\alpha) \\
&= \sum_\beta H^l_{\alpha\beta}\gamma_\beta - l_\alpha \sum_\beta H^g_{\alpha\beta} l_\beta \left[\boldsymbol{s}_\alpha \otimes \boldsymbol{s}_\beta\right] : \left[\boldsymbol{\nabla}_\mathrm{r} \otimes \boldsymbol{\nabla}_\mathrm{r}\right]\gamma_\beta, \qquad (3.1.5) \\
\kappa_\alpha^{(\mathrm{b})} &= \boldsymbol{N} \cdot \left[\sum_\beta l_\alpha H^g_{\alpha\beta} l_\beta \left[\boldsymbol{\nabla}_\mathrm{r}\gamma_\beta \cdot \boldsymbol{s}_\beta\right] \boldsymbol{s}_\alpha\right]. \qquad (3.1.6)
\end{aligned}$$

Clearly, the extension of a regular local hardening is represented by the additional term $l_\alpha \sum_\beta H^g_{\alpha\beta} l_\beta \left[\boldsymbol{s}_\alpha \otimes \boldsymbol{s}_\beta\right] : \left[\boldsymbol{\nabla}_\mathrm{r} \otimes \boldsymbol{\nabla}_\mathrm{r}\right]\gamma_\beta$. This gradient term leads to grain size dependent hardening - although the grain size does not enter this term directly. The dissipative hardening stresses κ_α and $\kappa_\alpha^{(\mathrm{b})}$ exist within each grain and on each grain boundary, respectively.

Having introduced the basic underlying modeling ideas, we now turn to the governing equations. The mechanical problem is governed by the quasi-static balance of linear momentum

$$\boldsymbol{0} = \mathrm{Div}\boldsymbol{P} + \rho_0 \boldsymbol{b}. \qquad (3.1.7)$$

The first Piola–Kirchhoff stress tensor $\boldsymbol{P}$ is derived from the free energy as usual, i.e. $\boldsymbol{P} = \partial\psi/\partial\boldsymbol{F}$. Furthermore, $\boldsymbol{b}$ represents the volume force.

The grain problem is governed by the flow rule which relates the plastic slip γ_α to the stresses. We assume a (rate-dependent) viscoplastic flow rule of the type

$$\dot{\gamma}_\alpha = \frac{1}{t_*}\,\eta_\alpha(\Phi_\alpha)\,. \qquad (3.1.8)$$

Here, $t_* > 0$ is the relaxation time and $\eta_\alpha(\Phi_\alpha)$ are the overstress-functions of the Perzyna type (cf. Perzyna [210]). The latter are chosen as non-negative and monotonically increasing for all slip systems α. In particular, a power law is chosen

$$\eta_\alpha(\Phi_\alpha) = \left[\frac{< \Phi_\alpha >}{C_0}\right]^m. \qquad (3.1.9)$$

In this model, C_0 and m are constant material parameters which are the same for all slip systems α. The special case of rate-independent plasticity is retrieved in the limit when $t_*[C_0]^m \to 0$. Following Ekh et al. [85], the quasi-static yield functions Φ_α are defined as

$$\Phi_\alpha = \tau_\alpha - [Y_\alpha + \kappa_\alpha], \qquad (3.1.10)$$

where τ_α represents the resolved shear stress. Hence, the current slip resistance on each slip system α is given by $Y_\alpha + \kappa_\alpha$. Y_α is the initial yield stress and the dissipative hardening stresses κ_α are of the drag-stress type. Fully elastic behavior is characterized by $\Phi_\alpha < 0$. Consequently, then $\dot{\gamma}_\alpha = 0$. Summarizing, these considerations lead to the following viscoplastic flow rule

$$\dot{\gamma}_\alpha = \frac{1}{t_*}\left[\frac{< \tau_\alpha - [Y_\alpha + \kappa_\alpha] >}{C_0}\right]^m . \tag{3.1.11}$$

3.2. Numerical approximation

Since this system cannot be integrated analytically, this section briefly summarizes the formulation of the numerical approximation scheme we used. For more details and a comparison about different mechanical boundary condition assumptions, the reader is referred to [85]. For the temporal discretization, a backward (implicit) Euler integration for the evolution equations is applied. The state at $t = t_{n-1}$ is assumed to be known for a given time history of the pertinent loading. For example, this leads to the incremental, semi-discretized version of the equation for the rate of the inelastic deformation (i.e. given in Eq. $(3.1.4)_2$)

$$\boldsymbol{I} - \boldsymbol{F}_{\mathrm{P}\,n-1} \cdot \boldsymbol{f}_{\mathrm{P}\,n} - \Delta t \sum_\alpha \frac{\gamma_{\alpha\,n} - \gamma_{\alpha\,n-1}}{\Delta t} \left[\boldsymbol{s}_\alpha \otimes \boldsymbol{n}_\alpha\right] = \boldsymbol{0}, \tag{3.2.1}$$

with $\Delta t = t_n - t_{n-1}$ denoting the current time step. The inverse of the plastic part of the deformation gradient is initialized as $\boldsymbol{f}_{\mathrm{P}\,0} = \boldsymbol{I}$. Furthermore, we assume that no plastic slip exists in the beginning of the deformation process, i.e. $\gamma_\alpha(t = 0) = 0$.

The spatial discretization is done with a dual-mixed finite element algorithm, whereby the primary unknowns are the displacement $\boldsymbol{u}$ and the scalar g_α

$$g_\alpha := \boldsymbol{\nabla}_{\mathrm{r}} \boldsymbol{\gamma}_\alpha \cdot \boldsymbol{s}_\alpha . \tag{3.2.2}$$

g_α can be interpreted as the directional gradient of the slip γ_α along the slip direction $\boldsymbol{s}_\alpha$. Thereby, the plastic slip γ_α and the scalar g_α are approximated independently in the reference configuration $\mathcal{B}_0$ of the material in question and the gradient equation

$$g_\alpha - \boldsymbol{\nabla}_{\mathrm{r}} \boldsymbol{\gamma}_\alpha \cdot \boldsymbol{s}_\alpha = \boldsymbol{0} \tag{3.2.3}$$

is a global equation in space. Such an approach is denoted the dual mixed space-variational formulation, see [85] for further details. Via such a format, it is possible to choose the finite element approximation of the scalar g_α one order higher than the finite element approximation of the plastic slip γ_α. The slip γ_α is solved for iteratively on the element level.

In total, this leads to a three-level iteration scheme. First, in an outer iteration loop called “grain boundary iteration loop” we solve for the displacements $\boldsymbol{u}$ on the grain boundaries. Then, in the “inner grain iteration loop”, updated values of displacements

$\boldsymbol{u}$ and the scalars g_α within each grain are computed. During the "inner grain iteration loop", the displacements on the grain boundaries are kept fixed, given the updated values from the "grain boundary iteration loop". Therefore, the resulting algorithm is suitable for parallelization. In each "inner grain iteration loop", a monolithic Newton–Raphson solution strategy is applied.
In order to be able to apply this separation, the underlying finite element mesh has to respect the grain boundaries. In addition to the two loops, a third iteration loop is carried out on the element level. The purpose of this "local iteration loop" is to find updated values for the slip γ_α in each Gauss point, given the values of the displacement $\boldsymbol{u}$ and the artificial scalar g_α (as provided from the inner grain iteration loop).

3.3. Simulations

To gain further insight into the effect of latent hardening in the modeling approach being pursued here, we now look in detail at the hardening behavior of a two-dimensional inelastic polycrystal with side length L. This side length L does not enter the model formulation directly. Rather, it influences the results via the position of the global nodes which vary along with a variation of L. In order to capture the size-dependence stress-strain response, the side length L is varied during simulations. A double slip system is assumed in each grain which leads to $\mathfrak{g} = 4$, see Figure 3.2 (right). The RVE consists of 25 grains and is subdivided into 11392 finite elements, as depicted in Figure 3.2 (left). Grain boundaries are respected by the mesh. Each of the triangular elements has 3 nodes and each node has 6 degrees of freedom (two displacements and four slips). Moreover, nodes on the inner grain boundaries have been doubled in order to allow for a separate computation of the grains. During the simulations, 200 time steps have been used.

Plain strain is assumed and the case of simple shear on the macro-scale is studied. Consequently, the macroscopic deformation gradient reads $\boldsymbol{F} = \boldsymbol{I} + \bar{\gamma}\boldsymbol{e}_1 \otimes \boldsymbol{e}_2$, where $\bar{\gamma}$ is the macroscopic shear deformation. For the boundary conditions of the mechanical subproblem, we prescribe the displacements $\boldsymbol{u}$ at the whole RVE boundary, i.e. Dirichlet boundary conditions are prescribed on the entire boundary. The constant loading rate is set constant at 0.2 [1/s]. Computations are carried out with $\bar{\gamma}_{\max} = 0.15$.

For the grain subproblem, we assume micro-hard boundary conditions, i.e.

$$\gamma_\alpha = 0 \qquad \text{on} \quad \partial\mathcal{B}_{0,\text{grain}}. \tag{3.3.1}$$

For a more general type of micro boundary conditions, see Chapter 4.

The material parameters used in the simulations are stated in Table 3.1.

In order to systematically simulate size dependent material behavior of the polycrystal, the side length L has been varied. Moreover, simulations have been run for the model excluding and including latent hardening. The first option is done by choosing $h_{\alpha\beta} = \delta_{\alpha\beta}$, where $\delta_{\alpha\beta}$ denotes the Kronecker symbol. In order to compute the stress-strain curves for

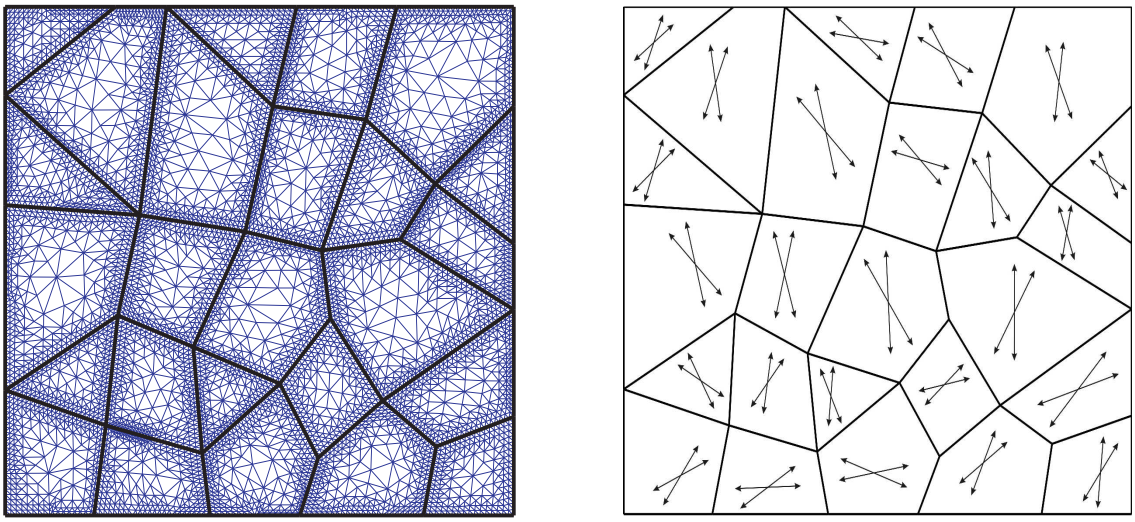

Figure 3.2.: On the left the geometry and its discretization of the RVE is depicted. It consists of 25 grains which are approximated by triangular elements. Grain boundaries are respected by the mesh. A random two-slip system is assumed. The random slip directions are illustrated schematically on the right. The boundary conditions are explained in the text.

parameter	symbol	value	
Young's modulus	E	$2 \cdot 10^5$	[MPa]
Poisson's ratio	ν	0.3	
local hardening modulus	H_0^l	500	[MPa]
gradient hardening modulus	H_0^g	$3 \cdot 10^7$	[MPa]
internal length scale	l_α	10^{-2}	[μm]
initial yield stress	Y_α	300	[MPa]
relaxation time	t_*	10^4	[s]
material constant	C_0	1	[MPa]
rate sensitivity parameter	m	1	

Table 3.1.: Material parameters used in the simulations. Usually, the initial yield stress Y_α and the local hardening modulus H_α^l are three orders lower than the elasticity modulus E - as chosen in this particular example. The local hardening modulus H_α^l is chosen in such a way that latent hardening effects are included: $H^{\mathrm{l}}_{\alpha\alpha} = H^{\mathrm{l}}_0$ and $H^{\mathrm{l}}_{\alpha\beta} = \frac{1}{10} H^{\mathrm{l}}_0$ for $\alpha \neq \beta$. Thus, the self-hardening contribution within the slip-system α is larger than the hardening latent hardening contribution.

the model including latent hardening we set $h_{\alpha\beta} = 1$ for $\alpha = \beta$ and $h_{\alpha\beta} = 0.25$ for $\alpha \neq \beta$. Thus, the latent hardening from one slip system to the next is less than the self-hardening on the active slip system.

First, we take a look at the stress-strain responses. In Figures 3.4 and 3.5, these are shown for $L = 5$ μm, $L = 10$ μm, $L = 20$ μm, $L = 40$ μm, and $L = 100$ μm - for both the cases without and with latent hardening. Clearly, the influence of the grain size can be seen. The smaller the RVE, the stiffer its material response. From the modeling point of view, this feature is accomplished by including a gradient contribution into the free energy density ψ and, consequently, into the slip law. A dependence on the grain size is seen. In Figure 3.4, the stress-strain curves are plotted for our model excluding the effect of latent hardening. The results including latent hardening are plotted in Figure 3.5. Once more, the grain size dependent hardening behavior can clearly be identified and is in accordance to the experimental findings of Hall [127] and Petch [213]: the smaller the grain size, the stiffer the polycrystals behave. The experiments of Hall [127] and Petch [213] also show a size-dependence of the yield stress. This feature is not captured by this basic model. However, enhancing this model in this direction is part of ongoing research. Moreover, for the smaller samples the latent hardening leads to a stiffer response than in the case of self-hardening. For larger samples, the effect is negligible.

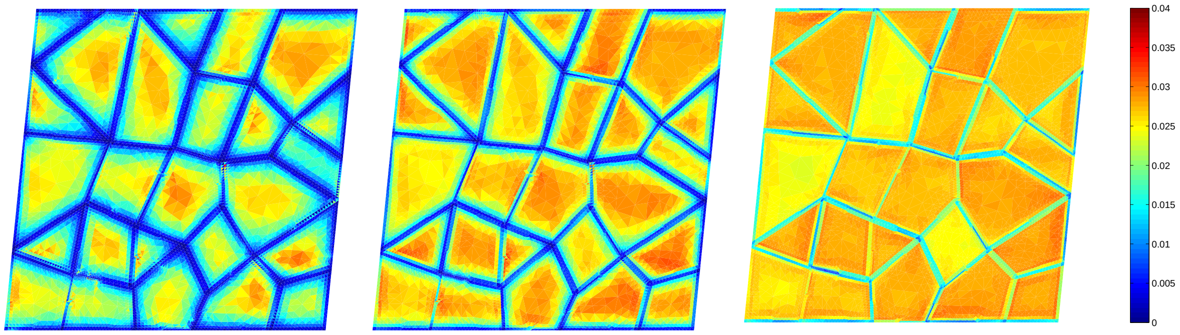

Figure 3.3.: Including latent hardening. The effective hardening strain $\gamma_{\text{eff}} = \sqrt{\sum_\alpha \gamma_\alpha}$ at $\bar{\gamma} = 0.05$ is depicted. From left to right the accumulated plastic strain field for grain-structure side lengths $L = 5$ μm, $L = 10$ μm, and $L = 40$ μm are depicted. The evolution of the slip-system shear γ_α is given in Eq. (3.1.11). The displacement field inside the grain-structure is unconstrained.

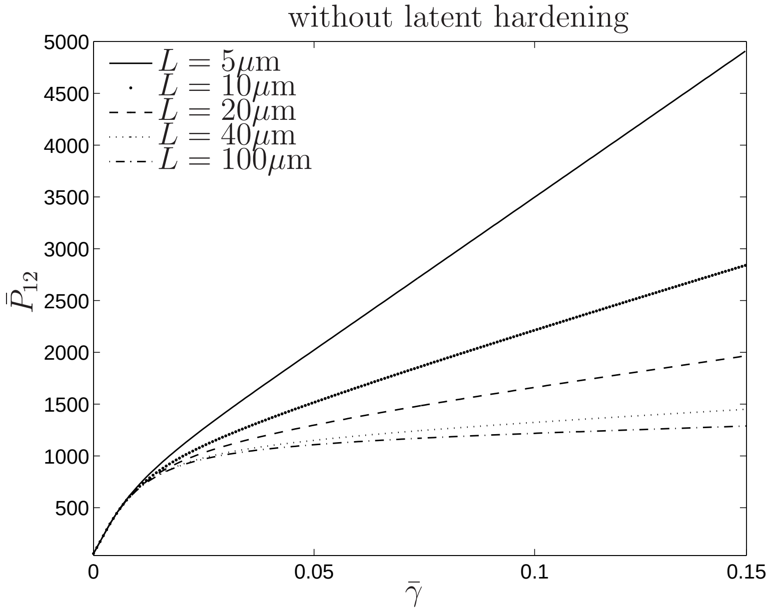

Figure 3.4.: The macroscopic stress–strain response ($\bar{P}_{12}$ vs. $\bar{\gamma}$) showing the size dependence on the amount of hardening is depicted for RVE lengths $L = 5$ μm, $L = 10$ μm, $L = 20$ μm, $L = 40$ μm, and $L = 100$ μm. The effect of latent hardening is neglected. The larger the grain size, the softer responses the material.

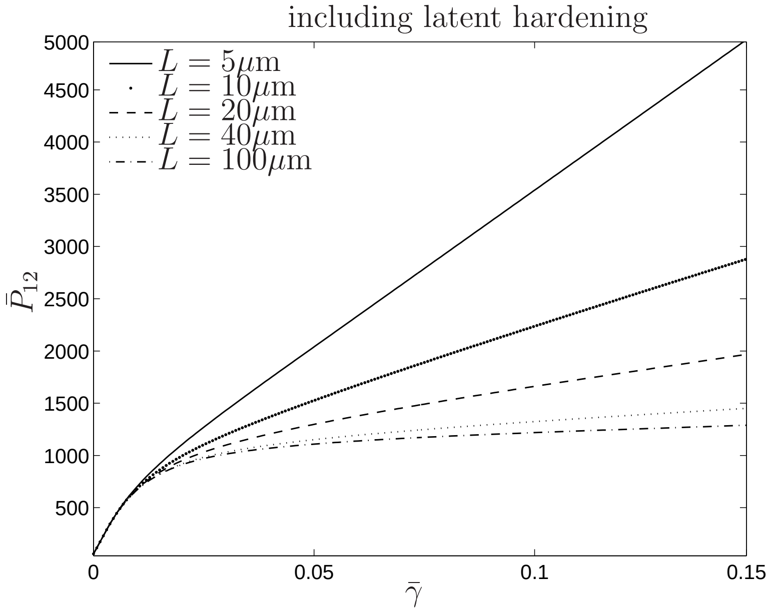

Figure 3.5.: The macroscopic stress–strain response ($\bar{P}_{12}$ vs. $\bar{\gamma}$) showing the size dependence on the amount of hardening is depicted for RVE lengths $L = 5$ μm, $L = 10$ μm, $L = 20$ μm, $L = 40$ μm, and $L = 100$ μm. During these simulations, the effect of latent hardening is included. This leads to a stiffer material response than in the case of pure self-hardening. Again, the larger the grain size, the softer responses the material.

4. Influence of grain boundary conditions on modeling of size-dependence in polycrystals

In this chapter, the focus is on the influence of the grain boundary conditions. A new type of grain boundary conditions is introduced, the so-called micro-flexible boundary conditions. In particular, it is compared to existing grain boundary conditions of plastic slip. Numerical results are given for the stress–strain response as well as for the plastic slip field in the grain-structure.

As part of a gradient crystal plasticity model it is necessary to define the grain boundary conditions for the plastic slip field. In the literature, there mainly exist two rather simple types: micro-hard (also referred to as micro-clamped) and micro-free boundary conditions, cf. Gurtin [125] for the terminology. By micro-hard it is meant that the plastic slip is assumed to be zero at the grain boundaries. The other main choice of boundary condition for the plastic slip field is the so-called micro-free condition which assumes that a microstress vanishes on the grain boundary. The latter can be regarded as being consistent with the macroscopic boundary condition $\boldsymbol{\sigma} \cdot \boldsymbol{n} = \mathbf{0}$, with $\boldsymbol{\sigma}$ being the macroscopic stress. The micro-hard assumption has been utilized in the numerical simulations in Ekh et al. [85], Evers et al. [93], Kuroda and Tvergaard [166], Lele and Anand [171], Ohno and Okumura [203], for example. On the other hand, micro-free boundary conditions were used in Geers et al. [105] at the outer grain boundaries to model the behavior of miniaturized components and the influence of the outer grain boundary condition on the homogenized behavior was investigated. Moreover, in Nicola et al. [198] micro-free boundary conditions are applied for the outer grain boundaries (and micro-hard at the inner grain boundaries).

In this chapter a more general and more complex type of boundary conditions which incorporates the micro-hard and micro-free conditions as limiting cases is suggested. Since those are more general, we refer to them as micro-flexible boundary conditions. One main feature is that they take the crystallographic misorientation of adjacent grains into account such that for a large misorientation the resistance against dislocation motion is large (with a large grain boundary energy), whereas for a low misorientation the resistance is small.

Grain boundaries are the interfaces between adjacent grains in a polycrystalline material. They hinder dislocations (defects) to move through the polycrystal. During deformation, geometrically necessary dislocations and strain gradients arise at grain boundaries to accommodate for the incompatibility of the crystals joined at the boundaries, cf., Ashby [16]. Thereby, increased resistance to plastic slip is induced in a region near the grain boundaries which is the physical explanation for the size-dependent stress-strain response in polycrystals (Hall–Petch effect). Furthermore, grain boundaries tend to decrease the material's electrical and thermal conductivity, depending on the number of misfit dislocations.

As stated in Bieler et al. [40] a grain boundary can act as either an impenetrable boundary, or as a penetrable boundary through which the slip can pass from one grain into the neighboring one with some degree of continuity, or, in case of low angle boundaries, dislocations can flow freely without any (or very small) resistance.

This chapter is organized as follows: In Section 4.1 a prototype gradient crystal plasticity model, presented in more detail in Ekh et al. [85], is summarized. The thermodynamically consistent model is rather simple but very effective and, therefore, it is well suited in order to study the influence of the chosen micro boundary conditions (without being influenced by other effects). Next, different boundary conditions for the crystallographic slip are presented and discussed in Section 4.2. This includes the more general micro-flexible boundary conditions. Hereby, the focus is on the dependence of degree of penetrability on the angle of mismatch between the slip directions of neighboring grains. Further, in Section 4.3 numerical results are given and discussed. The stress–strain response as well as the plastic slip field is compared for different boundary conditions in order to point out the influence of the choice of inner boundary conditions in the grain structure model. Finally, some concluding remarks are stated in Section 4.4.

4.1. Prototype gradient crystal plasticity model

The numerical simulations presented in Section 4.3.2 are based on the gradient crystal plasticity model presented in Ekh et al. [85]. In Ekh et al. [85] the model is introduced in a thorough thermodynamically founded formulation. Here, only its basic equations are reiterated.

In analogy to Section 2.3.2, a hardening stress κ_α is introduced, where the local hardening is extended by a gradient (size dependent) component in the following fashion

$$\kappa_\alpha := H^l \gamma_\alpha - l^2 H^g \boldsymbol{s}_\alpha \cdot \boldsymbol{\nabla} g_\alpha \tag{4.1.1}$$

with the directional gradient g_α being defined in Eq. (2.4.2).

Here, γ_α is the internal variable corresponding to accumulated plastic slip on slip system α, H^l is the local hardening modulus [Pa] and $l^2 H^g$ is the gradient hardening modulus [N]. The extension of the regular local theory is represented by the addition of the gradient term. A hardening stress of this form can be thermodynamically derived in a hyperelastic setting by assuming that the free energy is dependent on the plastic slip γ_α and also (in a "non-standard" fashion) on the gradient of the slip γ_α.

4.1.1. Basic evolution equations

In case a slip γ_α encounters a grain boundary which it cannot penetrate, dislocations originating from the same source (e.g. from the same slip system) pile up. Out of it, the stress at the boundary increases until it reaches a critical value, the so-called yield stress Y_α. If the stress concentration exceeds the yield stress it is relieved by plastic relaxation in form of yielding. From a mathematical modeling point of view, the evolution of plastic slip γ_α is governed by a viscoplastic law of Perzyna type

$$\dot{\gamma}_\alpha = \frac{1}{t_*}\left[\frac{\langle \Phi_\alpha \rangle}{C_0}\right]^m . \tag{4.1.2}$$

Here, t_* is a relaxation time, whereas C_0 is a constant material parameters (the same for all slip systems) which can be regarded as a drag stress and m is the rate sensitivity exponent. The special case of rate-independent plasticity is retrieved in the limit when $t_*[C_0]^m \rightarrow 0$. The quasistatic yield functions are defined in Eq.(3.1.10).

Moreover, the evolution equation for the inelastic deformation gradient $\boldsymbol{F}_\mathrm{P}$ is chosen of the associative type:

$$\dot{\boldsymbol{F}}_\mathrm{P} \cdot \boldsymbol{F}_\mathrm{P}^{-1} = \sum_\alpha \dot{\gamma}_\alpha \frac{\partial \Phi_\alpha}{\partial \bar{\boldsymbol{M}}_\mathrm{E}} = \sum_\alpha \dot{\gamma}_\alpha [\bar{\boldsymbol{s}}_\alpha \otimes \bar{\boldsymbol{m}}_\alpha]. \tag{4.1.3}$$

4.1.2. Dissipation inequality

As mentioned above, the model is based on a thermodynamic setting, see Ekh et al. [85], and fulfills the second law of thermodynamics. By following the arguments in [85] the dissipation inequality can be split into two parts, the local dissipation power expressions $D_\Omega + D_\Gamma \geq 0$, with

$$\begin{aligned} D_\Omega &= \int_\Omega [\,\tau_\alpha - \kappa_\alpha\,]\,\dot{\gamma}_\alpha \,\mathrm{d}V\,, \\ D_\Gamma &= \int_\Gamma \kappa_{\Gamma,\alpha}\,\dot{\gamma}_\alpha\,\mathrm{d}A \end{aligned} \tag{4.1.4}$$

where Γ is the grain boundary, $\kappa_{\Gamma,\alpha} := -l^2 H^g\, g_\alpha\, [\boldsymbol{N} \cdot \bar{\boldsymbol{s}}_\alpha]$ is the grain boundary micro stress, $\boldsymbol{N}$ is the outward normal on the grain boundary. In case a free energy density is defined, it acts as an potential for the micro stress κ_α as well as the grain boundary micro stress $\kappa_{\Gamma,\alpha}$. In the following, the latter will be used to define grain boundary conditions for the plastic slip γ_α.

4.2. Boundary conditions for the plastic slip field

The goal of this chapter is to study the influence of the plastic slip boundary condition on a finite element model of a grain structure. Each plastic slip system α and the corresponding plastic slip γ_α are only present in a single grain (crystal). Thus, the boundary conditions on the plastic slip should reflect the conditions on the grain boundaries. As shown in Figure 4.1, boundaries of a grain are either on the outer boundary of the grain structure or at a connection to adjacent grains.

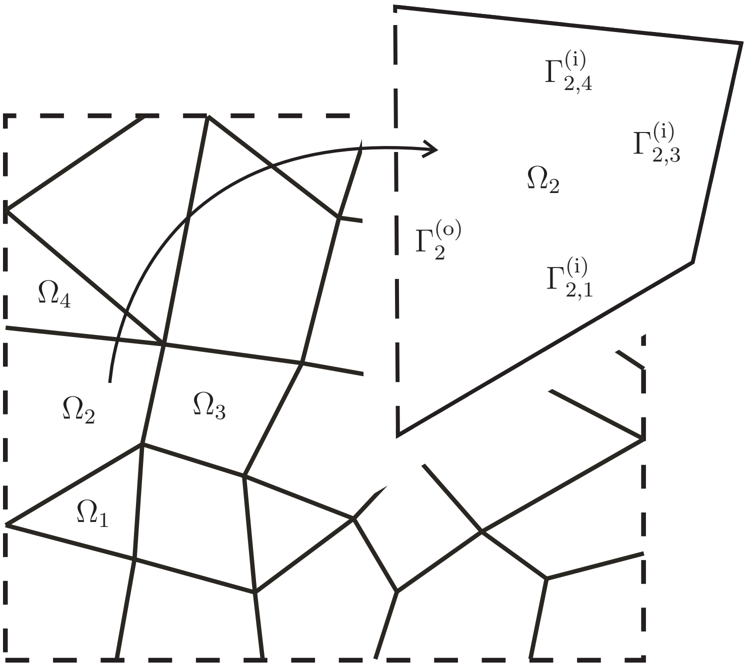

Figure 4.1.: Example of a grain aggregate. $\Gamma_2^{(o)}$ is an outer boundary on grain Ω_2 while $\Gamma_{2,1}^{(i)}$, $\Gamma_{2,3}^{(i)}$ and $\Gamma_{2,4}^{(i)}$ are inner boundaries to grains Ω_1, Ω_3 and Ω_4.

In literature, two types of boundary conditions are mainly used: micro-hard condition where the plastic slip γ_α is assumed to be zero, and micro-free condition where the micro-stress $\kappa_{\Gamma,\alpha}$ is assumed to be zero ($\rightsquigarrow g_\alpha = 0$). Both these conditions are very restrictive.

In this chapter a micro-flexible boundary condition is suggested where the alignment of crystal lattices in adjacent grains influences the plastic slip that can be transferred through the grain boundaries, see e.g. the observations of Lee et al. [169, 170] or the contribution by Bieler et al. [40] and Puri et al. [221]. As stated by Acharya et al. [4], "The issue of adequate boundary conditions [...] in any gradient theory is, of course, a difficult question because of the nonlinearities inherent in plastic response and due to the coupling between internal variables and actual total deformation."

Physically, our idea is motivated by the fact that the grain boundary resistance should depend on the degree of mismatch between the slip systems. The micro-hard condition corresponds to a boundary through which dislocations cannot pass, whereas the micro-free condition corresponds through which dislocations can flow freely without any resistance. Thus, the micro-hard and micro-free conditions present two extreme cases. In order to capture conditions in between, the following generalization is suggested: It is assumed that the slip resistance at the grain boundaries decreases with the level of slip system alignment between the grains. In addition, the resistance increases with the amount of plastic slip. The relation between the plastic slip γ_α and the micro-stress $\kappa_{\Gamma,\alpha}$ is then proposed as follows

$$\gamma_\alpha \;=\; C_{\Gamma,\alpha}(\varphi_{ab,\alpha})\,\kappa_{\Gamma,\alpha} \tag{4.2.1}$$

with

$$C_{\Gamma,\alpha}(\varphi_{ab,\alpha}) \;:=\; C_\Gamma \frac{1}{\tan(\varphi_{ab,\alpha})} \tag{4.2.2}$$

where C_Γ is a "flexibility" constant, and $\varphi_{ab,\alpha}$ is the angle of mismatch between slip direction $\bar{\boldsymbol{s}}_\alpha$ in grain a and the most compatible slip direction in grain b. To be specific, the angle of mismatch $\varphi_{ab,\alpha}$ is defined as

$$\varphi_{ab,\alpha} = \min_\beta\{\arccos|\boldsymbol{s}^a_\alpha \cdot \boldsymbol{s}^b_\beta|\}, \quad \beta = 1, ..., N_{\text{grain}}. \tag{4.2.3}$$

Here, $\text{sgn}(\boldsymbol{N} \cdot \bar{\boldsymbol{s}}_\alpha)$ is introduced to ensure the positiveness of the boundary. By this choice the dissipation at the grain boundaries D_Γ in Eq. $(4.1.4)_2$ is given by:

$$D_\Gamma = \int_\Gamma \frac{\gamma_\alpha\,\dot{\gamma}_\alpha}{C_{\Gamma,\alpha}(\varphi_{ab,\alpha})}\,\mathrm{d}A \geq 0. \tag{4.2.4}$$

Furthermore, the proposed boundary condition is continuous with respect to the angle of mismatch and fulfills the conditions that for maximum mismatch $\varphi_{ab,\alpha} = \pi/2$ then $\gamma_\alpha = 0$ (micro-hard condition), while for no mismatch $\varphi_{ab,\alpha} = 0$ then the micro-stress $\kappa_{\Gamma\alpha} \to 0$ (micro-free condition). Consequently, a complete alignment leads to soft boundaries (i.e., invisible boundaries), whereas complete misalignment results in hard boundaries.

Remark: According to Eq. (4.2.1), the flexibility constant $C_{\Gamma,\alpha}$ should approach infinity for $\varphi_{ab,\alpha} \to 0$. This is naturally impractical in a numerical setting, and may be avoided by limiting the flexibility constant $C_{\Gamma,\alpha}$ to a given upper threshold $C^{\max}_{\Gamma,\alpha}$.

As mentioned in the introduction, by far the most popular assumptions are the simple micro-free and micro-hard boundary conditions. However, there exist very few approaches on boundary conditions in between the micro-stress free boundary and hard interfaces. Fredriksson and Gudmundson [101], Gurtin and Needleman [125] and Shi and Zikry [235] introduce boundary conditions that may account for grain interactions. The first authors account for different kinds of interface conditions by introducing an interfacial free energy that depends on the plastic strain state at both sides of the interface. Their idea is motivated by the observation that at an internal boundary a thin layer of dislocation pile-up is usually evolving during plastic yielding. Gurtin and Needleman propose the so-called defect-free boundary conditions, see also the follow-up work of Gurtin [123]. Their idea is that the micro stress is related to the defect energy which is caused by the presence of geometrically necessary dislocations and therefore defined in terms of Nye's dislocation density tensor. Physically, their boundary conditions are driven by the same motivation as ours: The mismatch in crystal orientations results in an increase in the dislocation tensor and, thus, in less slip permeating the boundaries and a defect-free boundary (i.e., no mismatch) allows for free penetration. The defect-free condition is chosen in such a way that the Burgers vector flow out of one grain is equal to that into the neighboring grain. However, the defect-free condition cannot be defined at triple junctions.

Furthermore, Shi and Zikry [235] study crack behavior in polycrystals (however, without using a gradient theory). They control the amount of dislocation-boundary interaction via a factor which is based on the angles of mismatch between the slip planes of the two and the grain boundary.

4.3. Results

In order to get an understanding of the different grain boundary conditions, we briefly analytically study a one-dimensional polycrystal. In Section 4.3.2, the analysis is extended to a two-dimensional polycrystal. Numerical findings are presented, whereby the focus is on the comparison between the newly introduced micro-flexible and the well-established simple micro-hard and micro-free boundary conditions.

4.3.1. Preliminaries – 1D model

First, a one-dimensional case of a grain with length L is considered. The equation corresponding to Eq. (4.1.1) can in this case be written as

$$H_{\mathrm{g}}\, l^2 \,\frac{\mathrm{d}^2\gamma}{\mathrm{d}x^2} - H_{\mathrm{l}}\gamma = -\kappa. \tag{4.3.1}$$

The stress state in a one dimensional grain is homogeneous and is here assumed to have a given value, i.e., for rate independent plasticity (which is assumed in this section) κ is a given constant. Then Eq. (4.3.1) can be solved for different boundary conditions.

For micro-hard conditions (i.e. $\gamma(0) = \gamma(L) = 0$) the solution for the plastic slip γ can be obtained as:

$$\gamma(\xi) = \frac{\kappa}{H^l}\left[\frac{\exp(-\iota) - 1}{\exp(\iota) - \exp(-\iota)}\exp(\iota\,\xi) + \frac{1 - \exp(\iota)}{\exp(\iota) - \exp(-\iota)}\exp(-\iota\,\xi) + 1\right]. \tag{4.3.2}$$

where $\iota^2 = H^l/H^g\, L^2/l^2$ and $\xi = x/L$ are introduceded. This result can be compared with the solution for micro-free conditions (i.e. $\gamma'(0) = \gamma'(1) = 0$) which is obtained as follows:

$$\gamma(x) = \frac{\kappa}{H^l}. \tag{4.3.3}$$

For this case it is observed that the same solution as for a model without any gradient hardening (i.e. $H^g\, l^2 = 0$) is obtained. As a third case we adopt a micro-hard condition at the left end $x = 0$ (i.e. the plastic slip fulfills $\gamma(0) = 0$) and a micro-free condition at the right end $x = L$ (i.e. $\gamma'(1) = 0$). The solution for this case becomes:

$$\gamma(\xi) = \frac{\kappa}{H_\mathrm{l}} \left[-\frac{1}{1+\exp(2\iota)} \exp(\iota\,\xi) - \frac{\exp(2\iota)}{1+\exp(2\iota)} \exp(-\iota\,\xi) + 1 \right]. \qquad (4.3.4)$$

If we now use the numerical values of the parameters for the crystal gradient plasticity model given in Table 4.1, then the solutions of the plastic slip field $\gamma(\xi)$ for the different boundary conditions are obtained according to Figure 4.2.

	Parameter	Value	
Young's modulus	E	200	[GPa]
Poisson's ratio	ν	0.3	
local hardening modulus	H^l	10	[GPa]
gradient hardening modulus	H^g	$4 \cdot 10^4$	[GPa]
internal length	l	10^{-2}	[μm]
initial yield stress	Y_α	10^3	[MPa]
rate sensitivity exponent	m	1	
drag stress	C_0	1	[MPa]
relaxation time	t_*	$1 \cdot 10^4$	[s]

Table 4.1.: Simple academic material parameter values adopted for the crystal gradient plasticity model. Clearly, when the model is to be applied for a specific material, the parameters must be identified from experimental data.

The solutions clearly show that micro-hard boundary conditions will result in a stiffer response than the case of micro-free boundary conditions. In the next subsection two-dimensional grain structures are studied in order to examine the influence of the chosen grain boundary conditions. Due to fact that the stress (or hardening stress) is not homogeneous in the grains anymore, an analytical finding in the spirit of Figure 4.2 is not possible to find.

4.3.2. Grain structure – 2 D model

The FE models of grain structures that are used in the numerical examples are generated by Voronoi polygonization. The adopted algorithm, to solve the nonlinear and coupled FE problem, is a dual-mixed formulation of the spatial discretization and a backward Euler time integration. The algorithm is described in detail in Ekh et al. [85]. The numerical values of the parameters for the crystal gradient plasticity model that are applied are given in Table 4.1.

In the first example a 4-grain structure with constant side length $L = 8$ [μm] is studied. The deformation of the grain structure is controlled by linearly varying displacements of the boundaries to obtain macroscopic simple shear (plane strain assumption) with a

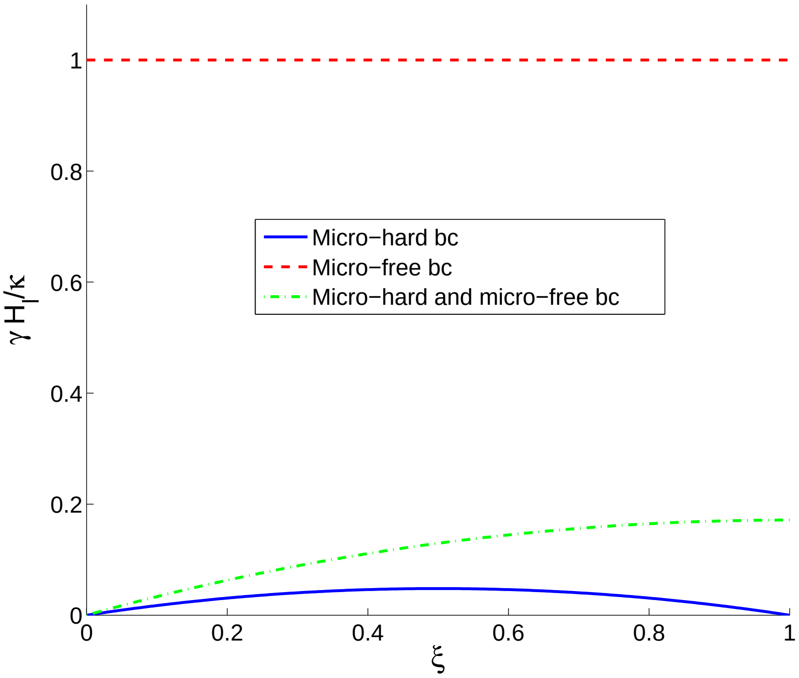

Figure 4.2.: Analytical solutions according to Eqs. (4.3.2)-(4.3.4) for a one dimensional case.

constant loading rate $\dot{\bar{\gamma}} = 0.01$ [1/s]. To investigate the influence of various grain boundary conditions only one slip direction in each grain is used. The effective plastic slip field $\gamma_{\text{eff}} := \sqrt{\sum_\alpha \gamma_\alpha^2}$ when $\bar{\gamma} = 0.05$ is illustrated for various grain boundary conditions in Figures 4.3-4.4. In these figures the slip directions of the grains, i.e. $\boldsymbol{s}_\alpha$, are depicted as encircled lines. To investigate the performance of the micro-flexible boundary condition only one slip direction $\boldsymbol{s}_\alpha$ per slip system in each grain is chosen to be activated.

In Figure 4.3 it is observed how the plastic slip field depends in the choice of outer grain boundary condition. Micro-hard conditions have been assumed in Figure 4.3 (a) for both outer and inner grain boundaries. While in Figure 4.3 (b) micro-free conditions have been assumed at outer grain boundaries. The plastic slip field is similar for both cases if the regions close to the outer grain boundaries are excluded. For micro-free outer boundaries the gradient of the plastic slip field is zero whole for micro-hard outer boundaries the plastic slip is zero. In corners where outer and inner grain boundaries meet we can observe from the results that the chosen boundary conditions might not be appropriate at least if we think of the grain model as a representative volume element of the material. At adjacent nodes/elements $\gamma_\alpha = 0$ is set for the plastic slip and $g_\alpha = 0$ for the scalar, respectively. This gives small regions where the plastic slip field changes a lot.

The influence of the inner grain boundary condition (between the grains) is investigated next. In Figure 4.4 the effective plastic slip fields are illustrated for micro-flexible inner

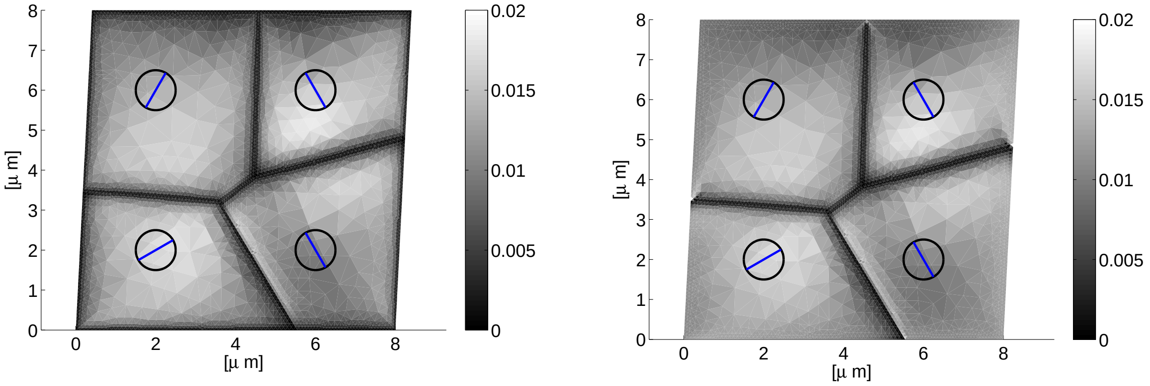

Figure 4.3.: A square 4–grain model deformed to 5% macroscopic shear. Contour plot of effective plastic slip γ_{eff}. Encircled lines show the slip directions $\boldsymbol{s}_\alpha$ in each grain. To the left: micro-hard at outer and inner grain boundaries; to the right: micro-free at outer and micro-hard at inner grain boundaries.

grain boundary conditions with the flexibility constant $C_\Gamma = 2.5$ [μm/N] to the left and for micro-free inner grain boundary conditions to the right.[1]

For the micro-flexible case it is observed that since the slip directions $\bar{\boldsymbol{s}}_\alpha$ of the two right grains are aligned there is no change of the plastic slip at the grain boundary. This means that the grains together behave in the same fashion as a single large grain would. In addition, at the grain boundaries with a large mismatch the micro-flexible condition forces the plastic slip γ_α to become equal or close to zero. Furthermore, the result for the micro-free case shows that the grain boundaries do not influence the plastic slip field. The only exception is the boundary between the two lower grains. The reason for that the plastic slip approaches zero there is that the angle of mismatch between the slip systems is exactly equal to $\pi/2$ and that a finite value of $C_\Gamma = 2.5 \cdot 10^7$ [μm/N] for the flexibility constant is chosen to model micro-free condition. This gives the flexibility constant $C_{\Gamma,\alpha} = 0$ which is the reason for that the plastic slip is equal to zero at that grain boundary.

In the second example, the stress-strain response for five different alternatives of boundary conditions of the plastic slip are compared: micro-hard conditions at inner and outer boundaries; micro-free conditions at outer and inner boundaries; micro-free condition at

---

[1] Note that micro-free boundary conditions are mainly applied for external boundaries. For internal boundaries, one can think of applying them in the case of polygonization. Polygonization refers to the process that subgrain boundaries develop due to formations of dislocations in heterogeneous loading cases. Some grains are better orientated for dislocation slip than others. During the deformation process grains can break apart (they polygonize) at these subgrain boundaries and the emerging new grains will have slightly different orientations. After polygonization, the micro-free conditions can be replaced (continuously) with micro-flexible conditions. In this section, micro-free conditions are applied to the inner boundary simply for the reason to further investigate the influence of the different types of grain boundary conditions.

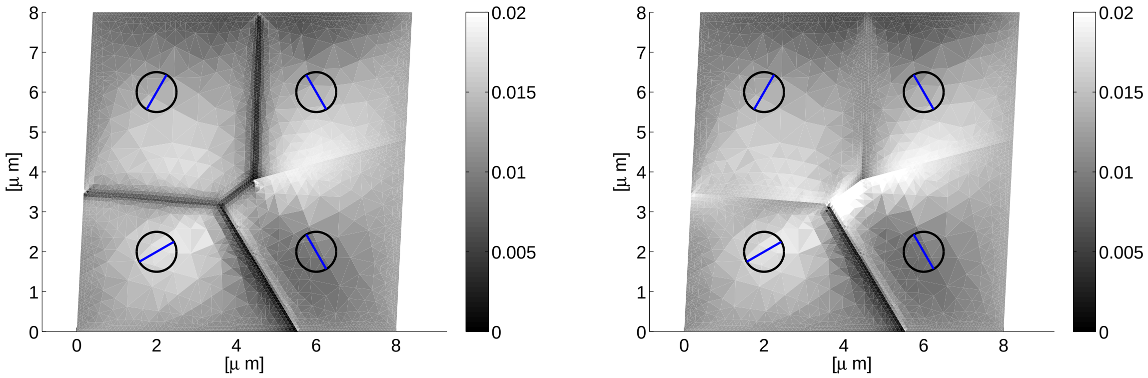

Figure 4.4.: A square 4–grain model deformed to 5% macroscopic shear. Contour plot of effective plastic slip γ_{eff}. Encircled lines show slip directions in each grain. To the left: micro-free at outer and micro-flexible $C_\Gamma = 2.5$ [μm/N] at inner grain boundaries; to the right: micro-free at outer and inner grain boundaries.

outer boundaries and micro-flexible conditions at inner boundaries with $C_\Gamma = 25$ [μm/N]; micro-free condition at outer boundaries and micro-flexible conditions at inner boundaries with $C_\Gamma = 2.5$ [μm/N]; micro-free conditions at outer and micro-hard conditions at outer boundaries. The same loading conditions as in the first example are used, but instead a structure consisting of 25 grains with 2 random orientated slip directions in each grain is investigated. Once more, the length of the grain structure is kept fixed with $L = 8$ μm. The results of the first Piola-Kirchhoff stress $\bar{P}_{12}$ versus the macroscopic shear $\bar{\gamma}$ is shown in Figure 4.5. As expected, the fully micro-hard case and the fully micro-free case gives the upper and lower limit, respectively. It is observed that the influence of the inner boundary condition is larger than of the outer boundary condition. This shows that the formulation of the boundary condition is of importance and must be done by taking physical mechanisms at the grain boundaries of the modeled material into account. In Figures 4.6-4.7 the resulting effective plastic slip fields at 5% macroscopic shear strain are shown. A general observation is that for lower flexibility C_Γ the plastic slip becomes lower at the grain boundaries which should model a more pronounced dislocation pile-up situation. This is also what is reflected by the stiffer stress-strain response in Figure 4.5.

4.4. Concluding remarks

Computational modeling of grain boundaries is still a challenging task in the modeling of heterogeneous deformation. In this chapter, the micro-flexible assumptions were applied to the thermodynamically based, rather simple but very effective theory introduced in Ekh et al. [85]. There exist several different gradient crystal plasticity theories - all of them showing the right qualitative trend. So far every theory has advantages and drawbacks and there is no such theory identified as “the best”. Thus, it is worth noting that the

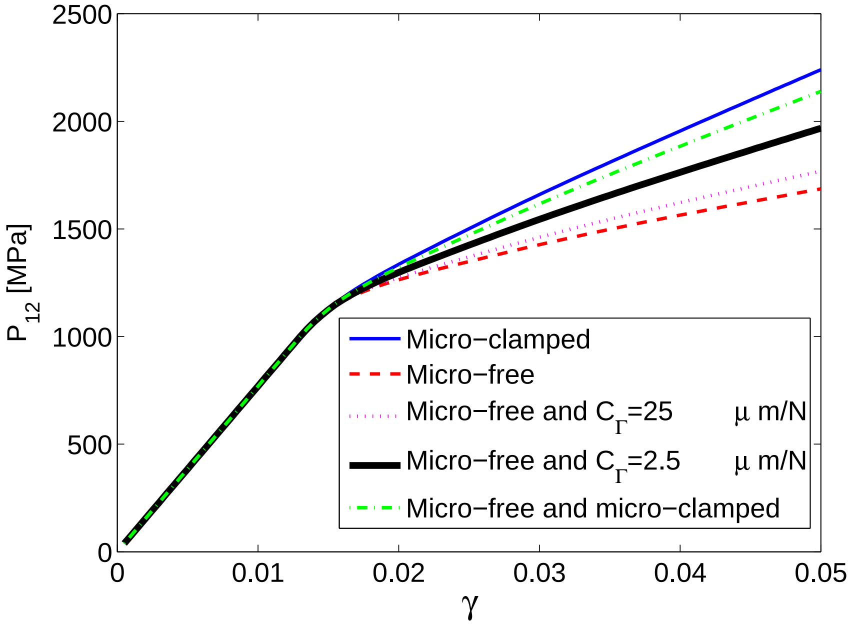

Figure 4.5.: Macroscopic stress–strain response (first Piola–Kirchhoff stress $\bar{P}_{12}$ vs. macroscopic shear $\bar{\gamma}$) for the 25-grain-example for various assumptions on the gradient problem boundary conditions at internal grain boundaries. The length of the grain structure, $L = 8$ μm, is kept fixed in all examples. As can be seen, the influence of the choice of boundary condition cannot be neglected. As expected, less plastic slip flexibility C_Γ at the grain boundaries gives a stiffer stress-strain response.

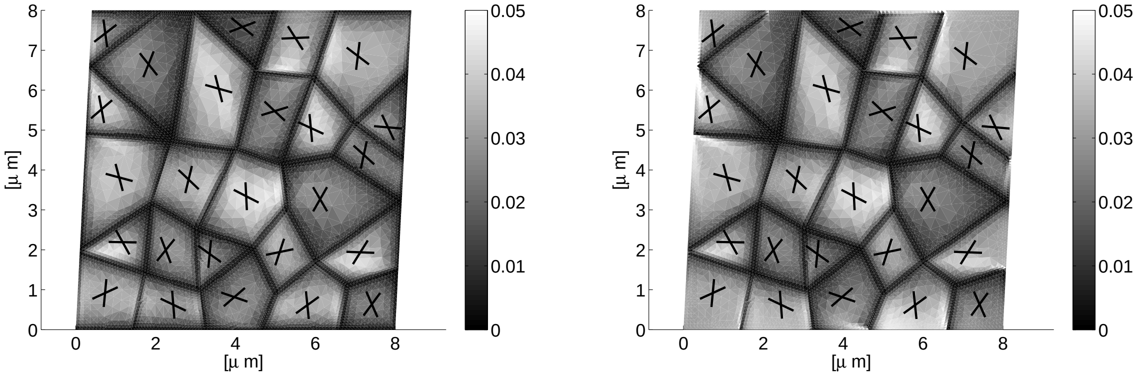

Figure 4.6.: A square 25–grain model deformed to 5% macroscopic shear. Contour plot of effective plastic slip γ_{eff}. Lines show slip directions in each grain, double slip is assumed. To the left: micro-hard at outer and inner grain boundaries; to the right: micro-free at outer and micro-hard at inner grain boundaries.

application of the micro-flexible boundary conditions is not limited to this theory. For

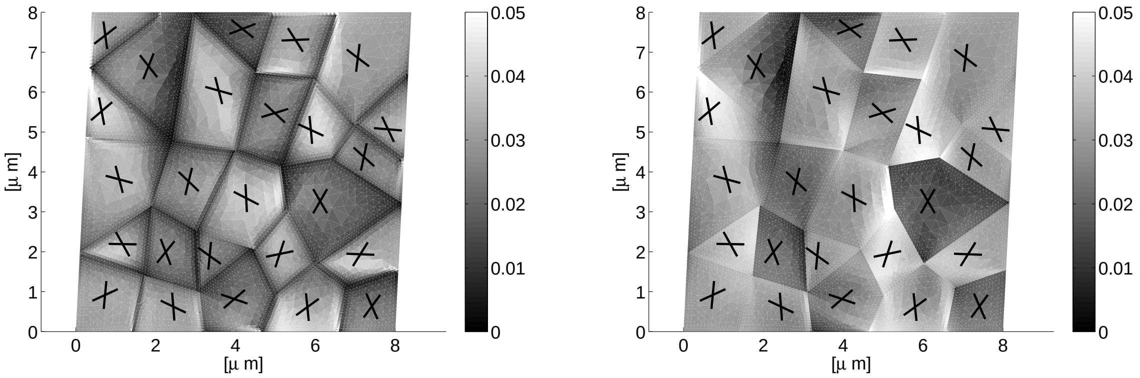

Figure 4.7.: A square 25–grain model deformed to 5% macroscopic shear. Contour plot of effective plastic slip γ_{eff}. Lines show slip directions in each grain, double slip is assumed. To the left: micro-free at outer and micro-flexible $C_{\Gamma} = 2.5$ [μm/N] at inner grain boundaries; to the right: micro-free at outer and inner grain boundaries.

example, Ertürk et al. [89] state that "boundary conditions in between the free surface and hard interfaces, which can be important for the interfaces like penetrable surface coating or grain boundaries, can also be incorporated into these models" - referring to the approach of Evers et al. [93] which is more sophisticated and driven by physical observations instead of thermodynamic considerations. Furthermore, although the derivation of Gurtin's theory [122] differs much from Ekh et al. [85], the micro-flexible boundary conditions can be applied to it. This is also true for the formulation of Lele and Anand [171], for example.

The numerical results presented in Section 4.3 show that the macroscopic stress–strain response is significantly affected by the modeling of grain boundary conditions for gradient crystal plasticity models. Therefore, when modeling grain size dependent behavior of a specific material the formulation of boundary condition is a very important issue. It is shown that especially the boundary conditions in the interior of the grain structure significantly influence the stress-strain response.

The formulation of micro-flexible boundary conditions takes into account the mismatch at the grain boundaries between then adjacent grains. In special cases of maximum mismatch and minimum mismatch at grain boundaries the formulation gives micro-hard and micro-free conditions, respectively. Results showing the performance of the micro-flexible formulation are given for a 4 grain example with one slip system in each grain and a 25 grain example with two slip systems in each grain. Already by means of the very simple 4 grain example, the influence of the grain boundary conditions is immediately apparent. The 25-grain-example with double slip shows the performance of the micro-flexible conditions in a more complex grain structure. As opposed to the defect-free boundary conditions of Gurtin and Needleman [125], the micro-flexible conditions can be applied at triple junctions.

Based on the results it is concluded that the chosen grain boundary condition of a grain structure is of significant importance for the stress–strain response. This finding is in agreement with that of Shi and Zikry [235] who report significant differences in the numerical simulation of crack propagation in polycrystals for cracks not interacting with grain boundaries as well for those which do.

5. An extended crystal plasticity model for latent hardening in polycrystals

In this contribution, a computational approach to modeling size-dependent self- and latent hardening in polycrystals is presented.
We focus attention on the investigation and prediction of slip patterning in single- and polycrystals due to glide system interaction, latent hardening and excess dislocation development. In particular, latent hardening results in a transition to patchy slip as a first indication and expression of the development of dislocation microstructures. To this end, following Nye [201], Kondo [162], and many others, local deformation incompatibility in the material is adopted as a measure of the density of geometrically necessary dislocations. Their development results in additional energy being stored in the material, resulting in additional kinematic-like hardening effects. A large-deformation model for latent hardening is introduced. The numerical implementation is done via a dual-mixed finite element method. A numerical example for polycrystals is presented.

Motivated by numerous experimental data of crystal-length dependent phenomena involving plastic deformation, conventional continuum theories of crystal plasticity have been extended in various ways. The experiments (see e.g. [96, 127, 213, 242, 243]) show the same tendency, i.e., the smaller the specimen size, the larger the increase in hardening. There exist several different strain-hardening and strengthening phenomena in (poly-) crystalline materials. One of the more important ones is latent hardening - the effect that an active slip system influences the hardening of a neighboring inactive slip system. It controls the shape of the single crystal yield surface. Among others, slip interactions and the development of geometrically necessary dislocations (GNDs) play a role in explaining latent hardening. In the early stages of experiments (primarily in monocrystals), it was found that the hardening of the latent system is larger or equal to the hardening of the primary system [251] - a result which was not expected.

For information on the basic concept of GNDs the reader is referred to “Viewpoint Set” initialized by Needleman and Sevillano [195]. The papers published in that special issue give answers to questions like ‘what is a geometrically necessary dislocation?’ or ’which size effects can be modeled in terms of geometrically necessary dislocations and which cannot?’, for example. Those works represent a very good overview over the general topic of GNDs.

Despite the incapability of modeling length-dependent effects, the conventional theory of crystal plasticity only accounts for effects of the history of crystallographic slip and not for effects due to other dislocation densities on the hardening. This has motivated a number of workers to propose a number of extensions to standard phenomenological plasticity and crystal plasticity theories. With respect to GNDs the pioneering work of Nye [201] (a similar work in the large deformation context has been published by Kondo [162]) who suggests that the incompatibility of local inelastic deformation represents a continuum measure of dislocation density. Continuum dislocations concepts are also followed by [2, 52] and [70, 93, 121, 163, 173, 186, 191, 236, 241, 247]. The second group presumes indirectly or directly a particular dependence of the free energy and/or other dependent constitutive quantities (e.g., yield stress) on the gradients of inelastic state variables. One possibility to incorporate GNDs into a model, is simply to introduce the GND density as an additional dislocation density, see e.g. [2, 3, 70, 93]. On the other hand, it is possible to assume that GND development and more generally local deformation incompability results in energy storage in the material, see e.g. [120, 121, 173, 247]. Then the free energy necessarily depends on the dislocation density tensor. In particular, in the crystal plasticity context, this assumption leads to a generalized, non-local glide-system flow rule representing an evolution field relation for the glide-system slips.

Thus, the purpose of this work is the formulation of constitutive models for the inelastic material behavior of single crystals and polycrystals in which geometrically necessary dislocations (GNDs) may develop and influence this behavior. To this end, we focus on the dependence of the development of such dislocations on the inhomogeneity of the inelastic deformation in the material. More precisely, in the crystal plasticity context, this is a relation between the GND densities and the inhomogeneity of inelastic deformation in slip systems. It involves a dependence of the inelastic state of a material point on the history of the inhomogeneity of the slip-system inelastic deformation. Consequently, their incorporation into crystal plasticity modelling necessarily implies a corresponding non-local generalization of this modelling.

This section begins with the introduction of a dislocation density labeled $\boldsymbol{g}_\alpha$. Following many others, the Burgers vector $\boldsymbol{b}$ plays a role in the definition of the dislocation density. Next, we turn to the dual-mixed finite element formulation (Section 5.2) which forms the basis for the numerical implementation. Subsequently, attention is turned to the formulation of a constitutive model allowing for cross-hardening. As mentioned above, slip interactions play a role in the process latent hardening. Therefore, the approach includes excess dislocations such as GNDs. Moreover, the model is based in a thermodynamic setting. Thereby, the free energy density depends on dislocation densities, i.e. on a quantity characterizing the dislocation state of the material in question. A representative two-dimensional numerical example is presented in Section 5.4. The paper ends with a discussion of the current approaches in Section 5.5.

5.1. Dislocation densities

The notion of GNDs has been shaped by Nye [201] and Ashby [16]. GNDs are generated during the deformation process, if the deformation inhomogeneity increases despite increasing hardening (e.g., Ashby [16]) and are often associated with gradients. GNDs arise via the net build-up of polar or excess dislocations at local obstacles to dislocation motion, e.g., precipitates or grain boundaries, facilitating local inhomogeneous and incompatible deformation which would otherwise take the form of energetically less-favorable local lattice deformation. The emergence of GNDs results in a lengthscale-dependent system and additional hardening (e.g., Ashby [16]).

In the following, in addition to the kinematical quantities defined in Section 2.2, the referential form of the dislocation tensor $\boldsymbol{G}_\mathrm{r}$ is used

$$\boldsymbol{G}_\mathrm{r} := \mathrm{curl}_\mathrm{r}\, \boldsymbol{F}_\mathrm{P}. \tag{5.1.1}$$

Here, curl_r is the curl operator of the differentiable second-order tensor field $\boldsymbol{F}_\mathrm{P}$ on the reference configuration $\mathcal{B}_0$. The rate form of the dislocation tensor relative to the intermediate configuration can be projected onto the glide-system level in the form

$$\dot{\boldsymbol{G}}_\mathrm{i} = \sum_\alpha \boldsymbol{b}_\alpha \otimes \dot{\boldsymbol{g}}_\alpha \tag{5.1.2}$$

(see e.g. Cemelli and Gurtin [52], Svendsen [247]) in terms of the Burgers vector $\boldsymbol{b}_\alpha = b\boldsymbol{s}_\alpha$ and the evolution relation

$$\dot{\boldsymbol{g}}_\alpha = \sum_\beta \left[\dot{\gamma}_\alpha[\boldsymbol{n}_\alpha \cdot \boldsymbol{s}_\beta]\boldsymbol{g}_\beta + \dot{\gamma}_\beta[\boldsymbol{n}_\beta \cdot \boldsymbol{g}_\alpha]\boldsymbol{s}_\beta\right] + b^{-1}\boldsymbol{\nabla}_\mathrm{i}\dot{\gamma}_\alpha \times \boldsymbol{n}_\alpha \tag{5.1.3}$$

for the vector-valued glide-system-based dislocation density $\boldsymbol{g}_\alpha$, with

$$\boldsymbol{\nabla}_\mathrm{i}\gamma_a := \boldsymbol{F}_\mathrm{P}^{-\mathrm{t}} \cdot \boldsymbol{\nabla}_\mathrm{r}\gamma_a \ . \tag{5.1.4}$$

The first term in the evolution relation (5.1.3) contains contributions from both self-hardening and interaction (i.e., latent) hardening mechanisms. The second term arises due to large deformations and the third term accounts for gradient hardening contributions. Note that both $\boldsymbol{G}_\mathrm{r}$ and $\boldsymbol{G}_\mathrm{i}$ have the same units (i.e., inverse length) as the square-root $\sqrt{\rho}$ of the classical scalar-valued dislocation density. As shown by Cermelli and Gurtin [52], the dislocation tensor $\boldsymbol{G}_\mathrm{i}$ represents the incompatibility of the plastic part of the deformation gradient $\boldsymbol{F}_\mathrm{P}$ relative to the surface element $\boldsymbol{n}_\mathrm{i}\mathrm{d}a_\mathrm{i}$ in the intermediate configuration. Furthermore, $\mathrm{curl}_\mathrm{r}\, \boldsymbol{F}_\mathrm{P}$ gives the same measure of GNDs with respect to surface elements in the reference configuration as does the dislocation tensor $\boldsymbol{G}_\mathrm{i}$ with respect to such elements in the intermediate configuration. The slip-system geometry implies that the projection of the vector-valued dislocation rate density $\boldsymbol{g}_\alpha$ onto the slip-system basis

$(\boldsymbol{s}_\alpha, \boldsymbol{n}_\alpha, \boldsymbol{t}_\alpha)$ yields

$$\begin{aligned}
\boldsymbol{s}_\alpha \cdot \dot{\boldsymbol{g}}_\alpha &= \sum_\beta \dot{\gamma}_\alpha [\boldsymbol{s}_\beta \cdot \boldsymbol{n}_\alpha][\boldsymbol{s}_\alpha \cdot \boldsymbol{g}_\beta] + \dot{\gamma}_\beta\, [\boldsymbol{s}_\alpha \cdot \boldsymbol{s}_\beta][\boldsymbol{n}_\beta \cdot \boldsymbol{g}_\alpha] + b^{-1} \boldsymbol{t}_\alpha \cdot \boldsymbol{\nabla}_{\mathrm{i}} \dot{\gamma}_\alpha \\
&\qquad \text{screw part} \;, \\
\boldsymbol{t}_\alpha \cdot \dot{\boldsymbol{g}}_\alpha &= \sum_\beta \dot{\gamma}_\alpha [\boldsymbol{s}_\beta \cdot \boldsymbol{n}_\alpha][\boldsymbol{t}_\alpha \cdot \boldsymbol{g}_\beta] + \dot{\gamma}_\beta [\boldsymbol{t}_\alpha \cdot \boldsymbol{s}_\beta][\boldsymbol{n}_\beta \cdot \boldsymbol{g}_\alpha] - b^{-1} \boldsymbol{s}_\alpha \cdot \boldsymbol{\nabla}_{\mathrm{i}} \dot{\gamma}_\alpha \\
&\qquad \text{edge part} \perp \boldsymbol{n}_\alpha \;, \\
\boldsymbol{n}_\alpha \cdot \dot{\boldsymbol{g}}_\alpha &= \sum_\beta \dot{\gamma}_\alpha [\boldsymbol{s}_\beta \cdot \boldsymbol{n}_\alpha][\boldsymbol{n}_\alpha \cdot \boldsymbol{g}_\beta] + \dot{\gamma}_\beta [\boldsymbol{n}_\alpha \cdot \boldsymbol{s}_\beta][\boldsymbol{n}_\beta \cdot \boldsymbol{g}_\alpha] \\
&\qquad \text{edge part} \parallel \boldsymbol{n}_\alpha \;,
\end{aligned} \tag{5.1.5}$$

for the case of constant b. $\boldsymbol{b}_\alpha$ is the Burgers vector of slip system α - representing the magnitude b and the direction $\boldsymbol{s}_\alpha$ of the lattice distortion of dislocation in a crystal lattice. In Svendsen [247], this model for dislocation density $\boldsymbol{g}_\alpha$ was referred to as the "continuum" model. In contrast to simpler assumption of Ashby [16], this approach does lead to a development of (edge) GNDs perpendicular to the slip plane (i.e., parallel to $\boldsymbol{n}_\alpha$). Even simplified to small deformation, i.e. disregarding the second term of Eq. (5.1.3),

$$\dot{\boldsymbol{g}}_{\alpha,\,\mathrm{reduced}} = b^{-1} \boldsymbol{\nabla}_{\mathrm{r}} \dot{\gamma}_\alpha \times \boldsymbol{n}_\alpha + \dot{\gamma}_\alpha \sum_\beta [\boldsymbol{n}_\alpha \cdot \boldsymbol{s}_\beta] \boldsymbol{g}_\beta \;, \tag{5.1.6}$$

this model still differs from almost all other gradient crystal plasticity models in the literature, see e.g. Evers et al. [93], which are invariably based on the slip-system model

$$\dot{\boldsymbol{g}}_{\alpha,\,\mathrm{Evers}} = b^{-1} \boldsymbol{\nabla}_{\mathrm{r}} \dot{\gamma}_\alpha \times \boldsymbol{n}_\alpha \tag{5.1.7}$$

for $\boldsymbol{g}_\alpha$ due in essence to Ashby [16]. Furthermore, in the concept presented in Evers et al. [93], a non-trivial initial value the referential dislocation tensor $\boldsymbol{G}_{\mathrm{r}}$ is attributed to the ideal of geometric-necessary boundaries. Comparison of these last two evolution relations for the dislocation density $\boldsymbol{g}_\alpha$ shows that, besides the large-deformation dependence, the Ashby model neglects the latent hardening contribution coming from the first term in Eq. (5.1.3).

During plastic deformation, two types of dislocations occur. One type, the so-called statistically stored dislocations (SSD) accumulate by a random trapping process. The elastic distortion of the crystal's lattice is not compatible with a deformation which is derivable from a continuously differentiable displacement field. This leads to the presence of the second type of dislocations that are called geometrically necessary dislocations (GNDs) (see Nye [201]) which, in other words, are stored due to the locally heterogeneous plastic shear strain. They are introduced to preserve lattice compatibility and give rise to inhomogeneous deformation (and, thus, stress) fields.

We are now ready to extend existing models for crystal plasticity to account for the effects of GNDs on their material behaviour, and in particular their effect on the hardening behaviour of the material. In the current thermodynamic context, such extensions are realized via the constitutive dependence of the free energy on GND density, and more generally on the dislocation state in the material.

For simplicity, attention is restricted here on isothermal processes. We assume the existence of a free energy density ψ_r

$$\psi_\mathrm{r} = \psi_\mathrm{r}(\boldsymbol{F}, \boldsymbol{F}_\mathrm{P}, \boldsymbol{\gamma}, \underline{\boldsymbol{g}}) \tag{5.1.8}$$

The vector $\underline{\boldsymbol{g}}$ contains the dislocation densities $\boldsymbol{g}_\alpha$ for all slip systems α and depends on the plastic slips $\boldsymbol{\gamma}$ as well as the slip gradients $\nabla_\mathrm{r}\boldsymbol{\gamma}$. Kinetic effects on dislocation processes, e.g., nucleation and activation, and the concomitant deviation from linearity, are described here in terms of the dissipation potential

$$\chi = \chi(\dot{\boldsymbol{\gamma}}, \nabla_\mathrm{r}\dot{\boldsymbol{\gamma}}). \tag{5.1.9}$$

The constitutive model here is based on the presumed existence of a dissipation potential χ, cf. Edelen [82]. Moreover, we define the rate potential r

$$r := \dot{\psi}_\mathrm{r} + \chi \tag{5.1.10}$$

determined by the forms of the free energy density ψ_r and the dissipation potential χ. Note that the dissipation principle will be sufficiently satisfied when the dissipation potential χ is non-negative and separately convex in its arguments. With these derivations at hand, we now turn to the algorithmic variational formulation of the proposed modeling approach.

5.2. Dual-mixed finite element formulation

The purpose of this section is to obtain governing equations in a dual-mixed finite element form. The dissipation principle is exploited to derive all field relations and (sufficient) forms of the constitutive relations as based on the free energy density ψ_r and dissipation potential χ.

The algorithmic formulation and numerical implementation of the current coupled multifield problem is carried out with respect to the reference configuration $\mathcal{B}_0$ on a time interval $I \subset \mathbb{R}$. For numerical purposes, this latter interval is discretized as usual into a disjoint union $\bigcup_{n=0}^{k-1}[t_n, t_{n+1}]$ of k finite subintervals $[t_0, t_1], \ldots, [t_{k-1}, t_k]$. In this context, consider the solution in the time interval $[t_n, t_{n+1}]$, and let $\Delta t := t_{n+1} - t_n$ be the length of the corresponding time interval. We apply a mixed implicit-explicit time-integration procedure, i.e., explicit for the local relations, implicit for the field relations.

In particular, forward-Euler integration of the evolution relation (2.2.7) for the local internal variable $\boldsymbol{F}_\mathrm{P}$ yields

$$\boldsymbol{F}_{\mathrm{P}\,n+1}(\boldsymbol{\gamma}_{n+1}) \quad = \quad \mathrm{uni}\left(\boldsymbol{I} + \sum_\alpha \gamma_{\alpha\, n+1,n}\, \boldsymbol{s}_\alpha \otimes \boldsymbol{n}_\alpha\right) \cdot \boldsymbol{F}_{\mathrm{P}\,n}\ , \tag{5.2.1}$$

in terms of the slip increment

$$\gamma_{\alpha\, n+1,n} \;\; := \;\; \gamma_{\alpha\, n+1} - \gamma_{\alpha\, n} \; . \tag{5.2.2}$$

In particular, Eq. (5.2.1) is obtained from the forward-Euler form by taking the unimodular part of both sides and requiring plastic incompressibility $\det(\boldsymbol{F}_{\mathrm{P}}) = 1$. Here, $\mathrm{uni}(\boldsymbol{A}) = \boldsymbol{A}/\det(\boldsymbol{A})^{1/3}$ represents the unimodular part of any second-order tensor $\boldsymbol{A}$. This form is used to algorithmically enforce plastic incompressibility and renders $\boldsymbol{F}_{\mathrm{P}\, n+1}(\boldsymbol{\gamma}_{n+1})$ nonlinear in $\boldsymbol{\gamma}_{n+1}$. Nevertheless, these local quantities are now explicit algorithmic functions of the current unknown field variables $\boldsymbol{\gamma}_{n+1}$ and their gradients $\nabla_{\mathrm{r}}\gamma_{n+1}$. Alternative to Eq. (5.2.1), one can work instead with the form

$$\boldsymbol{F}_{\mathrm{E}\, n+1}(\boldsymbol{\gamma}_{n+1}, \boldsymbol{F}_{n+1}) = \boldsymbol{F}^{\mathrm{tr}}_{\mathrm{E}\, n+1}(\boldsymbol{F}_{n+1}) \cdot \mathrm{uni}\left(\boldsymbol{I} - \sum_{\alpha} \gamma_{\alpha\, n+1,n}\, \boldsymbol{s}_{\alpha} \otimes \boldsymbol{n}_{\alpha}\right) \tag{5.2.3}$$

of the algorithmic flow rule in terms of $\boldsymbol{F}_{\mathrm{E}}$. Here,

$$\boldsymbol{F}^{\mathrm{tr}}_{\mathrm{E}\, n+1} = \boldsymbol{F}^{\mathrm{tr}}_{\mathrm{E}\, n+1}(\boldsymbol{F}_{n+1}) = \boldsymbol{F}_{n+1,n} \cdot \boldsymbol{F}_{\mathrm{E}\, n} \tag{5.2.4}$$

represents the usual trial value of $\boldsymbol{F}_{\mathrm{E}}$, and

$$\boldsymbol{F}_{n+1,n} := \boldsymbol{F}_{n+1} \cdot \boldsymbol{F}_{n}^{-1} \tag{5.2.5}$$

is the relative deformation gradient. In addition, we then have

$$\boldsymbol{E}_{\mathrm{E}\, n+1}(\gamma_{n+1}, \boldsymbol{F}_{n+1}) = \frac{1}{2}\left[\boldsymbol{C}_{\mathrm{E}\, n+1}(\gamma_{n+1}, \boldsymbol{F}_{n+1}) - \boldsymbol{I}\right] \tag{5.2.6}$$

for the corresponding elastic Green strain.

Moreover, the numerical integration of the evolution equation of the dislocation density $\boldsymbol{g}_{\alpha}$ based on forward Euler integration of Eq. (5.1.3) reads as follows:

$$\boldsymbol{g}_{\alpha\, n+1,n} = \sum_{\beta} \gamma_{\alpha\, n+1,n} [\boldsymbol{n}_{\alpha} \cdot \boldsymbol{s}_{\beta}] \boldsymbol{g}_{\beta\, n} + \gamma_{\beta\, n+1,n} [\boldsymbol{n}_{\beta} \cdot \boldsymbol{g}_{\alpha\, n}] \boldsymbol{s}_{\beta} + \frac{1}{b} \boldsymbol{\nabla}_{\mathrm{i}} \gamma_{\alpha\, n+1,n} \times \boldsymbol{n}_{\alpha}. \tag{5.2.7}$$

Point of departure for deriving the incremental governing equations is the numerical time integration of the rate potential r

$$r := \dot{\psi}_{\mathrm{r}} + \chi \tag{5.2.8}$$

over an arbitrary time interval starting at $t_n \in \mathbb{R}^{\geq 0}$. It determines the incremental potential density

$$w_{n+1,n} \;\; := \;\; \int_{t_n}^{t_{n+1}} r \, \mathrm{d}t = \psi_{\mathrm{r}\, n+1} - \psi_{\mathrm{r}\, n} + \int_{t_n}^{t_{n+1}} \chi \, \mathrm{d}t \tag{5.2.9}$$

together with the dissipation potential $\chi = \chi(\dot{\boldsymbol{\gamma}}, \boldsymbol{\nabla}_{\mathrm{r}}\dot{\boldsymbol{\gamma}})$ for the time interval $\Delta t = [t_n, t_{n+1}]$. Consequently, we have

$$\begin{aligned} w_{n+1,n}(\boldsymbol{\gamma}_{n+1}, \boldsymbol{F}_{n+1}, \boldsymbol{\nabla}_{\mathrm{r}}\boldsymbol{\gamma}_{n+1}) \;\approx\;& \psi_{\mathrm{r}\,n+1}(\boldsymbol{\gamma}_{n+1}, \boldsymbol{F}_{n+1}, \boldsymbol{\nabla}_{\mathrm{r}}\boldsymbol{\gamma}_{n+1}) - \psi_{\mathrm{r}\,n} \\ & + \Delta t\;\chi\left(\frac{\boldsymbol{\gamma}_{n+1}}{\Delta t}, \frac{\boldsymbol{\nabla}_{\mathrm{r}}\boldsymbol{\gamma}_{n+1}}{\Delta t}\right) \;, \end{aligned} \tag{5.2.10}$$

cf. e.g., Carstensen et al. [50], Miehe [187], Ortiz and Repetto [204], and Ortiz and Stainier [205], with $w_{n+1,n} = w_{n+1} - w_n$.

In the isothermal case, neglecting any body forces or supply-rate densities associated with the unknown fields (the deformation $\boldsymbol{\varphi}$ and the glide-system slips $\boldsymbol{\gamma} = (\gamma_1, \ldots, \gamma_{\mathfrak{g}})$, which represent non-normalized "phase-fields" for slip), this results in

$$\int_{\mathcal{B}_0} w_{n+1,n}\,\mathrm{d}V = \int_{\partial\mathcal{B}_0} \boldsymbol{t}_{\mathrm{r}\,n+1}\cdot\boldsymbol{\varphi}_{n+1,n} + \boldsymbol{d}_{\mathrm{r}\,n+1}\cdot\boldsymbol{\gamma}_{n+1,n}\,\mathrm{d}A \tag{5.2.11}$$

for such processes on the reference configuration $\mathcal{B}_0$ of the material in question, see e.g., Svendsen [248]. Here, $\boldsymbol{t}_{\mathrm{r}}$ and $\boldsymbol{d}_{\mathrm{r}}$ are the respective normal flux densities on the boundary $\partial\mathcal{B}_0$. Considering now the variation of Eq. (5.2.11) with respect to admissible variations $\delta\boldsymbol{\varphi}$ and $\delta\boldsymbol{\gamma}$ and taking their arbitrariness into account, we obtain the following governing field relations and boundary conditions

$$\begin{aligned} \boldsymbol{0} &= \mathrm{Div}(\partial_{\boldsymbol{F}_{n+1}} w_{n+1,n}) \quad \text{on } \mathcal{B}_0 \;, && (5.2.12)\\ \boldsymbol{t}_{\mathrm{r}\,n+1} &= \left[\partial_{\boldsymbol{F}_{n+1}} w_{n+1,n}\right]\cdot\boldsymbol{n}_{\mathrm{r}} \quad \text{on } \partial\mathcal{B}_0 \;, && (5.2.13)\\ \partial_{\boldsymbol{\gamma}_{n+1}} w_{n+1,n} &= \mathrm{Div}(\partial_{\boldsymbol{\nabla}_{\mathrm{r}}\boldsymbol{\gamma}_{n+1}} w_{n+1,n}) \quad \text{on } \mathcal{B}_0 \;, && (5.2.14)\\ \boldsymbol{\varphi}_{\mathrm{r}\,n+1} &= \left[\partial_{\boldsymbol{\nabla}_{\mathrm{r}}\boldsymbol{\gamma}_{n+1}} w_{n+1,n}\right]\cdot\boldsymbol{n}_{\mathrm{r}} \quad \text{on } \partial\mathcal{B}_0. && (5.2.15) \end{aligned}$$

These incremental relations form the basis of the finite element implementation.

In the implementation we follow a dual-mixed finite element approach similar to the one used in Sections 2-4. In each node and each time step, it is solved for the displacement $\boldsymbol{u}_{n+1}$ and the dislocation density $\boldsymbol{g}_{\alpha\,n+1}$, whereby the balance of momentum (5.2.12) and the definition (5.2.7) serve as governing equations. In each element, it is solved for the slips $\boldsymbol{\gamma}_{n+1}$ in each Gauß point.

5.3. Modeling assumptions for latent hardening

The free energy density ψ_{r} per unit intermediate volume is introduced as a function of the intermediate Green–Lagrange strain $\boldsymbol{E}_{\mathrm{E}}$, the slip-system shears γ_α and the dislocation density $\boldsymbol{g}_\alpha$. Assuming that elastic deformation, local hardening as well as microscopic material lengthscale-dependent processes contribute to the energy storage in the material, the following free energy density is postulated:

$$
\begin{aligned}
\psi_{\mathrm{r}}(\boldsymbol{F}, \boldsymbol{F}_{\mathrm{P}}, \boldsymbol{\gamma}, \underline{\boldsymbol{g}}) \;=\;& \frac{\lambda}{2}\left[\mathrm{tr}\boldsymbol{E}_{\mathrm{E}}\right]^2 + \mu\,\mathrm{tr}\left((\boldsymbol{E}_{\mathrm{E}})^2\right) + \frac{1}{2}\sum_{\alpha,\beta} H^{\mathrm{l}}_{\alpha\beta}\gamma_\alpha\gamma_\beta \\
&+\frac{1}{2} l_0^2 H_0^g \sum_{\alpha,\beta}[\boldsymbol{b}_\alpha \cdot \boldsymbol{b}_\beta][\boldsymbol{g}_\alpha \cdot \boldsymbol{g}_\beta]. \qquad (5.3.1)
\end{aligned}
$$

The contribution to energy storage in the form of $\psi_{\mathrm{r\,G}} = \frac{1}{2} l_0^2 H_0^g \sum_{\alpha,\beta}[\boldsymbol{b}_\alpha \cdot \boldsymbol{b}_\beta][\boldsymbol{g}_\alpha \cdot \boldsymbol{g}_\beta]$ stems from the quadratic form $\psi_{\mathrm{r\,G}} = \frac{1}{2} l_0^2 H_0^g \boldsymbol{G}_{\mathrm{i}} \cdot \boldsymbol{G}_{\mathrm{i}}$ - the contribution of excess dislocations to energy storage in the intermediate configuration relative to the dislocation measure $\boldsymbol{G}_{\mathrm{i}}$. Hereby, we have assumed that $\boldsymbol{G}_{\mathrm{i}}$ is initially zero for simplicity. This contribution to stored energy is scaled by the gradient hardening modulus H_0^g as well as the square of the effective material lengthscale l_0 for energy storage, not necessarily constant. As an example of the dissipation potential χ, we consider the following power-law

$$
\chi(\dot{\boldsymbol{\gamma}}) \;=\; \sum_\alpha Y_\alpha \dot{\gamma}_\alpha + \frac{m}{m+1}\,\frac{C_0}{t_*}\,\left[t_* \dot{\gamma}_\alpha\right]^{\frac{m+1}{m}}. \qquad (5.3.2)
$$

By definition, the dissipation potential χ is convex in its non-equilibrium arguments, i.e. the slip rates $\dot{\boldsymbol{\gamma}}$ and the slip rate gradients $\boldsymbol{\nabla}_{\mathrm{r}}\dot{\boldsymbol{\gamma}}$, and vanishes in equilibrium. Note that with the present assumptions for the referential free energy density ψ_{r} and the dissipation potential χ as stated above, neither one of them depends explicitly on the grain size (or the size length of the grain-structure). Moreover, the other lengths such as the length of the Burgers vector b or the effective material lengthscale l_0 are kept constant throughout the simulations. Rather, a grain size-dependent hardening will arise naturally.

Having specified the basic model relations, we are now in a position to formulate the forms of the incremental potential $w_{n+1,n}$ given in Eq. (5.2.10). Inserting the modeling assumptions made above, i.e. Eqs. (5.3.1) and (5.3.2), into the incremental potential density, i.e. Eq. (5.2.10), yields

$$
\begin{aligned}
w_{n+1,n} \;=\;& \frac{1}{2}\lambda\,\mathrm{tr}(\boldsymbol{E}_{\mathrm{E}\,n+1})^2 + \mu\,\boldsymbol{E}_{\mathrm{E}\,n+1} : \boldsymbol{E}_{\mathrm{E}\,n+1} \\
&+\frac{1}{2}\sum_{\alpha,\beta}\left[H^l_{\alpha\beta}\,\gamma_{\alpha\,n+1}\gamma_{\beta\,n+1} + l_0^2\,H_0^g\,[\boldsymbol{b}_\alpha \cdot \boldsymbol{b}_\beta][\boldsymbol{g}_{\alpha\,n+1} \cdot \boldsymbol{g}_{\beta\,n+1}]\right] \\
&+\sum_\alpha\left[Y_\alpha \gamma_{\alpha\,n+1,n} + \Delta t \frac{m}{m+1}\,\frac{C_0}{t_*}\left[\frac{t_*}{\Delta t}\gamma_{\alpha\,n+1,n}\right]^{\frac{m+1}{m}}\right] \\
&-\psi_{\mathrm{r}\,n}. \qquad (5.3.3)
\end{aligned}
$$

5.4. Representative two dimensional numerical example

To gain further insight into the modeling approach being pursued here, we now look in detail at the modeling of the mechanical response (i.e. the local and non-local hardening behavior) of a two-dimensional grain structure.

The numerical implementation of the strongly coupled and nonlinear system of equations is done with the help of the finite element method (in space) and a mixed implicit-explicit integration procedure in time. Besides the mechanical displacement $\boldsymbol{u}$, the dislocation densities $\boldsymbol{g}_\alpha$ are chosen as primary unknowns. The coupling of the equations is taken into account via a monolithic Newton–Raphson iteration scheme.

5.4.1. Set-up for modeling latent hardening in polycrystals

We consider a two-dimensional grain-structure consisting of 25 grains. It is discretized with 4642 elements in space, see Figure 5.1 (left). The individual grains consist of different numbers of finite elements. Triple slip is assumed and the slip directions $\boldsymbol{s}_\alpha$ are randomly distributed, see Figure 5.1 (right). We assume microhard boundary conditions, i.e.,

$$\gamma_\alpha = 0 \quad \text{on } \partial\mathcal{B}_{0,\text{grain}}. \tag{5.4.1}$$

Simulations are performed for the standard representative example of simple shear on the macro-scale in order to highlight the major characteristics of the models. Plane strain conditions are assumed[1]. Computations are carried out in monotonic loading with $\bar{\gamma}_{\max} = 0.10$ with the constant loading rate of 0.01 [1/s]. We applied 175 equidistant time steps. This, as well as the material parameters, are chosen in accordance to the values used in Evers et al. [93]. The values of the material parameters are chosen as stated in Table 5.1.

5.4.2. Numerical results

The macroscopic stress-strain response in terms of the nominal shear stress component $\bar{P}_{12}$ versus the macroscopic shear $\bar{\gamma}$ is shown in Figure 5.2. It depicts a grain size dependent hardening for fixed material parameters but for increasing side length L of the grain-structure. As expected and in accordance to the experimental findings of Hall [127] and Petch [213], stiffer response in the hardening regime can be seen for smaller grain size. The size effect can be seen during the plastic deformation as well as during the ongoing yielding. The size-dependence of the stress-strain response is due the existence of the slip gradient $\nabla_{\text{i}}\gamma_\alpha$ (indirectly via the dislocation density g_α) in the free energy density ψ_{r}. Moreover, in Figure 5.2 one can clearly see the influence of cross-hardening leading to a stiffer response material response if cross-hardening is included (at fixed size length L). The smaller the grain size, the stronger is the influence.

As reported by Kocks [160] and Thompson et al. [257], the GNDs are concentrated near the grain boundaries. This phenomenon is due to the lattice mismatch between neighboring grains and is mapped by the model presented in this contribution, see Figure 5.3. The dislocation density g_α is larger near the walls and vanishes towards the grain core. To illustrate this, the results are depicted for grain lengths $L = 1000$ μm and

---

[1] Thus, a reduction of the dislocation density $\dot{\boldsymbol{g}}_\alpha$ to $\dot{g}_\alpha = \boldsymbol{t}_\alpha \cdot \dot{\boldsymbol{g}}_\alpha$ is reasonable.

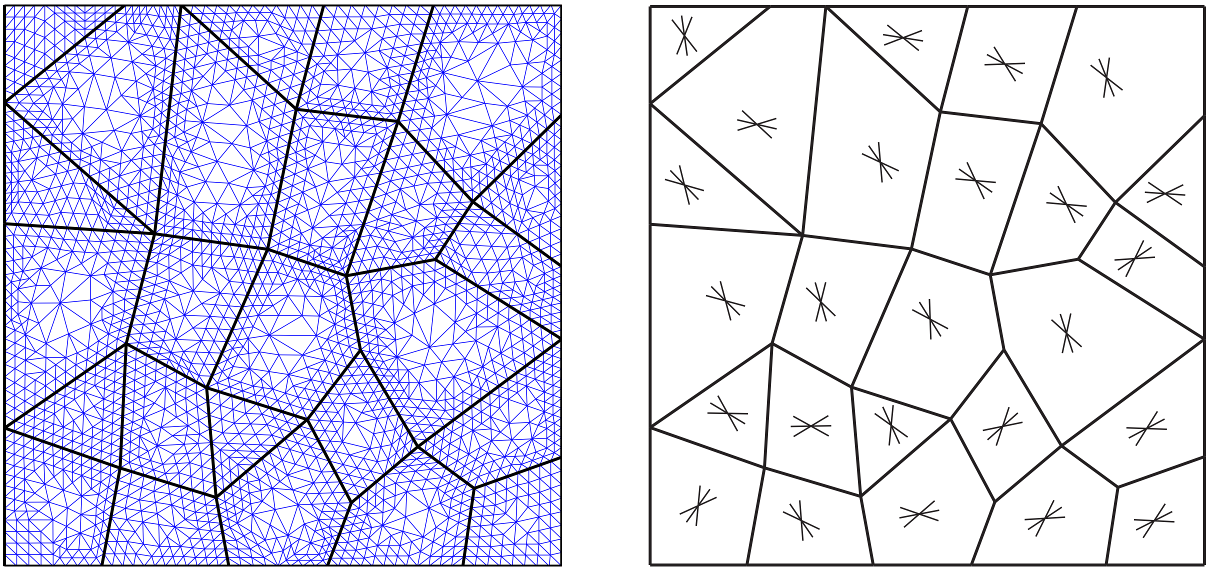

Figure 5.1.: Left: Discretization and grain geometry used during simulations. The square grain-structure consists of 25 grains and the thick black lines represent the grain boundaries. The grains are discretized with up to 318 elements, respectively. The mesh is refined near the grain boundaries. The side length L of the grain-structure is varied during simulations in order to capture the size effects.
Right: Schematic sketch of slip plane directions $\boldsymbol{s}_\alpha$. Triple slip is assumed and slip plane directions are randomly distributed.

$L = 2200\ \mu$m (Figure 5.3) in order to gain insight into the size dependent development of GNDs. Whether cross-hardening is involved or not hardly effects the development of GNDs. However, the grain size is not negligible. This can be explained by the fact that the plastic slip overcomes a smaller distance in case of a smaller grain structure in order to develop GNDs.

Figure 5.4 illustrates the distribution of the effective plastic slip $\gamma_{\text{eff}} := \sqrt{\gamma_1^2 + \gamma_2^2 + \gamma_3^2 + \gamma_4^2 + \gamma_5^2 + \gamma_6^2}$ for $L = 1000\ \mu$m and $L = 2200\ \mu$m.

5.5. Discussion

In this section, the analysis focused latent hardening (including the requirement of scale dependent stress-strain behavior). An extended crystal plasticity framework has been established within a thermodynamic setting. The governing equations for the mechanical as well as for the grain problem stem from an algorithmic variational formulation. The model presented in this contribution accounts for dislocation densities and allows for influences of one slip system onto another. In particular, cross-hardening is incorporated via the GNDs. To be specific, the free energy was additively splitted into an elastic and

Parameter	Symbol	Value	
Young's modulus	E	144	[GPa]
Poisson's ratio	ν	0.33	
local hardening modulus	H^l_α	600	[MPa]
gradient hardening modulus	H^g_0	$1.1 \cdot 10^5$	[MPa]
internal length scale	l_0	1	[μm]
initial yield stress	Y_α	20	[MPa]
relaxation time	t_*	10^3	[s]
material constant	C_0	1	[MPa]
rate sensitivity parameter	m	1	
magnitude of Burgers vector	b	0.256	[nm]

Table 5.1.: Material parameters used for the grain-structure. In order to allow for a comparison with the model and the numerical results of Evers et al. [93], the material parameters are chosen as in [93]. The hardening moduli H^l_α and H^g_α cannot be taken directly from [93]. However, for many metals at room temperature, the hardening modulus H^l_α is around three orders-of-magnitude lower than the elastic modulus E, which gives rise to the local hardening modulus $H^l_\alpha = 500$ [MPa]. Moreover, $l_0^2 H^g_\alpha$ can be identified with the term $\mu R^2/[8 - 8\nu] \approx 100.1$ [GPa] in [93].

an inelastic contribution. The latter was assumed to include local contributions from the plastic slips and a non-local contribution from the dislocation densities. The dislocation densities develop from the slip rate $\dot{\gamma}_\alpha$ as well as the slip gradient $\nabla_{\mathrm{i}}\gamma_\alpha$.

We computationally modelled the mechanical response of a grain structure specimen - assuming plain strain conditions. The size length L of the specimen was varied during the simulations in order to study its influence. The numerical results presented in Section 5.4 underline the influence of cross-hardening in material models of extended crystal plasticity. They show that the macroscopic strength increases with decreasing grain size as a result of gradient hardening. Furthermore, the simulations indicate that the model, besides being suitable for modeling size-dependent stress-strain responses, as well accounts for size-dependent development of dislocation densities. In accordance to experimental data, it was found that the dislocations densities g_α mainly develop near the grain boundaries and are negligible in the grain core.

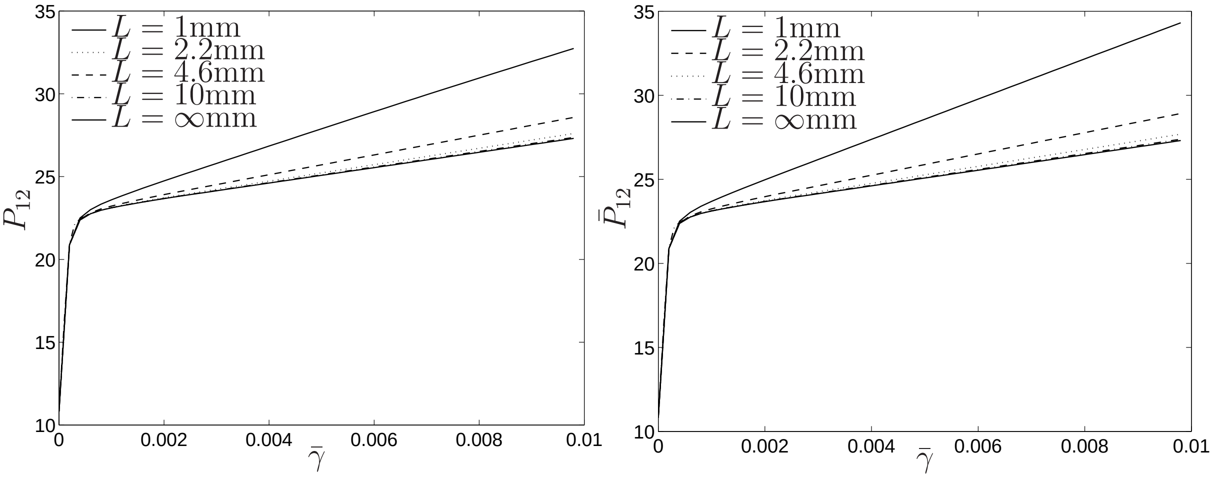

Figure 5.2.: Left: Macroscopic stress–strain response ($\bar{P}_{12}$ vs. $\bar{\gamma}$) showing the size dependence on the amount of hardening without cross-hardening.
Right: Macroscopic stress–strain response ($\bar{P}_{12}$ vs. $\bar{\gamma}$) showing the size dependence on the amount of hardening including cross-hardening.
For smaller grain sizes, cross-hardening leads to a stiffer material response.

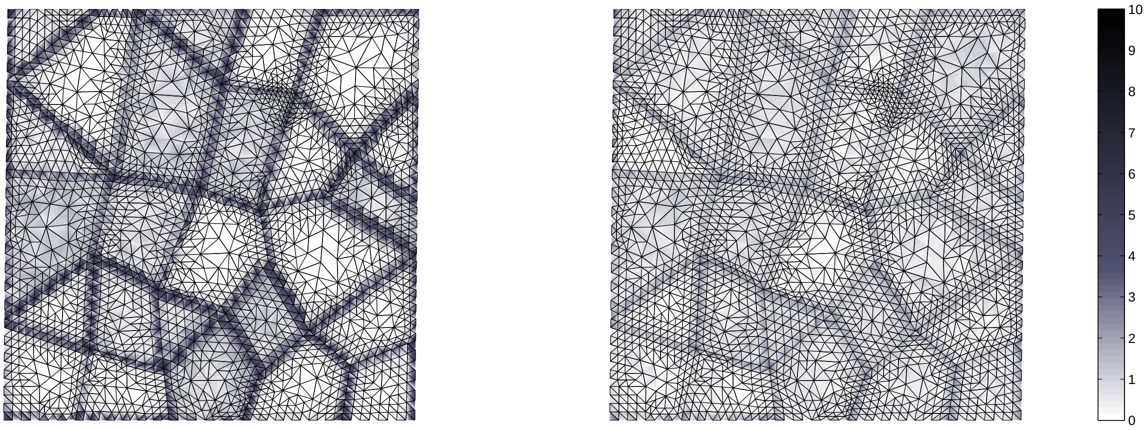

Figure 5.3.: Left: Distribution of the dislocation density g_α for a grain structure with sample side length $L = 1000$ μm (left) and $L = 2200$ μm (right) at $\bar{\gamma} = 0.01$. The dislocation density magnitude is significantly larger for the smaller grain size.

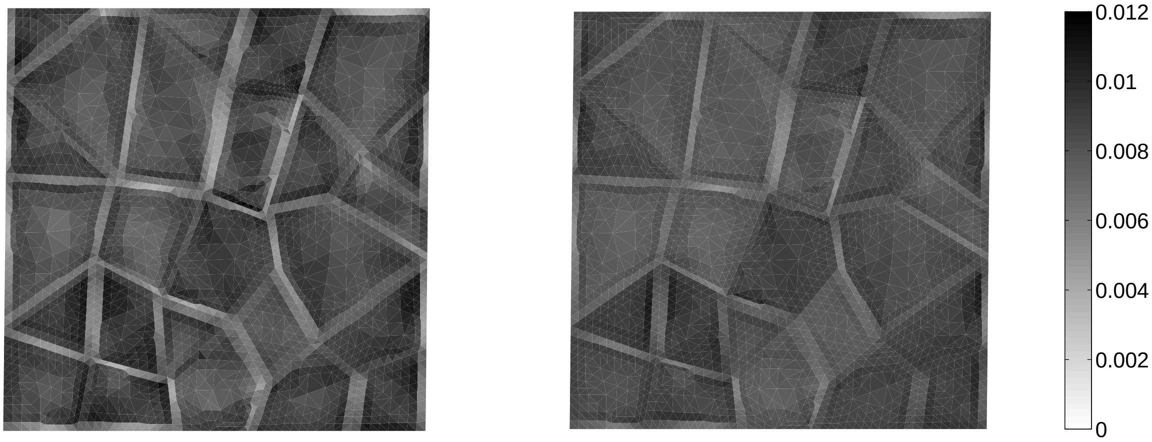

Figure 5.4.: Effective hardening strain $\gamma_{\mathrm{eff}} := \sqrt{\gamma_1^2 + \gamma_2^2 + \gamma_3^2 + \gamma_4^2 + \gamma_5^2 + \gamma_6^2}$. On the left the solution for a grain-structure side length $L = 1000$ μm and on the right the distribution for $L = 2200$ μm are depicted at $\bar{\gamma} = 0.01$ strain. The displacement field inside the grain-structure is unconstrained. For the grain problem microhard boundary conditions are assumed.

6. A gradient crystal plasticity theory that includes dissipative microstresses

This chapter investigates a model extension of that due to Gurtin [122, 123], and is guided by the viscoplastic model and algorithm of Ekh et al. [85] whose governing equations are equivalent to those of Gurtin for the purely energetic case as shown in Chapter 2. In contrast to the Gurtin formulation and in line with Chapters 3 and 4 as well as Ekh et al. [85], viscoplasticity in the present model is accounted for through a Perzyna-type regularization. The resulting theory includes three different types of hardening: standard isotropic hardening is incorporated as well as energetic hardening driven by the slip gradient. In addition, as a third type, dissipative hardening associated with plastic strain rate gradients is included. Numerical results investigating the different hardening cases are presented.

6.1. Introduction

Almost 150 years ago, Tresca [258] was the first to formulate a plasticity theory in a series of papers. The classical theory of plasticity has since undergone steady and significant development, resulting in an elegant set of theories which have served as the basis for numerous theoretical and computational studies (see for example [240, 239]).

It has been recognized for some time that the conventional theories of plasticity are not capable of modeling size effects at the mesoscale such as grain size-dependent hardening in polycrystals or widths of localized shear bands in materials undergoing strain-softening. In 1984 Aifantis [8] formulated an extended plasticity theory which has been followed by extensive work on the development of models that account for size effects. These generally have a non-local form, a popular example of which are the strain gradient plasticity models. A non-exhaustive list of theories for strain gradient crystal plasticity theories includes the works of Acharya et al. [3], Bassani [36], Borg [45], Ekh et al. [85], Evers et al. [93], Gurtin [120, 123] respectively Gurtin and Anand [124], Han et al. [128], Kuroda and Tvergaard [166], Levkovitch and Svendsen [173], Ohno and Okumura [203], to name a few. Within the context of general gradient plasticity even more publications can be found: see for example the work by Gudmundsen [117]. A large number of those are purely energetic, see for example Bargmann et al. [35], Ekh et al. [85], Evers et al. [93, 92], Gurtin [121], Kuroda and Tvergaard [165], just to name a few. However, the plastically deforming crystal exhibits energetic and dissipative processes. This paper introduces a gradient crystal plasticity theory that includes energetic and dissipative parts.

There have been relatively few computational investigations of problems involving strain gradient plasticity. Examples include the works [72, 76, 77, 175] which deal with the Aifantis model. With regard to gradient crystal plasticity, Bittencourt et al. [43] have developed and applied an algorithm for the energetic model of gradient plasticity presented in [121]. In this contribution we rely on the dual mixed finite element algorithm proposed by Svedberg and Runesson [245].

The goal of this work is to formulate and carry out a numerical implementation of a model of single crystal gradient plasticity that includes dissipative microstresses. The point of departure is the theory due to Gurtin [120, 123]. In this theory microforces are introduced as work-related conjugate quantities to slips and slip gradients; a principle of virtual power then leads to macro- and microforce balance equations. Constitutive equations for plastic flow are developed within a framework that is thermodynamically consistent.

Gurtin's theory is one of viscoplasticity. There is a power-law dependence on a generalized plastic strain rate, and no elastic region or yield surface delineates a threshold for plastic flow. In the model developed and considered in this work Gurtin's theory is extended to include the existence of a yield surface depending on the generalized stresses. Furthermore, viscoplasticity is accounted for as a Perzyna-type regularization (see [239] for a summary account) of the flow law. This approach borrows from the work of Ekh et al. [85] who use a Perzyna regularization in the context of a theory that is equivalent to the purely energetic version of Gurtin's theory[1].

The present work is guided further by that of Ekh et al. in that the finite element approximation is of dual-mixed type, in which an independent variable is introduced for the slip gradients. In addition to the modification of Gurtin's original model as described earlier, a further novel feature of the present work lies in the manner in which the dissipative microstress is incorporated into the algorithm of the dissipative microstress as an additional variable, together with a corresponding additional flow equation.

The approach taken is that of first formulating the rate-independent theory. This allows for the introduction of the yield function as well as an associative flow law, which play a central role and lead to a constitutive equation for a dissipative microstress $\boldsymbol{\xi}_\alpha^{\text{dis}}$. In a subsequent step the formulation is generalized to viscoplasticity in the spirit of the ideas of Ekh et al. [85], that is, via a Perzyna-type regularization. The approach smoothly unites and extends the ideas of Gurtin and co-workers [122, 123, 172] and Ekh et al. [85].

---

[1] Gurtin's microforce balance is also applied by Kuroda and Tvergaard [166], but they only study energetic microforces. Ohno and Okumura [203] incorporated their theory into Gurtin's microforce balance theory studying only energetic contributions. Moreover, Ertürk et al. [89] investigated in detail how the model of Evers et al. [93] can be recast within Gurtin's microforce formulation. The microforce is derived via the physical definition of the Evers type back stress which plays the main role in their formulation [93].

The rest of this chapter is structured as follows. Section 6.2 is devoted to a brief reiteration of the microforce balance equations as set out in Gurtin [120]. Still following the approach in the last-mentioned work, the free energy and dissipation inequality are introduced in Section 6.3. The hardening part of the free energy depends on the slip gradient $\nabla_{\mathrm{r}}\gamma_\alpha$, and this leads to the definition of energetic and dissipative microstresses, and a reduced dissipation inequality which forms the basis of the associative flow theory.

The extension to viscoplasticity is presented in Section 6.4 and the set of equations to be solved formulated. The theory is implemented into a two-dimensional finite element code within the context of the dual-mixed finite element method. The fully coupled problem then comprises the global finite element equations for the displacement and slip gradients together with local equations for the slips and dissipative microstresses. Finally, some numerical examples are discussed in Section 6.5.

6.2. Force balances

The underlying notation of the kinematics and the stress and strain measures is introduced in Section 2.2.

The macroscopic problem is governed by the balance of momentum, here stated in its quasi-static form

$$\mathrm{Div}\boldsymbol{P} + \boldsymbol{b} = \boldsymbol{0}, \tag{6.2.1}$$

with $\boldsymbol{P}$ and $\boldsymbol{b}$ denoting respectively the first Piola–Kirchhoff stress tensor and the body force. Along with the momentum balance (6.2.1) goes the traction condition

$$\boldsymbol{t}(\boldsymbol{N}) := \boldsymbol{P} \cdot \boldsymbol{N}, \tag{6.2.2}$$

where $\boldsymbol{t}$ denotes the macroscopic traction vector and $\boldsymbol{N}$ is the macroscopic outward unit normal vector on a surface in the material configuration.

At the microlevel, the approach due to Gurtin (see for example [120, 123]) is followed: specifically, a scalar microforce π_α and vector microstress $\boldsymbol{\xi}_\alpha$ work-conjugate to slip-rate $\dot{\gamma}_\alpha$ and slip-rate gradient $\nabla_{\mathrm{r}}\dot{\gamma}_\alpha$ respectively are introduced, together with a surface microtraction χ_α conjugate to $\dot{\gamma}_\alpha$. The microscopic virtual power relation leads to the microscopic force balance

$$\mathrm{Div}\,\boldsymbol{\xi}_\alpha + \tau_\alpha - \pi_\alpha = 0, \tag{6.2.3}$$

The microforce balance (6.2.3) has to hold for every slip system α. The micro- and the macrolevel are coupled via the Schmid stress τ_α, i.e. Eq. (2.2.8). In case of a pure elastic deformation (6.2.3) reduces to the relation $\pi_\alpha = \tau_\alpha$.

In analogy to Eq. (6.2.2), a microscopic traction condition is defined on the crystal boundaries by

$$\chi_\alpha(\boldsymbol{N}) := \boldsymbol{\xi}_\alpha \cdot \boldsymbol{N}, \tag{6.2.4}$$

with χ_α denoting the microscopic traction.

6.3. The free energy

We assume the existence of a free energy Ψ per unit reference volume which depends on the elastic deformation and the slip gradients $\nabla_{\mathrm{r}}\gamma_\alpha$. The free energy is assumed to be decomposed additively into elastic and hardening contributions; that is,

$$\Psi = \Psi_{\mathrm{E}}(\boldsymbol{E}^e) + \Psi_{\mathrm{h}}(\{\nabla_{\mathrm{r}}\gamma_\alpha\}) \tag{6.3.1}$$

where each of the components is quadratic in its arguments. In particular the elastic part Ψ_{E} has the standard St. Venant form

$$\Psi_{\mathrm{E}}(\boldsymbol{E}^e) = \frac{\lambda}{2}\left[\mathrm{tr}\boldsymbol{E}^e\right]^2 + \mu \mathrm{tr}\left([\boldsymbol{E}^e]^2\right), \tag{6.3.2}$$

with λ and μ being the Lamé parameters, while the hardening terms are given by

$$\Psi^{\mathrm{h}}(\{\nabla_{\mathrm{r}}\gamma_\alpha\}) = \frac{1}{2}\sum_\alpha H^l_\alpha \gamma^2_\alpha + \frac{1}{2}\sum_\alpha l^2_\alpha \nabla_{\mathrm{r}}\gamma_\alpha \cdot \boldsymbol{H}^g_\alpha \cdot \nabla_{\mathrm{r}}\gamma_\alpha\,, \tag{6.3.3}$$

where $\boldsymbol{H}^g_\alpha$ is a tensor of hardening moduli and ℓ_α is a material parameter corresponding to a length scale, in both cases specified for each slip plane.

The free energy imbalance is used to guide the construction of a set of constitutive relations for elastic behavior and plastic flow. It takes the form

$$\dot{\Psi} - [\boldsymbol{F}\cdot\boldsymbol{P}] : \dot{\boldsymbol{E}}_{\mathrm{E}} - \sum_\alpha \left[\pi_\alpha \dot{\gamma}_\alpha + \boldsymbol{\xi}_\alpha \cdot \nabla_{\mathrm{r}}\dot{\gamma}_\alpha\right] \leq 0 \tag{6.3.4}$$

(cf. the arguments by Gurtin [120]). Substitution of Eqs. (6.3.1) and (6.3.2) in this inequality leads, after the usual arguments, to the elastic law

$$\boldsymbol{P} = \boldsymbol{F}\cdot\frac{\partial \Psi_{\mathrm{E}}}{\partial \boldsymbol{F}} = \lambda \mathrm{tr}\,\boldsymbol{E}_{\mathrm{E}} + 2\mu \boldsymbol{E}_{\mathrm{E}} \tag{6.3.5}$$

and the reduced dissipation inequality

$$\sum_\alpha \left[\pi_\alpha \dot{\gamma}_\alpha + (\boldsymbol{\xi}_\alpha - \boldsymbol{\xi}^{\mathrm{en}}_\alpha)\cdot \nabla_{\mathrm{r}}\dot{\gamma}_\alpha\right] \geq 0 \tag{6.3.6}$$

where

$$\boldsymbol{\xi}^{\mathrm{en}}_\alpha \quad := \quad \frac{\partial \Psi^{\mathrm{d}}}{\partial \nabla_{\mathrm{r}}\gamma_\alpha} = l^2_\alpha \boldsymbol{H}^g_\alpha \cdot \nabla_{\mathrm{r}}\gamma_\alpha \tag{6.3.7}$$

is the energetic component of the internal microstress. The microstress may be decomposed additively into energetic and dissipative components $\boldsymbol{\xi}^{\mathrm{en}}$ and $\boldsymbol{\xi}^{\mathrm{dis}}$, so that

$$\boldsymbol{\xi}^{\mathrm{dis}}_\alpha \quad := \quad \boldsymbol{\xi}_\alpha - \boldsymbol{\xi}^{\mathrm{en}}_\alpha \tag{6.3.8}$$

(see for example Gurtin [123] in the context of single crystal plasticity or Anand et al. [13] and Lele and Anand [171, 172] in the context of isotropic materials).

Using this definition, the reduced dissipation inequality (6.3.6) becomes

$$\sum_\alpha \left[\pi_\alpha \dot{\gamma}_\alpha + \boldsymbol{\xi}_\alpha^{\mathrm{dis}} \cdot \nabla_{\mathrm{r}} \dot{\gamma}_\alpha\right] \geq 0\,. \tag{6.3.9}$$

Elastic region and yield function.

We begin the formulation of the flow law within a rate-independent context, and later generalize to the case of viscoplasticity.

Guided by the reduced dissipation inequality, i.e. Eq. (6.3.9), we define the generalized stress

$$\mathsf{S}_\alpha = \begin{pmatrix} \pi_\alpha \\ l_d^{-1} \boldsymbol{\xi}_\alpha^{\mathrm{dis}} \end{pmatrix} \tag{6.3.10}$$

where l_d is a dissipative length scale, and the elastic region on the α th slip plane by

$$\Phi(\mathsf{S}_\alpha) = |\mathsf{S}_\alpha| - [Y_\alpha + \kappa_\alpha] \leq 0\,. \tag{6.3.11}$$

Here Y_α is the initial yield stress on the αth slip plane and κ_α the hardening stress. Furthermore,

$$|\mathsf{S}_\alpha| = \left[|\pi_\alpha|^2 + l_d^{-2}|\boldsymbol{\xi}_\alpha^{\mathrm{dis}}|^2\right]^{1/2}\,. \tag{6.3.12}$$

Assuming a normality law we have

$$\begin{aligned} \dot{\gamma}_\alpha &= \dot{\lambda}_\alpha \frac{\partial \Phi_\alpha}{\partial \pi_\alpha} = \dot{\lambda}_\alpha \frac{\pi_\alpha}{|\mathsf{S}_\alpha|}\,, \\ \nabla_{\mathrm{r}} \dot{\gamma}_\alpha &= \dot{\lambda}_\alpha \frac{\partial \Phi_\alpha}{\partial \boldsymbol{\xi}_\alpha^{\mathrm{dis}}} = \dot{\lambda}_\alpha \frac{l_d^{-2} \boldsymbol{\xi}_\alpha^{\mathrm{dis}}}{|\mathsf{S}_\alpha|}\,, \end{aligned} \tag{6.3.13}$$

where $\dot{\lambda}_\alpha \geq 0$ is a scalar multiplier, together with the complementarity conditions

$$\Phi_\alpha \leq 0\,, \quad \dot{\lambda}_\alpha \geq 0\,, \quad \dot{\lambda}_\alpha \Phi_\alpha = 0\,. \tag{6.3.14}$$

At flow, when $\Phi_\alpha = 0$, we have $|\mathsf{S}_\alpha| = Y_\alpha + \kappa_\alpha$ and

$$\left[(\dot{\gamma}_\alpha)^2 + l_d^2 |\nabla_{\mathrm{r}} \dot{\gamma}_\alpha|^2\right]^{1/2} = \dot{\lambda}_\alpha := d_\alpha \tag{6.3.15}$$

where d_α is the dissipation associated with the αth slip surface. It is thus convenient to define a generalized strain measure

$$\Gamma_\alpha = \begin{pmatrix} \gamma_\alpha \\ l_d \nabla_{\mathrm{r}} \gamma_\alpha \end{pmatrix} \tag{6.3.16}$$

so that

$$|\dot{\Gamma}_\alpha| = d_\alpha\,. \tag{6.3.17}$$

In the case of plastic flow equations (6.3.13) may be inverted to give

$$\begin{aligned} \pi_\alpha &= \frac{|\mathsf{S}_\alpha|}{d_\alpha}\dot{\gamma}_\alpha\,, \\ \boldsymbol{\xi}_\alpha^{\text{dis}} &= \frac{|\mathsf{S}_\alpha|}{d_\alpha} l_d^2 \nabla_{\text{r}}\dot{\gamma}_\alpha\,. \end{aligned} \tag{6.3.18}$$

For convenience linear isotropic hardening is assumed, so that

$$\kappa_\alpha := H_\alpha^1 k_\alpha \tag{6.3.19}$$

where k_α is the equivalent plastic strain on the αth slip plane, defined by

$$\dot{k}_\alpha := \dot{\lambda}_\alpha = d_\alpha \tag{6.3.20}$$

and H_α^1 is a positive material constant. This definition is a natural extension of the approach by Ekh et al. [85], where $\dot{k}_\alpha = \dot{\gamma}_\alpha$ was used. Furthermore, it leads to a consistent model in this contribution.

The procedure of Ekh et al. [85] differs from that of Gurtin and co-authors and thus from what is described above. Ekh et al. [85] derive a microstress, here denoted by $\kappa_{\text{Ekh}\,\alpha}$, via the second law of thermodynamics. The microstress is defined through the free energy Ψ which in addition to the gradient contribution stated in Eq. (6.3.3) depends quadratically on the plastic slip $\{\gamma_\alpha\}$. Moreover, it is split up additively into local and gradient hardening contributions in the form

$$\begin{aligned} \kappa_{\text{Ekh}\,\alpha} &:= \kappa_{\alpha,l} + \kappa_{\alpha,g} \\ &:= \frac{\partial \Psi}{\partial \gamma_\alpha} - \text{Div}\left(\frac{\partial \Psi}{\partial \nabla_{\text{r}}\gamma_\alpha}\right) \quad \text{in } \mathcal{B}_{0,\,\text{grain}},\ \alpha = 1, 2, ..., n_{\text{slip}} \end{aligned} \tag{6.3.21}$$

where $\mathcal{B}_{0,\,\text{grain}}$ denotes the material domain associated with a grain. As stated in Bargmann et al. [22], the gradient contribution of the microstress can be identified with the divergence of the energetic microforce of Gurtin: that is, $\kappa_{\alpha,g}$ corresponds to $\text{Div}\,\boldsymbol{\xi}_\alpha^{\text{en}}$. Both play the role of an energetic backstress. Moreover, in case of pure energetic hardening, the hardening stresses stated in Eqs. (6.3.19) and (6.3.21) are equivalent.

The formulation presented here is a rate-independent one that is based on the Gurtin-type approach. Some key distinctions are worth noting:

(i) The notion of an elastic region, yield function and normality law are explicitly introduced in the present formulation. These in turn are defined on the basis of the structure of the reduced dissipation inequality.

(ii) Local hardening is captured via the hardening law in a conventional way, while non-local effects appear through the inclusion of the microstress in the microforce balance and through the hardening term in the free energy.

Both approaches necessitate the existence of microscopic boundary conditions.

6.4. A viscoplastic model with dissipative microstress

In this section the constitutive equations for plastic flow are generalized to the case of viscoplasticity. In the works of Gurtin, Anand and coworkers (see for example [120, 123, 124, 171, 172]), viscoplastic regularization entails extensions of Eq. (6.3.18) which take the form

$$\begin{aligned} \pi &\propto \mathcal{S} R(d_\alpha)\dot{\gamma}_\alpha \\ \boldsymbol{\xi}^{\text{dis}} &\propto \mathcal{S} R(d_\alpha)\nabla_{\text{r}}\dot{\gamma}_\alpha \end{aligned} \tag{6.4.1}$$

where $R(d_\alpha) = (d_\alpha/d_0)^q$, d_0 is a reference generalized strain rate, and q is a positive real exponent. Furthermore $\mathcal{S}$ denotes the positive-valued flow resistance. This is also the approach taken by other authors such as Evers et al. [93]. It follows that in these approaches the dissipative microstress $\boldsymbol{\xi}^{\text{dis}}$ is defined via Eq. $(6.4.1)_2$. However, the approach by these authors does not allow for elastic behavior, for the case in which the generalized stress lies in the elastic region.

The approach to viscoplastic regularization taken in this work differs from that just described. Here the goal is to extend the approach of Ekh et al. [85] by introducing a regularization of Perzyna type: in the case of a solely energetic microstress, as in [85], which can be obtained by setting $l_d = 0\,\mu$m in the set of equations in the previous section, the flow law

$$\dot{\gamma}_\alpha = \dot{\lambda}_\alpha \operatorname{sgn} \pi_\alpha \tag{6.4.2}$$

becomes

$$\dot{\gamma}_\alpha = \frac{1}{t_{\star,\alpha}} \langle \Phi_\alpha \rangle^m \operatorname{sgn} \pi_\alpha \tag{6.4.3}$$

or equivalently

$$\dot{\lambda}_\alpha = \frac{1}{t_{\star,\alpha}} \langle \Phi_\alpha \rangle^m \,, \tag{6.4.4}$$

where

$$\langle x \rangle := \frac{1}{2}[x + |x|]$$

and where $t_\star$ is a relaxation time and m the rate sensitivity parameter. Moreover, the restriction on the sign of the yield function Φ_α, i.e. Eq. $(6.3.14)_1$, does not hold any more, of course. In other words, the yield function can be positive, negative or zero.

In the present approach the elastic region is defined by $\Phi_\alpha < 0$ and the plastic by $\Phi_\alpha \geq 0$. The objective in this work is to extend this approach to the case of dissipative microstresses in a manner that is amenable to computational implementation.

Thus the viscoplastic flow law is defined by

$$\dot{\Gamma}_\alpha = \frac{1}{t_{\star,\alpha}} \langle \Phi_\alpha \rangle^m \frac{\mathsf{S}_\alpha}{|\mathsf{S}_\alpha|}. \tag{6.4.5}$$

From Eqs. (6.3.17) and (6.4.5) it follows that

$$|\dot{\Gamma}_\alpha| = d_\alpha = \frac{1}{t_{\star,\alpha}} \langle \Phi_\alpha \rangle^m . \tag{6.4.6}$$

In the case of flow, that is, when $\Phi_\alpha > 0$, equation (6.4.6) is equivalent to

$$|\mathsf{S}_\alpha| = (t_{\star,\alpha} d_\alpha)^{1/m} + Y_\alpha + \kappa_\alpha, \tag{6.4.7}$$

where local hardening enters via the last term on the right-hand side. Thus from Eqs. (6.4.5) and (6.4.6) follows

$$\dot{\Gamma}_\alpha = \left[\frac{d_\alpha}{(t_{\star,\alpha} d_\alpha)^{1/m} + Y_\alpha + \kappa_\alpha}\right] \mathsf{S}_\alpha\,. \tag{6.4.8}$$

In component form

$$\dot{\gamma}_\alpha = \left[\frac{d_\alpha}{(t_{\star,\alpha} d_\alpha)^{1/m} + Y_\alpha + \kappa_\alpha}\right] \pi_\alpha\,, \tag{6.4.9}$$

$$\nabla_{\mathrm{r}}\dot{\gamma}_\alpha = \left[\frac{d_\alpha}{(t_{\star,\alpha} d_\alpha)^{1/m} + Y_\alpha + \kappa_\alpha} l_d^{-2}\right] \boldsymbol{\xi}_\alpha^{\mathrm{dis}}\,. \tag{6.4.10}$$

The next step is to eliminate the dissipative microstress $\boldsymbol{\xi}_\alpha^{\mathrm{dis}}$ from these equations.

Substitution in Eq. (6.4.9) for the internal microforce π_α using the microforce balance equation (6.2.3) leads to the non-local flow rule

$$\dot{\gamma}_\alpha = \frac{d_\alpha}{(t_{\star,\alpha} d_\alpha)^{1/m} + Y_\alpha + \kappa_\alpha} \left[\tau_\alpha + \mathrm{Div}\,\boldsymbol{\xi}_\alpha^{\mathrm{en}} + \mathrm{Div}\,\boldsymbol{\xi}_\alpha^{\mathrm{dis}}\right]. \tag{6.4.11}$$

An explicit expression for the dissipative microstress[2] $\boldsymbol{\xi}_\alpha^{\mathrm{dis}}$ is obtained by inverting Eq. (6.4.10), which gives

$$\boldsymbol{\xi}_\alpha^{\mathrm{dis}} = \frac{(t_{\star,\alpha} d_\alpha)^{1/m} + Y_\alpha + \kappa_\alpha}{d_\alpha} l_d^2 \nabla_{\mathrm{r}}\dot{\gamma}_\alpha, \tag{6.4.12}$$

showing the dependence of the dissipative microstress $\boldsymbol{\xi}_\alpha^{\mathrm{dis}}$ on the plastic slip rate gradient $\nabla_{\mathrm{r}}\dot{\gamma}_\alpha$. This dependence is highly non-linear because d_α depends on the slip rate gradient $\nabla_{\mathrm{r}}\dot{\gamma}_\alpha$ as well. A similar expression for dissipative hardening, being linear in the plastic slip rate gradient $\nabla_{\mathrm{r}}\dot{\gamma}_\alpha$ has been derived by Anand et al. [13], Fredriksson and Gudmundson [101] and Lele and Anand [171, 172] for isotropic materials and in the contribution of Gurtin [123] for single crystal plasticity (see also Remark below).

Finally, the use of Eq. (6.4.12) and the expression (6.3.7) for $\boldsymbol{\xi}_\alpha^{\mathrm{en}}$ in Eq. (6.4.11) leads to an expression for the plastic slip rate that is entirely in terms of $\nabla_{\mathrm{r}}\gamma_\alpha$, d_α, and the hardening variable $\kappa_{\alpha,l}$. It is worth noting that in this contribution the regularization is introduced from the start via the evolution equation (6.4.5). Then, in turn, the relation between the dissipative microstress $\boldsymbol{\xi}_\alpha^{\mathrm{dis}}$ and the slip rate gradient $\nabla_{\mathrm{r}}\dot{\gamma}_\alpha$ is a derived result (see Eq. (6.4.12)) and not a definition.

In the case of purely energetic microstress, that is, for $l_d = 0\,\mu\mathrm{m}$, the evolution equation (6.4.5) reduces to the flow law

$$\dot{\gamma}_\alpha = \frac{1}{t_{\star,\alpha}} \left\langle \Phi_\alpha \right\rangle^m\,, \tag{6.4.13}$$

---

[2] Since the scalar d_α is not constant, this gives rise to an additional complexity in terms of the divergence term $\mathrm{Div}\,\boldsymbol{\xi}_\alpha^{\mathrm{dis}}$.

which is the expression used in Ekh et al. [85]. For the dissipative case, for which $l_d \neq 0$, the generalization captured in Eqs. (6.4.5)-(6.4.12) essentially flows from the dissipation inequality in the form (6.3.9).

6.5. Numerical example

The finite element algorithm used for the computations is similar to the dual mixed framework of the preceeding sections. Here, the definition differs in the use of the vector-valued gradient $\boldsymbol{g}_\alpha$ instead of the scalar directional gradient $g_\alpha := \nabla_{\mathrm{r}}\gamma_\alpha \cdot \boldsymbol{s}_\alpha$. Microhard boundary conditions are assumed so that

$$\gamma_\alpha = 0 \qquad \text{on } \partial\mathcal{B}_{0,\mathrm{grain}}, \tag{6.5.1}$$

(see for example the statement in Gurtin and Needleman [125]:
“When the theory is generalized to allow each of the microstress $\boldsymbol{\xi}_\alpha$ to have a dissipative contribution on the slip-gradient rates, then the hard slip conditions are appropriate.”).

In this section the behavior of the proposed model is studied by means of simple but effective numerical examples. The approach can be applied to single crystals as well as polycrystals. In the following, we investigate the hardening behavior of a specimen with side length L and comprising four grains. The length L is varied during the simulations in order to illustrate the grain size dependence of the hardening behavior of the crystal. The deformation of the grain structure is controlled by linearly varying displacements of the boundaries to obtain macroscopic simple shear with a constant loading rate $\dot{\bar{\gamma}} = 0.01$ [1/s]. Plain strain is assumed. A total of 100 time steps have been used. The finite element meshes of the grain structures used in the numerical examples are generated by Voronoi polygonization and are depicted in Figure 6.1. The meshes are refined near the grain boundaries. The set of material parameters used in the examples are summarized in Table 6.1.

As a first step, the macroscopic stress-strain response depicted in Figure 6.2 is discussed. The curves are plotted for different values of the side length L. On the left the stress-strain curve for the model including dissipative strengthening ($l_d \neq 0$) is depicted, while the curves on the right show the response in the absence of dissipative strengthening ($l_d = 0\,\mu$m). As the length L decreases, the material response is stiffer in both cases, as expected. The size-dependence of the stress-strain response is due the existence of the slip gradient $\nabla_{\mathrm{r}}\gamma_\alpha$ in the hardening free energy density (Eq. (6.3.3)) and, as a consequence, its existence in the governing equations. Moreover, the proposed model is capable of modeling a size-dependent yield stress if dissipative strengthening is included.

The model captures purely elastic response in line with the elastic-viscoplastic nature of the flow law. With an initial yield stress of $Y_\alpha = 120$ [MPa] the stress-strain response is initially linear elastic. At approximately $\bar{\gamma} = 0.003$ plastic behavior in the polycrystal with hardening becomes apparent.

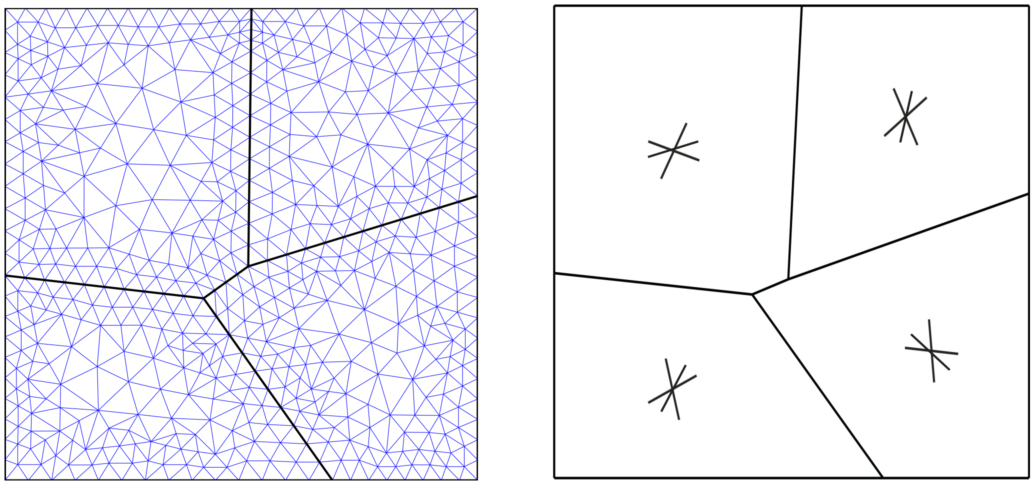

Figure 6.1.: Left: Discretization and grain geometry used during simulations. The square grain structure consists of four grains and the thick black lines represent the grain boundaries. The grains are discretized with 726 (upper left grain), 620 (upper right), 630 (lower left), and 614 (lower right) elements, respectively. The mesh is refined near the grain boundaries. The side length L of the grain structure is varied during simulations in order to capture the size effects. A simple shear test as well as a tension test are performed.
Right: Schematic sketch of slip plane directions $\boldsymbol{s}_\alpha$. Triple slip is assumed and slip plane directions are randomly distributed.

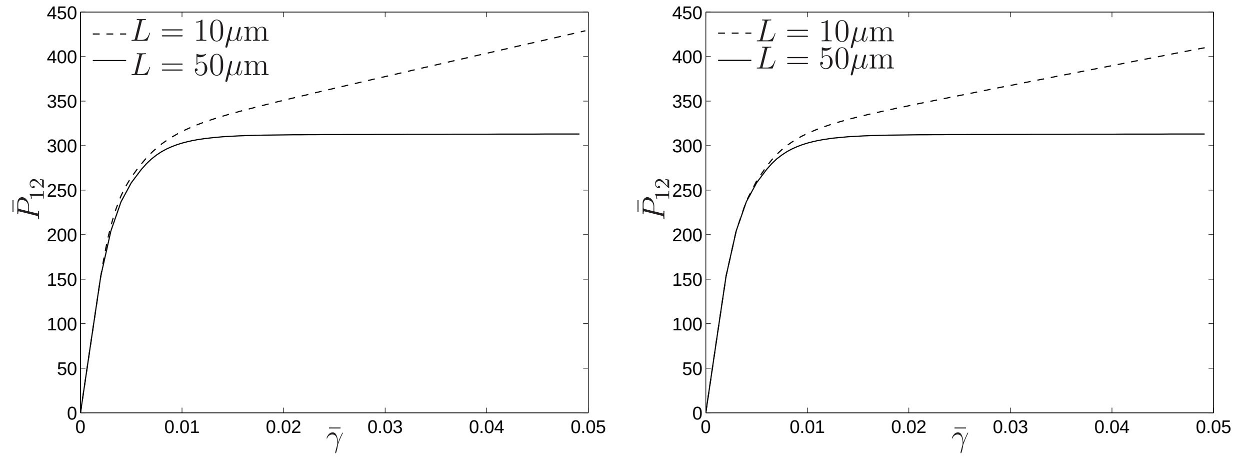

Figure 6.2.: Simple shear test; macroscopic tress-strain response ($\bar{P}_{12}$ vs. $\bar{\gamma}$) for the four-grain structure.
Left: Dissipative strengthening ($l_d = 5 \cdot 10^{-9}\,\mu$m) included.
Right: Dissipative strengthening ($l_d = 0\,\mu$m) neglected.

In addition, a computational tension test is performed with the four-grain structure. The

Parameter	Symbol	Value	
Young's modulus	E	$2 \cdot 10^5$	[MPa]
Poisson's ratio	ν	0.3	
local hardening modulus	H_α^l	200	[MPa]
gradient hardening modulus	H_α^g	$2.5 \cdot 10^3$	[MPa]
internal length scale	l_α	1	[μm]
initial yield stress	Y_α	120	[MPa]
relaxation time	t_*	10^4	[s]
drag stress	C_0	1	[MPa]
rate sensitivity parameter	m	1	

Table 6.1.: Material parameters used

stress-strain response is shown in Figure 6.3. Here, the von Mises stress $\bar{\sigma}$, defined by

$$\bar{\sigma} = \sqrt{\tfrac{3}{2}\boldsymbol{\sigma}_{\mathrm{d}} : \boldsymbol{\sigma}_{\mathrm{d}}} \qquad \text{with } \boldsymbol{\sigma}_{\mathrm{d}} = \boldsymbol{\sigma} - \tfrac{1}{3}\mathrm{tr}\boldsymbol{\sigma}\boldsymbol{I}, \tag{6.5.2}$$

is (like the Piola–Kirchhoff stress component $\bar{P}_{12}$) volume-averaged over the entire sample. Further, the effective generalized strain Γ_{eff} is illustrated in Figure 6.4.

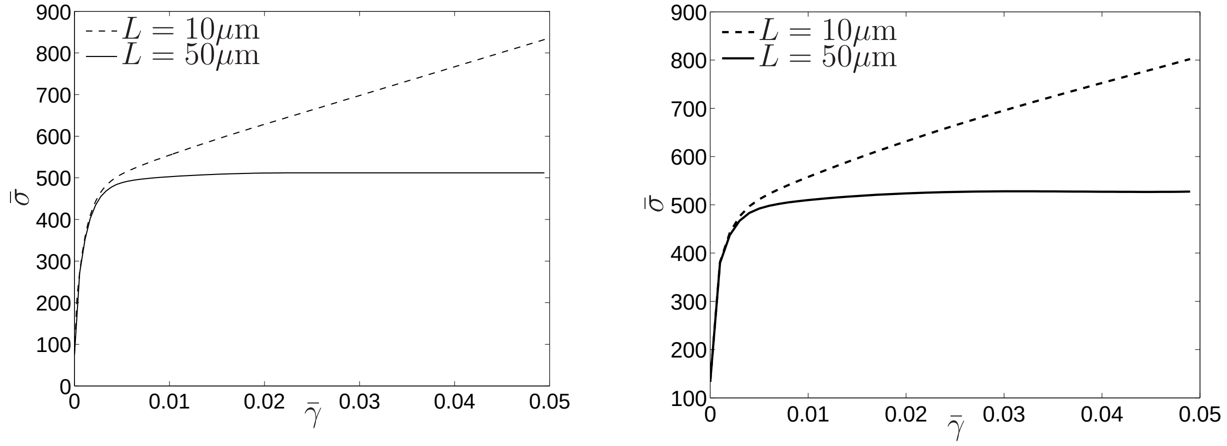

Figure 6.3.: Tension test, macroscopic tress-strain response ($\bar{\sigma}$ vs. $\bar{\gamma}$) for the four-grain structure.
Left: Dissipative strengthening ($l_d = 5 \cdot 10^{-9}\,\mu$m) included.
Right: Dissipative strengthening ($l_d = 0\,\mu$m) neglected.

The second example is that of a 25-grain structure, shown in Figure 6.5. Again, random triple slip is assumed in each grain. The macroscopic stress-strain response for simple shear test is shown in Figure while Figure 6.7 illustrates the distribution of the generalized

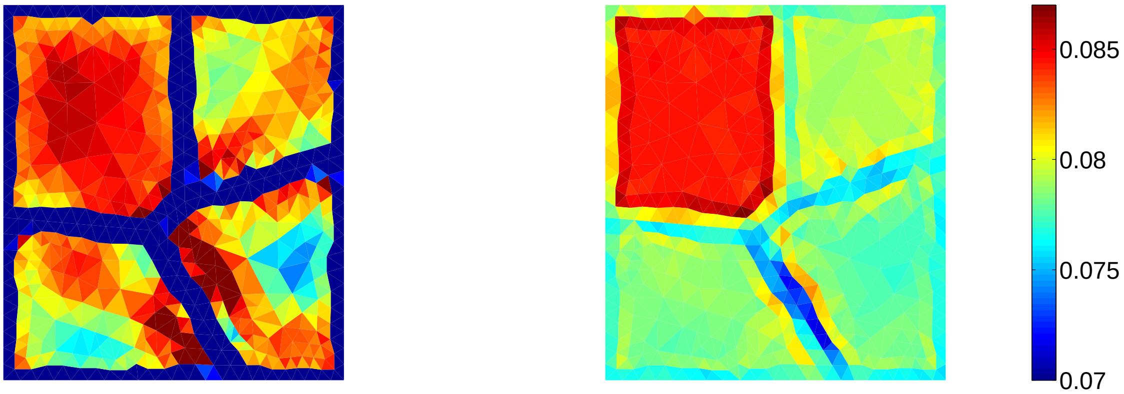

Figure 6.4.: Simple shear test; $l_d = 5 \cdot 10^{-9}$ μm. The effective generalized strain Γ_{eff} is shown for grain-structure side lengths $L = 10$ μm (left) and $L = 50$ μm (right). The difference in the distribution of the effective strain can clearly be seen.

strain inside the grain structure at $\bar{\gamma} = 0.05$ for side lengths $L = 20\mu$m and $L = 50\mu$m, and for the case of dissipative strengthening ($l_d = 10^{-8}$ μm).

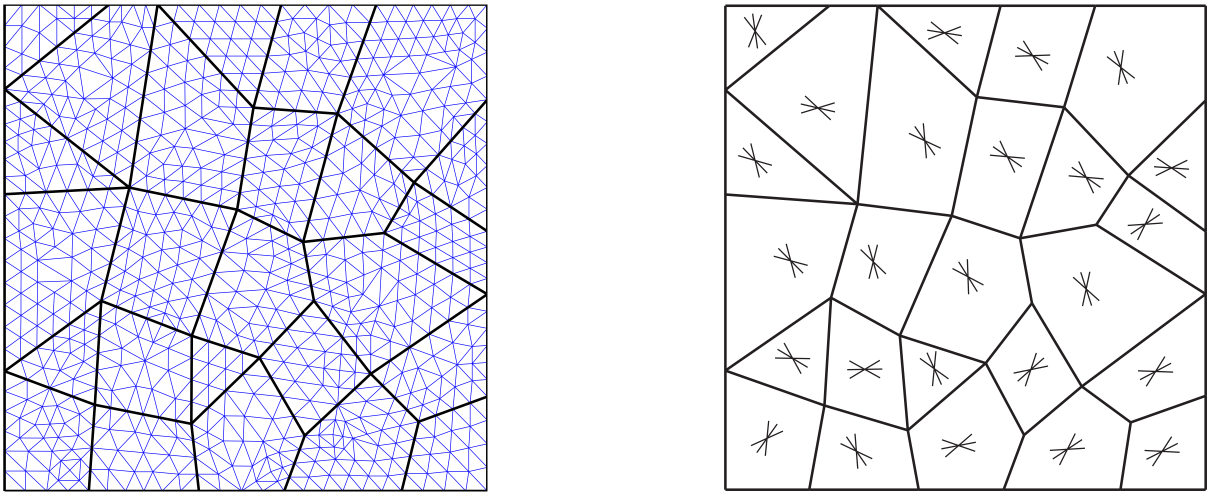

Figure 6.5.: Left: Discretization and grain geometry of the 25-grain-structure used during simulations. A simple shear test is performed.
Right: Schematic sketch of slip plane directions $\boldsymbol{s}_\alpha$. Triple slip is assumed and slip plane directions are randomly distributed.

It is assumed that the dislocation motion is blocked at the grain boundaries which is realized by assuming micro-hard boundary conditions. Thus, the plastic slip γ_α vanishes there. The non-uniformity of the plastic deformation is due to the dislocation pile-up which results from the slip being blocked at the grain boundaries. The boundary layer thickness increases, and the deformation inhomogeneity becomes more pronounced, as the length L decreases. The effective generalized strain is illustrated in Figure 6.7.

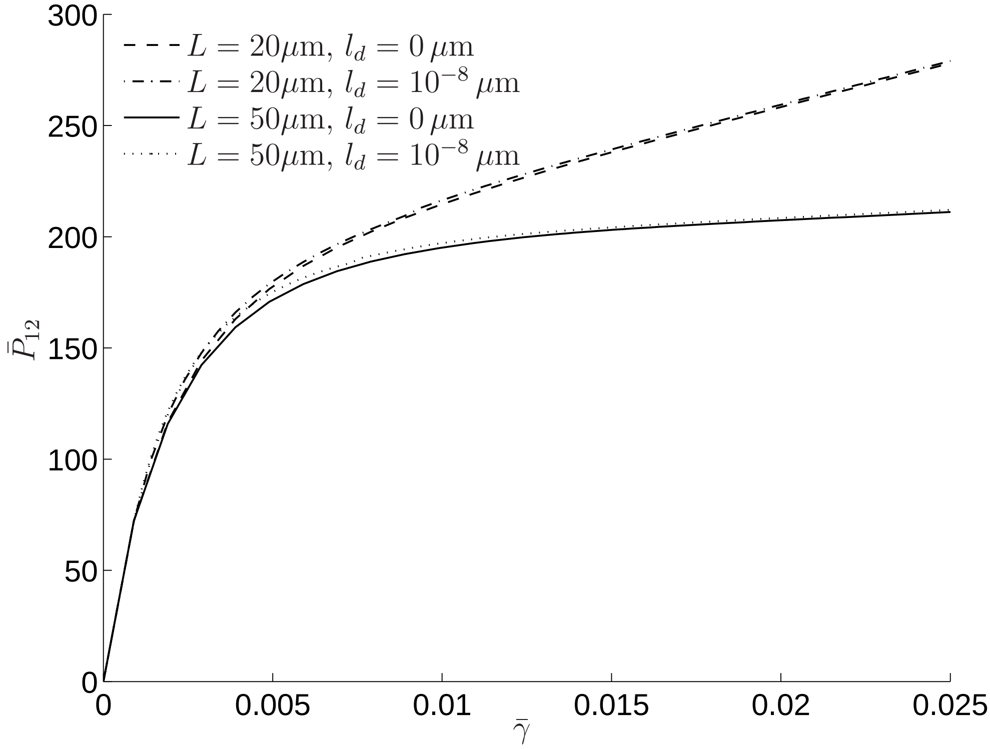

Figure 6.6.: 25 grain structure. Macroscopic stress–strain response ($\bar{P}_{12}$ vs. $\bar{\gamma}$) showing the size dependence on the amount of hardening and the effect of dissipative strengthening

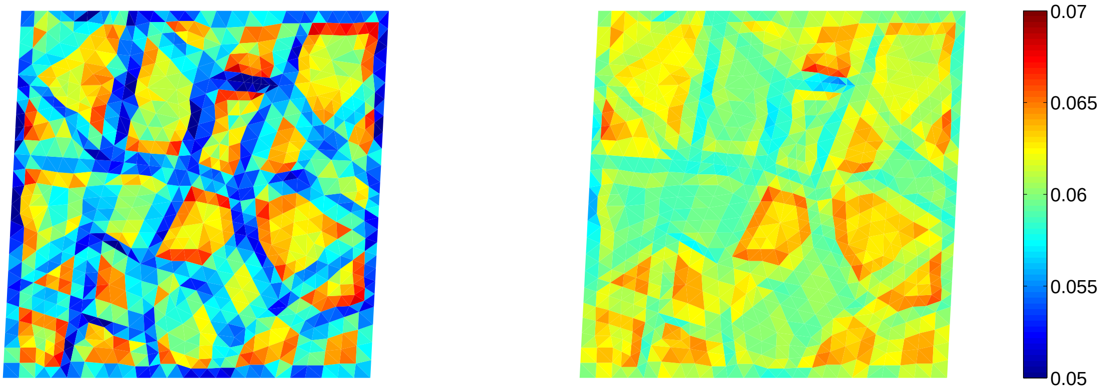

Figure 6.7.: Effective strain Γ_{eff} for $l_d = 10^{-8}$ μm. The solutions for grain-structure side lengths $L = 20$ μm (left) and $L = 50$ μm (right) are depicted for the 25-grain-polycrystal. Computations are carried out for monotonic loading with a maximum macroscopic shear deformation $\bar{\gamma}_{\max} = 0.05$.

6.6. Concluding remarks

A strain gradient theory of plasticity incorporating dissipative microstresses has been presented. The theory is viscoplastic and follows closely the model due to Gurtin and co-authors [122, 123], but differs from these and other treatments in that a viscoplastic regularization of Perzyna type is used. In particular provision is made for an elastic range followed by viscoplastic flow. The link to the approach by Ekh et al. [85] is made clear. It is noted that the energetic theory of Gurtin [123] and the theory due to Ekh et al. [85] (which is purely energetic) are equivalent. In contrast to most approaches, strain gradients enter the model via the free energy Ψ and the dissipative microforce $\boldsymbol{\xi}_\alpha^{\text{dis}}$.

The energetic theory of Ekh et al. [85] has been extended by inclusion of a vector dissipative microstress in the spirit of Lele and Anand [171]. This leads inter alia to a size-dependent yield stress. Dissipative hardening in polycrystals has hardly been studied. Others works accounting for dissipative hardening in a strain gradient theory are for example Anand et al. [13], Fredriksson and Gudmundson [101], Gurtin [123], Voyiadjis and Deliktas [270] in the context of single crystal plasticity and in Lele and Anand [171, 172] for isotropic materials. The dissipative hardening associated with the mathematical term $\text{Div}\boldsymbol{\xi}_\alpha^{\text{dis}}$ results in a size-dependent yield stress.

The algorithm presented and implemented is an extension of that due to Ekh et al. [85] in that it employs a dual-mixed approach. The algorithm used here differs in a significant respect, however, in that provision has to be made for the additional variable in the form of the dissipative microstress. Lele and Anand [171] report that their (energetic) model "possesses a mathematically attractive structure, our experience with numerical experiments which use these constitutive equations is that they are too tightly coupled". In the results presented here it is found that the energetic scheme ($l_d = 0\,\mu\text{m}$) is more robust than the dissipative one ($l_d \neq 0$). Further, it has been noted that the manner in which the local governing equation (6.4.11) is used is a delicate matter: whereas the code runs smoothly if Eq. (6.4.11) is multiplied throughout by the denominator, difficulties ensue if Eq. (6.4.11) is implemented as written.

7. Computational modeling of the flow of anisotropic polar ice at Antarctica

7.1. Introduction

About 98% of the Earth's southernmost continent Antarctica are covered by ice with an average ice thickness of 1.6 km. With this, it has about 70% of the world's fresh water and it is by far the largest single land ice body at the moment. In addition, the ice contains an abundance of historic climate information. Researchers hope to obtain full documentation of the climatic and atmospheric records archived in the Antarctic ice and to reconstruct large parts of the climate history by analyzing the ice particles. Two of the deep ice core drilling sites in Antarctica are run by the European Project for Ice Coring in Antarctica (EPICA), see Figure 7.1 (left). One of the two, the EDML deep ice core, was drilled near the Kohnen Station in Dronning Maud Land. This region has a relatively high snow accumulation rate and, therefore, provides more details on the ancient climatic history. The EDML site is 2892 m above sea level and has an average ice thickness of approximately 2782 m. Drilling started in January 2002 and was completed in the beginning of 2006, reaching a drilling depth of 2774.15 m. The diameter of the drilled ice is 10 cm. Approximately, the ice core stores information about the climatic changes during the last 150 000 years. Present-day mean annual surface temperature at EDML is -44.6° C.

Natural ice consists of hexagonal crystals. The place of a layer of hexagonal rings is called basal plane and the direction orthogonal to the basal plane is referred to as the *c*-axis. Slip along basal planes is favored over slip along other directions. In glaciology, this is often referred to as the deck of card behavior of ice because it can be compared to the deformation of a deck of cards. Deformation in direction of the basal plane is ca. 100-1000 times easier than in other directions, see Weertman [274].

The flow of thick polar ice masses is of particular interest in climate studies. Polycrystalline ice under conditions that occur in the ice sheet of Antarctica is influenced by different parameters, such as the dislocation density, the grain size or the lattice orientation. In the following, we focus on the effect of the latter, i.e. of the distribution of the lattice orientations.

The continuum-mechanical, anisotropic flow model based on an anisotropic flow enhancement factor (short: CAFFE model) has been developed in [216, 217]. The theory of mixtures with continuous diversity builds the basis for the CAFFE model and the approach belongs to the mesoscopic continuum theories. In general, mesoscopic continuum theories

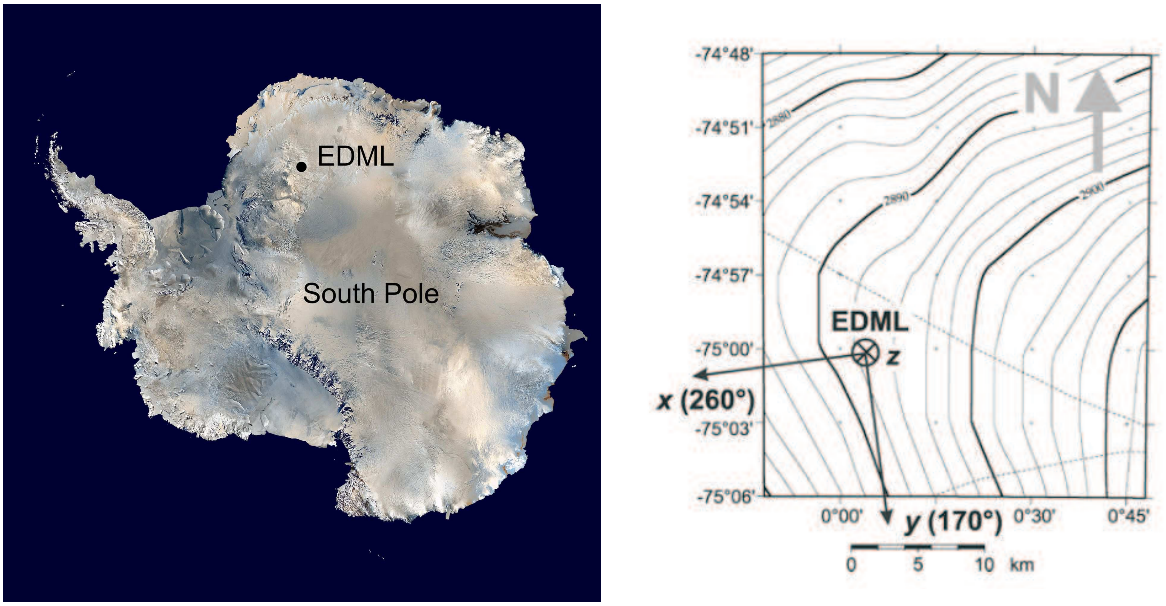

Figure 7.1.: left: Map of Antarctica. The EDML deep-drilling site is run by the European Project for Ice Coring in Antarctica (EPICA) and lies in Dronning Maud Land. In this region, the ice is ca. 2782 m thick. (picture credit: NASA Goddard Space Flight Center)
right: The local coordinate system for the EDML site is illustrated (following Seddik et al. [233]). The dashed lines indicate the ice divide as reported in Bamber and Bindschadler [21]. The x-axis points in the 260° direction, the y-axis in the 170° direction and the z-axis downwards. The underlying topographical map is taken from Wesche et al. [276].

are used to model materials whose underlying microstructure influences the macroscopic behavior with the aid of a continuum theory. In addition to the general macroscopic field quantities which depend on position and time, a mesoscopic field is introduced which depends on a mesoscopic variable. The latter is governed by a mesoscopic balance equation. Some of the macroscopic quantities are then defined in terms of the mesoscopic fields. This is a clear advantage in comparison to ordinary continuum mechanical theories as the additional information from the mesoscopic level is not lost. However, the underlying mesostructure is only modeled phenomenologically, thus, the mesoscopic equations do not govern the evolution of the crystallites. Rather, it is hidden in the theory and taken into account indirectly. Moreover, the CAFFE model has a thermodynamic setting: it is postulated in accordance to all material modeling principles, such as e.g. objectivity and determinism, and fulfills the second law of thermodynamics.

The CAFFE model has been set up for the case of large polar ice masses in which induced anisotropy occurs. The grain size (and with it the number of grains per cross section) respectively the position of the grain are not explicitly part of the the theory. Rather, the grain orientations are modeled as a continuous distribution. The anisotropy is governed by the evolution of the lattice orientations distribution of the ice crystallites. The distribution of grain orientations (fabric) is described by the orientation mass balance and influenced by four distinct recrystallization effects: local rigid body rotation (1), grain rotation (2), rotation recrystallization (3) and grain boundary migration (4). In this contribution, the terminology "recrystallization" refers to processes during which the grains change either their shape or their positions in the microstructure. The effects are explained in more detail in Section 7.2.1.

In contrast to approaches which derive the macroscopic material behavior via homogenization techniques, the CAFEE model is computationally much more efficient. Therefore, it is much more convenient to be used for long-time simulations since the numerical effort is significantly smaller.

The CAFFE model is introduced in the works of Placidi [216] and Placidi et al. [217] and parts of the theory are implemented by Seddik et al. [233, 234]. In [233, 234] numerical results are presented as well. The findings of Seddik et al. [233] prove that an anisotropic modeling approach is necessary for the ice flow of the EDML drilling site. However, only the effects of local rigid body rotation and grain rotation are taken into account. As mentioned above, the evolution of the fabric additionally depends on the important effects of grain boundary migration (also referred to as migration recrystallization) and rotation recrystallization (polygonization). Whereas rotation recrystallization is a diffusive process and can, therefore, be described by a diffusive flux term, grain boundary migration is modeled by a production term.

This contribution is structured as follows: First, the basic ideas of the CAFFE model introduced in Section 7.2. The orientation mass density ρ^*, its distribution function f^* and the orientation mass balance, which governs its evolution, are stated. Furthermore, quantities such as the orientation transition rate $\boldsymbol{u}^*$, the orientation production rate Γ^* and the orientation flux $\boldsymbol{q}^*$ are defined and characterized, for example. Subsequently, an anisotropic generalization of Glen's flow law is discussed in Section 7.2.2. The extension is necessary due to the ice anisotropy in the depth and it is realized via a scalar enhancement factor. This is followed by the description of the set-up of the numerical model (Section 7.3) and its discretization (Section 7.4). The approximation is done with a finite volume approach. Finally, the numerical simulation results are illustrated in Section 7.5.

7.2. Continuum mechancial model

In this section, the mesoscopic continuum mechanical model is described, largely following Placidi et al. [217]. As mentioned above, thick polar ice masses behave anisotropic, see e.g. Azuma and Higashi [20] and Gow and Williamson [108]. In order to take the ice's internal structure into account, a mesoscopic field quantity is introduced. Here, the mesoscopic field is the orientation mass density ρ^*. Like the ordinary macroscopic field quantities it depends on the position $\boldsymbol{x}$ and time $\boldsymbol{t}$. Moreover, an additional dependence on a so called mesoscopic variable, the orientation $\boldsymbol{n}$ of the grain, is assumed. The orientation $\boldsymbol{n}$ is the normal unit vector parallel to the crystal c-axis in the unit sphere S^2. Thus, each point of the S^2 represents one particular orientation $\boldsymbol{n}$, or in other words: the orientations belong

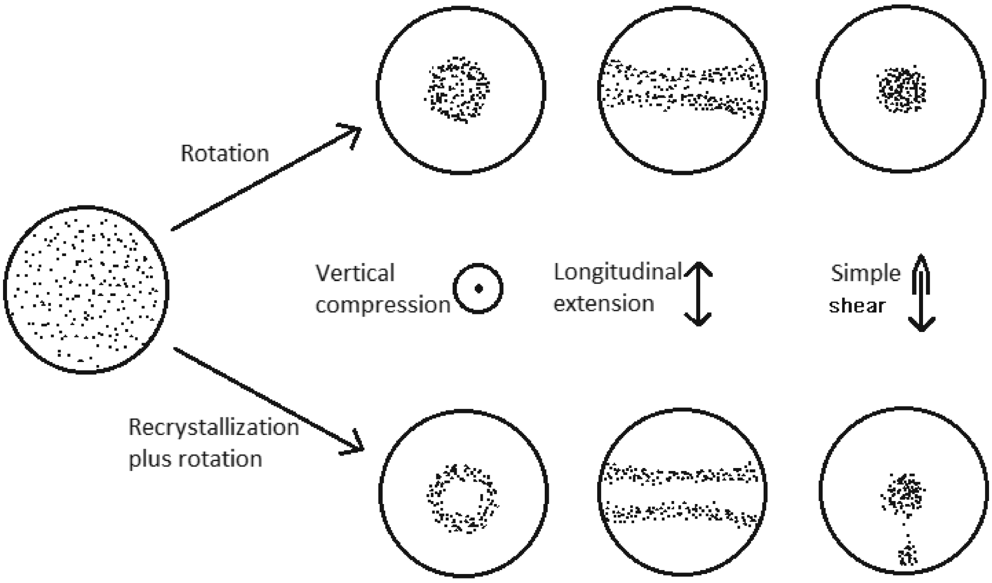

Figure 7.2.: The ice texture's development strongly depends on the stress state. The schematic evolution of the fabric's crystallographic axis is shown. On the top, the response in case of a pure mechanical process is depicted. On the bottom, recrystallization processes are active in addition to the mechanical one. Initially, a random (isotropic) *c*-axis distribution is assumed. Longitudinal extension leads to the formation of a girdle, whereas simple shear results in a single maximum. See also Alley [12].

to a continuous space. In the following, all quantities referring to the mesoscopic level and, therefore, having an orientational dependence are marked with "*".

7.2.1. Orientation mass density ρ^*

One characteristic of a mesoscopic field quantity is that a so-called distribution function can be defined. The distribution function is a statistical measurement of the quantity. The orientation mass density $\rho^*(\boldsymbol{x}, t, \boldsymbol{n})$ is defined as mass per volume and orientation. When integrated over all orientations, it yields the macroscopic mass density $\rho(\boldsymbol{x}, t)$:

$$\int_{S^2} \rho^*(\boldsymbol{x}, t, \boldsymbol{n}) \; \mathrm{d}^2 n = \rho(\boldsymbol{x}, t). \tag{7.2.1}$$

Consequently, $\rho^*(\boldsymbol{x}, t, \boldsymbol{n}) \; \mathrm{d}^2 n$ represents the mass fraction of crystallites with orientations $\boldsymbol{n}$ within the solid angle increment $\mathrm{d}^2 n$. Thus, its orientation distribution function f^*

can be defined as

$$f^*(\boldsymbol{x}, t, \boldsymbol{n}) = \frac{\rho^*(\boldsymbol{x}, t, \boldsymbol{n})}{\rho(\boldsymbol{x}, t)}, \tag{7.2.2}$$

and it describes the relative number of grains with a certain orientation $\boldsymbol{n}$. Since in each case there exist two intersection points opposite to each other in S^2, f^* is symmetric with respect to the orientation: $f^*(\boldsymbol{x}, t, \boldsymbol{n}) = f^*(\boldsymbol{x}, t, -\boldsymbol{n})$. In other words, the orientation distribution function is normalized, i.e.

$$\int_{S^2} f^* \, \mathrm{d}^2 n = 1. \tag{7.2.3}$$

An isotropic fabric is characterized by $\rho^* = \rho/[4\pi]$, with 4π being the surface area of a unit sphere.

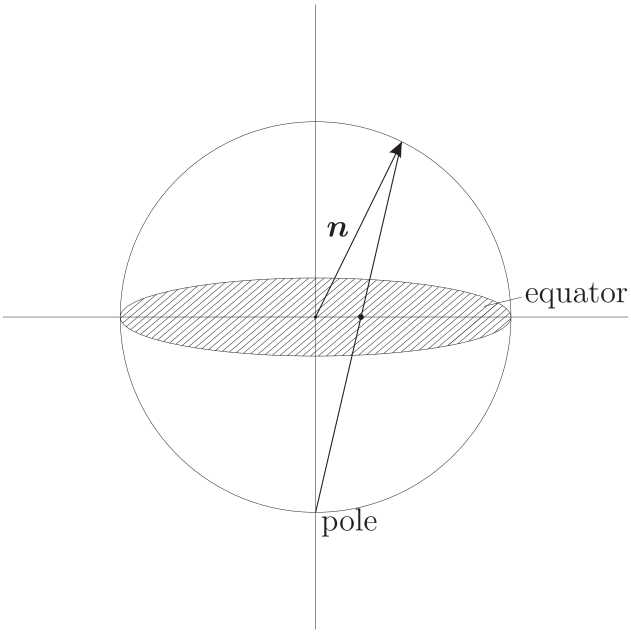

Figure 7.3.: A Schmidt diagram is a two-dimensional representation of the orientations. The intersection of an orientation $\boldsymbol{n}$ with its unit sphere S^2 is projected onto the centered circular cross section. Consequently, a vertical orientation is plotted in the center and an orientation lying flat is plotted on the edge.

The orientation mass density ρ^* is governed by a mesoscopic balance equation (the orientation mass balance[1]) which is defined on the mesoscopic space $\mathbb{R}^3 \times \mathbb{R}_{\geq 0} \times S^2$

$$\frac{\partial \rho^*}{\partial t} + \mathrm{div}(\rho^* \boldsymbol{v}) + \mathrm{div}_{S^2}(\rho^* \boldsymbol{u}^*) = \rho^* \Gamma^*. \tag{7.2.4}$$

---

[1] The macroscopic mass balance $\partial\rho/\partial t + \mathrm{div}(\rho \boldsymbol{v}) = 0$ follows from Eq. (7.2.4) by integrating over the unit sphere S^2.

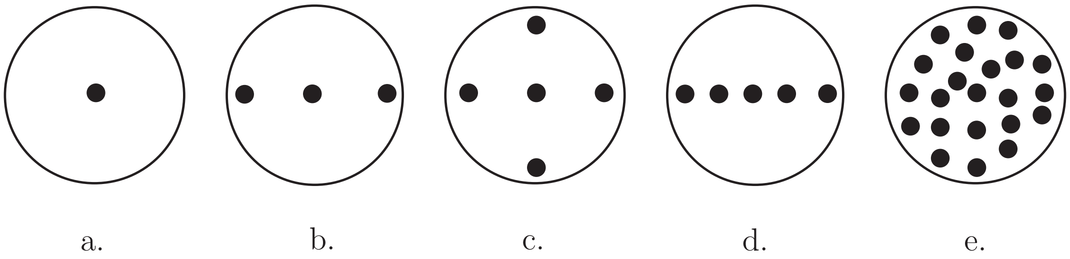

Figure 7.4.: Schmidt diagrams for typical fabrics which can be observed are illustrated: a. vertical single maximum. b. two maxima. c. three maxima. d. girdle. e. isotropic fabric. A Schmidt diagram is a two-dimensional representation of the orientations, see Figure 7.3.

The classical velocity is denoted by $\boldsymbol{v}(\boldsymbol{x},t)$. Its gradient is given by

$$\begin{aligned}\boldsymbol{L} &= \nabla \boldsymbol{v} = \boldsymbol{D} + \boldsymbol{W} \\ &= \mathrm{sym}\boldsymbol{L} + \mathrm{skw}\boldsymbol{L},\end{aligned} \tag{7.2.5}$$

where $\boldsymbol{D}$ and $\boldsymbol{W}$ are the strain rate and the spin tensor, respectively. The orientation change velocity rate $\boldsymbol{u}^*(\boldsymbol{x},t,\boldsymbol{n}) = \dot{\boldsymbol{n}}$ describes the transition of mass with one orientation to another (neighboring) orientation on the unit sphere S^2. Furthermore, $\boldsymbol{u}^*$ is orthogonal to $\boldsymbol{n}$. The orientation production rate $\Gamma^*(\boldsymbol{x},t,\boldsymbol{n})$ corresponds to the physical phenomenon of grain boundary migration (migration recrystallization), see Figures 7.7 and 7.8 for further explanations.

The non-standard divergence operator div_{S^2} is defined as

$$\mathrm{div}_{S^2}(\bullet^*) = \mathrm{tr}\left(\frac{\partial(\bullet^*)}{\partial \boldsymbol{n}} - \left[\frac{\partial(\bullet^*)}{\partial \boldsymbol{n}} \cdot \boldsymbol{n}\right]\boldsymbol{n}\right) \tag{7.2.6}$$

The orientation transition rate $\boldsymbol{u}^*$ can be decomposed additively into (see Placidi and Hutter [218])

$$\begin{aligned}\boldsymbol{u}^* &= \boldsymbol{u}^*_{\mathrm{rbr}} + \boldsymbol{u}^*_{\mathrm{gr}} + \boldsymbol{u}^*_{\mathrm{rc}} \\ &= \boldsymbol{W}\cdot\boldsymbol{n} + \iota\left[\left[\boldsymbol{n}\cdot\boldsymbol{D}\cdot\boldsymbol{n}\right]\boldsymbol{n} - \boldsymbol{D}\cdot\boldsymbol{n}\right] + \frac{\boldsymbol{q}^*}{\rho^*}.\end{aligned} \tag{7.2.7}$$

The first term describes the contribution of the polycrystal's local rigid body rotation to the orientation transition rate. The second term $\boldsymbol{u}^*_{\mathrm{gr}}$ maps the physical effect of grain rotation. For example, in the special cases of pure shear and uniaxial compression, if $\iota > 0$, it implies that the crystallite's c-axis always rotates towards the compression axes and away from the extension axes. Moreover, in case of simple shear, for shape factor $\iota = 1$ and the geometry depicted in Figure 7.5, the fabric evolves into a vertical single maximum. If this steady state has been reached, equalizing contributions from the local rigid body rotation (rbr) and the grain rotation (gr) exist. The local rigid body rotation will then try to rotate the fabric away from the vertical, but grain rotation exactly compensates it. Thus, there are no further changes[2]. This case leads to an affine rotation and the orientation $\boldsymbol{n}$ remains orthogonal to the associated material area element, see Dafalias [69] for further information.

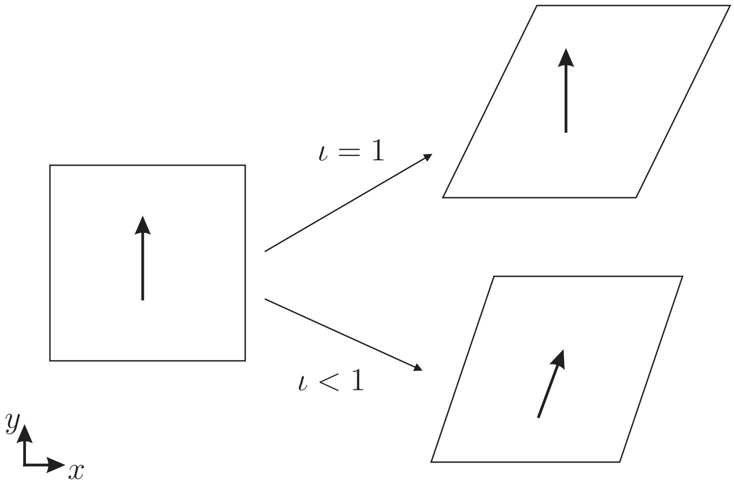

Figure 7.5.: Geographic interpretation of the shape factor ι. Simple shear deformation in a single crystal with an orientation parallel to the y-axis is depicted. On the left, a vertical single maximum is depicted. For $\iota = 1$ the orientation local rigid body rotation wants to turn the arrow to the right (following the crystal's deformation), but grain rotation turns the arrow back to the left by the same amount. Consequently, the crystal's orientation does not change. For $\iota < 1$ the transition of the orientation is slowed down, but it follows the direction of the deformation because the local rigid body contribution is larger than the grain rotation contribution.

The effect of rotation recrystallization (polygonization) is mapped by the third term in Eq. (7.2.7) in terms of the orientation flux $\boldsymbol{q}^*$ and is described by Fick's law [94] of diffusion. Polygonization refers to the process that subgrain boundaries develop due to formations of dislocations in heterogeneous loading cases, see e.g. Humphreys and Hatherly [141], Poirier [219] or Weertman and Weertman [273]. Some grains are better orientated for dislocation slip than others. During the deformation process grains can break apart (they polygonize) at these subgrain boundaries and the emerging new grains will have slightly different orientations. Usually, this part of the process is referred to as rotation recrystallization. It is modeled as a non-orientation-dependent diffusive process on the unit sphere

$$\boldsymbol{q}^* = -\lambda \nabla^* \rho^*, \tag{7.2.8}$$

with λ being the diffusivity. Mathematically speaking, orientations move from harder to softer configurations - soft referring to the property that those grains are well orientated

---

[2] In our example, the value $\iota = 0.9$ (see Section 7.3), thus the local rigid body rotation contribution slightly predominates.

for dislocation glide. Here, ∇^* denotes the the non-standard gradient operator which is applied to the orientational variable $\boldsymbol{n}$ in the following way

$$\nabla^*(\bullet^*) = \frac{\partial(\bullet^*)}{\partial \boldsymbol{n}} - \left[\frac{\partial(\bullet^*)}{\partial \boldsymbol{n}} \cdot \boldsymbol{n}\right] \boldsymbol{n}. \tag{7.2.9}$$

Montagnat and Duval [189] state that grain boundary migration and rotation recrystallization are concurrent processes. Grain boundary migration refers to the growth of grains (at the expense of neighboring grains) which are better oriented for the ongoing deformation process than others. Thus, subgrains which developed due to rotation recrystallization are supposed to merge again to some extent during grain boundary migration processes. Inspired by the suggestion of [216, 217], we postulate a temperature-dependent orientation production rate Γ^*

$$\Gamma^* = \Gamma_c \frac{A(T')}{A(-10°C)} \left[\mathcal{A}^* - \mathcal{A}\right], \tag{7.2.10}$$

see also Figure 7.7 (left). $\Gamma_c > 0$ is a constant material parameter with unit $[\mathrm{s}^{-1}]$. The rate factor $A(T')$ is the one of the flow law for ice (see Section 7.2.2) given by the Arrhenius law

$$A(T') = A_0 \exp\left(-\frac{Q}{RT'}\right). \tag{7.2.11}$$

Here, A_0 is the pre-exponential constant, Q denotes the activation energy and R is the universal gas constant, see Figure 7.6 for the explicit function used in this contribution. It depends on the temperature relative to pressure melting $T' = T - T_m + T_0$, where T is the absolute temperature. The melting temperature of ice T_m is pressure-dependent. In thick polar ice masses, the pressure-melting point is given by the linear relation $T_m = T_0 - \beta p$, where $T_0 = 273.16$ K is the melting point at zero pressure and $\beta = 9.8 \cdot 10^{-2}$ K/MPa denotes the Clausius–Clapeyron constant for ice. In general, the melting point of ice is lowered by approximately 1 K per kilometer of ice thickness.

The deformability $\mathcal{A}$ of polycrystalline is given by weighting the deformability $\mathcal{A}^*$ of a single crystal with the orientation distribution function f^*

$$\begin{aligned} \mathcal{A} &= \int_{S^2} \mathcal{A}^*(\boldsymbol{n})\, f^*(\boldsymbol{n})\ \mathrm{d}^2 n \\ &= 5 \int_{S^2} \frac{[\boldsymbol{S} \cdot \boldsymbol{n}]^2 - [\boldsymbol{n} \cdot \boldsymbol{S} \cdot \boldsymbol{n}]^2}{\mathrm{tr}\left(\boldsymbol{S}^2\right)} f^*(\boldsymbol{n})\ \mathrm{d}^2 n. \end{aligned} \tag{7.2.12}$$

The reader is referred to Seddik et al. [233] for a detailed justification of this definition. Physically, $[\boldsymbol{S} \cdot \boldsymbol{n}]^2 - [\boldsymbol{n} \cdot \boldsymbol{S} \cdot \boldsymbol{n}]^2$ corresponds to the square of the resolved stress on the basal plane. Both quantities are dimensionless. The factor 5 is a convention and one can show that both deformabilities $\mathcal{A}$ and $\mathcal{A}^*$ only take values between 0 and 2.5. The deviatoric part of the Cauchy stress $\boldsymbol{\sigma}$ is denoted by $\boldsymbol{S}$

$$\boldsymbol{S} = \boldsymbol{\sigma} - \frac{\mathrm{tr}\boldsymbol{\sigma}}{3}\boldsymbol{I}. \tag{7.2.13}$$

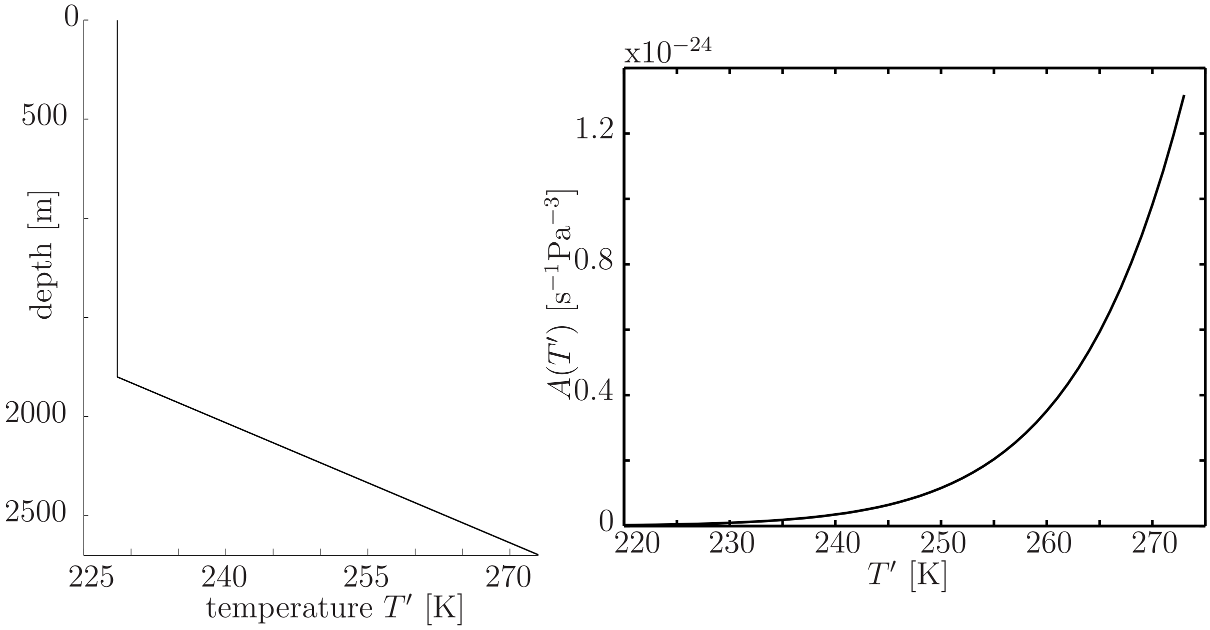

Figure 7.6.: left: The temperature relative to pressure melting T' is assumed to follow a Dansgaard–Johnsen distribution [272]: Up to two thirds of the ice thickness the temperature is constant and below this point the dependence in linear. The surface and basal temperatures match the measured ice-core data of the EDML drilling.
right: Arrhenius law as stated in Eq. (7.2.11) for a temperature range of 220 K to 273 K . Suitable values for the pre-exponential constant A_0 are $A_0 = 3.985 \cdot 10^{-13}$ s^{-1}Pa^{-3} for $T' \leq 263.15$ K and $A_0 = 1.916 \cdot 10^{3}$ s^{-1}Pa^{-3} for $T' \geq 263.15$ K. Moreover, $Q = 60$ kJ mol^{-1} for $T' \leq 263.15$ K and $Q = 139$ kJ mol^{-1} for $T' \geq 263.15$ K, cf. Greve and Blatter [110]. Note that the rate factor $A(T')$ is continuous despite its piecewise definition.

Physically, Eq. (7.2.10) means that the orientation production rate Γ^* is positive when the deformability is high. Thus, crystallites which are well-oriented for deformation will grow in agreement with the experimental findings of Kamb [156] and this results in an anisotropic fabric.

Remark: An experimental determination of the diffusivity λ and the material parameter Γ_c is rather difficult. The relevant time scales are too large and the strain rates are too low in order to be easily reproduced in the laboratory. However, it is known that at the EDML site the vertical strain rate D_{zz} is of magnitude order 10^{-5} [a^{-1}] (see e.g. Wesche et al. [276]). If rotation recrystallization and grain boundary migration act on the same time scale, thus contributing to (but not dominating) fabric evolution, the parameters λ and Γ_{c} should be of similar orders of magnitude ($\sim 10^{-13}\,\mathrm{s}^{-1}$).

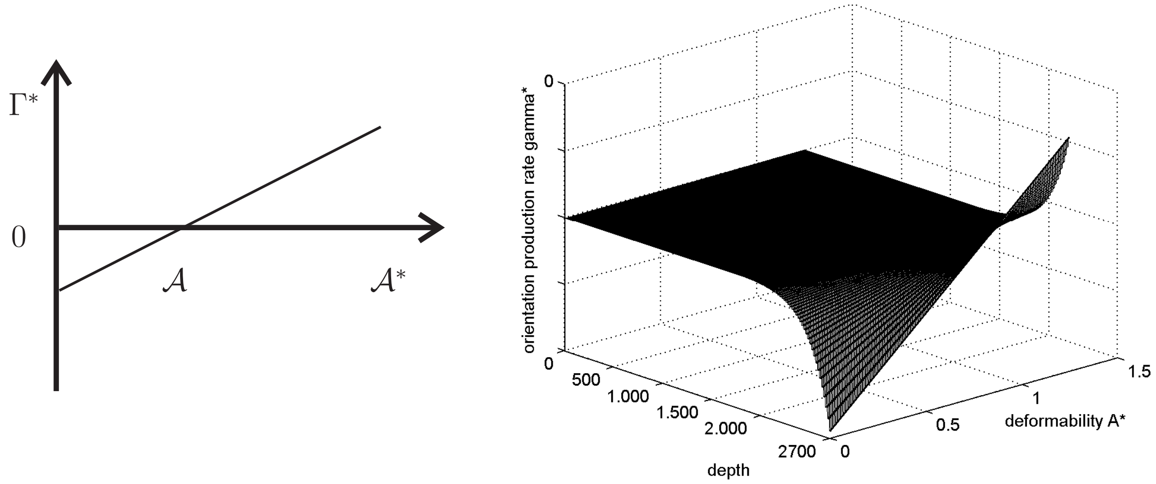

Figure 7.7.: left: The orientation production rate Γ^*, defined in Eq. (7.2.10) in dependence on the deformability $\mathcal{A}^*$ of a single crystal. $\mathcal{A}$ denotes the deformability of the entire crystal.
right: The orientation production rate Γ^* in dependence on the deformability $\mathcal{A}^*$ of a single crystal and the depth z. It can clearly be seen that the influence of the orientation production rate is strongest in the deep regions of the ice mass.

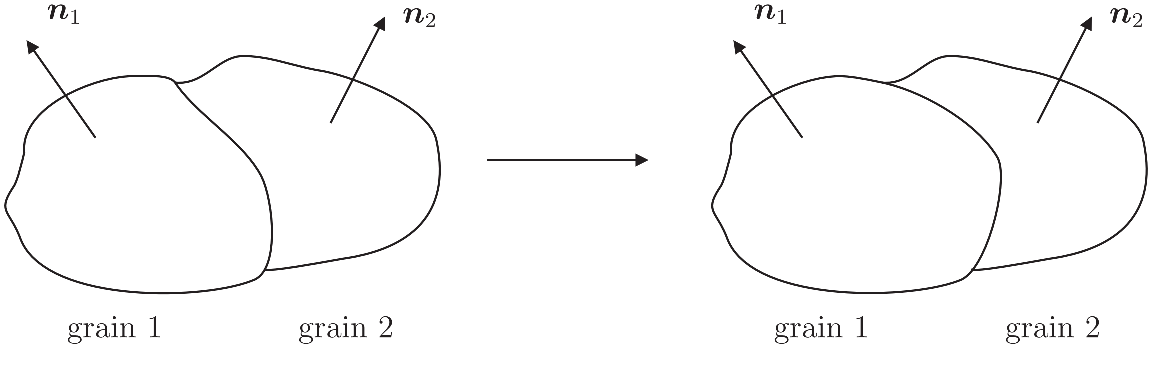

Figure 7.8.: Grain boundary migration expresses that the fraction of grains with a certain orientation $\boldsymbol{n}_1$ changes due to the fact that the boundary between grain 1, which is well-orientated for the deformation process, and grain 2 (with an unfavorable orientation $\boldsymbol{n}_2$) moves (migrates) in favor of grain 1. Grain boundary migration belongs to the recrystallization processes. It is temperature-dependent and exists only for “warm” temperatures, i.e. approximately above $-10°C$. Consequently, it only plays a role in the deeper regions of the ice core.

7.2.2. Non-classical, anisotropic Glen's flow law

In continuum mechanics, ice is treated as an incompressible and extremely viscous non-Newtonian fluid. Since natural ice is composed of a large number of individual crystals with randomly distributed orientations, its macroscopic mechanical behavior of the ice is generally regarded as isotropic. However, this assumption does not hold for thick polar ice masses whose behavior is anisotropic. Thus, Glen's flow law (which has been formulated for the isotropic case by Glen [106], see also Greve and Blatter [110] or Hooke [136]) has to be enhanced. Following Placidi et al. [217] and Seddik et al. [233] the anisotropic generalization of Glen's flow law reads

$$\boldsymbol{D} = A(T')\hat{E}(\mathcal{A})\sigma^{n-1}\boldsymbol{S}. \tag{7.2.14}$$

Here, n is the same stress exponent as in the case of the classical flow law by Glen and $\sigma = \sqrt{\left[\mathrm{tr}(\boldsymbol{S}^2)\right]/2}$ denotes the effective stress. The experiments of Azuma [19] and Miyamoto [188] show that the scalar anisotropic enhancement factor $\hat{E}(\mathcal{A})$ depends on the shear stress in the basal plane (i.e. the Schmid factor) to the fourth power in the interval $[1, 2.5]$. Consequently, it has to depend on the square of the deformability $\mathcal{A}$. Furthermore, we require that the enhancement factor $\hat{E}$ is a strictly monotonically increasing function of the deformability $\mathcal{A}$ and continuously differentiable, see Figure 7.9:

$$\hat{E}\left(\mathcal{A}\right) = \begin{cases} E_{\mathrm{min}} + \left[1 - E_{\mathrm{min}}\right]\mathcal{A}^{\frac{8}{21}\frac{E_{\mathrm{max}}-1}{1-E_{\mathrm{min}}}}, & \text{if } 0 \leq \mathcal{A} \leq 1, \\ \\ \frac{4\mathcal{A}^2[E_{\mathrm{max}}-1]+25-4E_{\mathrm{max}}}{21}, & \text{if } 1 \leq \mathcal{A} \leq 2.5 \end{cases} \tag{7.2.15}$$

Thus, the material behavior for a polycrystal with an anisotropic orientation distribution function f^* (Eq. (7.2.2)) changes under axis rotation and, therefore, the material behavior is anisotropic (cf. Placidi et al. [217]). Note that in the anisotropic formulation of Glen's law as done in Eq. (7.2.14), the anisotropic scalar enhancement factor $\hat{E}$ is nicely separated from the mechanical nonlinearity. This is in contrast to many other theories, such as e.g. Svendsen and Hutter [250], which relate the strain rate tensor $\boldsymbol{D}$ and the deviatoric stress tensor $\boldsymbol{S}$ by tensor quantities. Although the collinear anisotropic flow law Eq. (7.2.14) implies that a single viscosity of the polycrystal is the same for all stress deviator components for a given fabric and a given state of deformation, it has the clear advantage that the enhancement is only based on the two parameters E_{min} and E_{max} which are known from experiments.

7.3. Model set up for EDML deep-drilling site

7.3.1. Flow regime

Following Seddik et al. [233], the Cartesian coordinate system is defined in such a way that the EDML drilling site is located at the origin and the x-axis is approximately aligned

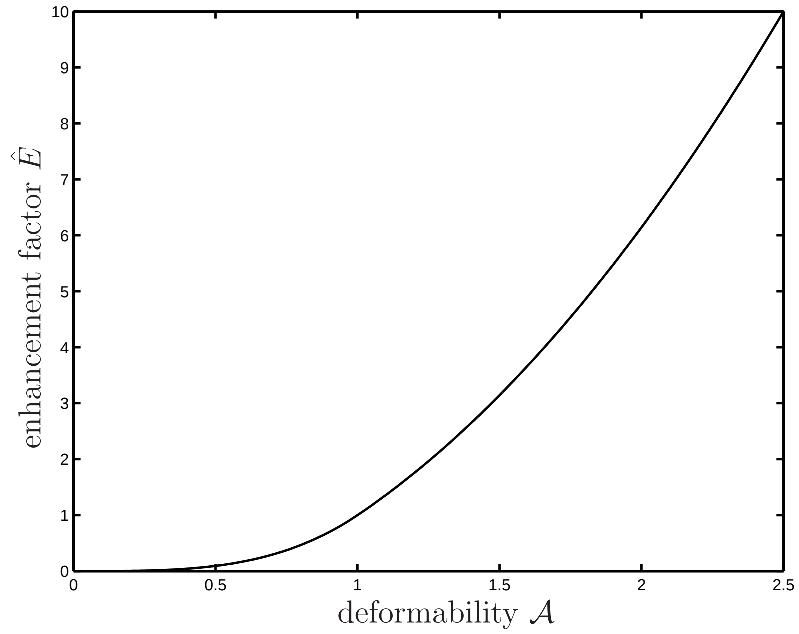

Figure 7.9.: The scalar anisotropic enhancement factor $\hat{E}(\mathcal{A})$ is a strictly monotonically increasing function of the deformability $\mathcal{A}$. Its minimum $\hat{E}(0) = E_{\min}$ represents uniaxial compression on a single maximum whereas its maximum $\hat{E}(2.5) = E_{\max}$ corresponds to simple shear on a single maximum. Arbitrary stress on an isotropic fabric which has a deformability of $\mathcal{A} = 1$ is expressed by $\hat{E}(1) = 1$.

with the downhill direction, see Figure 7.1 (right) and cf. Wesche et al. [276]. Thus, the gradient of the free surface elevation, h, is

$$\frac{\partial h}{\partial x} = -9 \cdot 10^{-4} \pm 10\%, \qquad \frac{\partial h}{\partial y} = 0, \tag{7.3.1}$$

cf. [276]. Consequently, the only non-vanishing shear-stress component is S_{xz}, given by

$$S_{xz} = \rho g z \frac{\partial h}{\partial x}, \tag{7.3.2}$$

where g is the acceleration due to gravity. Combination with the x-z-component of the anisotropic Glen's flow law (7.2.14) and subsequent integration over the z-component yields the anisotropic horizontal velocity[3],

$$v_x = -2\rho g \frac{\partial h}{\partial x} \int_z^H \hat{E}(\mathcal{A}) A(T')\, \sigma^{n-1}\, \bar{z}\ \mathrm{d}\bar{z}, \tag{7.3.3}$$

where H is the ice thickness. No-slip conditions have been assumed at the ice base, that is, $v_x(H) = 0$. Per definition of the coordinate system v_y vanishes. The vertical

---

[3] The horizontal velocity at EDML drilling site is rather low: $|v_x| = 0.7\ \mathrm{m\,a^{-1}}$ [276]. In general, drilling sites are built in regions with small shear strains because the primary goal of the drilling is to gain climatic data and the smaller the shear strain the older the deep ice.

velocity v_z results from integrating the prescribed vertical strain rate D_{zz}. The latter is prescribed and set to follow a Dansgaard–Johnsen type distribution [272] which assumes that the vertical strain rate D_{zz} is constant from the free surface down to two thirds of the ice thickness. Below, D_{zz} is linearly decreasing, see Figure 7.10 for illustration. The strain rate at the surface is chosen such that the downward vertical velocity v_z equals the accumulation rate. A similar distribution is employed for the temperature T', see Figure 7.6 (left).

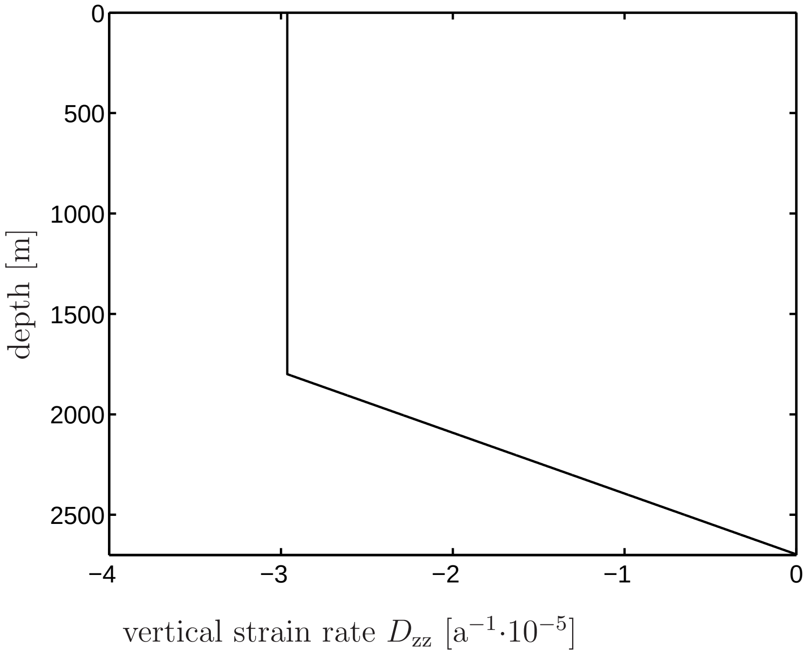

Figure 7.10.: The vertical strain rate D_{zz} is assumed to follow a Dansgaard–Johnsen distribution [272], in analogy to the temperature T': Up to two thirds of the ice thickness the values are constant and below this point the dependence in linear. The strain rate at the surface $D_{\mathrm{zz}}(O)$ is chosen such that the downward vertical velocity v_z equals the accumulation rate.

Moreover, we introduce the vertical compression rate $\varepsilon = -D_{zz} = -\partial v_z/\partial z$. Horizontal extension is parameterized by

$$D_{xx} = \frac{\partial v_x}{\partial x} = a\varepsilon, \quad D_{yy} = \frac{\partial v_y}{\partial y} = [1-a]\varepsilon. \tag{7.3.4}$$

In case of isotropic horizontal extension, the parameter $a \in [-1, 1]$ is equal to 1/2 and equal to unity for extension in the x-direction only (pure shear). The horizontal shear rate $\gamma := \partial v_x/\partial z$ results from Equation (7.3.3) and depends on the deformability $\mathcal{A}$,

$$\gamma = 2\rho g \frac{\partial h}{\partial x}\, \hat{E}(\mathcal{A})\, A(T')\, \sigma^{n-1}\, z. \tag{7.3.5}$$

The velocity gradient $\boldsymbol{L} = \nabla \boldsymbol{v}$ then renders

$$\boldsymbol{L} = \begin{pmatrix} a\varepsilon & 0 & \gamma \\ 0 & [1-a]\varepsilon & 0 \\ 0 & 0 & -\varepsilon \end{pmatrix}. \tag{7.3.6}$$

Consequently, we obtain for the strain-rate tensor $\boldsymbol{D}$ and the spin tensor $\boldsymbol{W}$

$$\boldsymbol{D} = \begin{pmatrix} a\varepsilon & 0 & \frac{1}{2}\gamma \\ 0 & [1-a]\varepsilon & 0 \\ \frac{1}{2}\gamma & 0 & -\varepsilon \end{pmatrix}, \qquad \boldsymbol{W} = \begin{pmatrix} 0 & 0 & \frac{1}{2}\gamma \\ 0 & 0 & 0 \\ -\frac{1}{2}\gamma & 0 & 0 \end{pmatrix}. \tag{7.3.7}$$

7.3.2. Governing equation

In Antarctica the thick polar ice masses have developed over many years in a very slow progress. Consequently, the effect of time on the orientation mass density is negligible and $\partial\rho^*/\partial t = 0$. Moreover, the width of the ice core is very small compared to its length, since the main interest is directed to the change of the orientation mass density ρ^* with respect to depth. Therefore, we only allow a dependence of ρ^* on the z-coordinate and on the orientation $\boldsymbol{n}$. The data gained in the EDML drilling site shows that the formation of subgrain boundaries and, thus, polygonization indeed play an important role in ice-sheet deformation and may not be neglected. Consequently, Eq. (7.2.4) yields

$$\frac{\partial\rho^*}{\partial z} v_z + \mathrm{div}_{S^2}(\rho^* \boldsymbol{u}^*) = \rho^* \Gamma^*. \tag{7.3.8}$$

Application of the divergence theorem and the definition of the non-standard divergence (Eq. (7.2.6)) leads to

$$\frac{\partial\rho^*}{\partial z} v_z + u_i^* \partial_i + \rho^* \partial_i u_i^* = \rho^* \Gamma^* \tag{7.3.9}$$

where we switched to index notation for clarity and $\partial_i = \partial/\partial n_i - n_i n_j \partial/\partial n_j$. Einstein's summation convention holds, thus it is summed over repeated indices. By inserting Eq. (7.2.7), Eq. (7.2.8) and Eq. (7.2.10) and after some rearrangements we obtain

$$\frac{\partial\rho^*}{\partial z} v_z + [W_{ij} - \iota D_{ij}] n_j \partial_i + \rho^* [3\iota D_{kl} n_k n_l] - \lambda \partial_i \rho^*_{,i} = \rho^* \Gamma^* \tag{7.3.10}$$

Finally, we rewrite Eq. (7.3.10) in spherical coordinates and subsequently insert Eq. (7.3.7) for the strain rate tensor $\boldsymbol{D}$ and the spin tensor $\boldsymbol{W}$

$$\begin{aligned} &\frac{\partial\rho^*}{\partial z} v_z + \frac{3}{4}\iota\rho^* \left\{\varepsilon[2[2a-1]\sin^2\theta\cos(2\varphi) - 1 - 3\cos(2\theta)] + 2\gamma\sin(2\theta)\cos\varphi\right\} \\ &+ \frac{1}{2}\frac{\partial\rho^*}{\partial\varphi}\left\{\varepsilon\iota[2a-1]\sin(2\varphi) + \gamma[\iota-1]\frac{\sin(\varphi)}{\tan(\theta)}\right\} \\ &+ \frac{1}{2}\frac{\partial\rho^*}{\partial\theta}\left\{-\frac{1}{2}\iota\varepsilon\sin(2\theta)[[2a-1]\cos(2\varphi)+3] + \gamma[1-\iota\cos(2\theta)]\cos\varphi - \lambda\frac{1}{\tan\theta}\right\} \\ &- \lambda\frac{\partial^2\rho^*}{\partial\theta^2} - \frac{\lambda}{\sin^2(\theta)}\frac{\partial^2\rho^*}{\partial\varphi^2} = \rho^*\Gamma_c \frac{A(T')}{A(-10°C)}\left[\mathcal{A}^* - \mathcal{A}\right], \end{aligned} \tag{7.3.11}$$

The polar and the azimuth angles are denoted by θ and φ, respectively. On the unit sphere in spherical coordinates the explicit form of the non-standard divergence operator is given by

$$\begin{aligned} \operatorname{div}_{S^2}(\bullet^*) &= \left[\cos\theta\cos\varphi\frac{\partial(\bullet^*)}{\partial\theta} - \frac{\sin\varphi}{\sin\theta}\frac{\partial(\bullet^*)}{\partial\varphi}\right] \\ &\quad + \left[\cos\theta\sin\varphi\frac{\partial(\bullet^*)}{\partial\theta} + \frac{\cos\varphi}{\sin\theta}\frac{\partial(\bullet^*)}{\partial\varphi}\right] - \sin\theta\frac{\partial(\bullet^*)}{\partial\theta} \end{aligned} \tag{7.3.12}$$

and the orientation vector $\boldsymbol{n}$ reads

$$\boldsymbol{n} = \begin{pmatrix} \sin\theta\cos\varphi \\ \sin\theta\sin\varphi \\ \cos\theta \end{pmatrix}. \tag{7.3.13}$$

7.3.3. Material parameters

At the surface of the ice core, the natural ice is composed of a large number of individual crystals with a random orientation distribution. Consequently, we assume isotropic conditions at the surface: $\mathcal{A}(z = 0) = 1$.

From experimental data Eisen et al. [83] and Wesche et al. [276] conclude that the horizontal strain field shows extension lateral to the flow direction and smaller compression in longitudinal direction. Thus, we choose $a = -0.5$ such that $D_{\mathrm{xx}} = 0.5\,D_{\mathrm{zz}}$ and $D_{\mathrm{yy}} = -1.5\,D_{\mathrm{zz}}$ and the incompressibility condition $D_{\mathrm{xx}} + D_{\mathrm{yy}} + D_{\mathrm{zz}} = 0$ is fulfilled. Note that this differs from the assumptions for the strain rate made in the simulations of Seddik et al. [233].

The material parameters are listed in Table 7.1. It is a reasonable approximation to take the parameter ι to be constant and positive, see Placidi [216]. In the special case $\iota = 1$, the basal planes carry out an affine rotation. We choose a value a bit smaller because due to geometric incompatibilities of the deformation of individual crystals, perfect affine rotations are not plausible. In fact, $\iota = 0.9$ results in the best fit between the modeled and measured fabrics for the EDML ice core. As stated in the remark at the end of Section 7.2.1, a direct experimental determination of the material parameters λ and Γ_c is not possible. However, both should be of the same order since rotation recrystallization and grain boundary migration act on the same time scale. The order of magnitude can be estimated via the vertical strain rate D_{zz} which is known from experiments. A best fit between the modeled and the measured fabrics is achieved for $\lambda = 2 \cdot 10^{-15}$ [s^{-1}] and $\Gamma_c = 1 \cdot 10^{-5}$ [s^{-1}].

7.4. Finite volume discretization

Eq. (7.3.11) can only be solved by using numerical approximation methods. The one-dimensional model formulation is discretized with the help of a finite volume method, which is an extension of the scheme used by Seddik et al. [232, 233].

parameter	symbol	value	
shape factor	ι	0.9	
mass density of ice	ρ	910	$[\mathrm{kg\,m^{-3}}]$
orientation diffusivity	λ	$2.0 \cdot 10^{-15}$	$[\mathrm{s^{-1}}]$
constitutive parameter	Γ_c	$1.0 \cdot 10^{-15}$	$[\mathrm{s^{-1}}]$
stress exponent	n	3	
maximum enhancement factor	$E_{\max}$	10	
minimum enhancement factor	$E_{\min}$	0	
vertical compression rate	ε	acc. to	Fig. 7.10
universal gas constant	R	8.314	$[\mathrm{J\,mol^{-1}K^{-1}}]$
gravity acceleration	g	9.81	$[\mathrm{m\,s^{-1}}]$
Clausius–Clapeyron constant	β	$9.8 \cdot 10^{-8}$	$[\mathrm{K\,Pa^{-1}}]$
melting temperature at zero pressure	T_0	273.16	$[\mathrm{K}]$
material parameter	a	-0.5	

Table 7.1.: Material parameters and standard physical parameters used in the simulations. The stress exponent is given in e.g. Alley [12], Budd and Jacka [48], Greve and Blatter [110], Paterson [208], van der Veen [263], Weertman [274] for the isotropic version of Glen's flow law. Thus, the strain rate increases with the third power of the stress. The maximum enhancement factor $E_{\max}$ is estimated by the experiment of e.g. Budd and Jacka [48], Pimienta et al. [215], Russell–Head and Budd [230].

Eq. (7.3.11) can be rewritten in the following more general form

$$
\begin{aligned}
0 \;=\;& \frac{\partial \rho^*(z,\theta,\varphi)}{\partial z} v_z(z) + G(\theta,\varphi)\frac{\partial^2 \rho^*(\theta,\varphi)}{\partial \theta^2} + \frac{H(\theta,\varphi)}{\sin\theta}\frac{\partial^2 \rho^*(\theta,\varphi)}{\partial \varphi^2} \\
&+ \left[D(\theta,\varphi) + \frac{1}{\sin\theta}E(\theta,\varphi)\right]\frac{\partial \rho^*(\theta,\varphi)}{\partial \varphi} \\
&+ \left[B(\theta,\varphi) + \frac{F(\theta,\varphi)}{\sin\theta}\right]\frac{\partial \rho^*(\theta,\varphi)}{\partial \theta} + C(\theta,\varphi),
\end{aligned}
\tag{7.4.1}
$$

with

$$
\begin{aligned}
B &= \frac{1}{2}\left[-\frac{1}{2}\iota\varepsilon\sin(2\theta)\,[[2a-1]\cos(2\varphi)+3]+\ \gamma[1-\iota\cos(2\theta)]\cos(\varphi)\right],\\
C &= \frac{3}{4}\iota\rho^*\big[\varepsilon[[4a-2]\sin^2(\theta)\cos(2\varphi)-1-3\cos(2\theta)]+2\gamma\sin(2\theta)\cos(\varphi)\big]\\
&\quad -\frac{\rho^*\Gamma_c A(T')}{A(-10°C)}\left[\mathcal{A}^*-\mathcal{A}\right],\\
D &= \frac{1}{2}\varepsilon\iota[2a-1]\sin(2\varphi),\\
E &= \frac{1}{2}\gamma[\iota-1]\frac{\sin(\varphi)}{\tan(\theta)},\\
F &= -\lambda\cos\theta,\\
G &= -\lambda,\\
H &= -\frac{\lambda}{\sin\theta}.
\end{aligned}
\tag{7.4.2}
$$

The domain is discretized into a finite number of cells (volumes). In analogy to finite difference and finite element methods, values are calculated at discrete nodes on the meshed geometry. Each node point on the mesh is surrounded by a small volume (the unit sphere S^2 in our case).

The location of the grid points are given by

$$
\begin{aligned}
\theta_i &= \left[\frac{1}{2}+i\right]\Delta\theta \quad \text{with } \Delta\theta := \frac{\pi}{N_\theta} && \text{for } i=0,\dots,N_\theta-1\\
\varphi_j &= j\Delta\varphi \quad \text{with } \Delta\varphi = \frac{2\pi}{N_\varphi} && \text{for } j=0,\dots,N_\varphi\\
z_{h+1} &= z_h + v_{z_h}\Delta t && \text{for } j=0,\dots,N_z.
\end{aligned}
\tag{7.4.3}
$$

The simulation starts at the surface ($z=0$) and subsequently deepens into the ice. Δt denotes the time interval and, therefore, defines the step size with respect to depth z. Furthermore, the latitudes are monotonically increasing, starting at the north pole $\theta=\frac{\Delta\theta}{2}$ and ending at the south pole $\theta=\pi-\frac{\Delta\theta}{2}$.

Volume integration of the partial differential Eq. (7.4.1) yields

$$
0=\int_\theta \sin\theta \int_\varphi \frac{\partial\rho^*}{\partial z}v_z + G\frac{\partial^2\rho^*}{\partial\theta^2}+\frac{H}{\sin\theta}\frac{\partial^2\rho^*}{\partial\varphi^2}+\left[D+\frac{1}{\sin\theta}E\right]\frac{\partial\rho^*}{\partial\varphi}+B\frac{\partial\rho^*}{\partial\theta}+C\ \mathrm{d}\varphi\ \mathrm{d}\theta. \tag{7.4.4}
$$

For any inner point of the spherical domain, i.e. $i=1,\dots,N_\theta-2$, $j=0,\dots,N_\varphi-1$ and $h=0,\dots,N_z$, we employ a second-order accurate central difference scheme for the spatial derivatives. Thus, carrying out the volume integration given in Eq. (7.4.4) leads to

$$
\begin{aligned}
0 = \; & v_{z_h} \frac{\rho^*(z_{h+1},\theta_i,\varphi_j) - \rho^*(z_h,\theta_i,\varphi_j)}{\Delta z} \left[\cos(\theta_i - \frac{\Delta\theta}{2}) - \cos(\theta_i + \frac{\Delta\theta}{2})\right] \Delta\varphi \\
& + D(\theta_i,\varphi_j) \frac{\rho^*(z_h,\theta_i,\varphi_{j+1}) - \rho^*(z_h,\theta_i,\varphi_{j-1})}{2\Delta\varphi} \left[\cos(\theta_i - \frac{\Delta\theta}{2}) - \cos(\theta_i + \frac{\Delta\theta}{2})\right] \Delta\varphi \\
& + E(\theta_i,\varphi_j) \frac{\rho^*(z_h,\theta_i,\varphi_{j+1}) - \rho^*(z_h,\theta_i,\varphi_{j-1})}{2\Delta\varphi} \Delta\theta\Delta\varphi \\
& + B(\theta_i,\varphi_j) \frac{\rho^*(z_h,\theta_{i+1},\varphi_j) - \rho^*(z_h,\theta_{i-1},\varphi_j)}{2\Delta\theta} \left[\cos(\theta_i - \frac{\Delta\theta}{2}) - \cos\left(\theta_i + \frac{\Delta\theta}{2}\right)\right] \Delta\varphi \\
& + C(\theta_i,\varphi_j) \left[\cos(\theta_i - \frac{\Delta\theta}{2}) - \cos(\theta_i + \frac{\Delta\theta}{2})\right] \Delta\varphi \\
& + F(\theta_i,\varphi_j) \frac{\rho^*(z_h,\theta_{i+1},\varphi_j) - \rho^*(z_h,\theta_{i-1},\varphi_j)}{2\Delta\theta} \Delta\theta\Delta\varphi \\
& + G(\theta_i,\varphi_j) \frac{\rho^*(z_h,\theta_{i+1},\varphi_j) - 2\rho^*(z_h,\theta_i,\varphi_j) + \rho^*(z_h,\theta_{i-1},\varphi_j)}{(\Delta\theta)^2} \Delta\varphi \\
& \left[\cos\left(\theta_i - \frac{\Delta\theta}{2}\right) - \cos\left(\theta_i + \frac{\Delta\theta}{2}\right)\right] \\
& + H(\theta_i,\varphi_j) \frac{\rho^*(z_h,\theta_i,\varphi_{j+1}) - 2\rho^*(z_h,\theta_i,\varphi_j) + \rho^*(z_h,\theta_i,\varphi_{j-1})}{(\Delta\varphi)^2} \Delta\theta\Delta\varphi
\end{aligned}
\tag{7.4.5}
$$

Rearranging and solving for the orientation mass density $\rho^*(z_{h+1},\theta_i,\varphi_j)$ at the new step leads to

$$
\begin{aligned}
\rho^*(z_{h+1},\theta_i,\varphi_j) = \; & \rho^*(z_h,\theta_i,\varphi_j) - \frac{D\Delta z}{v_{z_h} 2\Delta\varphi} \left[\rho^*(z_h,\theta_i,\varphi_{j+1}) - \rho^*(z_h,\theta_i,\varphi_{j-1})\right] \\
& - \frac{E\Delta z\Delta\theta \left[\rho^*(z_h,\theta_i,\varphi_{j+1}) - \rho^*(z_h,\theta_i,\varphi_{j-1})\right]}{v_{z_h} 2\Delta\varphi \left[\cos\left(\theta_i - \frac{\Delta\theta}{2}\right) - \cos\left(\theta_i + \frac{\Delta\theta}{2}\right)\right]} \\
& - \frac{B\Delta z}{v_{z_h} 2\Delta\theta} \left[\rho^*(z_h,\theta_{i+1},\varphi_j) - \rho^*(z_h,\theta_{i-1},\varphi_j)\right] - \frac{C\Delta z}{v_{z_h}} \\
& - \frac{F\Delta z\Delta\theta}{2v_{z_h} \left[\cos(\theta_i - \frac{\Delta\theta}{2}) - \cos(\theta_i + \frac{\Delta\theta}{2})\right]} \left[\rho^*(z_h,\theta_{i+1},\varphi_j) - \rho^*(z_h,\theta_{i-1},\varphi_j)\right] \\
& - \frac{G\Delta z}{v_{z_h} (\Delta\theta)^2} \left[\rho^*(z_h,\theta_{i+1},\varphi_j) - 2\rho^*(z_h,\theta_i,\varphi_j) + \rho^*(z_h,\theta_{i-1},\varphi_j)\right] \\
& - \frac{H\Delta z\Delta\theta \left[\rho^*(z_h,\theta_i,\varphi_{j+1}) - 2\rho^*(z_h,\theta_i,\varphi_j) + \rho^*(z_h,\theta_i,\varphi_{j-1})\right]}{v_{z_h} (\Delta\varphi)^2 \left[\cos\left(\theta_i - \frac{\Delta\theta}{2}\right) - \cos\left(\theta_i + \frac{\Delta\theta}{2}\right)\right]}
\end{aligned}
\tag{7.4.6}
$$

At the north pole of the spherical domain, i.e. at $\theta = \frac{\Delta\theta}{2}$, we apply a similar, but slightly different procedure: forward differences are used for the latitude. In analogy to Eq. (7.4.6), we obtain for $j = 0, \dots, N_\varphi - 1$ and $h = 0, \dots, N_z$

$$\begin{aligned}
\rho^*(z_{h+1}, \frac{\Delta\theta}{2}, \varphi_j) \;=\; & \rho^*(z_h, \frac{\Delta\theta}{2}, \varphi_j) - \frac{D\Delta z}{v_{z_h} 2\Delta\varphi} \left[\rho^*(z_h, \frac{\Delta\theta}{2}, \varphi_{j+1}) - \rho^*(z_h, \frac{\Delta\theta}{2}, \varphi_{j-1})\right] \\
& - \frac{E\Delta z}{v_{z_h} 2\Delta\varphi\,[1-\cos(\Delta\theta)]} \left[\rho^*(z_h, \frac{\Delta\theta}{2}, \varphi_{j+1}) - \rho^*(z_h, \frac{\Delta\theta}{2}, \varphi_{j-1})\right] \Delta\theta \\
& - \frac{B\Delta z}{v_{z_h}\Delta\theta} \left[\frac{1}{2}\rho^*(z_h, \frac{3\Delta\theta}{2}, \varphi_j) + \frac{1}{2}\rho^*(z_h, \frac{\Delta\theta}{2}, \varphi_j) - \frac{1}{N_\varphi}\sum_{l=0}^{N_\varphi-1} \rho^*(z_h, \frac{\Delta\theta}{2}, \varphi_l)\right] \\
& - \frac{C\Delta z}{v_{z_h}} \\
& - \frac{F\Delta z}{v_{z_h}\,[1-\cos(\Delta\theta)]} \left[\frac{1}{2}\rho^*(z_h, \frac{3\Delta\theta}{2}, \varphi_j) + \frac{1}{2}\rho^*(z_h, \frac{\Delta\theta}{2}, \varphi_j) - \frac{1}{N_\varphi}\sum_{l=0}^{N_\varphi-1} \rho^*(z_h, \frac{\Delta\theta}{2}, \varphi_l)\right] \\
& - \frac{G\Delta z}{v_{z_h}(\Delta\theta)^2} \left[\frac{1}{4}\rho^*(z_h, \frac{5\Delta\theta}{2}, \varphi_j) + \frac{1}{2}\rho^*(z_h, \frac{3\Delta\theta}{2}, \varphi_j) + \frac{1}{4}\rho^*(z_h, \frac{\Delta\theta}{2}, \varphi_j) - \frac{1}{N_\varphi}\sum_{l=0}^{N_\varphi-1} \rho^*(z_h, \frac{\Delta\theta}{2}, \varphi_l)\right] \\
& - \frac{H\Delta z\Delta\theta}{v_{z_h}\,[1-\cos(\Delta\theta)]\,(\Delta\varphi)^2} \left[\rho^*(z_h, \frac{\Delta\theta}{2}, \varphi_{j+1}) - 2\rho^*(z_h, \frac{\Delta\theta}{2}, \varphi_j) + \rho^*(z_h, \frac{\Delta\theta}{2}, \varphi_{j-1})\right]
\end{aligned} \tag{7.4.7}$$

The south pole of the spherical domain ($\theta = \pi - \frac{\Delta\theta}{2}$) backward differences are applied for the latitude and once more $j = 0, \dots, N_\varphi - 1$ and $h = 0, \dots, N_z$, yielding

$$\begin{aligned}
\rho^*(z_{h+1}, \pi - \frac{\Delta\theta}{2}, \varphi_j) \;=\; & \rho^*(z_h, \pi - \frac{\Delta\theta}{2}, \varphi_j) \\
& - \frac{D\Delta z}{v_{z_h} 2\Delta\varphi} \left[\rho^*(z_h, \pi - \frac{\Delta\theta}{2}, \varphi_{j+1}) - \rho^*(z_h, \pi - \frac{\Delta\theta}{2}, \varphi_{j-1})\right] \\
& - \frac{E\Delta z}{v_{z_h} 2\Delta\varphi\,[1-\cos(\Delta\theta)]} \left[\rho^*(z_h, \pi - \frac{\Delta\theta}{2}, \varphi_{j+1}) - \rho^*(z_h, \pi - \frac{\Delta\theta}{2}, \varphi_{j-1})\right] \Delta\theta \\
& - \frac{B\Delta z}{v_{z_h}\Delta\theta} \left[\frac{1}{N_\varphi}\sum_{l=0}^{N_\varphi-1} \rho^*(z_h, \pi - \frac{\Delta\theta}{2}, \varphi_l) - \frac{1}{2}\rho^*(z_h, \pi - \frac{3\Delta\theta}{2}, \varphi_j) - \frac{1}{2}\rho^*(z_h, \pi - \frac{\Delta\theta}{2}, \varphi_j)\right] - \frac{C\Delta z}{v_{z_h}} \\
& - \frac{F\Delta z}{v_{z_h}\,[1-\cos(\Delta\theta)]} \left[\frac{1}{N_\varphi}\sum_{l=0}^{N_\varphi-1} \rho^*(z_h, \pi - \frac{\Delta\theta}{2}, \varphi_l) - \frac{1}{2}\rho^*(z_h, \pi - \frac{3\Delta\theta}{2}, \varphi_j) - \frac{1}{2}\rho^*(z_h, \pi - \frac{\Delta\theta}{2}, \varphi_j)\right] \\
& - \frac{G\Delta z}{v_{z_h}(\Delta\theta)^2} \left[\frac{1}{N_\varphi}\sum_{l=0}^{N_\varphi-1} \rho^*(z_h, \pi - \frac{\Delta\theta}{2}, \varphi_l) - \frac{1}{4}\rho^*(z_h, \pi - \frac{5\Delta\theta}{2}, \varphi_j) - \frac{1}{2}\rho^*(z_h, \pi - \frac{3\Delta\theta}{2}, \varphi_j) - \frac{1}{4}\rho^*(z_h, \pi - \frac{\Delta\theta}{2}, \varphi_j)\right] \\
& - \frac{H\Delta z\Delta\theta}{v_{z_h}\,[1-\cos(\Delta\theta)]\,(\Delta\varphi)^2} \left[\rho^*(z_h, \pi - \frac{\Delta\theta}{2}, \varphi_j) - 2\rho^*(z_h, \pi - \frac{\Delta\theta}{2}, \varphi_{j-1}) + \rho^*(z_h\pi -, \frac{\Delta\theta}{2}, \varphi_{j-2})\right].
\end{aligned} \tag{7.4.8}$$

This provides a complete set of discretized equations for the EDML ice. The advantage of the discretization scheme described above is that no boundary conditions are required at the two poles. This clearly makes sense because in reality the poles are just an ordinary grid point of the unit sphere. Moreover, the singularity of Eq. (7.3.11) does not cause any problems.

For the results presented in Section 7.5, the angular resolution of the unit sphere is discretized as stated in Eq. (7.4.3) is $\Delta\theta = \Delta\varphi = 5°$. Moreover, $\Delta t = 1$ day is chosen for the time step.

7.5. Numerical results

Figure 7.11 depicts the fabric data from the antarctic EDML ice core. Near the surface the ice is anisotropic. At 854 m the evolution of a girdle is seen which sharpens until about 1845 m. From 2035 m the data reveal a vertical single maximum, thus the ice is highly anisotropic. The single maxima have a noticeable deviation from the vertical, i.e. from the center of the Schmidt diagrams.

Figure 7.12 illustrates the numerical simulations. For the sake of easy comparison with the fabric data, the depths are the same as in Figure 7.11.

During the drilling process the orientation of the core cannot be fixed. The orientation of the girdle is calculated in Eisen et al. [83] and Wesche et al. [276]. The direction of ice flow derived in our simulations meets the results of Eisen et al. [83] and Wesche et al. [276] much better than the simulation results presented in Seddik et al. [233].

Figure 7.12 shows that the orientation distribution function develops a single maximum. The agreement with the experimental data illustrated in Figure 7.11 is very good. The numerical results capture the isotropic fabric near the surface. The broad and the narrow girdle at 854 m respectively 1364 m are captured well. Moreover, the evolution towards a single maximum at about 2000 m is nicely shown. The dataset published in Wesche et al. [276] identifies the flow direction to be 274.4°, roughly parallel to the ice divide. This is supported by the findings of Eisen et al. [83]. The computed girdle fabrics are aligned with the x-axis, thus, in direction of the flow and, therefore, perfectly meet the experimental findings.

At depths of 2035 m and 2045 m, the obtained single-maximum fabrics have a small, but noticeable deviation from the vertical (center of the Schmidt diagrams). This is also in agreement with the data, and is an effect of the transition of the deformation regime from mainly pure shear to mainly bed-parallel simple shear.

Figure 7.13 (left) shows the variation of the enhancement factor $\hat{E}(\mathcal{A})$ along the ice core. In the beginning it is close to unity which reflects that the fabric is approximately isotropic in that region. Further down, the fabric develops towards a single maximum with its crystal basal planes orientated in such a way that large deformations arise. Consequently, the enhancement factor increases significantly.

Next, the evolution of the alignment tensor (also called orientation tensor) $\boldsymbol{a}^2$ is discussed, cf. Appendix A.2 for its definition. The orientation distribution function itself is not directly measurable. However, its anisotropic moment, i.e. the alignment tensor, represents a measurement for the orientational order. A large value of a_{33} represents a concentration of the grains in vertical direction. An ideal vertical single maximum fabric would result in $a_{33} \rightarrow 1$. a_{11} and a_{22} indicate the symmetry with respect to the vertical direction in the sense that if $a_{11} = a_{22}$ the cross section is symmetric and $|a_{11} - a_{22}|$ represents the degree of anisotropy.
The alignment tensor is calculated in a post-processing step and illustrated in Figure 7.13 (right). Downwards, a_{33} increases with increasing depth. Thus, the c-axes concentrate around the vertical direction, i.e. the z-direction (= '3'-direction). The development of

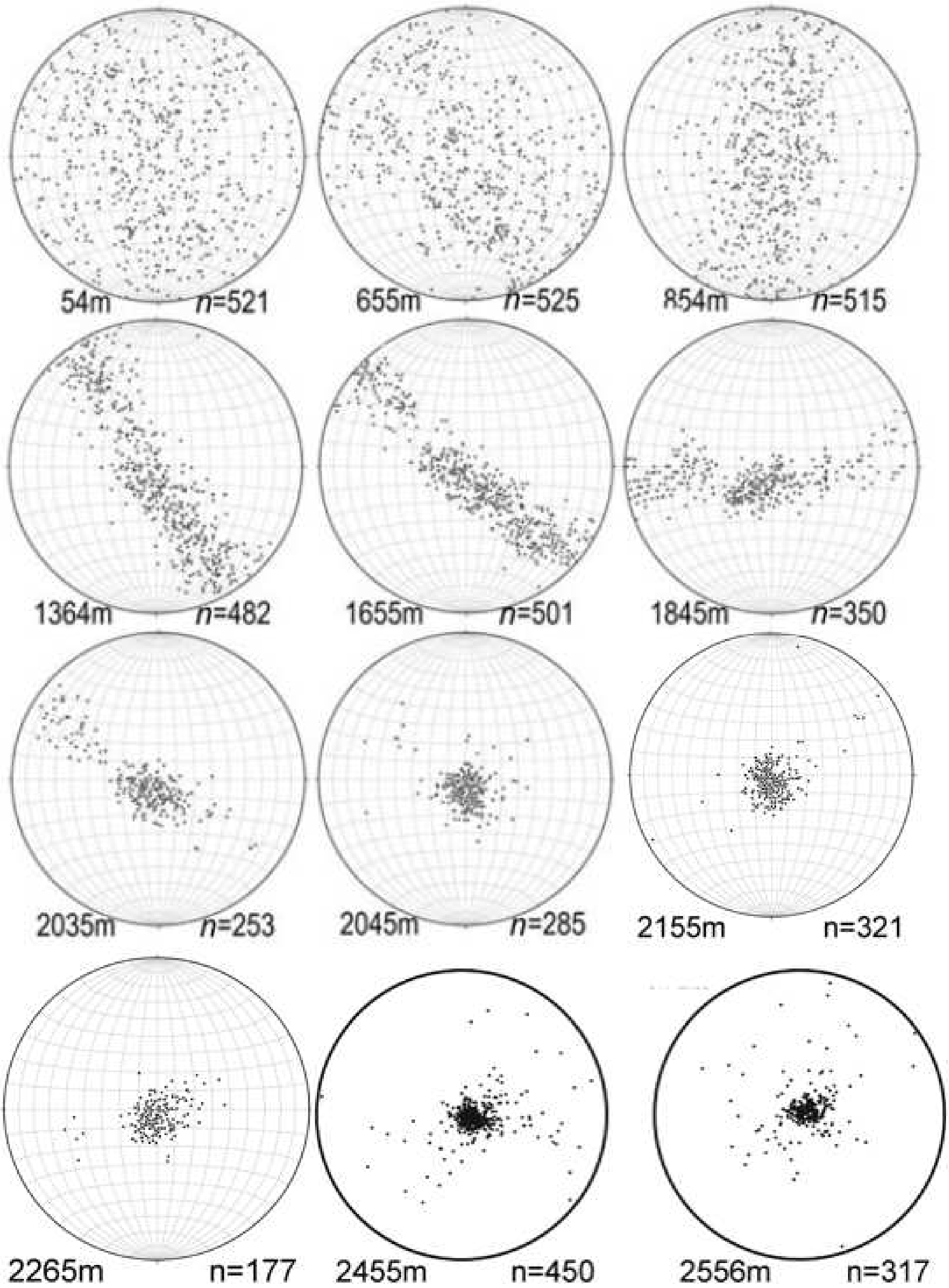

Figure 7.11.: Orientation distributions are illustrated for different samples of the EDML ice core (I. Weikusat, personal communication 2007 and 2009, partly published by Seddik et al. [233]). The center of the Schmidt diagrams coincide with the core axis. The data displayed in this figure originates from vertically cut thin section. During the drilling process, the original orientation of the samples with respect to the flow direction cannot be maintained. Thus, it is unknown. Near the surface the ice is isotropic. At 854 m the evolution of a girdle is seen which sharpens until about 1845 m. From 2035 m the data reveals a vertical single maximum, thus the ice is highly anisotropic.

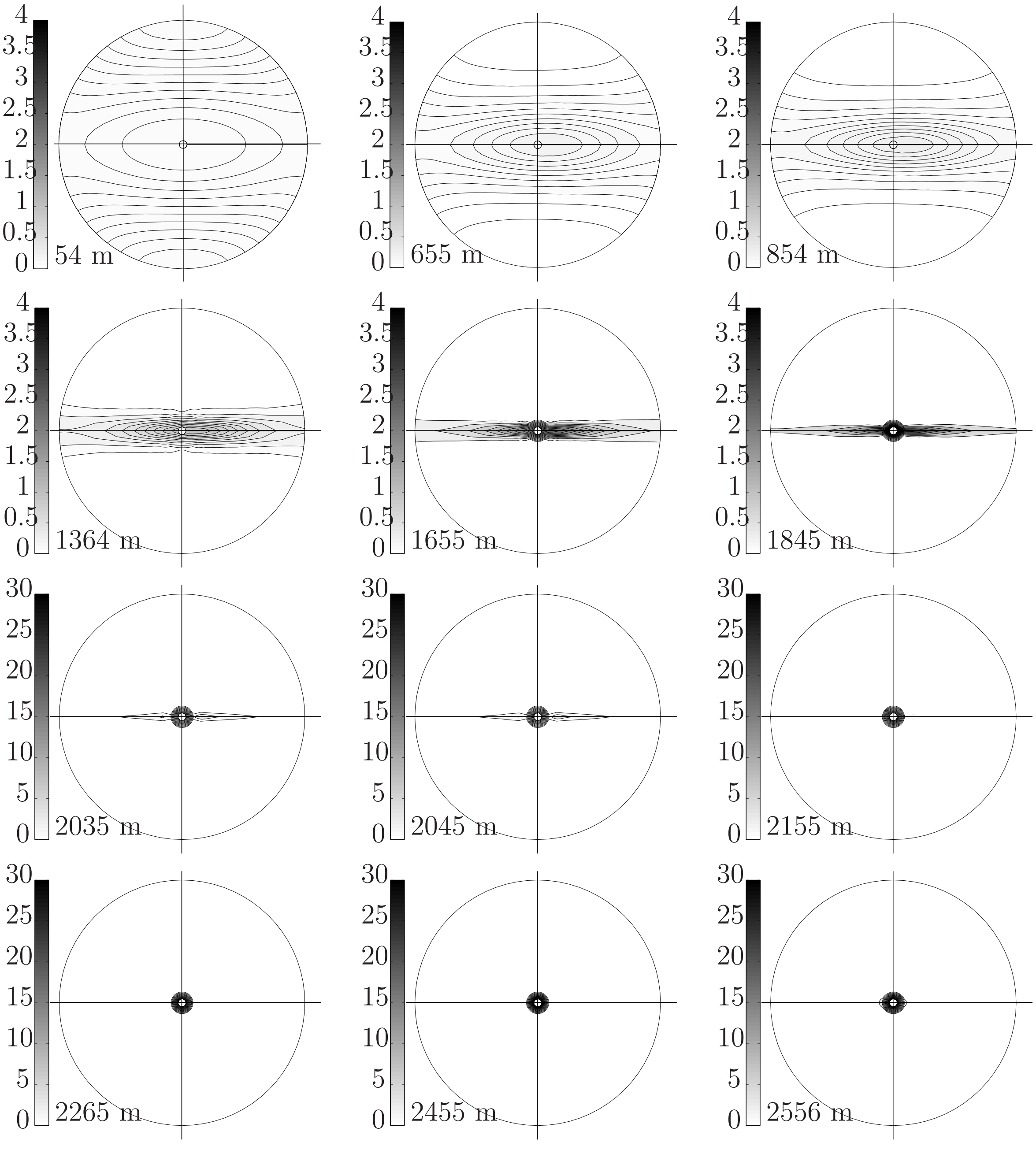

Figure 7.12.: Schmidt diagram representations of the EDML fabrics (ODF) are depicted at depths between 54 and 2556 m. As in Figure 7.11, the centers of the diagrams coincide with the core axis and the projection is on the horizontal (x-y) plane. The numerical results fit well with the experimental data as given in Figure 7.11. The girdle is orientated along the x-axis which is in accordance to the findings of Eisen et al. [83] and Wesche et al. [276].

a_{33} illustrates the fabric's evolution from isotropy to an anisotropic single maximum close to the core bottom.

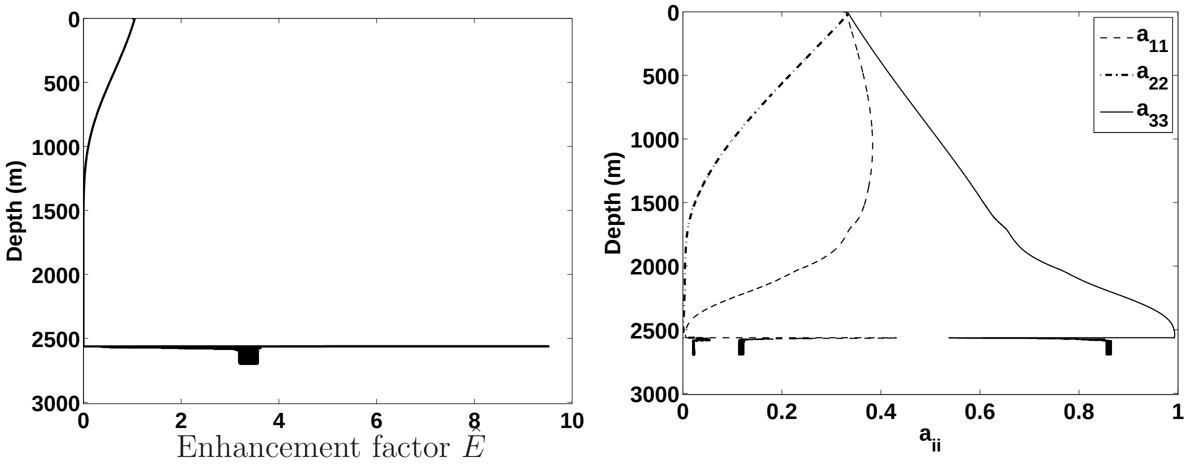

Figure 7.13.: Variation along the EDML ice core of the enhancement factor $\hat{E}$ (left) and the three non-zero components of the second-order orientation tensor $\boldsymbol{a}^2$ (right). A large value of a_{33} represents a concentration of the grains in vertical direction, i.e. the formation of a vertical single maximum. Between ca. 1500 m and 2550 m the enhancement factor $\hat{E}$ is close (but not equal to) zero.

Wesche et al. [276] report an annual mean velocity of 0.756 m/a. The surface velocities are measured at 12 survey points in the vicinity of the EDML core between the years 2000 and 2005 and varies between 0.62 m/a and 0.96 m/a, see Wesche et al. [276]. Figure 7.18 shows the variation of the horizontal velocity v_x along the ice core. The absolute value of 0.80 m/a of the surface velocity agrees well with the measurements of Wesche et al. [276].

In order to separate the effects of the two deformation regimes (vertical compression, simple shear), we ran two further simulations; each of them neglecting one of the two deformation regimes. Vertical compression is defined by ignoring the horizontal shear rate, i.e. $\gamma = 0$. The development in case of pure shear/vertical compression is depicted in Figure 7.14. A strong single maximum fabric forms in the near-basal parts of the core. As expected, the contribution of the vertical compression outweighs the simple shear contribution in case of the EDML core. In case of the underlying deformation regime at the EDML core, the vertical compression is an elongation in one direction which is responsible for the girdle's orientation. However, the latter may not be neglected. First of all because in reality, simple shear is involved in the deformation process at the EDML core. This leads to the small deviation from the horizontal (center of Schmidt diagrams) in the numerical results in the deeper regions of the ice core. This effect is also seen in the experimental data in Figure 7.11 and it is due to the change of the deformation regime from mainly pure shear to mainly bed-parallel simple shear[4].

---

[4] Deep drilling sites are usually chosen in regions with a small amount of simple shear because the drilling takes place over few years and the drilling hole should be subject to as little simple shear deformation as possible. Moreover, the drilling is usually sponsored in order to obtain historic climate information and the less simple shear the older the ice at the bottom. Thus, in case of the EDML core the amount

The Schmidt diagrams in case of simple shear can be seen in Figure 7.15. With increasing depth, the distribution of crystals orientations is non-symmetric - with an off-set to the East (right). Below 2400 m the simple shear model becomes numerically unstable, see also Figure 7.17. The fact that it becomes unstable in the deeper regions is due to the temperature increase and the induced exponential increase of the rate factor $A(T')$ and, consequently, a greater amount of shear. The influence of the simple shear is a lot smaller than the influence of vertical compression as suggested by the experimental findings.

Comparison of Figures 7.16 and 7.17 shows a large difference in the development of the enhancement factor $\hat{E}$. In case of simple shear, the enhancement factor remains close to unity until approximately 2100 m - representing almost isotropic fabrics. This finding is supported by the development of the orientation tensor $\boldsymbol{a}^2$ with $a_{11} \approx a_{22} \approx a_{33} \approx 1/3$ and the Schmidt diagrams in Figure 7.15. On the other hand, in case of vertical compression, the formation of a girdle and later a vertical single maximum starts a lot earlier, see Figure 7.16. Moreover, at 2500 m depth, component a_{33} of the orientation tensor $\boldsymbol{a}^2$ is closer to unity than in case of the full deformation regime as depicted in Figure 7.13 (b). The development of an ideal vertical single-maximum fabric results in $a_{33} = 1$. The small difference in the value of a_{33} for those two cases corresponds to the small deviation from the fabric's center.

7.6. Conclusion

The CAFFE model is a mesoscopic continuum theory which fulfills all material modeling principles and satisfies the second law of thermodynamics. Moreover, it only contains a limited number of material parameters, all of which have a physical meaning, i.e. the model does not rely on any artificial parameters. The introduction of an orientation distribution function as a statistical measurement, instead of evaluating the mesoscopic space directly, is numerically very efficient. Consequently, an implementation is possible and computation time is relatively short.

In this chapter, the CAFFE model is applied to the ice of the EDML deep-drilling site.

Numerical results presented in Seddik et al. [233] showed that the CAFFE model is capable of reproducing essential characteristics of the anisotropic ice flow in the EDML core, Antarctica. However, as remarked in Seddik et al. [233], below 1600 m depth the numerical results of Seddik et al. [233] showed a small discrepancy and below 2100 m depth deviations from experimental data became rather large. Moreover, the computed direction of the girdle did not match the calculations of Eisen et al. [83] and Wesche et al. [276]. In this contribution, migration and rotation recrystallization effects were taken into account. This led to a single maximum fabric even below 2100 m depth- a condition most favorable for bed-parallel simple-shear deformations. Moreover, the comparison of the numerical results from Seddik et al. [233] and the ones in this contribution with the experimental data shows that rotation recrystallization and grain boundary migration

---

of simple shear is rather low compared to other regions of Antarctica.

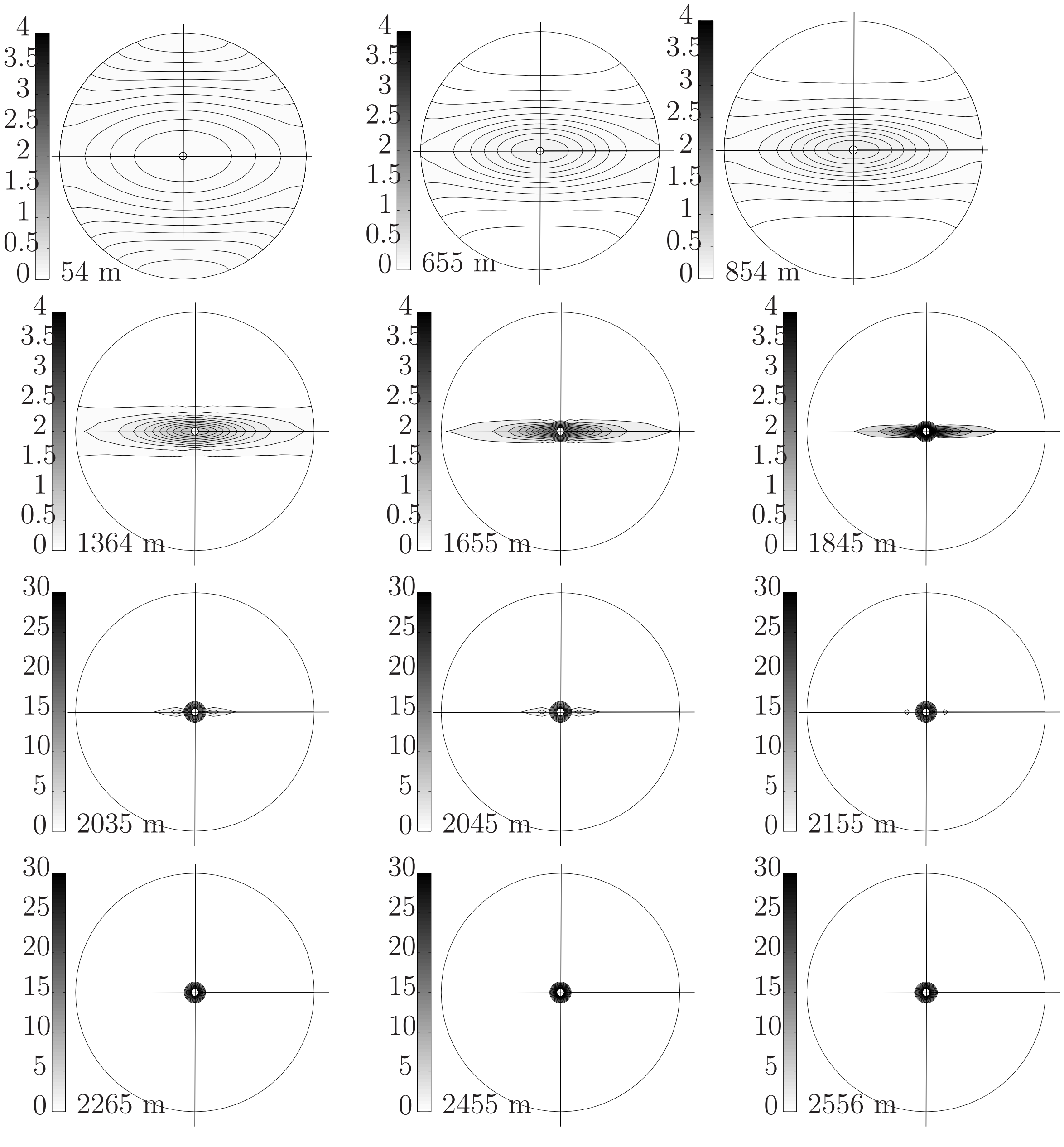

Figure 7.14.: Separation of effects of the two deformation regimes. Vertical compression, i.e. the horizontal shear rate $\gamma = 0$. Schmidt diagram representations of the EDML fabrics (ODF) are illustrated at depths between 54 m and 2556 m. The centers of the diagrams coincide with the core axis and the projection is on the horizontal (x-y) plane.

should not be neglected. This is in accordance to the findings of Weikusat et al. [275]. Furthermore, due to slightly more complex assumptions for the strain rate, the direction of the girdle corresponds to the calculated direction of Eisen et al. [83] and Wesche et al. [276]. Additionally, the effects of the two underlying deformation regimes of vertical

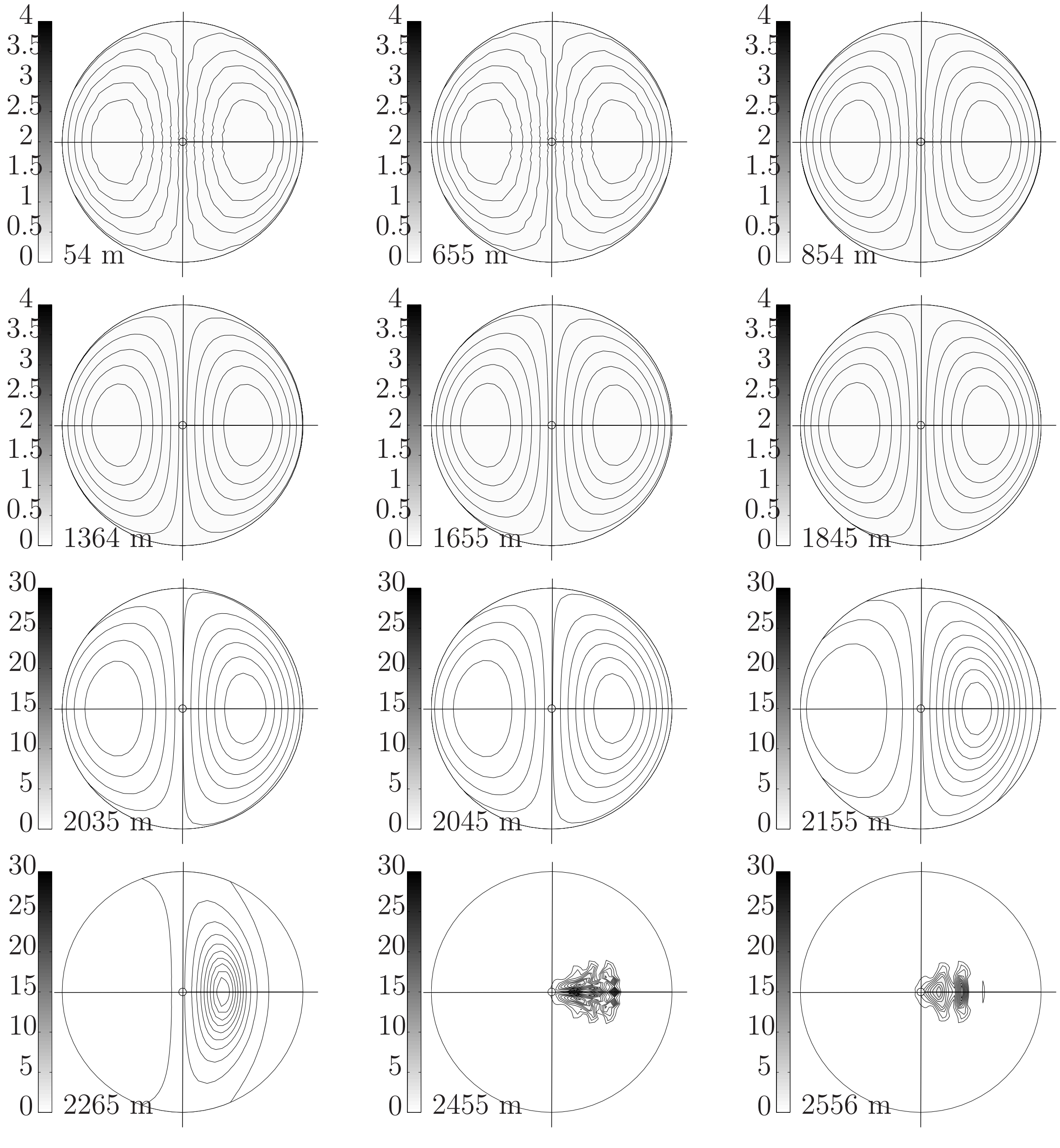

Figure 7.15.: Separation of effects of the two deformation regimes. Simple shear, i.e. the vertical compression rate ϵ is neglected. Schmidt diagram representations of the EDML fabrics (ODF) are shown at depths between 54 and 2556 m. Once more, the centers of the diagrams coincide with the core axis and the projection is on the horizontal (x-y) plane. The influence of the simple shear is a lot smaller than the influence of vertical compression. Below 2400 m numerical problems arise for this special case.

compression and simple shear were examined separately in order to study their influence. The numerical finite volume discretization scheme is robust.

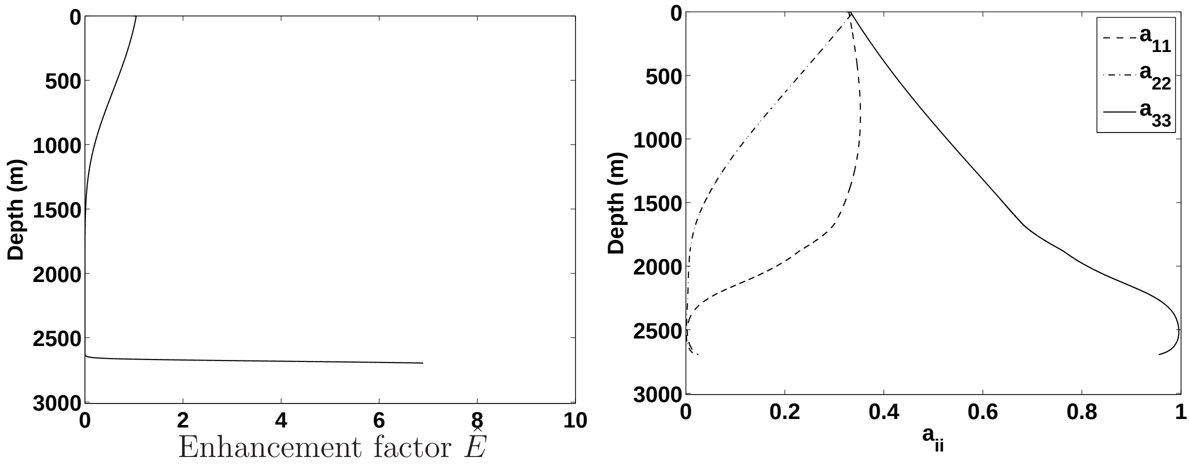

Figure 7.16.: Separation of effects of the two deformation regimes. Vertical compression. Variation along the ice core of the enhancement factor $\hat{E}$ (left) and the three non-zero components of the second-order orientation tensor $\boldsymbol{a}^2$ (right). Between ca. 1500 m and 2550 m the enhancement factor $\hat{E}$ is close (but not equal to) zero, representing the formation of a girdle.

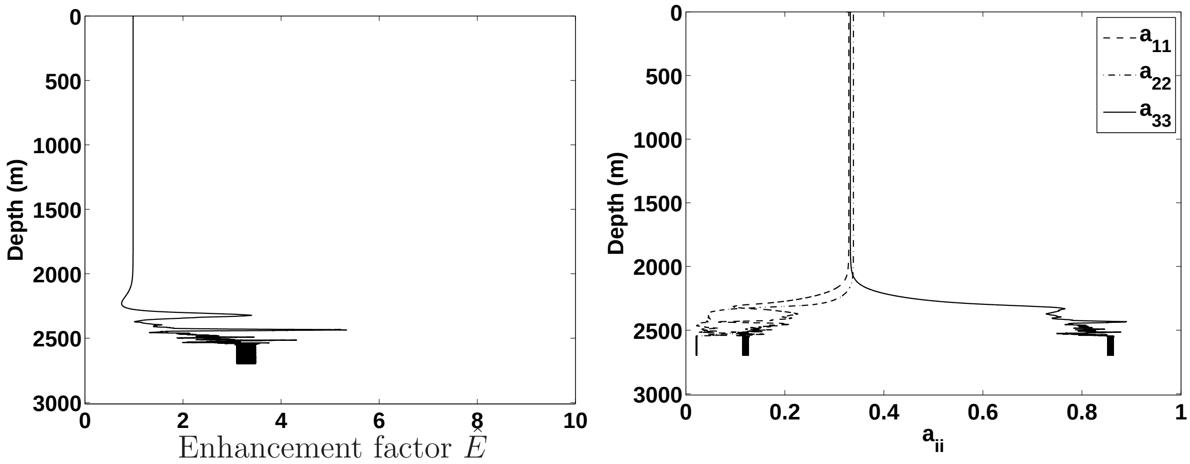

Figure 7.17.: Separation of effects of the two deformation regimes. Simple shear. Variation along the ice core of the enhancement factor $\hat{E}$ (left) and the three non-zero components of the second-order orientation tensor $\boldsymbol{a}^2$ (right).

The CAFFE model represents a great compromise between physical adequateness and simplicity. In conclusion, the effects of migration and rotation recrystallization have to be taken into account in the simulations. The agreement of the numerical results and the experimental data is very high.

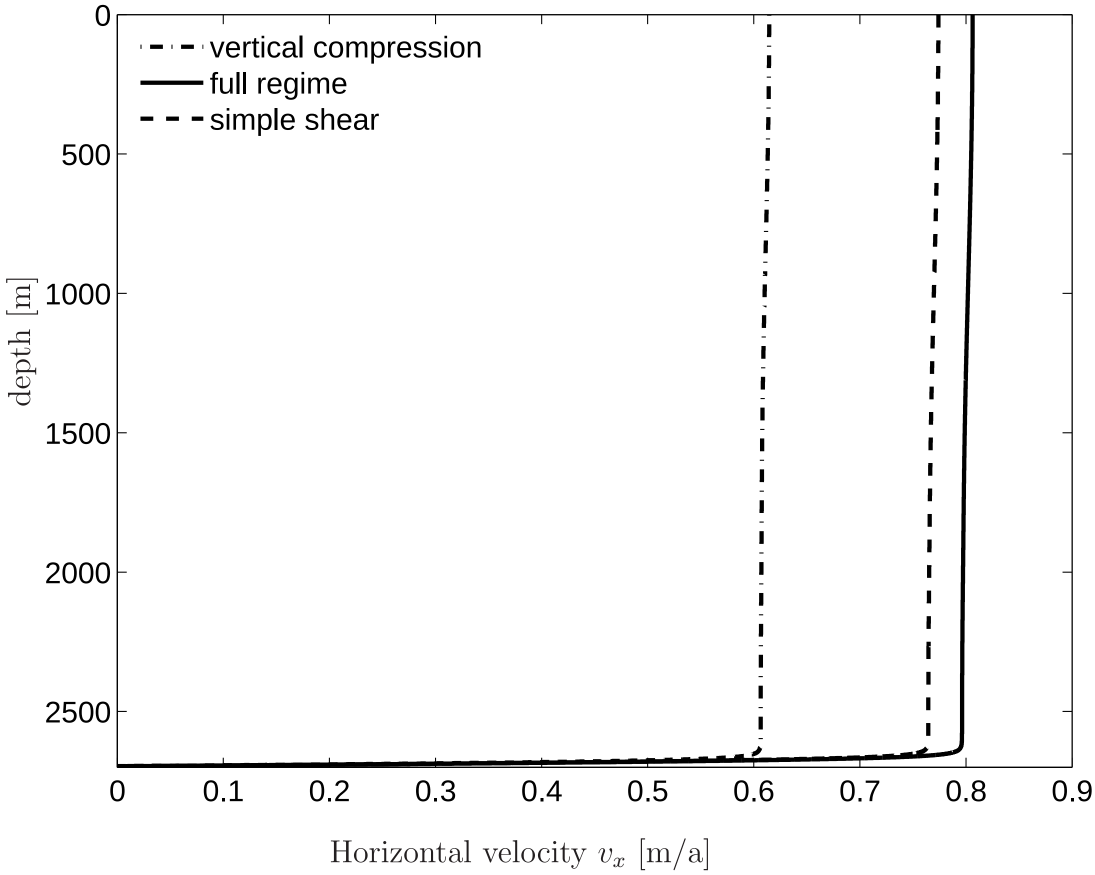

Figure 7.18.: Variation along the ice core of the horizontal velocity v_x. The simple shear predicts significantly larger horizontal velocities compared to the vertical compression. The surface velocity obtained for the full regime agrees well with the experimental data of Wesche et al. [276].

8. Review on models of solvent penetration in glassy polymers (case II diffusion)

The objective of this review is to provide an overview and a classification of the key literature on models of non-Fickian case II type diffusion. Several extensive review articles concerning non-Fickian diffusion exist in the literature; our objective is not to reproduce these worthy contributions. Rather, we focus on a limited number of, seemingly disparate, notable models and attempt to unify them using the language of thermodynamics and continuum mechanics. This attempted unification of selected models arising from various modeling communities serves to elucidate the key strengths and potential weaknesses of the models.

8.1. Introduction

The problem of interest is the diffusion of a solvent within a polymeric solid. Classical diffusion (also termed Fickian diffusion) is characterized by a process wherein the solid material undergoes negligible rearrangement due to the presence of the diffusing solvent, or indeed where the molecular rearrangements within the polymer happen so fast as to be instantaneous from the perspective of the diffusing species. Fick's first law [94], with its assumption that the diffusive flux is proportional to the gradient of the concentration, proves adequate to describe a broad range of diffusion processes. The general structure of Fick's law for diffusion is present in various other models of physical phenomena such as those describing the flow of liquid and gas in porous media, heat conduction and electrostatics.

The diffusion of a low-molecular weight solvent within a glassy polymeric solid can exhibit significant deviations from classical Fickian diffusion. The diffusion of the solvent particles is initially restrained by the tightly knit polymeric network. The pressure exerted by the solvent causes the polymer network to rearrange to accommodate the solvent. This rearrangement of the polymer chains takes a finite amount of time and manifests itself as a viscoelastic response at the scale of the polymeric solid. Concurrently, the presence of the solvent increases the rate of polymer relaxation. The polymeric solid is observed to undergo a glass–rubber transition with a sharp front separating the two regions propagating through the polymeric solid at a finite speed. In the swollen rubber-like region behind the front the concentration gradient of the solvent is negligible. In the glass-like region ahead of the front the solvent concentration drops rapidly. A small Fickian precursor is often observed directly ahead of the front. The mass uptake of the solvent by the polymer is linear in time; this is in stark contrast to classical diffusion where the mass uptake is proportional to the square-root of time. This non-classical type of diffusion was coined case II diffusion by Alfrey et al. [11] who were the first to document it. Extensive descriptions of the key features, models and experimental observations of case II type diffusion exist in the literature. De Kee et al. [74] and Vesely [266] present general reviews of non-Fickian diffusion which contain sections devoted to case II diffusion. Both contain numerous references. Furthermore, Collins [62] describes the phenomenon of case II diffusion in the context of controlled release from drug-impregnated monoliths.

The widespread commercial use of processes involving diffusion in polymeric materials, e.g. in the pharmaceutical and automotive industries and semiconductor lithography, used in the fabrication of integrated circuits, motivates the need to develop robust predictive models. Numerous models have been proposed to describe case II diffusion, see e.g. Astarita and Sarti [18], Thomas and Windle [254, 255, 256], Cohen [58], Durning [79], Hui and Wu [139, 140], Cohen and White [59], Jou et al. [153], Kalospiros et al. [154], Govindjee and Simo [107], Wu and Peppas [279], Rossi et al. [229], Friedman and Rossi [102], El Afif [86], Qian and Taylor [222], El Afif and Grmela [87], Vijalapura and Govindjee [267, 268], De Kee [74], Riviére and Shaw [227], Vesely [266], amongst others. To date, however, no single theoretical model is capable of describing all of the phenomena observed during case II diffusion [107, 74].[1] The strong coupling between the diffusion and deformation processes as well as the extreme inherent non-linearities makes the robust solution of the more comprehensive models challenging, even in one space dimension, see e.g. Vijalapura and Govindjee [267, 268].

This review paper focuses on three related modeling approaches (Aifantis [7], Govindjee and Simo [107], Grmela and Öttinger [113]) and attempts to classify them based on their common features and differences. The various features of these models become apparent when one views how they are obtained by extending the classical model of diffusion to incorporate time-dependence in the diffusive flux and stress-assisted diffusion. Once the relation of these models to the various extensions of classical diffusion is made clear, an attempt is then made to classify them using the general equation for the non-equilibrium reversible-irreversible coupling (GENERIC) framework developed by Grmela and Öttinger [113, 207]. This framework provides an overarching description of most of the approaches in the literature and is thus of significant value.

The first modelling approach reviewed is a subset of the diffusion model of Aifantis [7] wherein the momentum of the diffusing species is accounted for. Accounting for the momentum of the diffusing species results in a hyperbolic diffusion model, capable of describing the shock-like diffusion wave that travels through the polymer at a finite speed. The second approach is the strongly-coupled model of Govindjee and Simo [107]. This model rigorously accounts for the complex, non-linear coupled interactions between the

---

[1] The model of Kalospiros et al. [154] purports to capture all anomalous experimental observations concerning mass transfer in solids.

polymeric solid and the diffusing solvent. Their model is derived from thermodynamic principles and presented within the framework of contemporary non-linear continuum mechanics. A further attractive feature is that the numerical implementation of the model, and others with similar challenging features, within the context of the finite element method, is extensively detailed, see e.g. the works of Vijalapura et al. [267, 268, 269]. Although this model is arguably one of the more comprehensive in the literature it has received relatively little attention. The third approach reviewed is that of El Afif and Grmela [87] which is developed directly within the GENERIC framework and broadly encompasses the two aforementioned modelling approaches. The GENERIC formalism was developed as a general and thermodynamically consistent framework for systems containing both reversible and irreversible mechanisms. Two key features of the formalism are the rigorous connection between various scales of observation and the direct linkage to statistical mechanics based descriptions. The formalism therefore accommodates the underlying physics in a manner that is not always possible, or obvious, when using traditional continuum mechanics based approaches. These features of the GENERIC framework make it well suited to describing materials with microstructure and the coupling between the micro- and macro-scales. Initially the GENERIC framework was applied to problems in hydrodynamics and non-equilibrium thermodynamics (see [206] for a description of the evolution of the GENERIC framework). More recently the approach has been used as a framework for solid mechanics (Grmela [111], Hütter and Tervoort [145]) and continuum damage mechanics [144], albeit in a relatively abstract sense. Their work provides a rigorous methodology to develop models for multi-scale diffusion processes in two-component fluids wherein the polymer material is viewed as a complex fluid (i.e. a fluid with microstructure). This fluids based viewpoint is reflected in their choice of an Eulerian setting to describe coupled diffusion and deformation processes.

The structure of this paper is as follows. The notation adopted and basic concepts pertaining to non-linear continuum mechanics are presented in Section 8.2. Section 8.3 details classical and non-classical models of diffusion wherein the deformation of the diffuser is not accounted for. These classical models form the basis for the more elaborate models developed to describe coupled diffusion–deformation discussed in Section 8.4. The model of El Afif and Grmela [87], developed directly within the GENERIC framework, for describing coupled diffusion–deformation in polymers is presented in Section 8.5. The location of the models of Aifantis [7] and Govindjee and Simo [107] within this framework is made clear. In Section 8.6 we conclude.

8.2. Notation and basic concepts

The purpose of this section is to present a brief overview of aspects of non-linear continuum mechanics and to introduce the notation adopted here. Detailed expositions on non-linear continuum mechanics can be found in Gurtin [119], Ogden [202] Truesdell and Noll [259] and Ciarlet [55], amongst others.

8.2.1. Kinematics

We denote by $\Omega \subset \mathbb{R}^{n_{\text{dim}}}$, where n_{dim} refers to the space dimension, the reference placement of a continuum, as shown in Fig. 8.1, with material particles labeled $\boldsymbol{X}$. The boundary of Ω, assumed smooth, is denoted $\partial\Omega$. Let $\mathbb{I} \in \mathbb{R}_+$ denote the time domain. We denote by the bijective, orientation preserving map $\boldsymbol{\varphi}_t \; : \; \Omega \to \mathbb{R}^{n_{\text{dim}}}$ a smooth motion of the reference placement for a time $t \in \mathbb{I}$. The current placement of the body at time t associated with the motion $\boldsymbol{\varphi}$ is denoted $\mathcal{S}_t = \boldsymbol{\varphi}_t(\Omega)$, with material points designated as $\boldsymbol{x} = \boldsymbol{\varphi}(\boldsymbol{X}, t) = \boldsymbol{\varphi}_t(\boldsymbol{X}) \in \mathcal{S}_t$. Isothermal conditions are assumed and the temperature T in the continuum body is thus constant.

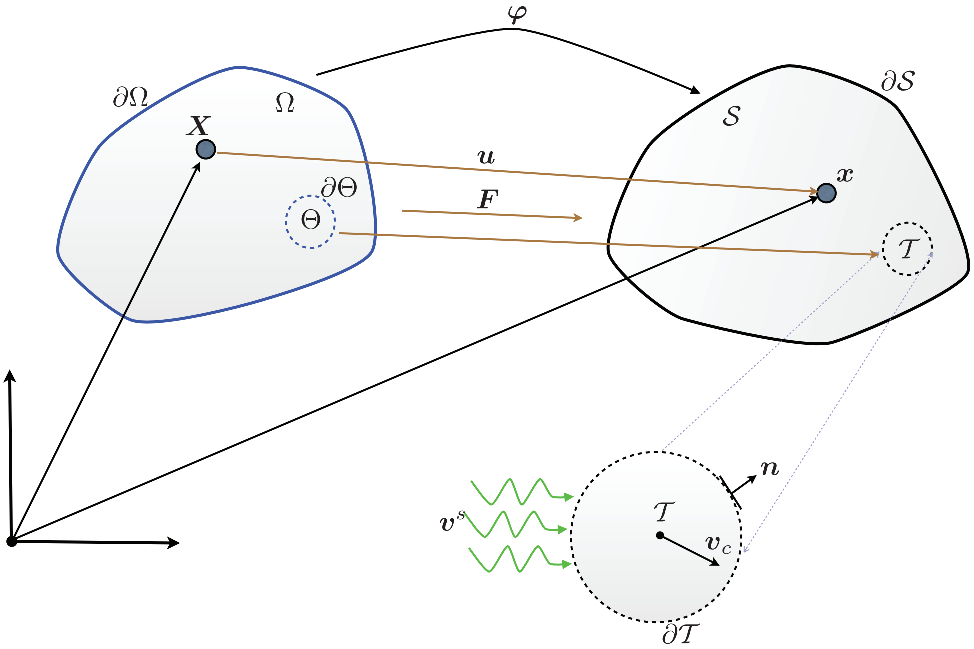

Figure 8.1.: Motion from the reference configuration Ω to the current configuration $\mathcal{S}$.

In order to derive the solvent mass balance in later sections we consider a region $\Theta \in \Omega$ with boundary $\partial\Theta$. This region is mapped via the motion $\boldsymbol{\varphi}$ to the current configuration $\mathcal{S}$ as $\mathcal{T} = \boldsymbol{\varphi}_t(\Theta)$. The boundary of $\mathcal{T}$ is denoted $\partial\mathcal{T}$ with outward normal $\boldsymbol{n}$. The velocity of the center of the region Θ is denoted $\boldsymbol{v}_c$ while the velocity of the solvent is denoted $\boldsymbol{v}^s$.

To avoid confusion, where necessary, variables pertaining to the polymeric solid and the solvent are identified with a superscript p and s, respectively. A subscript 0 is used, where necessary, to identify a variable in the reference configuration.

The deformation gradient, denoted $\boldsymbol{F}$, is defined as the derivative of the motion with respect to the reference configuration; that is,

$$\boldsymbol{F}(\boldsymbol{X}, t) = \nabla_{\text{r}} \boldsymbol{\varphi}_t(\boldsymbol{X}) \; ,$$

where $\nabla_{\mathrm{r}} \{\bullet\} := \partial \{\bullet\} / \partial \boldsymbol{X}$ is the gradient operator with respect to the reference configuration. The action of the gradient operator with respect to the current configuration is denoted $\boldsymbol{\nabla} \{\bullet\} := \partial \{\bullet\} / \partial \boldsymbol{x}$. The determinant of the deformation gradient is denoted $J(\boldsymbol{X}, t) := \det(\boldsymbol{F}(\boldsymbol{X}, t)) > 0$. The displacement at time t of a material point relative to the reference configuration is denoted $\boldsymbol{u}(\boldsymbol{X}, t) := \boldsymbol{\varphi}_t(\boldsymbol{X}) - \boldsymbol{X}$. The right Cauchy–Green tensor is defined as $\boldsymbol{C} := \boldsymbol{F}^T \cdot \boldsymbol{F}$.

8.2.2. Lagrangian and Eulerian descriptions of motion

The motion of a continuum can be described in either a Lagrangian (material) or an Eulerian (spatial) framework. In the Lagrangian description the coordinates defining the reference placement of the body are taken as independent variables, while in an Eulerian description it is the spatial coordinates that define the current placement that are the independent variables.

The material velocity $\boldsymbol{V}(\boldsymbol{X}, t)$ is defined as time derivative of the motion

$$\boldsymbol{V}(\boldsymbol{X}, t) = \frac{\partial \boldsymbol{\varphi}(\boldsymbol{X}, t)}{\partial t} = \partial_t \boldsymbol{\varphi}_t(\boldsymbol{X}) \, .$$

An Eulerian description of the motion can be obtained from the Lagrangian description by transforming the independent variables from the material coordinates to the spatial coordinates. The spatial velocity field, denoted $\boldsymbol{v}(\boldsymbol{x}, t)$, is obtained from the material velocity field as

$$\boldsymbol{v}(\boldsymbol{x}, t) = \boldsymbol{v}(\boldsymbol{\varphi}(\boldsymbol{X}, t), t) = \boldsymbol{V}(\boldsymbol{X}, t) \, .$$

The condition on the motion that $J(\boldsymbol{X}, t) > 0$ implies that the motion is invertible and hence $\boldsymbol{v} = \boldsymbol{V} \circ \boldsymbol{\varphi}^{-1}$, where $f \circ g$ denotes the composition of two functions f and g. The material time derivative of an arbitrary spatial field $\{\bullet\}(\boldsymbol{x}, t)$ is denoted

$$\dot{\overline{\{\bullet\}}} := \mathrm{d}_t \{\bullet\} + \boldsymbol{\nabla} \{\bullet\} \cdot \boldsymbol{v} \, ,$$

where $\mathrm{d}_t \{\bullet\}$ denotes the time derivative of the spatial field keeping $\boldsymbol{x}$ constant. Here, a superposed dot will often be used to designate both the material time derivative of a spatial field and the time derivative of a material field. Thus, for a Lagrangian variable $\{\bullet\}(\boldsymbol{X}, t)$ the notation $\partial_t \{\bullet\}$ and $\dot{\overline{\{\bullet\}}}$ is equivalent.

8.2.3. Stress measures

The symmetric Cauchy stress tensor, denoted $\boldsymbol{\sigma}$ and defined on the current placement, is the fundamental measure of stress. The Cauchy stress tensor is defined by the relationship $\boldsymbol{\sigma} \cdot \boldsymbol{n} = \boldsymbol{t}^n$, where $\boldsymbol{n}$ is the outward unit normal vector to an arbitrary surface Γ^n at a point $\boldsymbol{x}$ in the current configuration $\mathcal{S}$, and $\boldsymbol{t}^n$ is the traction force per unit area of Γ^n.

The non-symmetric nominal stress tensor, denoted $\boldsymbol{P}$, is defined on the reference configuration as $\boldsymbol{P} \cdot \boldsymbol{N} = \boldsymbol{t}^N$, where $\boldsymbol{N}$ is the outward unit normal to the arbitrary plane Γ^N

in the reference configuration, and $\boldsymbol{t}^N$ is the traction expressed as a force per unit area of Γ^N.

The second Piola–Kirchhoff stress tensor $\boldsymbol{S}$ is a symmetric Lagrangian quantity defined by $\boldsymbol{S} = \boldsymbol{F}^{-1} \cdot \boldsymbol{P}$.

8.2.4. Conservation of solvent mass

The concentration of a solvent and polymer mixture, denoted c, is defined here as the amount of substance (i.e. the number moles) per volume of mixture. The units of c are thus $\frac{\mathrm{mol}}{\mathrm{m}^3}$. The mass density of the solvent, denoted ρ^s, is defined here as the mass of the solvent per volume of mixture and has units of $\frac{\mathrm{kg}}{\mathrm{m}^3}$. The mass density is related to the concentration as $\rho^s = Mc$ where M is the molar mass of the solvent with units of $\frac{\mathrm{kg}}{\mathrm{mol}}$.

8.3. Mathematical modelling of diffusion

The classical equations governing Fickian diffusion [94] are parabolic and ignore the influence of external stresses on the diffusion process. These two shortcomings are essential to address in order to accurately predict the coupled diffusion–deformation processes that occur in case II diffusion. Various alternative models of diffusion, or related physical phenomena, have been proposed in the literature to remedy such shortcomings. These models predate their more recent adoption to describe case II diffusion.

The objective of this section is to describe the classical model of diffusion and the various adaptations thereof pertinent to coupled non-classical diffusion–deformation processes.

8.3.1. Fickian diffusion

The tenet upon which almost all models for describing case II type diffusion are based is the classical model of Fickian diffusion [94]. Within this description, or more specifically according to Fick's first law, the mass flux of solvent $\boldsymbol{h}^\rho$ (resp. the diffusion flux $\boldsymbol{h}^c$) in an ideal solution is assumed proportional to the gradient of the mass density of the solvent ρ^s (resp. the gradient of the concentration of the solvent c) as

$$\boldsymbol{h}^\rho = -\boldsymbol{D}^\rho \cdot \boldsymbol{\nabla} \rho^s \quad \text{or} \quad \boldsymbol{h}^c = -\boldsymbol{D}^c \cdot \boldsymbol{\nabla} c\,, \tag{8.3.1}$$

where $\boldsymbol{D}$ is the positive-definite diffusivity tensor (i.e. $\boldsymbol{a} \cdot \boldsymbol{D} \cdot \boldsymbol{a} \geq 0 \ \forall\ \boldsymbol{a}$, where $\boldsymbol{a}$ is an arbitrary first-order tensor). Following Govindjee and Simo [107], we define the term "density" to refer to the constituent mass divided by the mixture volume in the limit as the volume goes to zero. We shall restrict attention to isotropic diffusion where $\boldsymbol{D} = D\boldsymbol{I}$ for $D > 0$ and $\boldsymbol{I}$ is the second-order identity tensor. For non-ideal mixtures, the driving force for mixing is the gradient of the chemical potential μ. Fick's first law in Eq. (8.3.1) can be restated as a function of the chemical potential μ (Crank [66]) as

$$\boldsymbol{h}^{\rho} = -B^{\rho}(\rho^{s})\rho^{s}\boldsymbol{\nabla}\mu \quad \text{or} \quad \boldsymbol{h}^{c} = -B^{c}(c)c\boldsymbol{\nabla}\mu\,, \tag{8.3.2}$$

where $B^{\{\bullet\}} \geq 0$ is the, potentially solvent density (resp. concentration) dependent, mobility. The relation in Eq. (8.3.2) can be recast in terms of variables in the reference placement Ω as

$$\boldsymbol{H} = -B^{\rho}(\rho_{0}^{s})\rho_{0}^{s}\boldsymbol{C}^{-1}\cdot\nabla_{\mathrm{r}}\mu\,, \tag{8.3.3}$$

where the pull back of the relative liquid flux $\boldsymbol{H} := J\boldsymbol{F}^{-1}\cdot\boldsymbol{h}^{\rho}$ and the liquid density in the current configuration ρ^{s} is related to the nominal liquid density ρ_{0}^{s} as $\rho_{0}^{s} = \rho^{s}J$. Here and henceforth we shall only distinguish between the mass flux and the concentration flux where necessary.

The classical linear model of Fickian diffusion has been extended to the non-linear regime to account for non-classical effects. For example, Crank [65] introduced the notion of history-dependent diffusion to account for non-Fickian diffusion. This dependence was accounted for by assuming the diffusivity to be a non-linear function of the solvent concentration c. Models of this form are, however, not capable of describing the sharp propagating front that is characteristic of case II diffusion.

The next key step in the development of a diffusion model is the relationship between the time rate of change of the solvent density and the solvent mass flux obtained from the statement of the conservation of solvent mass. The large deformation exhibited by the polymer structure during case II diffusion makes the distinction between the reference and deformed configurations critical. The well-developed tools of non-linear continuum mechanics are ideally suited to describe such finite material deformations. With this in mind, following the approach of Govindjee and Simo [107], a Lagrangian representation of the conservation principle is the most natural setting. With the exception of Govindjee and Simo [107] the vast majority of models for coupled case II diffusion–deformation are restricted to infinitesimal deformations. The assumption of infinitesimal deformations appears overly restrictive when one considers the large deformations that occur during case II diffusion. Indeed, with the exception of the aforementioned model, the majority of models are furthermore restricted to one space dimension.

Consider the region $\mathcal{T}$ in the current placement $\mathcal{S}$ as depicted in Fig. 8.1. The region is open to the solvent. The conservation of liquid mass over the region $\mathcal{T}$ with boundary $\partial\mathcal{T}$ and outward normal $\boldsymbol{n}$ is given by

$$\frac{\partial}{\partial t}\int_{\mathcal{T}}\rho^{s}\,\mathrm{d}x = -\int_{\partial\mathcal{T}}\rho^{s}\left[\boldsymbol{v}^{s}-\boldsymbol{v}_{c}\right]\cdot\boldsymbol{n}\,\mathrm{d}\gamma\,, \tag{8.3.4}$$

where $\boldsymbol{v}^{s}$ is the velocity of the solvent and $\boldsymbol{v}_{c}$ is the velocity of the control volume. The expression for the conservation of solvent mass in Eq. (8.3.4) in the reference configuration (i.e. the Lagrangian representation) is obtained by transforming the domain of integration to the reference configuration Ω, pulling back all variables from the current to the reference configuration, applying the divergence theorem to the term involving the boundary integral, and finally applying the localization theorem to obtain

$$\dot{\rho}_0^s(\boldsymbol{X}, t) = -\mathrm{Div}\boldsymbol{H}\,, \tag{8.3.5}$$

where the divergence operator with respect to the reference configuration is defined as $\mathrm{Div}\,\{\bullet\} := \nabla_{\mathrm{r}} \cdot \{\bullet\}$. This is the Lagrangian expression of Fick's second law. Note, the procedure to derive the conservation relation in terms of the concentration c follows from substituting c for ρ^s in Eq. (8.3.4).

The localized expression for the conservation of solvent mass in Eq. (8.3.4) in the current configuration (i.e. the Eulerian representation) is obtained by applying the divergence theorem to the boundary term, and then applying Reynold's transport theorem to the term involving the time derivative to obtain

$$\mathrm{d}_t\rho^s = -\mathrm{div}\,\underbrace{(\rho^s\boldsymbol{v}^s)}_{\boldsymbol{h}^\rho}\,, \tag{8.3.6}$$

where the divergence operator with respect to the current configuration is defined as $\mathrm{div}\,\{\bullet\} := \boldsymbol{\nabla} \cdot \{\bullet\}$. This is the Eulerian expression of Fick's second law and is widely adopted in the literature on non-Fickian diffusion.

Substitution of Fick's first law given in Eq. (8.3.1) into his second gives the parabolic equation predicting the diffusion of a solvent. It is important to recall at this point that case II diffusion is characterized by a sharp front moving at a constant velocity through the polymeric solid. This type of behavior is characteristic of a system that can exhibit a hyperbolic-like response. It is thus clear that additional time-dependent relations need to be incorporated into the diffusion flux expression to account for the finite rate at which the polymeric solid responds to the diffusing solvent.

Irrespective as to the choice of framework, the feature that distinguishes the various models of diffusion is the constitutive relation of the flux $\boldsymbol{h}$ to the solvent density ρ^s or, respectively, the chemical potential μ.

Many of the more macroscopic models developed in the literature assume the diffusivity D to be a function of the solvent density ρ^s, resp. the chemical potential μ (this loose definition of macroscopic will be clarified in due course and is described in detail by El Afif and Grmela [87]). This form of dependence has been studied extensively, see e.g. Crank [66] and references therein. In short, the more microscopic the point of view, the fewer the assumptions on the form of the material parameters.

Furthermore, in order to couple the response of the polymeric solid to the diffusing solvent the chemical potential μ is often assumed to be a function of the solvent concentration c and the volumetric deformation of the polymer or osmotic pressure. The models of Thomas and Windle [254, 255, 256], Cohen [58], Durning [79], Hui and Wu [139, 140], Cohen and White [59], Wu and Peppas [279], Govindjee and Simo [107], Rossi et al. [229], Friedman and Rossi [102], Vijalapura and Govindjee [267, 268], amongst others, adopt a model of diffusion of this form.

8.3.2. Hyperbolic diffusion models

As stated in the preceding discussion, the equations governing classical Fickian diffusion are parabolic. Hence, disturbances are propagated instantaneously throughout the domain. An infinite speed of disturbance propagation is physically unrealistic. This description is clearly inadequate when attempting to address phenomena observed during case II diffusion where a sharp front propagates at a finite speed through the medium.

Aifantis [7] addresses this shortcoming of the classical Fickian model of diffusion by developing a diffusion theory based on the conservation of momentum of the diffusing species. Specialization of his broader theory (which includes solvents with viscosity and memory, non-local effects and stress-assisted diffusion) to the case of pure diffusion results in an evolution relationship for the diffusion flux given by

$$\mathrm{d}_t \boldsymbol{h}^c + \alpha(c)\boldsymbol{h}^c = -\alpha(c) D^c(c) \boldsymbol{\nabla} c \,, \tag{8.3.7}$$

where the positive parameter α is a function of the solvent concentration. Equation (8.3.7) represents the classical Fickian diffusion relation in Eq. $(8.3.2)_2$ for $\alpha >> 1$ (i.e. if one can disregard the contribution of the term involving the time derivative of the diffusion flux). [185] originally included the time derivative term when developing the equations governing heat conduction from the classical kinetic theory of gases but subsequently discarded it as he viewed the contribution as insignificant. A hyperbolic diffusion model developed by Kalospiros et al. [154] captures many of the key phenomena that characterize case II diffusion. The relative importance of the temporal term is made clear in the framework of El Afif and Grmela [87] presented in Section 8.5. This modified diffusion equation is hyperbolic thereby implying that a disturbance propagates at a finite speed.

The one limitation of adopting a hyperbolic model for case II diffusion is that no experimental evidence of the reflection of concentration waves exists, see e.g. Kalospiros et al. [154]. This limitation was recognized by Kalospiros et al. [154] but no steps were taken to remedy this shortcoming.

It is worth recalling that the structure of the equations governing diffusion are identical to Fourier's law governing heat conduction. In a phenomenon similar to the propagation of the diffusing species in a wave-like manner in case II diffusion, heat can propagate as a thermal wave in fluids [211, 212, 209] and solids [5, 6, 146, 193]; a phenomena known as second sound. It is thus not surprising that an equation corresponding to Eq. (8.3.7) was developed independently by [51] and [265] for non-standard heat conduction phenomena.

8.4. Coupled diffusion–deformation models

The influence of external stresses on the diffusing solvent in a rigid body was considered in detail by Aifantis and co-workers [7, 261, 278], amongst others.

The deformation of the polymeric solid due to the influence of the solvent is captured to varying degrees by certain of the models proposed in the literature. In the weakly-coupled diffusion–deformation models the balance of linear momentum of the polymeric solid does not directly enter into the governing system of equations. Rather, the influence of the solid on the diffusion process is accounted for by an additional stress-dependent term in the diffusion flux. By contrast, strongly-coupled diffusion–deformation models directly account for the balance of linear momentum of the polymeric solid and the coupling with the diffusion process.

This classification of models is somewhat incomplete as it does not consider the form of the free energy of mixing and, more specifically, if the assumption of full swelling (perfect mixing) has been made. The full-swelling assumption implies that the volume of the solvent–polymer system is equal to the volume of the dry polymer plus the volume of the solvent. The seminal work of Govindjee and co-workers [107, 267] clearly shows that this assumption implies a simple relation between the Jacobian J of the deformation $\boldsymbol{\varphi}$ and the concentration c, and hence violates the independence of the primary field variables. Under certain conditions it is acceptable to assume full swelling (e.g. when modelling the free-swelling of polyelectrolyte gels [135, 134]); case II diffusion, however, is clearly not such a situation.

A further factor that distinguishes the various models is the manner in which the response of the solid is described. The vast majority of the publications in the literature on case II diffusion adopt a rheological model for the solid as opposed to a continuum solids description. These rheological models are typically formulated within an Eulerian framework as is typical in the models of fluid mechanics. The Eulerian framework is not, however, well suited to describing the complex finite deformations that the polymeric solid undergoes [239]. This limitation of the Eulerian description is not obviously apparent as the these models assume the deformation to be infinitesimal. An exception is the Lagrangian model of [107] wherein finite deformations are rigorously accounted for.

The objective of this section is to classify several widely adopted and/or significant models of case II diffusion in the literature according to their deformation–diffusion coupling and, if applicable, the assumption made concerning the form of the free energy of mixing.

8.4.1. Weakly-coupled diffusion–deformation models

Weakly-coupled models of diffusion and deformation do not directly account for the deformation of the polymeric solid. The rate limiting influence of the solid on the diffusion process is, however, accounted for.

Stress-assisted diffusion

The weakly-coupled diffusion–deformation models generally take as their point of departure a simple model of stress-assisted diffusion due to [64]. In the one-dimensional context that is the setting of the majority of models of case II diffusion the modified equation for the diffusion flux becomes

$$h^c = -D^c c' - E\sigma' \,, \tag{8.4.1}$$

where E is the elastic diffusion coefficient, σ is the external stress, and $\{\bullet\}'$ denotes the spatial gradient of an arbitrary variable in one space dimension.[2] The first term on the right-hand side of Eq. (8.4.1) is the standard diffusive component (see Eq. $(8.3.1)_2$) and the second term accounts for the influence of the stress field in the polymer on the diffusion process. In higher dimensions, [64] equates σ to the trace of the stress in the solid. Thus, the stress affects diffusion only through its hydrostatic component.

Aifantis and co-workers [7, 261, 278] developed a general theory of stress-assisted diffusion that rigorously accounts for the influence of the stress in the solid on the diffusion process. The theory encompasses a host of other stress-assisted diffusion theories in the literature. Furthermore, the theory can account for the effect of stress gradients on diffusion and the non-linear dependence of the diffusion process on the stress.

More recently, Zohdi and Wriggers [285] investigated the effect of micro-stress on diffusion processes in highly heterogeneous material using computational homogenization.

The approach of Thomas and Windle [254, 255, 256]

Thomas and Windle [254, 255, 256] developed a model for case II diffusion based on their experimental investigations [252, 253]. The diffusion flux $\boldsymbol{h}^c$ is assumed proportional to the gradient of the chemical potential μ, in the spirit of Eq. $(8.3.2)_2$. A key feature of their pioneering model is the dependence of the chemical potential μ of the solvent on the solvent concentration c and the osmotic pressure, expressed in terms of a viscous model (the reader is referred to Hui and Wu [139, 140], De Kee [74] for additional details and illuminating comparisons with alternative models). Thus, their model recognizes the central role that the relaxation of the polymeric material plays in controlling the diffusion process. The solvent-induced osmotic pressure causes swelling to occur which, in turn, creates additional space for the solvent molecules. The solvent causes the polymer to transform from a glassy to a rubber-like state: a process termed plasticization. The polymer deformation is assumed proportional to the solvent concentration c, hence the label of a weakly-coupled model. The rate at which the solvent diffuses is controlled by the relaxation rate of the polymer. Thus, the time-dependence in the diffusion flux relation is dictated by the indirect dependence of the chemical potential μ on the osmotic pressure, which in turn is dependent on the swelling and hence the relaxation rate of the solid. This form of time-dependence in the diffusion flux $\boldsymbol{h}^c$ should be contrasted with the more direct dependence exhibited by the model proposed by Aifantis [7] (see Eq. (8.3.7)).

The model of Thomas and Windle [254, 255, 256] has several limitations, see e.g. Durning [79] and Jou et al. [153]. The model cannot differentiate between the solvent induced osmotic pressure and the stresses that develop in the polymer. The simple viscous model is also unable to describe the general response of the polymeric solid and is restricted to one space dimension. Moreover, their model under- and overestimates the swelling rate

---

[2] We adopt here the sign convention widely used in the fluid mechanics literature wherein a compressive stress is defined as positive. Aifantis [7] adopts a sign convention standard in solid mechanics wherein a tensile stress is defined as positive.

if the mass fraction is very low, respectively very high, see e.g. Hui and Wu [139, 140], Jou et al. [153]. Finally, the model is unable to account for the Fickian precursor in the glassy region ahead of the moving front.

Various phenomenological models have been presented to extend the Thomas and Windle [253] model. The model of Durning [79] was developed to describe non-Fickian diffusion in viscoelastic polymeric fluids subject to a small driving force and contains many features present in the Thomas and Windle [253] model. The gradient of the osmotic pressure is included in the driving force leading to a third-order linear partial differential equation for the solvent concentration distribution. Variations of this approach are found in Durning and Tabor [80] and Fu and Durning [103]. The model of Qian and Taylor [222] accounts for the Fickian precursor in the glassy region ahead of the moving front. This model addresses some shortcomings of the phenomenological model proposed by Rossi and co-workers [229, 102] that also accounts for diffusion in the glassy region. The model proposed by Rossi and co-workers is founded on the belief that two distinct process govern case II diffusion. Firstly, the solvent transport is governed by Fick's law. The second governing process is the transition from the glassy to the rubber-like state. Rossi et al. [229] adopt a simple phenomenological model that only accounts for the reversal of the glassy state but does not consider non-Fickian behavior and the influence of macroscopic stresses. Their model shares many features with the one of Astarita and Sarti [18].

The approach of Cohen et al. [58, 59]

The aforementioned inability of the model of Thomas and Windle [256] to describe the state of deformation in the polymeric solid was addressed, to a limited degree, by Cohen et al. [58, 59, 60]. Following an approach identical to that used in models of stress-assisted diffusion in one dimension (see Section 8.4.1), the diffusion flux h^c is defined as in Eq. (8.4.1).

The time-dependence in the diffusion flux relation is achieved in an indirect manner by choosing a viscoelastic evolution relation for the external stress σ. The general constitutive relation for a standard viscoelastic solid in one dimension, as depicted in Fig. 8.2(a), is given by Simo [240] as

$$\sigma = \underbrace{[E_\infty + E]}_{E_0}\,\varepsilon - E\alpha\,, \qquad \textit{where}\ \dot{\alpha} + \frac{\alpha}{\tau} = \frac{\varepsilon}{\tau}\,, \tag{8.4.2}$$

E_∞ and E are spring constants and $\tau = \eta/E$ is the relaxation time, where η is the viscosity of the dashpot. The simple choice made by Cohen and White [59] to describe the response of the solid is based on the Maxwell model obtained by setting $E_\infty = 0$ in Eq. (8.4.2) as depicted in Fig. 8.2(b), rewriting the resulting relation in terms of the stress σ, and assuming the deformation to be a linear function of the concentration to obtain

$$\mathrm{d}_t\sigma + \frac{\sigma}{\tau(c)} = \mathcal{F}c\,, \tag{8.4.3}$$

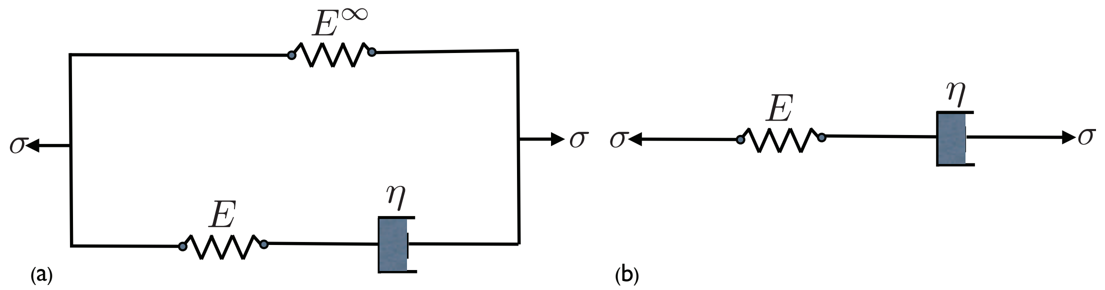

Figure 8.2.: One-dimensional representation of (a) a standard solid and (b) a Maxwell solid. When modelling case II diffusion in polymers, the viscosity η may depend on the solvent concentration c, see e.g. Govindjee and Simo [107].

where is $\mathcal{F}$ a proportionality constant. The deformation can therefore not be viewed as an independent variable.

The key feature of the Cohen and White [59] model is that the relaxation time τ is dependent upon the concentration c, thereby allowing for the significant change in relaxation time as the polymer transforms from a glassy medium to a rubber-like one.

The model proposed by Cohen and White [59] can be recast into one in which the chemical potential μ is a function of the solvent concentration c and the external stress σ (Wu and Peppas [279]), as is the case for the Thomas and Windle [253] model. Starting from Eq. $(8.3.2)_2$, applying the chain rule, and assuming that the stress driving the diffusion process is a linear function of the Jacobian J of the deformation $\boldsymbol{\varphi}$ in the polymer, one obtains

$$\begin{aligned} h^c &= -B^c c\mu'(c,\sigma) \\ &= -B^c c\left[\frac{\partial\mu}{\partial c}\frac{\partial c}{\partial x} + \frac{\partial\mu}{\partial\sigma}\frac{\partial\sigma}{\partial x}\right] \\ &= -D^c(c)c' - E(c)\sigma' \,, \end{aligned} \tag{8.4.4}$$

which is the one-dimensional stress-assisted diffusion relation given in Eq. (8.4.1).

Riviére and Shaw [227] have recently presented a discontinuous Galerkin finite element approximation and an analysis of a simplified version of the Cohen and White [59] model.

8.4.2. Strongly-coupled diffusion–deformation models

Strongly-coupled models of diffusion and deformation directly account for the deformation of the polymeric solid due to the diffusion of the solvent and the rate limiting influence of the solid on the diffusion process.

The approach of Wu and Peppas [279]

Wu and Peppas [279] presented an extension of the weakly-coupled model proposed by Durning [79]. General information about the continuum thermodynamical setting of case II diffusion can be found in the contribution by [180]. One of the primary developments was the introduction of a momentum balance equation to describe the response of the polymer and thereby to account for polymer swelling. The approach is, significantly, limited to one dimension, small deformations, and perfect mixing.

The theory of [97] and [138], which assumes perfect mixing, is used to express the solvent activity as a function of the penetrant volume fraction. As mentioned previously, the perfect mixing assumption implies a simple relationship between the Jacobian J of the deformation $\boldsymbol{\varphi}$ and the concentration c, thereby violating the independence of the primary fields [107]. Thus, while the model of Wu and Peppas [279] is classified as strongly-coupled, the coupling is trivialized due to the perfect mixing assumption [267]. The work of Vijalapura and Govindjee [267] identifies further shortcomings of the Wu and Peppas [279] model and the proposed numerical solution procedure.

The diffusion flux relation adopted by Wu and Peppas [279] is expressed in the form of Eq. (8.3.2) where the chemical potential μ is a function of the solvent activity and the swelling pressure p due to osmosis. The swelling pressure provides the mechanism to couple the polymeric solid's response to the presence of the solvent. The one-dimensional expression for the balance of linear momentum takes the form

$$\sigma' - p' = 0\,, \tag{8.4.5}$$

where σ is the stress in the polymer. This relation for the gradient of the swelling pressure is then substituted into the expression for the diffusional flux $\boldsymbol{h}$ in Eq. $(8.3.2)_1$. The diffusional flux is thus proportional to the gradient of the stress in the polymer.

The response of the polymer is assumed to be viscoelastic and a simple Maxwell model is adopted. For a comprehensive account of the theory of viscoelasticity in solids, the reader is referred to [240]. The viscosity of the dashpot is chosen to be an exponential function of the solvent concentration c to account for the dependence of the relaxation of the polymer on the solvent concentration c and thus the significant differences between the glass- and rubber-like states of the polymer.

The model of Govindjee and Simo [107]

Govindjee and Simo [107] presented a truly strongly-coupled model of diffusion and deformation in the same year that Wu and Peppas [279] published their model. The model shares various features with the Wu and Peppas [279] model: a system of coupled partial differential equations describe the evolution of the polymer and the diffusion of the solvent. The model of Govindjee and Simo [107] is, however, more advanced in several aspects. Firstly, the complete theory is carefully derived from classical thermodynamic principles. The macroscopic formulation is based on microscopic considerations that are reflected in the construction of the free energies. Furthermore, and importantly, the Flory–Huggins mixing model is deemed inapplicable as it assumes full equilibrium swelling. In part, this choice is due to the fact that Govindjee and Simo [107] do not assume additivity of solvent and polymers volumes. For this reason, an extension of the model to the transient regime as proposed by Hildebrand [131] is adopted. The Govindjee and Simo [107] model is also developed for a three-dimensional system and assumes that the polymer undergoes a finite deformation. The final distinguishing feature of this model is that it assumes that the polymer response is that of a standard solid [182, 240] as opposed to the simplified rheological Maxwell model adopted by Wu and Peppas [279].

The model of Govindjee and Simo [107] has been extended and elaborated on in a series of later works, Vijalapura and Govindjee [267, 268, 269]. Vijalapura and Govindjee [267] specialized the original model to one space dimension to elucidate various key features and to facilitate a direct comparison with the model of Wu and Peppas [279]. A considerable amount of attention is dedicated to detailing a robust adaptive scheme for the temporal integration and solution of the highly non-linear governing equations. The other two works [269, 268] consider algorithmic, and algorithmic and modelling issues respectively. The interested reader is also referred to the online discussion [137] for a comparison with models for polyelectrolyte gels [135, 134].

Govindjee and Simo [107] consider the balance of linear momentum for the solvent–polymer system, in the absence of inertial and body forces, given by

$$\mathrm{Div}\,(\boldsymbol{F}\cdot\boldsymbol{S}) = \boldsymbol{0}\,,$$

where $\boldsymbol{S}$ is the symmetric second Piola–Kirchhoff stress tensor as defined in Section 8.2.

A Lagrangian description for the solvent mass balance, as presented in Section 8.3.1 (see Eqs. (8.3.3) and (8.3.5)), is used. The mobility B^ρ is here a function of the chemical potential μ.

Standard thermodynamic arguments, see e.g. [61], are used to derive the constitutive relations for the second Piola–Kirchhoff stress $\boldsymbol{S}$ and the chemical potential μ. The expression for the balance of internal energy, denoted U, is obtained directly from the first law of thermodynamics. The time rate of change of the internal energy in the open region $\mathcal{T} \in \mathcal{S}$ (see Fig. 8.1) is equated to the body force power plus the total traction power on the boundary less the liquid enthalpy leaving the domain. The resulting expression for the balance of internal energy is given by

$$\rho_0^p \dot{U} = \tfrac{1}{2}\boldsymbol{S} : \dot{\boldsymbol{C}} - \nabla_{\mathrm{r}}\,(h\circ\boldsymbol{\varphi})\cdot\boldsymbol{H} + [h\circ\boldsymbol{\varphi}]\,\dot{\rho}_0^s\,, \tag{8.4.6}$$

where $\boldsymbol{C} := \boldsymbol{F}^T\cdot\boldsymbol{F}$ is the right Cauchy–Green strain tensor and h is the solvent enthalpy per unit mass of solvent. Using the global statement of the balance of total entropy of the mixture per unit mass of solid s given by $\int_{\mathcal{T}} \rho^p s \ \mathrm{d}x \geq -\int_{\partial\mathcal{T}} s^s \boldsymbol{h}^\rho \cdot \boldsymbol{n} \ \mathrm{d}\gamma$, where s^s is the solvent entropy per unit mass of solvent, the definition of the rate of change of internal energy U given in Eq. (8.4.6), and standard thermodynamic arguments, the local balance of entropy inequality is obtained as

$$\rho_0^p \dot{S} + \nabla_{\mathrm{r}}\,(s^s\circ\boldsymbol{\varphi})\cdot\boldsymbol{H} - [s^s\circ\boldsymbol{\varphi}]\,\dot{\rho}_0^s \geq 0\,, \tag{8.4.7}$$

where $S = s \circ \boldsymbol{\varphi}$. The entropy S in Eq. (8.4.7) is then rewritten in terms of the Helmholtz free energy of the mixture per unit mass of solid defined as $\Psi := U - TS$ and the internal energy U

$$-\rho_0^p \dot{\Psi} + \tfrac{1}{2}\boldsymbol{S} : \dot{\boldsymbol{C}} + [\mu \circ \boldsymbol{\varphi}]\, \dot{\rho}_0^s - \nabla_{\mathrm{r}} (\mu \circ \boldsymbol{\varphi}) \cdot \boldsymbol{H} \geq 0\,, \tag{8.4.8}$$

where the chemical potential of the liquid is defined as $\mu := h - Ts^s$ with T being the temperature.

The next key step in the derivation of the constitutive relations for the stress $\boldsymbol{S}$ and the chemical potential μ is the description of the polymeric solid (in both the glass and rubber-like states) as a viscoelastic material, and more specifically, as a standard solid [182, 240] (the one-dimensional representation of a standard solid is shown in Fig. 8.2). As in the model of Wu and Peppas [279], the viscosity of the polymer is assumed to be concentration dependent to describe the glass–rubber transition.

The Helmholtz free energy Ψ in Eq. (8.4.8) is chosen to be composed of two parts

$$\begin{aligned} \Psi &= \bar{\Psi}(\boldsymbol{C}, \boldsymbol{\Gamma}) + \Psi^M(\rho_0^s, J) \\ &= \underbrace{\Psi^R(\boldsymbol{C}) + \Psi^\Gamma(\boldsymbol{C}, \boldsymbol{\Gamma})}_{\bar{\Psi}(\boldsymbol{C},\boldsymbol{\Gamma})} + \Psi^M(\rho_0^s, J)\,, \end{aligned} \tag{8.4.9}$$

where $\bar{\Psi}$ is the internal free energy of the polymer, $\boldsymbol{\Gamma}$ is a tensorial internal variable dependent on the deformation via the Cauchy–Green tensor $\boldsymbol{C}$ and the concentration history, Ψ^M is the free energy of mixing, Ψ^R is the free energy for the rubber-like material and Ψ^Γ represents the free energy due to non-equilibrium effects.

Substituting the expression for the free energy in Eq. (8.4.9) into the reduced entropy inequality given by Eq. (8.4.8) and applying standard thermodynamic arguments one obtains the following constitutive relations for the second Piola–Kirchhoff stress $\boldsymbol{S}$ and chemical potential μ:

$$\boldsymbol{S} = 2\rho_0^p \frac{\partial \Psi^R}{\partial \boldsymbol{C}} + \boldsymbol{Q} + \rho_0^p J \frac{\partial \Psi^M}{\partial J} \boldsymbol{C}^{-1}\,, \tag{8.4.10}$$

$$\mu \circ \boldsymbol{\varphi} = \rho_o^p \frac{\partial \Psi^M}{\partial \rho_0^s}\,, \tag{8.4.11}$$

where the non-equilibrium stress $\boldsymbol{Q} := -\partial \Psi^\Gamma / \partial \boldsymbol{\Gamma}$. The reduced entropy inequality given in Eq. (8.4.8) becomes

$$\underbrace{\rho_0^p \boldsymbol{Q} : \dot{\boldsymbol{\Gamma}}}_{\text{history term}} \underbrace{- \nabla_{\mathrm{r}} (\mu \circ \boldsymbol{\varphi}) \cdot \boldsymbol{H}}_{\text{diffusion term}} \geq 0\,. \tag{8.4.12}$$

The evolution equation for the history variable is chosen to be of the form

$$\dot{\boldsymbol{\Gamma}} = \mathbb{F}(\boldsymbol{C}, \boldsymbol{\Gamma}, \rho_0^s) : \boldsymbol{Q}\,,$$

where $\mathbb{F}$ is the fourth-order positive definite fluidity tensor.

By analogy with the viscoelastic model for a standard solid, the expression for the non-equilibrium stress [240] is chosen as

$$\boldsymbol{Q}(t) = \int_{-\infty}^{t} \beta \exp\left(\frac{-\xi(t) - \xi(s)}{\tau_0} \right) \frac{\partial}{\partial s} \left[2\rho_0^p \frac{\partial \Psi^R}{\partial \boldsymbol{C}} \right] \mathrm{d}s$$

where β is the ratio of the glassy modulus to the rubber modulus,

$$\xi(t) = \int_{-\infty}^{t} \frac{1}{a(f)} \, \mathrm{d}s \quad \text{where} \quad a = \exp\left(\frac{B_D \left[f - f_0 \right]}{2.303 f f_0} \right) ,$$

and B_D is an empirical constant of the order of unity. The variable f denotes the available free volume. The glass–rubber transition is accounted for by defining the relaxation time to be a function of the available free volume as $\tau = \frac{\tau|_{t=0}}{a(f)}$, where the notation $g\left(\bullet, t\right)|_{t=0}$ refers to a function $g\left(\bullet, t\right)$ evaluated in the initial state of the solvent-free polymer.

The final ingredient in resolving the constitutive relations is the definition of the free energy of mixing Ψ^M. A key contribution of Govindjee and Simo [107] is the use of the extension of the Flory–Huggins model proposed by Hildebrand [131]. With this in hand, the free energy of mixing becomes

$$\begin{aligned} \Psi^M &= H^M - T S^M \\ &= \underbrace{k T \chi_{FH} \left[1 - f_0 \right] \frac{\rho_0^s \kappa}{m_2 \rho_0^p}}_{H^M} \\ &\quad + T \underbrace{k \left[\frac{\rho_0^s}{\rho_0^p m_1} \ln\left(\frac{1 - f_*}{f_*} \left[\frac{\rho_0^p}{\rho_0^s \kappa} h - 1 \right] \right) + \frac{1}{m_2} \ln\left(\frac{1 - f_0}{f_0} \left[h - \frac{\rho_0^s}{\rho_0^p} \kappa \right] \right) \right]}_{S^M} , \end{aligned} \qquad (8.4.13)$$

where H^M is the heat of mixing per unit mass of polymer, k is the Boltzmann constant, S^M is the entropy of mixing, f_* is the initial free volume of the pure solvent, m_1 is the mass of a single solvent molecule, m_2 is the mass of an individual polymer chain, $h = h(J) := \frac{J}{1-f_0} - 1$ and κ is a function of m_1, m_2 and the hard-core volume of the species (Govindjee and Simo [107]). Importantly, the free energy of mixing Ψ^M is a function of both the deformation and the solvent mass density. Note that whereas the entropy of mixing S^M does not depend on the polymer's relaxational state, the heat of mixing H^M in reality is history-dependent. However, this contribution is very small and therefore neglected by Govindjee and Simo [107].

The final step in the development of the model is to rewrite the constitutive relation for the chemical potential μ given in Eq. (8.4.11) in terms of the activity using a non-linear transformation. This critical step is required for three reasons, cf. Govindjee and Simo [107], Vijalapura and Govindjee [267, 268]. Firstly, the reformulation of the governing equations in terms of the activity circumvents a singularity that arises in the solvent free polymer system. Secondly, the physically relevant diffusion boundary conditions are expressed in terms of the activity and the flux given in terms of the gradient of the activity (or equivalently the chemical potential μ). The final benefit is that the reformulation circumvents the prohibitive continuity requirements on the displacement field $\boldsymbol{u}$. These continuity requirements would dictate the use of C^1 interpolation functions for the displacement field (the class C^1 consists of all differentiable functions whose derivatives are continuous) or alternative non-standard strategies if the finite element method is used to approximate the governing equations. Due to the reformulation, the mobility B^ρ is now a function of the activity and the Jacobian determinant J.

The later work of Vijalapura and Govindjee [268] extends the model of Govindjee and Simo [107] presented above in various ways. The mobility coefficient B^ρ is assumed, as before, to be dependent on the activity and the Jacobian determinant J, and an additional dependence on the concentration of reacted sites is included. This feature of the model accounts for the addition of a reactant to the solvent. An evolution law for the concentration of the reacted sites is included in the governing equations.

8.5. The GENERIC framework of Grmela and Öttinger [113, 207]

The GENERIC framework developed by Grmela and Öttinger [113, 207] constitutes a methodology to predict the macroscopic time evolution of systems based on mesoscopic levels of description [112]. The GENERIC framework represents an extension of the standard mesoscopic equilibrium thermodynamics description to account for non-equilibrium reversible–irreversible coupling. The key motivation for the framework is to describe the mixing behavior of simple and complex fluids (that is, fluids with microstructure, such as polymeric fluids). The framework is of particular merit as it encompasses the majority of the modelling approaches discussed heretofore in this review. Additional insight into the regimes of applicability of the various approaches is thus provided. It should also be emphasized that the GENERIC framework is founded on a fundamentally different basis to all other models of case II diffusion. The framework allows for multiple levels of description. The evolution equations for the state variables arise from a Hamiltonian description and are required to reproduce equilibrium behavior. This ensures that the framework is thermodynamically consistent. It should be stressed at this point that, like the majority of the approaches in the literature on case II diffusion, a rheological view of the polymeric solid is taken.[3]

The GENERIC framework has been applied to model diffusion in simple and complex fluids by [88]. This work was extended to consider non-Fickian mass transport in polymers by El Afif and Grmela [87]. Similar approaches exist in the literature (Kalospiros et al. [154], Jou et al. [153], Doi and Onuki [78], Manero and Rodríguez [183]). Their relation to the GENERIC approach is discussed in detail by El Afif and Grmela [87]. It is the later work of El Afif and Grmela [87] that is the focus of this discussion as, in the authors' opinion, it represents the most complete and promising approach.

---

[3] For a comprehensive review of polymeric fluids the reader is referred to [41, 42].

8.5.1. Overview

The key steps in the GENERIC framework, see e.g. El Afif et al. [88], El Afif and Grmela [87], are: the selection of the state variables, identification of their kinematics using a Hamiltonian approach, identification of the dissipation mechanisms, and specification of the potentials in the form of the free energies. A brief description of these steps is now given.

Collectively, the state variables chosen to describe the rheology and diffusion of a simple and polymeric fluid mixture are denoted

$$\bar{\boldsymbol{\Lambda}} := \{\rho^s, \boldsymbol{p}^s, \rho^p, \boldsymbol{p}^p, \boldsymbol{m}\} \ ,$$

where $\boldsymbol{p}$ denotes the momentum of the solvent or polymer and $\boldsymbol{m}$ is the conformation tensor. The conformation tensor $\boldsymbol{m}$ describes the internal structure (i.e. the stretching and orientation of the polymer chains) of the polymeric fluid and is defined in terms of the configuration space distribution function $\zeta(\boldsymbol{x}, t)$ and the polymer end-to-end vector $\boldsymbol{R}$ (see Fig. 8.3) as $\boldsymbol{m} := \int \boldsymbol{R} \otimes \boldsymbol{R} \ \zeta(\boldsymbol{x}, \boldsymbol{R}, t) \ \mathrm{d}\boldsymbol{R}$. The configuration space distribution function ζ allows the probability that a property of a molecule is within a certain range to be ascertained and is derivable from statistical mechanics [42, 133]. The conformation tensor $\boldsymbol{m}$ is thus the second moment of the end-to-end vector $\boldsymbol{R}$ and represents average conformation of the polymer structure [49]. The end-to-end vector $\boldsymbol{R}$ can be related to the entropy state of the polymer chain [133]. Roughly speaking, the longer the end-to-end vector $\boldsymbol{R}$ the lower the entropy of the polymer molecule, i.e. the number of possible configurations the molecule can take decreases as the length of the end-to-end vector $\boldsymbol{R}$ decreases. The conformation tensor $\boldsymbol{m}$ in the model of El Afif and Grmela [87] takes a similar role as the Cauchy–Green strain tensor in non-linear solid mechanics and hence describes the evolution of the polymer structure. For a discussion on conformation tensor based rheological models the reader is referred to [49] and the references therein.

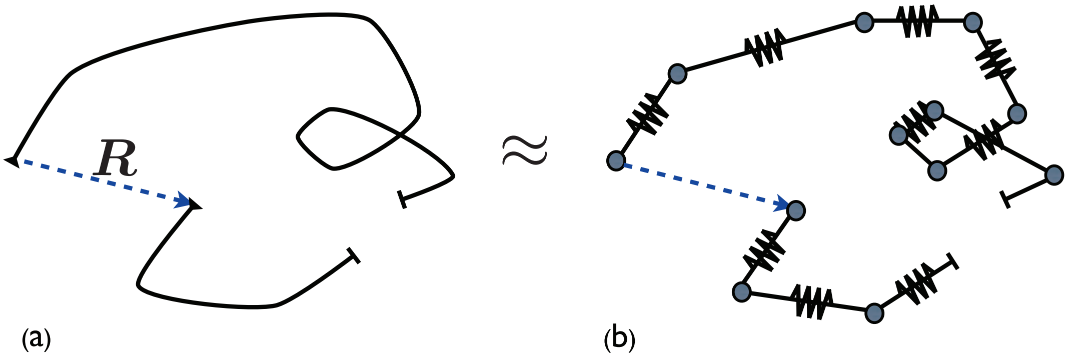

Figure 8.3.: Schematic representation of (a) a single polymer molecule, and (b) its idealization as a series of masses connected via non-linear springs.

An alternative set of state variables, denoted

$$\boldsymbol{\Lambda} := \{\rho, \tilde{c}, \boldsymbol{p}, \boldsymbol{w}, \boldsymbol{m}\} \ ,$$

proves more convenient to use and is defined in terms of $\bar{\boldsymbol{\Lambda}}$ as

$$\begin{aligned}
&\rho = \rho^s + \rho^p && \text{(mixture mass density)}\,,\\
&\tilde{c} = \frac{\rho^s}{\rho} && \text{(relative solvent concentration)}\,,\\
&\boldsymbol{p} = \boldsymbol{p}^s + \boldsymbol{p}^p && \text{(total momentum)}\,,\\
&\boldsymbol{w} = \frac{\rho^p}{\rho}\boldsymbol{p}^s - \frac{\rho^s}{\rho}\boldsymbol{p}^p && \text{(relative momentum)}\,,\\
&\boldsymbol{m} && \text{(conformation tensor)}\,.
\end{aligned}$$

As shown by El Afif and Grmela [87], the relative momentum corresponds to the diffusion flux.

The expressions governing the kinematics of the state variables $\boldsymbol{\Lambda}$ are developed using the framework of Hamiltonian mechanics. The conventional Hamiltonian description of an assembly of N particles, parameterized in terms of their generalized momenta $\tilde{\boldsymbol{P}} = \{p_1, p_2, \ldots, p_N\}$ and coordinates $\boldsymbol{Q} = \{q_1, q_2, \ldots, q_N\}$, expresses the rate of change of position and momenta as

$$\dot{\tilde{\boldsymbol{P}}} = -\frac{\partial \mathcal{H}}{\partial \boldsymbol{Q}} \quad \text{and} \quad \dot{\boldsymbol{Q}} = \frac{\partial \mathcal{H}}{\partial \tilde{\boldsymbol{P}}}\,,$$

where $\mathcal{H}$ is termed the Hamiltonian and represents the total energy of the system. The rate of change of an arbitrary Lagrangian function f of the generalized positions and momenta can be expressed as

$$\begin{aligned}
\dot{f} &= \frac{\partial f}{\partial \boldsymbol{Q}} \cdot \dot{\boldsymbol{Q}} + \frac{\partial f}{\partial \tilde{\boldsymbol{P}}} \cdot \dot{\tilde{\boldsymbol{P}}}\\
&= \frac{\partial f}{\partial \boldsymbol{Q}} \cdot \frac{\partial \mathcal{H}}{\partial \tilde{\boldsymbol{P}}} - \frac{\partial f}{\partial \tilde{\boldsymbol{P}}} \cdot \frac{\partial \mathcal{H}}{\partial \boldsymbol{Q}}\\
&= \{f, \mathcal{H}\}\,,
\end{aligned} \tag{8.5.1}$$

where the Poisson bracket of two arbitrary functions g and h of the generalized positions and momenta is defined as $\{g, h\} := \frac{\partial g}{\partial \boldsymbol{Q}} \cdot \frac{\partial h}{\partial \tilde{\boldsymbol{P}}} - \frac{\partial g}{\partial \tilde{\boldsymbol{P}}} \cdot \frac{\partial h}{\partial \boldsymbol{Q}}$. The extension of the Hamiltonian approach for a particle system to a binary fluid system is detailed by [88].[4]

The equations governing the evolution of the primary variables $\boldsymbol{\Lambda}$ are chosen to ensure that the equilibrium behavior of the system is well described by equilibrium thermodynamics. Thus the Helmholtz free energy $\tilde{\Psi} := E - TS$, where E is the total energy of the system (kinetic and potential), under isothermal conditions must satisfy

$$\dot{\tilde{\Psi}} \leq 0 \quad \text{and} \quad \frac{\partial \tilde{\Psi}}{\partial \boldsymbol{\Lambda}}|_{\boldsymbol{\Lambda}=\boldsymbol{\Lambda}_{\text{eq}}} = \boldsymbol{0}\,,$$

---

[4] While not widely adopted, the Hamiltonian setting can be used to describe the deformation of solids [184].

where $\mathbf{\Lambda}_{\text{eq}}$ denotes the system variables at the equilibrium state.[5] The form of the system of governing equations that satisfies the above requirements is suggested as

$$\dot{f} = \underbrace{\left\{f, \tilde{\Psi}\right\}}_{\text{kinematics of } \mathbf{\Lambda}} - \underbrace{\left[f, \tilde{\Psi}\right]}_{\text{dissipation bracket}} , \tag{8.5.2}$$

where $f(\mathbf{\Lambda})$ is a sufficiently regular function of the state variables $\mathbf{\Lambda}$. The definition stated in Eq. (8.5.2) is linked to the generalized bracket approach introduced by [39]. The kinematics of $\mathbf{\Lambda}$ are described via the Poisson brackets using the Hamiltonian framework discussed previously. Dissipative mechanisms are introduced into the system via the dissipation bracket, a positive semi-definite bilinear form of the generalized derivatives of the function f and the free energy $\tilde{\Psi}$. The dissipation bracket accounts for all dissipative (i.e. irreversible) mechanisms in the system. If one ignores dissipative contributions then Eq. (8.5.2) is equivalent to Eq. (8.5.1). Thus, in order to complete the model one chooses a form for the free energy $\tilde{\Psi}$ and the dissipation brackets.

8.5.2. Modelling of solvent–polymer systems

Governing equations

The equations governing the mixing of a simple and a complex fluid were developed by [88] within the GENERIC framework. El Afif and Grmela [87] imposed the following restrictions on the simple and complex fluid mixing model in order to approximate the coupled diffusion and deformation processes that occur in solvent–polymer systems:

$$\boldsymbol{p} = \mathbf{0} \,, \tag{8.5.3}$$

$$\boldsymbol{\nabla} p + \operatorname{div} \boldsymbol{\sigma}^{\text{overall}} = \mathbf{0} \,, \tag{8.5.4}$$

$$\rho = \text{constant} \,, \tag{8.5.5}$$

where p is the scalar pressure.

The first constraint, Eq. (8.5.3), implies that the total momentum of the system is zero. A similar assumption that the volume averaged velocity of the system (defined as $\boldsymbol{v}^s V^s - \boldsymbol{v}^p V^p$ where $V^{\{\bullet\}}$ denotes the volume of the relevant phase) is zero is widely made in models of case II diffusion that are restricted to one space-dimension and assume perfect mixing.

The second constraint, Eq. (8.5.4), imposes that the system is in overall equilibrium. The overall extra stress tensor is defined as $\boldsymbol{\sigma}^{\text{overall}} := \boldsymbol{w} \otimes \frac{\partial \tilde{\Psi}}{\partial \boldsymbol{w}} - \boldsymbol{\sigma}^p$ where the first term on the right-hand side represents the non-dissipative part of the stress and the second term the stress in the polymer. For a comprehensive discussion of the physical meaning of the stress terms, the reader is referred to [88].

---

[5] The definition of the Helmholtz free energy adopted by Govindjee and Simo [107], i.e. $\Psi = U - TS$, excludes contributions from the kinetic energy.

The final constraint, Eq. (8.5.5), imposes that the solvent–polymer system is incompressible. In the original work of Govindjee and Simo [107] incompressibility was also assumed. This assumption was dropped in their later works for both numerical and physical reasons [137].

The application of the restrictions given in Eqs. (8.5.3)–(8.5.5) to the model of [88] for the mixing of a simple and a complex fluid produces the following system of governing equations for the solvent–polymer system:

$$\mathrm{d}_t \tilde{c} = -\mathrm{div}\left(\frac{\boldsymbol{w}}{\rho}\right), \tag{8.5.6}$$

$$\tilde{c}\dot{\boldsymbol{w}} = -\tilde{c}\boldsymbol{\nabla}\left(\frac{\partial \tilde{\Psi}}{\partial \tilde{c}}\right) - \Lambda \boldsymbol{w}, \tag{8.5.7}$$

$$\dot{\boldsymbol{m}} + \boldsymbol{m}\mathrm{div}\boldsymbol{v}^p = \boldsymbol{m}\cdot[\boldsymbol{\nabla}\boldsymbol{v}^p]^T + \boldsymbol{\nabla}\boldsymbol{v}^p\cdot\boldsymbol{m}^T - \underbrace{2\lambda\boldsymbol{m}\cdot\frac{\partial\tilde{\Psi}}{\partial\boldsymbol{m}}}_{\boldsymbol{\sigma}^p}. \tag{8.5.8}$$

An interpretation of the above system of governing equations will be presented after the details of the free energy function $\tilde{\Psi}$ have been given.

Definition of the free energy

As mentioned in the previous section, the free energy $\tilde{\Psi}$ needs to be specified to complete the model. El Afif and Grmela [87] assume a free energy wherein the kinetic energy is uncoupled from the other terms, that is

$$\tilde{\Psi}(\rho^s, \boldsymbol{p}^s, \rho^p, \boldsymbol{p}^p, \boldsymbol{m}) = \underbrace{\int_V \left[\frac{\boldsymbol{p}^{s2}}{2\rho^s} + \frac{\boldsymbol{p}^{p2}}{2\rho^p}\right] \mathrm{d}x}_{\text{kinetic energy}} + \underbrace{\int_V \psi(\rho^s, \rho^p, \boldsymbol{m})\, \mathrm{d}x}_{\text{energy independent of velocity}},$$

(or equivalently by using the restriction in Eq. (8.5.3) and the definition of the state variables)

$$= \int_V \frac{\boldsymbol{w}^2}{2\rho\tilde{c}(1-\tilde{c})}\,\mathrm{d}x + \int_V \psi(\rho, \tilde{c}, \boldsymbol{m})\,\mathrm{d}x, \tag{8.5.9}$$

where ψ denotes the density of the free energy independent of the velocity, resp. momentum. It is clear that $\rho\tilde{c}(1-\tilde{c})\frac{\partial\tilde{\Psi}}{\partial\boldsymbol{w}} = \boldsymbol{w}$ and thus that the mass flux density and the relative momentum density coincide. Thus, $\boldsymbol{w}$ can be interpreted as either the relative momentum or the mass flux (see El Afif and Grmela [87] for further details).

The form of the free energy density independent of velocity ψ in Eq. (8.5.9) is chosen by El Afif and Grmela [87] as

$$\psi(\tilde{c}, \boldsymbol{m}) = \psi^M(\tilde{c}) + \psi^{\mathrm{mol}}(\tilde{c}, \boldsymbol{m}).$$

There are obvious similarities to the free energy adopted by Govindjee and Simo [107] presented in Eq. (8.4.9). The first term on the right hand side ψ^M is the Flory–Huggins free energy of mixing and the second term ψ^{mol} is the molecular contribution to the free energy due to the deformation of the polymeric molecules.

The use of the Flory–Huggins model implies equilibrium full swelling, as mentioned previously. This assumption is inadequate when modelling case II diffusion [107] because physically an energetically easily accessible space (referred to as free volume) exists in the polymer and, thus, a full swelling cannot be achieved. However, the assumption can be explained by the mesoscopic rheological description of the polymeric solid as a complex fluid subject to various restrictions that El Afif and Grmela [87] adopt. In contrast, the more macroscopic view of Govindjee and Simo [107] describes the solid as a standard solid and allows for a free volume by enforcing the assumption that the Jacobian J (and thus the deformation) and the solvent mass density are independent of each other.

The chosen molecular free energy function ψ^{mol} is a member of the family of finitely extensible non-linear elastic (FENE) bead–spring models [41, 42]. Herein, a polymer molecule is represented as a series of point masses connected via non-linear springs as depicted in Fig. 8.3. More specifically, the molecular response is described using the FENE-P model: an approximation to the FENE model based on a closed constitutive equation. The free energy is a function of solvent concentration $\tilde{c}$ and the conformation tensor $\boldsymbol{m}$ and reduces to the Maxwellian model as the maximum extension of the macromolecules tends to infinity.

This molecular view is adequate for a rheological description of a polymeric fluid [41, 42] but will not provide macroscopic deformation data. To overcome this deficiency, i.e. to describe the swelling of the polymer, a molecular and a macroscopic conformation tensor are introduced. In the pragmatic approach adopted by El Afif and Grmela [87] the microscopic and macroscopic conformation tensors are linked as a function of the volume fraction of the polymer.[6]

The rationale of this linkage is as follows: when the polymer is in a dry state, no slip occurs between the fibers. As the solvent ingresses into the polymer network it causes slip to occur due to lubrication. Thus, for a lubricated polymer, not all of the molecular deformation will lead to macroscopic deformation.

A comparison of the free energy used by El Afif and Grmela [87] with that of Govindjee and Simo [107] given in Eq. (8.4.9) reveals that, aside from the modification to the free energy to account for non-equilibrium effects and the adoption of a macroscopic standard solid viscoelastic model by Govindjee and Simo [107], the free energy functions are extremely similar.

---

[6] A promising alternative methodology to link the meso- and macro-scales is numerical homogenization. For example, Zohdi et al. [284] use homogenization to determine the diffusivity coefficient in heterogeneous material.

Interpretation of the governing equations

Eq. (8.5.6) is Fick's second law for the concentration in terms of the diffusion flux $\boldsymbol{w}$. The equivalence of Eq. (8.5.6) to the expression for Fick's second law in Eq. (8.3.6) can be seen more clearly by performing the following manipulations

$$\frac{\boldsymbol{w}}{\rho} = \frac{\boldsymbol{p}^s}{\rho} = \tilde{c}\boldsymbol{v}^s \,,$$

and using the relations $\boldsymbol{w} = \boldsymbol{p}^s$, $\boldsymbol{v}^s = \frac{\boldsymbol{p}^s}{\rho^s}$ and $\rho^s = \rho\tilde{c}$.

The second of the reduced governing equations given in Eq. (8.5.7) can be recast in a more transparent form using the chain rule and taking into account the decoupled nature of the free energy in Eq. (8.5.9) as

$$\tilde{c}\dot{\boldsymbol{w}} = -\Lambda \left[\boldsymbol{w} + \rho\tilde{D}\left[\boldsymbol{\nabla}\tilde{c} + \boldsymbol{L}\cdot\boldsymbol{\nabla}\boldsymbol{m}\right]\right] \,, \tag{8.5.10}$$

where

$$\tilde{D}(\tilde{c},\boldsymbol{m}) = \frac{\tilde{c}}{\rho\Lambda}\frac{\partial^2\tilde{\Psi}}{\partial c^2} \quad \text{and} \quad \boldsymbol{L}(\tilde{c},\boldsymbol{m}) = \left[\frac{\partial^2\tilde{\Psi}}{\partial\tilde{c}\partial\boldsymbol{m}}\right]\left[\frac{\partial^2\tilde{\Psi}}{\partial\tilde{c}^2}\right]^{-1} \,. \tag{8.5.11}$$

The quantity $\tilde{D}$ can be interpreted as a diffusion coefficient on the $(\tilde{c},\boldsymbol{w},\boldsymbol{m})$ level and $\boldsymbol{L}$ as a measure of the relative significance of the molecular and mixing parts of the free energy. Thus, Eq. (8.5.7) is an expression for Fick's first law that accounts for the diffusional inertia of the solvent species and the influence of polymer deformation on the diffusion process. The relation of the modified expression for Fick's first law to the model of hyperbolic and stress-assisted diffusion presented in Sections 8.3.2 and 8.4.1 will be made clear shortly.

Eq. (8.5.8) gives the, in general, non-linear evolution equation for the conformation tensor $\boldsymbol{m}$ and indicates that the conformation tensor is advected by the velocity of the polymer $\boldsymbol{v}^p = \frac{-\boldsymbol{w}}{\rho(1-\tilde{c})}$.

It is important to note that, as indicated by El Afif and Grmela [87], Eqs. (8.5.7) and (8.5.8) govern the time evolution of the mass density ρ^s and the conformation tensor $\boldsymbol{m}$ of a polymeric fluid subjected to mass flow.

The system of Eqs. (8.5.6)–(8.5.8) is denoted the $(\tilde{c},\boldsymbol{w},\boldsymbol{m})$ model as these three variables are the independent constitutive quantities. This model is parameterized by the free energy density ψ that is independent of the velocity, the variable Λ which is proportional to the relaxation time of the relative momentum $\boldsymbol{w}$, and λ which is proportional to the relaxation time of the conformation tensor $\boldsymbol{m}$.

An important aspect of the $(\tilde{c},\boldsymbol{w},\boldsymbol{m})$ model is that it encompasses the key features of many of the models for coupled diffusion deformation discussed in previous sections. These models emerge as various restrictions are placed on the $(\tilde{c},\boldsymbol{w},\boldsymbol{m})$ model. The regime of applicability of these models is thus made clear.

8.5.3. The reduced $(\tilde{c}, \boldsymbol{m})$ model

In the $(\tilde{c}, \boldsymbol{m})$ model the momentum of the solvent is disregarded. It is assumed that the relaxation time Λ^{-1} for the mass flux $\boldsymbol{w}$ is much shorter than the characteristic time for diffusion. That is, $\boldsymbol{w}$ evolves rapidly towards equilibrium and the time derivative of the mass flux $\boldsymbol{w}$ in Eq. (8.5.10) is approximately zero. Eq. (8.5.10) thus becomes the following algebraic relation for $\boldsymbol{w}$:

$$\boldsymbol{w} = -\rho \tilde{D} \left[\boldsymbol{\nabla} \tilde{c} + \boldsymbol{L} \cdot \boldsymbol{\nabla} \boldsymbol{m} \right] . \tag{8.5.12}$$

Accordingly, the second term accounts for changes in the flux due to structural changes of the polymer.

The $(\tilde{c}, \boldsymbol{m})$ model is prototypical of the weakly- and strongly-coupled models discussed in Section 8.4. Eq. (8.5.12) includes contributions due to classical diffusion and a deformation-assisted component in the spirit of the models of stress-assisted diffusion discussed in Section 8.4.1. The relation between the conformation tensor $\boldsymbol{m}$ and the stress given by Eq. (8.5.8) still holds and is non-linear. The models of Cohen and White [59] and Wu and Peppas [279] can be obtained if a Maxwell rheological model for the fluid is assumed and the non-linear terms in Eq. (8.5.8) ignored El Afif and Grmela [87].

The model of Govindjee and Simo [107] can also be regarded as an extension of the $(\tilde{c}, \boldsymbol{m})$ model. The primary difference however is that their model does not view the polymeric solid from a rheological perspective. Rather, the solid is approximated as a viscoelastic non-linear continuum evolving as per the constitutive relations for a standard solid. This view of the solid deformation taken by Govindjee and Simo [107] is more macroscopic, although completely consistent from a thermodynamic perspective. It is important to note however that in their implementation, El Afif and Grmela [87] assume a simple linkage between the more microscopic deformation captured by the conformation tensor $\boldsymbol{m}$ and the macroscopic deformation. The conformation tensor can thus be interpreted as the right Cauchy–Green tensor $\boldsymbol{b} := \boldsymbol{F} \cdot \boldsymbol{F}^T$. In essence then, Eq. (8.5.8) acts as an evolution equation for the deformation at the macro-scale.

8.5.4. The further reduced $(\tilde{c})$ model

The $(\tilde{c})$ model describes diffusion without inertia and is applicable to situations well described by Fickian diffusion. If the term involving the measure $\boldsymbol{L}$ in Eq. (8.5.12) is ignored one obtains the following relation

$$\boldsymbol{w} = -\rho \tilde{D} \boldsymbol{\nabla} \tilde{c} .$$

This is Fick's first law as given in Eq. (8.3.1) with non-linear diffusion due to the coupling of the diffusion coefficient $\tilde{D}$ to the conformation $\boldsymbol{m}$ given in Eq. $(8.5.11)_1$. This reduced model is prototypical of the early approach of Crank [65] discussed in Section 8.3.1. Models of this form are, however, not capable of describing the sharp propagating front that is characteristic of case II diffusion.

8.5.5. The $(\tilde{c}, \boldsymbol{w})$ model

The $(\tilde{c}, \boldsymbol{w})$ model describes diffusion including inertial terms. In the $(\tilde{c}, \boldsymbol{w})$ model it is assumed that the relaxation time Λ^{-1} is large with respect to the characteristic time for diffusion and that the term involving $\boldsymbol{L}$ is negligible. Furthermore, one chooses to neglect the influence of the conformation tensor $\boldsymbol{m}$ on the diffusion process. In other words, the model takes a more macroscopic view of the coupled diffusion–deformation process. Application of these restrictions to Eqs. (8.5.6)–(8.5.8) produces the following set of governing equations:

$$\mathrm{d}_t\tilde{c} = -\mathrm{div}\left(\boldsymbol{v}^s\tilde{c}\right) \,, \tag{8.5.13}$$

$$\dot{\overline{v^s\tilde{c}}} = \tfrac{-1}{\rho}\boldsymbol{\nabla}\pi(\tilde{c}) - \Lambda(\tilde{c})\tilde{c}\boldsymbol{v}^s \,. \tag{8.5.14}$$

In this more macroscopic view, the parameters π and Λ are themselves functions of the solvent concentration $\tilde{c}$ to be fitted with experimental observations. This is a key aspect of the GENERIC model: the more macroscopic the perspective, the more emphasis needs to be placed on quantifying the material parameters via constitutive assumptions.

Eq. (8.5.14) is near identical to that proposed by Aifantis [7] in Eq. (8.3.7). These equations govern a solvent wave in a rigid diffuser. The model has been successfully applied to modelling case II diffusion in glassy polymers that do and do not undergo a glass–rubber transition, see El Afif [86], El Afif and Grmela [87].

8.6. Conclusions

The review has focused on contextualizing and comparing several key models of diffusion developed to describe the anomalous phenomena that characterize case II type diffusion. The emphasis of the presentation has been on the structure of the models as opposed to their phenomenological features. Moreover, the linkage of the models investigated to earlier models of non-linear, hyperbolic, and stress-assisted diffusion has been made clear.

The approach introduced by Aifantis [7] accounts for inertia in the diffusion equation and is hyperbolic from the outset. The Govindjee and Simo [107] model allows for independent deformation and concentration fields in the formulations – something that is not possible if one invokes the Flory–Huggins theory of mixing. This leads to the elegant approach of defining the free energy of mixing in terms of the deformation and the solvent mass density with those two variables being independent of each other. Their approach is based on the micromechanical argument that an energetically easily accessible space (referred to as free volume) exists in the polymer and, thus, a full swelling cannot be achieved. Consequently, the solvent and the polymer volumes are not assumed to be additive. The model of Govindjee and Simo [107] also appears to be the only one capable of describing the three-dimensional large deformations that the polymeric solid undergoes. For these reasons, the model of Govindjee and Simo [107] is, arguably, still the most complete and advanced one currently available.

The mesoscopic theory developed by El Afif and Grmela [87] takes an Eulerian viewpoint since it is phrased for a polymeric fluid rather than solid. In addition to the relative solvent concentration $\tilde{c}$, El Afif and Grmela [87] introduce a conformation tensor $\boldsymbol{m}$ to account for structural changes of the polymer due to external stress effects. Their modelling approach does not, in its present form, fully capture the polymer's swelling response. The remedy they propose is to introduce a second conformation tensor on the molecular level. These two conformation tensors would then describe the coupling between the polymer's molecular and macroscopic deformations during the solvent penetration process. The model of [88] incorporates rheological effects. Moreover, the method is based on a sound mathematical basis. It uses the Hamiltonian formulation together with Poisson brackets and a dissipation bracket (in case of irreversible processes) to derive the governing equations for the selected state variables. The assumption that the viscosity be a strongly decreasing function of the solvent concentration, as made in the models of Thomas and Windle [254, 255, 256], Durning and Tabor [80] and Wu and Peppas [279], in order to capture features of case II diffusion is not required in the model of El Afif and Grmela [87]. Moreover, the other approaches mentioned are more of the ad hoc type in comparison to the El Afif and Grmela [87] approach which automatically satisfies the laws of thermodynamics. A further aspect of the El Afif and Grmela [87] approach is that it is developed for modeling the evolution of a polymeric fluid. Their formulation is for multiple space dimensions but the results presented are restricted to one dimension. In higher space dimensions it would be problematic to adopt the approach of El Afif and Grmela [87] of linking the conformation tensor $\boldsymbol{m}$ to the deformation response of the polymeric solid.

The application of the GENERIC framework to case II diffusion by El Afif and Grmela [87] was presented here as it unifies and extends the majority of the models for case II diffusion presented in the literature and is hence of considerable value.

9. Non-Fickian reaction-diffusion models in biological and physical sciences

The propagation of kinematic waves in one-dimension media described by the inertia-Green–Naghdi-type II model is investigated. Hereby, Fick's classical law of diffusion is replaced by the non-classical flux law proposed by Green and Naghdi [109] which leads to a strictly hyperbolic partial differential equation. Exact traveling wave solutions are determined of the nonlinear equations arising from the nonlinear source terms considered. Moreover, shock wave amplitude analyses are performed for each of the source terms leading to exact amplitude expressions for shock waves. In this contribution, our main focus is on obtaining analytical results, specifically exact as well as approximate solutions.

9.1. Introduction

The classical theory of diffusion is based on Fick's flux law [94], which is a constitutive assumption stating that diffusive flux is directly proportional to the concentration/density gradient, i.e. $q = -\nu \rho_x$, where ν is the diffusion coefficient or diffusivity. Combining this assumption with the law of conservation of species/mass leads to the well-known diffusion equation

$$\rho_t - \nu \rho_{xx} = R(\rho) \tag{9.1.1}$$

which is the balance law for the species. Here, x and t subscripts denote partial differentiation with respect to space and time, respectively. Unfortunately, the parabolic nature of this partial differential equation (9.1.1) implies that parts of an initial concentration pulse will propagate with infinite speed. Thus, such perturbations are felt instantly, but unequally, everywhere in an infinite medium. The infinite propagation speed contradicts the argument of causality as infinite speeds do not exist in nature. A constitutive relation of the Fick type describes a diverse array of physical phenomena, including e.g. mathematical models of both the dynamics of biological populations in which dispersal/ aggregation is occurring, or traffic flow which take into account vehicular diffusion. Although Fick's law describes many applications fairly appropriate, there also exist various situations in which they have proven to be inadequate. In order to overcome this drawback of the classical theory, and based on experimental observations, i.e., where the classical theory fails, numerous research efforts have been devoted to the formulation of non-Fickian transport theories (see e.g. Refs. [149, 164, 256]).

From the mathematical point of view, Fick's law is structurally identical to Fourier's law of heat conduction. Consequently, the latter also possesses the shortcoming of infinite propagation speed. Moreover, it fails to model the second sound phenomenon, i.e. the propagation of thermal waves. A very promising non-classical thermal theory overcoming those drawbacks has been published by Green and Naghdi [109]. Their theory of type II represents a thermal wave equation and is, in this work, transferred to the diffusion equation. Green–Naghdi-type II theory can be derived from the well-known Maxwell–Cattaneo–Vernotte approach which was also developed in the heat conduction community and which introduces a relaxation time τ_0 in order to delay the flux in the following way

$$q + \tau_0 q_t = -\nu \rho_x. \tag{9.1.2}$$

By letting go the relaxation time $\tau_0 \to \infty$ and assuming the fraction $\nu/\tau_0 \to \text{const} := c_\infty^2$, one obtains

$$q_t = -c_\infty^2 \rho_x; \tag{9.1.3}$$

the constitutive assumption which is known as Green–Naghdi type II in thermal theories. Works dealing with the Green–Naghdi theory are e.g. [28, 29, 30, 32, 34, 33, 109, 147].

In particular, we examine wave phenomena predicted by the following class of semilinear, strictly hyperbolic[1] systems:

$$\rho_t + q_x = R(\rho), \qquad \text{with} \;\; q_t = -c_\infty^2 \rho_x. \tag{9.1.4}$$

Here, $\rho = \rho(x,t)$ represents the per-unit-length concentration of some species, either chemical or biological; the flux q is assumed to satisfy the 'inertia' law of Joseph and Preziosi [152, p. 42], which can be considered as a special case of the flux relation predicted by the more rigorously formulated type-II theory of Green and Naghdi (see, e.g., Refs. [150] those therein). The positive constant c_∞ is called the finite wave (i.e., characteristic) speed with (SI) units of ms^{-1}. Differentiation of Eq. $(9.1.4)_1$ with respect to time and subsequent inserting Eq. $(9.1.4)_2$ leads to the following partial differential equation

$$\rho_{tt} = c_\infty^2 \rho_{xx} + (R(\rho))_t. \tag{9.1.5}$$

Consequently, instead of the diffusion equation implied by Fick's law [94], the material's mass density ρ is now governed by a wave equation. Note that due to the growth term, damping is involved in Eq. (9.1.5). In the following, the propagation behavior under two different nonlinear source terms $R(\rho)$ is studied, see also Figure 9.1.

$$R(\rho) = \gamma \begin{cases} \rho_\mathrm{s}[\rho/\rho_\mathrm{s}]^2[1-\rho/\rho_\mathrm{s}], & \text{Zel'dovich law,} \\ \rho[1-\rho^2/\rho_\mathrm{s}^2], & \text{Newman (Newell–Whitehead) law} \end{cases} \qquad \rho \in [0, \rho_\mathrm{s}]. \tag{9.1.6}$$

Zel'dovich law comes from chemical kinetics (to be precise: from autocatalytic reactions). The Newmann or Newell–Whitehead law is originally proposed by Newell and Whitehead [196] to to describe Rayleigh–Benard convection, respectively later applied by Newman [197] in the context of diffusion problems in population genetics.

---

[1] Since the common coefficient matrix shared by these systems admits real, but distinct, eigenvalues, all are strictly hyperbolic, with characteristics defined by $\mathrm{d}x/\mathrm{d}t = \pm c_\infty$.

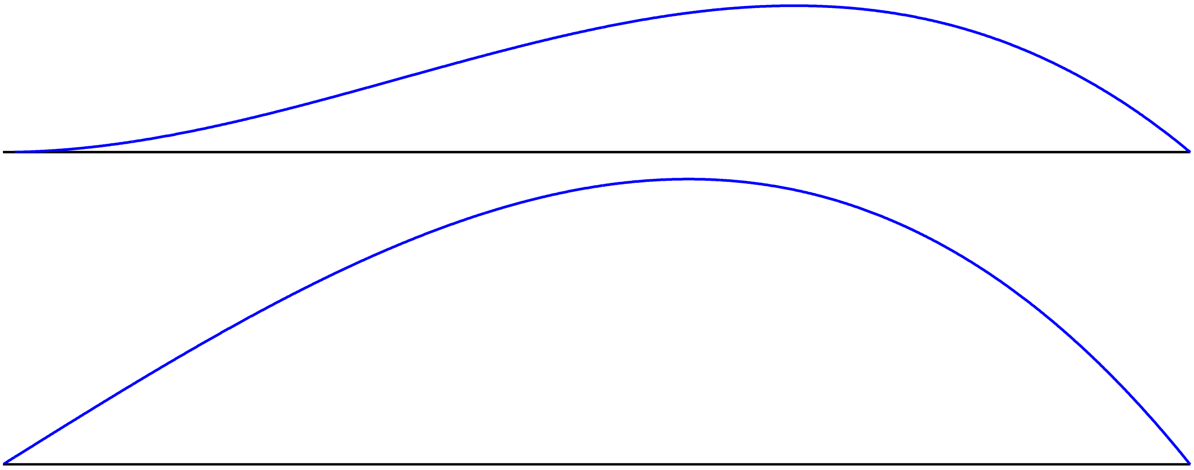

Figure 9.1.: Two types of nonlinear source terms $R(\rho)$ are considered: Zel'dovich (top) and Newman resp. Newell–Whitehead (bottom). Graphs are sketched according to Eq. (9.1.6). Whereas the Newman law has a positive slope at $\rho = 0$, reaching a positive maximum and, subsequently, going down to zero again, the Zel'dovich law has a zero slope in at $\rho = 0$. It then goes up to a positive maximum and back to zero as well.

First, a modified SIR epidemic dynamics model is considered. It describes the spread of an epidemic outbreak through a population. In this context, the population is divided into susceptible (S), infected (I) and recovered (R) persons. In the following, a modified model is studied, wherein Ficken-based diffusion is replaced by the inertia-type II flux relation, for the spatial spread of an epidemic:

$$\begin{aligned} S_t + Q_x &= -rSI, \quad Q_t = -\mathfrak{c}_1^2 S_x; \\ J_t &= -\mathfrak{c}_2^2 I_x, \quad I_t + J_x = rSI - aI. \end{aligned} \tag{9.1.7}$$

Here Q and J are the fluxes corresponding to S and I, respectively; and $\mathfrak{c}_{1,2}$, r, and a are positive constants. A large diffusion coefficient $\mathfrak{c}_2$ corresponds to a fast and wide spread of the disease, e.g. as in case of the black death (1347–1353), the Spanish flu in 1918 or the H1N1 virus in 2009. Furthermore, r denotes the infection rate and a the recovery rate. An epidemic begins if $I_t > 0$, i.e. if the fraction of infected persons increases.

It should also be noted that, since a momentum balance equation is not involved, all of the above systems, like their better known parabolic counterparts of classical reaction-diffusion theory, describe kinematic wave phenomena; see Whitham [277]. Contrary to classical waves, kinematic waves are described by a functional relation between the density and the flux of a physically observed quantity and differ physically from the classical waves. Instead of applying a reaction-diffusion approach as done in this contribution in order to model, diffusive biological problems such as biological growth can also be model via different approaches, see e.g. Preziosi [220], Rajagopal and Tao [223] or Rao et al. [224].

To this end, the present contribution is structured as follows. First, in Section 9.2, traveling wave solutions for a SIR-model are sought. The primary aim of Section 9.3.1 is to carry out an analytical study of type-II diffusion under the Zel'dovich growth law. An exact traveling wave solution is derived and the shock wave amplitude is analyzed. We employ the theory of propagating singular surfaces (e.g. Chen [54]) to determine how an initial jump discontinuity in the material's density ρ propagates and evolves over time under the governing system. It should be noted that the singular surface analysis is performed here without approximation. Finally, in Section 9.3.2 the same procedure is applied for a Newman type growth law and a traveling wave solution for a type-II flux law is derived.

9.2. Inertia-type II based SIR model

The SIR model is used in simulations of epidemic deseases for the description of the transmission of communicable diseases through individuals. The SIR model is introduced by Kermack and McKendrick [159] in 1927 who split the population into three groups: susceptible (S), infected (I) and recovered, now immune, (R) humans. The population is assumed to be homogeneous. Nowadays different variations of the model originally used by Kermack and McKendrick exist. Here, the model as defined in Eq. (9.1.7) is applied.

Differentiating Eqs. $(9.1.7)_{1,4}$ with respect to time t and inserting Eqs. $(9.1.7)_{2,3}$ yields

$$S_{tt} - \mathfrak{c}_1^2 S_{xx} = -r(SI)_t, \qquad I_{tt} + aI_t - \mathfrak{c}_2^2 I_{xx} = r(SI)_t. \tag{9.2.1}$$

Introducing the following dimensionless variables: $S^\diamond = S/S_0$, $I^\diamond = I/S_0$, $x^\diamond = x/l_0$, and $t^\diamond = t(rS_0)$, where $l_0(> 0)$ is again used to denote a characteristic length and $S_0(> 0)$ denotes a characteristic value of the susceptibles S, Eqs. (9.2.1) are further reduced to

$$S_{tt} - c_1^2 S_{xx} = -(SI)_t, \qquad I_{tt} + \lambda I_t - c_2^2 I_{xx} = (SI)_t, \tag{9.2.2}$$

where $\lambda := a/[rS_0]$. Moreover, $c_{1,2} := \mathfrak{c}_{1,2}/[rl_0S_0]$, and the superposed diamonds have been omitted but remain understood. Both, Eq. $(9.2.2)_1$ and Eq. $(9.2.2)_2$ have the same source term with the exception of the sign. Whereas Eq. $(9.2.2)_1$ is a wave equation for the susceptibles, Eq. $(9.2.2)_2$ denotes a damped wave equation with the damping term λI_t for the infected.

In terms of these quantities, and employing matrix notation, System (9.2.1) assumes the somewhat simpler (dimensionless) form

$$\begin{pmatrix} S \\ Q \\ I \\ J \end{pmatrix}_t + \mathbf{A} \begin{pmatrix} S \\ Q \\ I \\ J \end{pmatrix}_x = - \begin{pmatrix} SI \\ 0 \\ (\lambda - S)I \\ 0 \end{pmatrix}, \quad \text{with,} \quad \mathbf{A} = \begin{pmatrix} 0 & 1 & 0 & 0 \\ c_1^2 & 0 & 0 & 0 \\ 0 & 0 & 0 & 1 \\ 0 & 0 & c_2^2 & 0 \end{pmatrix}; \tag{9.2.3}$$

where $1/\lambda$ is known as the reproduction rate[2]. Clearly, the eigenvalues of the matrix $\mathbf{A}$ are $\mu_{1,3} = \pm c_1$ and $\mu_{2,4} = \pm c_2$, where the μ_i $(i = 1, 2, 3, 4)$ are the roots of the characteristic

---

[2] According to Murray [192], $\lambda \approx 0.75$ in the case of the Black death (1347–1353).

polynomial $\det(\mathbf{A} - \mu \mathbf{I}_4)$ and $\mathbf{I}_4$ denotes the 4×4 identity matrix. Since all the $\mu_i \in \mathbb{R}$, this system is clearly hyperbolic. However, there are, in general, two cases to be considered here: (i) $c_1 \neq c_2$, in which case System (9.2.3) is strictly hyperbolic [178]; and (ii) $c_1 = c_2$, a degenerate case, for which the characteristic polynomial has two distinct roots, each of multiplicity two.

9.2.1. Traveling wave analysis

In case of a SIR model in terms of a Maxwell–Cattaneo–Vernotte flux law, i.e. Eq. (9.1.2), it does not appear possible to integrate the system once. However, for a type-II-flux law as applied here, it easily possible as shown in the following.

Seeking traveling wave solutions, it is observed that Eqs. (9.2.2) are invariant under the transformation $x \mapsto -x$. Hence, we set

$$S(x,t) = s(\varkappa) \qquad \text{and} \qquad I(x,t) = \iota(\varkappa), \tag{9.2.4}$$

where $\varkappa := x - ct$ is the wave variable and the wave speed c is a positive constant, and then substitute this ansatz into Eqs. (9.2.2). After integrating once with respect to the wave variable $\varkappa$ and simplifying, we obtain the system of ODEs

$$[c^2 - c_1^2]s' = \mathfrak{K}_1 + c[s\iota], \quad [c^2 - c_2^2]\iota' - c\lambda\iota = \mathfrak{K}_2 - c[s\iota] \quad \text{with } c \neq c_{1,2}, \tag{9.2.5}$$

where $\mathfrak{K}_{1,2}$ are the constants of integration and in this section a prime denotes differentiation with respect to the wave variable, i.e. $\mathrm{d}/\mathrm{d}\varkappa$.

As discussed by Murray [192], $0 < s(-\infty) < s < 1$ holds for the traveling wave solution $s(\varkappa)$, where $s \to 1, s(-\infty)$ as the wave variable $\varkappa \to \pm\infty$, respectively, and the traveling wave solution $\iota \to 0$ as $\varkappa \to \pm\infty$. That is, the traveling wave solution s is in the form of a kink and ι takes the shape of a pulse spread out across the $\varkappa$-axis. Consequently, the integration constants fulfill $\mathfrak{K}_1 = \mathfrak{K}_2 = 0$. Eliminating the traveling wave solution ι between Eqs. $(9.2.5)_1$ and $(9.2.5)_2$, using the fact that the former can be rewritten as

$$\iota = \frac{[c^2 - c_1^2]s'}{cs} \quad \text{with } c \neq c_1, \tag{9.2.6}$$

yields the single ODE

$$p\left[s\frac{\mathrm{d}p}{\mathrm{d}s} - p - \lambda b s + b s^2\right] = 0, \tag{9.2.7}$$

where $p = s'$ and $b := c/[c^2 - c_2^2]$. Clearly, Eq. (9.2.7) is satisfied either when $p = 0$ or when the ODE in parentheses, which we recognize as a first order Cauchy–Euler equation, is satisfied. Solving this linear, inhomogeneous ODE using the standard substitution method leads us to consider the nonlinear ODE

$$s' = bs[1 - s + \lambda \ln(s)], \tag{9.2.8}$$

where the resulting constant of integration was determined using the condition $s(\infty) = 1$. To the authors' best knowledge, this is the first time an ODE of this format arises. Consequently, it can be shown that the other equilibrium solution, $s(-\infty) > 0$, is given by

$$s(-\infty) = -\lambda W_0[-\lambda^{-1}\exp(-1/\lambda)], \qquad \text{with } \lambda < 1, \tag{9.2.9}$$

where the restriction on λ has been imposed here to ensure that $s(-\infty) < 1$, and where $W_0(\cdot)$ denotes the principal branch of the Lambert W-function (see Appendix A). Additionally, we observe that $b > 0$, i.e., $c > c_2$, must henceforth be assumed so that the equilibrium solutions $s(\pm\infty)$ are stable and unstable, respectively. In other words, the model is fixing the amount of susceptibles behind the wavefront and therefore fixing the impact they have on the disease.

If we now set the traveling wave solution $s = \exp(-[1-v]/\lambda)$, separate variables, and integrate, then Eq. (9.2.8) becomes

$$\int \frac{\mathrm{d}v}{v - \exp(-[1-v]/\lambda)} = b\lambda\varkappa + \mathfrak{K}, \tag{9.2.10}$$

where $\mathfrak{K}$ is the constant of integration. Observing that $s(-\infty) < s < 1$ implies $v^{-1}\exp(-[1-v]/\lambda) < 1$, we expand the integrand and then integrate the resulting binomial series term-by-term. After solving for the integration constant $\mathfrak{K}$ using the condition $s(0) = s_0$ and simplifying, the exact, but implicit, solution

$$b\lambda\varkappa = \ln\left(\frac{v}{v_0}\right) - \sum_{m=1}^{\infty} \exp\left(-\frac{m}{\lambda}\right)\left(-\frac{m}{\lambda}\right)^m \left[\Gamma\left(-m, -\frac{mv}{\lambda}\right) - \Gamma\left(-m, -\frac{mv_0}{\lambda}\right)\right], \tag{9.2.11}$$

is obtained. Here $\Gamma(\cdot,\cdot)$ denotes the incomplete Gamma function, $v := 1 + \lambda\ln(s)$ and $v_0 = 1 + \lambda\ln(s_0)$, and $s(-\infty) < s_0 < 1$.

The corresponding solution for j can be obtained by first eliminating s' between Eqs. (9.2.6) and (9.2.8), thus yielding

$$j(\xi) = \mathcal{A}_0\left[(1-s) + \lambda\ln(s)\right] \qquad \text{with } c > c_{\max}, \tag{9.2.12}$$

and then, if one desires, solving for s in terms of j, which gives

$$s(\xi) = -\lambda W_{-1}\left\{-\lambda^{-1}\exp(-1/\lambda)\exp\left[\frac{(c^2 - c_2^2)j(\xi)}{\lambda(c^2 - c_1^2)}\right]\right\} \qquad \text{with } c > c_{\max}. \tag{9.2.13}$$

Here, $W_{-1}(\cdot)$ denotes a second branch of the Lambert W-function [63] and, for convenience, we have set $\mathcal{A}_0 := bc^{-1}(c^2 - c_1^2)$ and $c_{\max} := \max\limits_{c_{1,2}>0}(c_1, c_2)$.

9.2.2. Analytical and numerical results for the traveling wave solutions

Critical values

Having derived exact traveling wave solutions for s and j, we now proceed to determine the maximum of $j(\xi)$ over the real line. Using the relation

$$j'(\xi) = \mathcal{A}_0 \left(-1 + \lambda s^{-1}\right) s'(\xi) \qquad \text{with } c > c_{\max}, \tag{9.2.14}$$

which is obtained by simply differentiating both sides of Eq. (9.2.12) with respect to the wave variable ξ, and recalling that $s' > 0$, it is not difficult to see that $j' = 0$ only when $s = \lambda$. Thus, from Eq. (9.2.12) we find that

$$\max_{\xi \in \mathbb{R}}[j(\xi)] = j(\xi^*) = \mathcal{A}_0 \left[(1-\lambda) + \lambda \ln(\lambda)\right] \qquad \text{with } c > c_{\max}, \tag{9.2.15}$$

where

$$b\lambda\xi^* = \ln\left[\frac{v(\lambda)}{v(s_0)}\right] - \sum_{m=1}^{\infty} (-m/\lambda)^m \\ \times \left\{\Gamma\left[-m, -\frac{mv(\lambda)}{\lambda}\right] - \Gamma\left[-m, -\frac{mv(s_0)}{\lambda}\right]\right\} \exp(-m/\lambda). \tag{9.2.16}$$

From Eq. (9.2.15) it can also be established that $j(\xi^*) > \lambda$ (resp. $j(\xi^*) < \lambda$) for $\lambda < \lambda_{\text{crt}}$ (resp. $\lambda > \lambda_{\text{crt}}$), while $j(\xi^*) = \lambda$ when $\lambda = \lambda_{\text{crt}}$, where

$$\lambda_{\text{crt}} := \frac{-1}{W_{-1}\left\{-\exp\left[-\left(1 + \frac{c^2 - c_2^2}{c^2 - c_1^2}\right)\right]\right\}} \qquad \text{with } 0 < \lambda_{\text{crt}} < 1. \tag{9.2.17}$$

Remark: An inspection of Eq. (9.2.15) reveals that $j(\xi^*) \in (0, \mathcal{A}_0)$, for $\lambda \in (0,1)$, where $j(\xi^*) \to 0, \mathcal{A}_0$ as $\lambda \to 1, 0$, respectively. This indicates that the peak intensity of an epidemic can be mitigated both/either by somehow "pushing" λ closer to unity and/or "pushing" $\mathcal{A}_0$ closer to zero, assuming such parameter manipulations are possible. (From a practical standpoint, however, the latter approach to reducing $j(\xi^*)$ should instead read "pushing $\mathcal{A}_0$ closer to unity" since $c_2 > c_1$ does not appear to be likely.)

Asymptotic results

Being both implicit and complicated in its mathematical structure, Eq. (9.2.11) clearly does not lend itself to probing by analytical methods. We therefore seek simpler (i.e., analytically tractable) asymptotic expressions that, while approximate, accurately capture the behavior of our model over various intervals of the ξ-axis, and/or various parameter regimes.

To this end, we return to Eq. (9.2.8) and expand its right-hand side about $s = 1, s_1$. On neglecting terms of $\mathcal{O}[(1-s)^3]$, $\mathcal{O}[(s-s_1)^3]$, respectively, and then solving the resulting Bernoulli equations, the following, rather accurate, large-$|\xi|$ approximations are obtained. For $\xi \to \infty$:

$$s(\xi) \simeq 1 - \frac{2[1-\lambda]}{2-\lambda-[[2-\lambda]-2[1-\lambda][1-s_0]^{-1}]\exp(b[1-\lambda]\xi)} \quad \text{with } \lambda \ll \lambda^*, \tag{9.2.18}$$

where $\lambda^* := 2s_0(1+s_0)^{-1}$.
For $\xi \to -\infty$:

$$s(\xi) \simeq s_1 - \frac{2s_1[s_1-\lambda]}{[2s_1-\lambda]-[[2s_1-\lambda]+2s_1[s_1-\lambda][s_0-s_1]^{-1}]\exp(b[s_1-\lambda]\xi)} \tag{9.2.19}$$

with $\lambda \gg s_1$. Turning our attention now to obtaining an explicit approximation valid for small-ξ, we once again expand the right-hand side of Eq. (9.2.8), but this time about $s = \lambda$. On neglecting terms of $\mathcal{O}(\mathfrak{s}^3)$, where $\mathfrak{s} := s - \lambda$, and simplifying, we end up with a special case of Riccati's equation, namely,

$$2\mathfrak{s}' \approx b[2\lambda(1-\lambda+\lambda\ln\lambda) + 2(1-\lambda+\lambda\ln\lambda)\mathfrak{s} - \mathfrak{s}^2]. \tag{9.2.20}$$

Integrating this well known ODE subject to $s_0 = (1+s_1)/2$, the following Taylor shock approximation is obtained:

$$\begin{aligned} s(\xi) \simeq 1 + \lambda\ln(\lambda) &+ \sqrt{1-\lambda^2+2\lambda\ln(\lambda)+\lambda^2\ln^2(\lambda)} \\ &\times \tanh\left[\tfrac{1}{2}(b\xi+2\xi_\lambda)\sqrt{1-\lambda^2+2\lambda\ln(\lambda)+\lambda^2\ln^2(\lambda)}\right], \quad |\xi-\xi^*| \ll \tfrac{1}{2}\ell. \end{aligned} \tag{9.2.21}$$

Here, the shock thickness $\ell(>0)$ corresponding to Eq. (9.2.11) is given by

$$\ell = \left|\frac{(c^2-c_2^2)(1-s_1)}{cs_0[1-s_0+\lambda\ln(s_0)]}\right|, \tag{9.2.22}$$

where the defining relation for the shock thickness ℓ was borrowed from classical gasdynamics, and

$$\begin{aligned} \xi_\lambda := {}& [1-\lambda^2+2\lambda\ln(\lambda)+\lambda^2\ln^2(\lambda)]^{-1/2} \\ &\times \operatorname{Arctanh}\left\{[s_0-1-\lambda\ln(\lambda)][1-\lambda^2+2\lambda\ln(\lambda)+\lambda^2\ln^2(\lambda)]^{-1/2}\right\}. \end{aligned} \tag{9.2.23}$$

Of course, with the aid of Eq. (9.2.12), the corresponding approximations for j can be readily derived.

Results for $\lambda \to 1^-$

Using the fact that $(1-\lambda)+\lambda\ln(\lambda) \sim \frac{1}{2}(1-\lambda)^2$, as $\lambda \to 1$ from below, Eq. (9.2.20) reduces to the somewhat simpler Riccati equation

$$2\mathfrak{s}' \approx b[\lambda(1-\lambda)^2 + \mathfrak{s}(1-\lambda)^2 - \mathfrak{s}^2] \qquad \text{with } \lambda \to 1^-. \tag{9.2.24}$$

Thus, the s vs. ξ profile takes the approximate form of a Taylor shock in the $\lambda \to 1^-$ regime as well; specifically, for all $\xi \in \mathbb{R}$:

$$s(\xi) \approx \tfrac{1}{2}\left\{(1+\lambda^2) + (1-\lambda^2)\tanh\left[\tfrac{1}{4}(1-\lambda^2)(b\xi - 4(1+\lambda)^{-2})\right]\right\} \tag{9.2.25}$$

with $\lambda \to 1^-$. Here, we have taken $s(0) = s_0 \approx \lambda$, since $s_1 \sim 2\lambda - 1$ as $\lambda \to 1$ from below.

Numerical results: Traveling wave profiles

While Eq. (9.2.11) is an exact result, its usefulness is limited by the fact that the series it contains converges quite slowly, especially in the vicinity of the equilibrium solution $s(\infty) = 1$. It for this reason that we now turn to the `NDSolve[·]` routine, which is part of the software package MATHEMATICA, to numerically solve Eq. (9.2.8) for various values of the physical parameters.

Now, an inspection of Figs. 1–4, all of which were generated for $c_1 \geq c_2$, reveals that the curves they contain are, qualitatively, the same as those appearing in [192, Fig. 20.1]. More importantly, however, we see, on comparing Figs. 1, 3, and 4, that for a given $\lambda \in (0,1)$, the maximum value of j varies directly with $\mathcal{A}_0$. Moreover, Figs. 2 and 4 clearly illustrate the fact that when $\lambda = \lambda_{\text{crt}}$, the s and j traveling wave profiles actually have two points in common, one of which of course is $s(\xi^*) = j(\xi^*) = \lambda_{\text{crt}}$, and the other lies below and to the left of the former. And finally, on comparing Figs. 3 and 4 we see the development of both steeping and asymmetry in the j vs. ξ profile as λ is reduced, but $\mathcal{A}_0$ is kept fixed.

9.2.3. Singular surface results: Shock waves

We now turn our attention from traveling waves propagating along the entire real line to what is commonly referred to in the acoustics literature as a “signaling problem”, wherein only waveforms propagating to the right along the $+x$-axis are possible.

To this end, let us assume that the initial conditions $S(x,0) = 1$ and $I(x,0) = 0$ (i.e., $I^+ = 0$) hold on the half-line $x > 0$. Then, at time $t = 0+$, the population density of infectives at the boundary $x = 0$ suddenly jumps to, and remains at, the value $I(0,t) = I^-$, where I^- is a positive constant. Under System (9.2.3), a planer shock-front $x = \Sigma_2(t)$, across which I suffers a jump, i.e., $[\![I]\!] \neq 0$ (see Appendix A), immediately begins propagating to the right along the $+x$-axis with speed c_2, where $\Sigma_2(t) = c_2 t$.

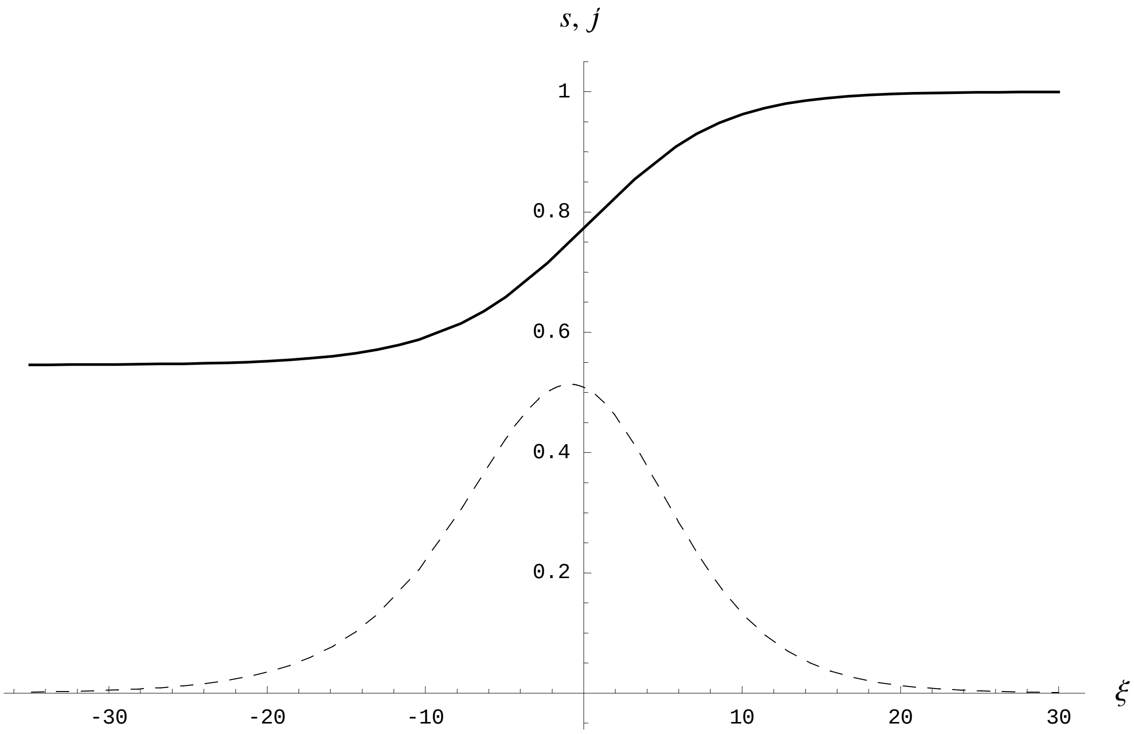

Figure 9.2.: The traveling wave solutions s vs. the wave variable ξ (bold-solid curve) and j vs. ξ (thin-broken curve) for $\mathcal{A}_0 = 15$ and $\lambda = 0.75$, for which $s_1 \approx 0.5456$, $s_0 = \frac{1}{2}(1 + s_1) \approx 0.7728$, and $\lambda_{\text{crt}} \approx 0.7088$.

If the density of the susceptibles across the shock front $x = 0$ also experiences a sudden change in its value at time $t = 0+$, say, $S(0, t) = S^-$, where S^- is a non-negative constant, then a second shock-front $x = \Sigma_1(t)$, across which now $[\![S]\!] \neq 0$, also begins propagating to the right along the $+x$-axis, but with speed c_1, i.e., $\Sigma_1(t) = c_1 t$.

Before beginning our singular surface analysis, it should be noted that under Case (i), i.e., $c_1 \neq c_2$, the function S (resp. I) is, $\forall\, t > 0$, continuously differentiable at all shock fronts $x > 0$, including $x = c_2 t$ (resp. $x = c_1 t$), except $x = c_1 t$ (resp. $x = c_2 t$). In contrast, under Case (ii), i.e., $c_1 = c_2 := c_{\text{c}}$, there is only a single shock-front, i.e., $\Sigma(t) = c_{\text{c}} t$, and S and I are, $\forall\, t > 0$, both continuously differentiable at all $x > 0$ except $x = c_{\text{c}} t$.

Case (i): $c_1 \neq c_2$

Taking jumps of the equations in System (9.2.3) under the assumption $c_1 \neq c_2$, and then applying the product rule given in Eq. (A.2) to the two terms involving $[\![SI]\!]$, yields the following.
Across $x = \Sigma_1(t)$:

$$[\![Q_t]\!] = -c_1^2 [\![S_x]\!], \qquad [\![S_t]\!] + [\![Q_x]\!] = -I_1^+ [\![S]\!]. \tag{9.2.26}$$

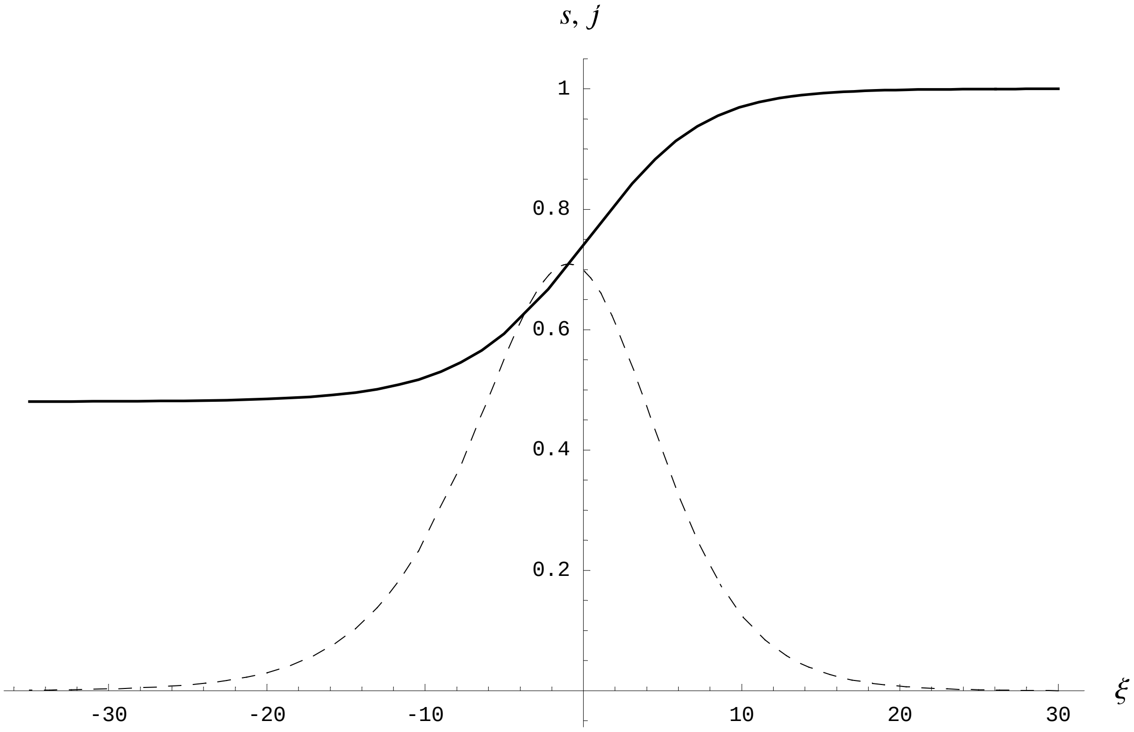

Figure 9.3.: The traveling wave solutions s vs. the wave variable ξ (bold-solid curve) and j vs. ξ (thin-broken curve) for $\mathcal{A}_0 = 15$ and $\lambda = \lambda_{\text{crt}}$, for which $s_1 \approx 0.4805$, $s_0 = \frac{1}{2}(1 + s_1) \approx 0.7402$, and $\lambda_{\text{crt}} \approx 0.7088$.

Across $x = \Sigma_2(t)$:

$$[\![J_t]\!] = -c_2^2[\![I_x]\!], \qquad [\![I_t]\!] + [\![J_x]\!] = S_2^+[\![I]\!] - \lambda[\![I]\!]. \tag{9.2.27}$$

Here, S_2^+ and I_1^+, both of which are (at most) functions of t only, denote the values of the susceptibles S and the infected I immediately ahead of $x = \Sigma_{2,1}(t)$, respectively.

Using these four jump relations, Hadamard's lemma (Eq. (9.3.18)), and the Rankine–Hugoniot relations

$$[\![\mathcal{Q}]\!] = c_0[\![\mathfrak{F}]\!], \tag{A.4}$$

where $\mathcal{Q}$ and $\mathfrak{F}$ denote the flux and concentration, respectively, which for System (9.2.3) take the form $[\![Q]\!] = c_1[\![S]\!]$ and $[\![J]\!] = c_2[\![I]\!]$, it is a relatively straightforward task to show that, for $c_1 \neq c_2$, the shock amplitudes satisfy the uncoupled pair of linear ODEs

$$\frac{\delta[\![S]\!]}{\delta t} + \tfrac{1}{2}I_1^+[\![S]\!] = 0 \quad \text{and} \quad \frac{\delta[\![I]\!]}{\delta t} - \tfrac{1}{2}\left(S_2^+ - \lambda\right)[\![I]\!] = 0, \tag{9.2.28}$$

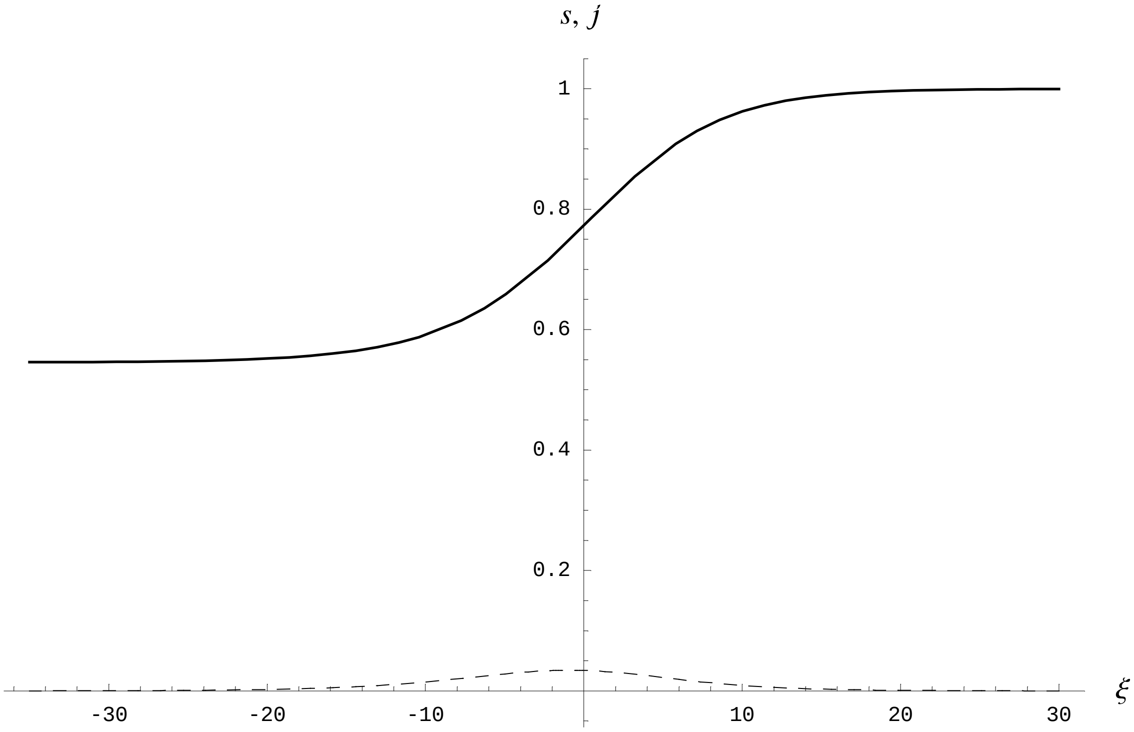

Figure 9.4.: The traveling wave solutions s vs. the wave variable ξ (bold-solid curve) and j vs. ξ (thin-broken curve) for $\mathcal{A}_0 = 1$ and $\lambda = 0.75$, for which $s_1 \approx 0.5456$, $s_0 = \frac{1}{2}(1 + s_1) \approx 0.7728$, and $\lambda_{\rm crt} \approx 0.3178$.

the exact solutions of which are

$$\begin{aligned} [\![S]\!] &= [\![S]\!]_0 \exp\left[-\tfrac{1}{2}\int^t I_1^+(\varkappa)\,\mathrm{d}\varkappa\right], \\ [\![I]\!] &= [\![I]\!]_0 \exp(-\tfrac{1}{2}\lambda t)\exp\left[\tfrac{1}{2}\int^t S_2^+(\varkappa)\,\mathrm{d}\varkappa\right], \end{aligned} \tag{9.2.29}$$

where the constants $[\![S]\!]_0 = S^- - 1$ and $[\![I]\!]_0 = I^-$ respectively denote the values of $[\![S]\!]$ and $[\![I]\!]$ at time $t = 0$.

Since it does not appear possible to analytically determine S and I in the interval between the shock-fronts $x = \Sigma_1(t)$ and $x = \Sigma_2(t)$, the following is the most we can say regarding the behavior of $[\![S]\!]$ and $[\![I]\!]$:

- If $c_1 > c_2$, which is extremely plausible, given that susceptibles are generally more mobile than infectives, and $I^+ = 0$, then $I_1^+ = 0$ and Eq. $(9.2.29)_1$ reduces to $[\![S]\!] = [\![S]\!]_0$, for all times $t >\geq 0$.
- If $c_2 > c_1$, which, as alluded to earlier, may not be likely, but is certainly possible, then $S_2^+ = 1$ and Eq. $(9.2.29)_2$ reduces to $[\![I]\!] = [\![I]\!]_0 \exp[\frac{1}{2}(1 - \lambda)]$.

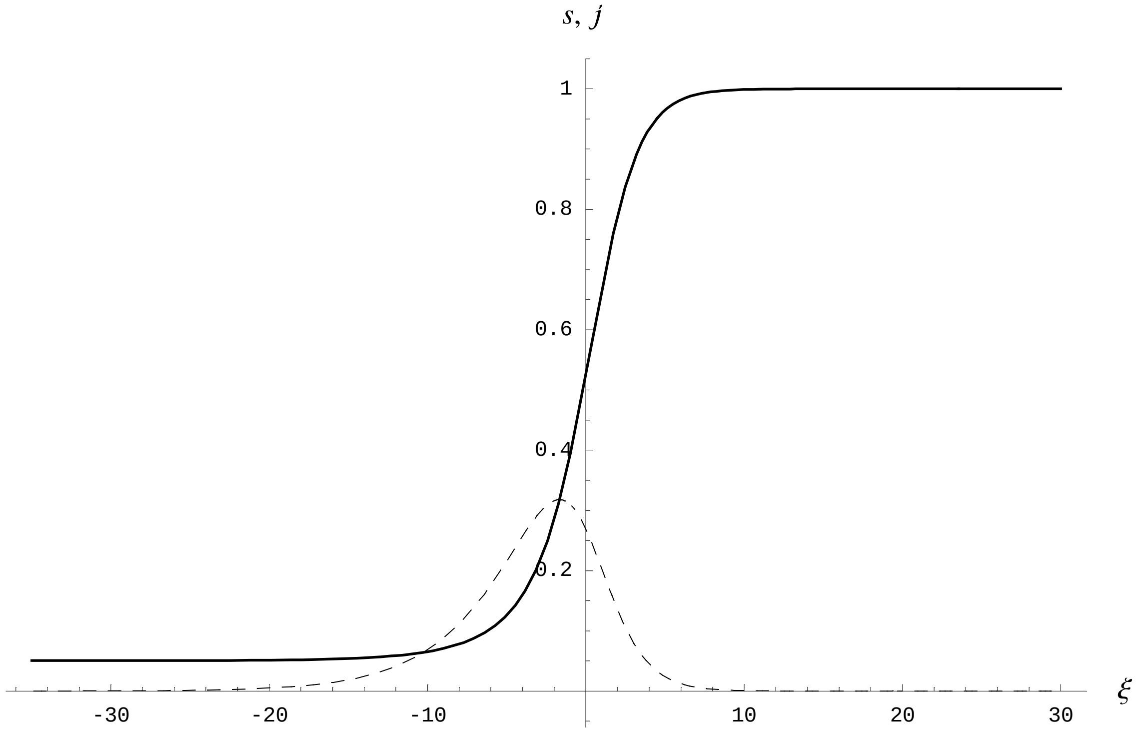

Figure 9.5.: s vs. ξ (bold-solid curve) and j vs. ξ (thin-broken curve) for $\mathcal{A}_0 = 1$ and $\lambda = \lambda_{\text{crt}}$, for which $s_1 \approx 0.0504$, $s_0 = \frac{1}{2}(1 + s_1) \approx 0.5252$, and $\lambda_{\text{crt}} \approx 0.3178$.

Remark: Since $\lambda \in (0, 1)$ must hold, as determined by the traveling wave studies carried out in [192] and in Sect. 3 of the present Letter, it follows that $[\![I]\!] \to \infty$, as $t \to \infty$ (i.e., a high-diffusivity epidemic will "blow-up" exponentially over time), when $c_2 > c_1$ and $[\![I]\!]_0 > 0$ hold simultaneously.

Case (ii): $c_1 = c_2$

On taking jumps of System (9.2.3) across the common wavefront $x = \Sigma(t)$, and once again making use of Eq. (A.2), we obtain

$$[\![Q_t]\!] = -c_{\text{c}}^2[\![S_x]\!], \qquad [\![S_t]\!] + [\![Q_x]\!] = -[\![I]\!] - [\![S]\!][\![I]\!]; \tag{9.2.30}$$

$$[\![J_t]\!] = -c_{\text{c}}^2[\![I_x]\!], \qquad [\![I_t]\!] + [\![J_x]\!] = (1 - \lambda)[\![I]\!] + [\![S]\!][\![I]\!], \tag{9.2.31}$$

where we recall that $S^+ = 1$ and $I^+ = 0$. Using these four jump relations and Eqs. (A.3) and (A.4), it is a relatively straightforward matter to derive the following system of ODEs:

$$\frac{\delta[\![S]\!]}{\delta t} + \tfrac{1}{2}(1 + [\![S]\!])[\![I]\!] = 0 \quad \text{and} \quad \frac{\delta[\![I]\!]}{\delta t} - \tfrac{1}{2}(1 - \lambda + [\![S]\!])[\![I]\!] = 0. \tag{9.2.32}$$

An inspection of System (9.2.32) reveals that the cases $[\![S]\!] = -1$ and $[\![S]\!] \neq -1$ must be considered separately. Taking the former first, it is easily shown that for $S^- = 0$:

$$[\![S]\!] = -1 \quad \text{and} \quad [\![I]\!] = [\![I]\!]_0 \exp(-\tfrac{1}{2}\lambda t) \qquad \forall\, t \geq 0, \tag{9.2.33}$$

where we observe that $[\![S]\!]_0 = -1$ implies $S^- = 0$ since $S^+ = 1$.

If we now assume $[\![S]\!] \neq -1$, then Eq. $(9.2.32)_1$ can be used to eliminate $[\![I]\!]$ Eq. $(9.2.32)_2$ and we end up with the single, second order ODE

$$2(1+\mathcal{S})\ddot{\mathcal{S}} - 2(\dot{\mathcal{S}})^2 = (1+\mathcal{S})(1-\lambda+\mathcal{S})\dot{\mathcal{S}} \qquad \text{with } S^- > 0, \tag{9.2.34}$$

where we have set $\mathcal{S} := [\![S]\!]$. Employing once again the "p-substitution" method, we integrate this ODE subject to the initial condition $2\dot{\mathcal{S}}(0) = -(1+\mathcal{S}_0)[\![I]\!]_0$, where we let $[\![S]\!]_0 := \mathcal{S}_0$, thus yielding

$$2\dot{\mathcal{S}} = (1+\mathcal{S})[K_1 + (1+\mathcal{S}) - \lambda \ln(1+\mathcal{S})] \qquad \text{with } S_0 > -1, \tag{9.2.35}$$

where $K_1 := \lambda \ln(1+\mathcal{S}_0) - (1+\mathcal{S}_0) - [\![I]\!]_0$. In turn, making the substitution $U(\mathcal{S}) := K_1 - \lambda \ln(1+\mathcal{S})$ and then integrating Eq. (9.2.35) in the same manner as Eq. (9.2.8), we find that $\mathcal{S}$ is given implicitly by

$$\begin{aligned} \lambda t = {} & -2\ln\left[\frac{U(\mathcal{S})}{U(\mathcal{S}_0)}\right] \\ & + 2\sum_{m=1}^{\infty} (-m/\lambda)^m \exp(mK_1/\lambda) \times \left\{\Gamma\left[-m,\, \frac{mU(\mathcal{S})}{\lambda}\right] - \Gamma\left[-m,\, \frac{mU(\mathcal{S}_0)}{\lambda}\right]\right\} \\ & \text{with } S_0 > -1, \end{aligned} \tag{9.2.36}$$

where we have imposed the second initial condition $\mathcal{S}(0) = \mathcal{S}_0$,

The sequence presented in Fig. 5 depicts the evolution of the jump amplitudes for various values of λ and correspond to the case $c_1 = c_2$; it was generated by first integrating Eq. (9.2.35) numerically using `NDSolve[]`, and then determining $[\![I]\!]$ using the former and Eq. $(9.2.32)_1$. Also, it should be kept in mind that, since we have taken $I^+ = 0$, the broken curves appearing in Fig. 5 actually depict I^- vs. t.

Now of particular interest is the fact that, while it always tends to zero as $t \to \infty$, the $[\![I]\!]$ vs. t plot develops a growing relative maximum, whose stationary point moves to the right, and a slowing decay rate as λ is decreased. In contrast, the $[\![S]\!]$ vs. t plot is strictly negative and tends monotonically to a constant value; specifically, $[\![S]\!] \to \overline{\mathcal{S}}$, as $t \to \infty$, where

$$\overline{\mathcal{S}} = -1 - \lambda W_0[-\lambda^{-1}\exp(-K_1/\lambda)] \qquad \text{with } S^- > 0, \tag{9.2.37}$$

and where we observe that $\overline{\mathcal{S}} \sim -1 + \exp(-K_1/\lambda)$ as $\lambda \to 0$.

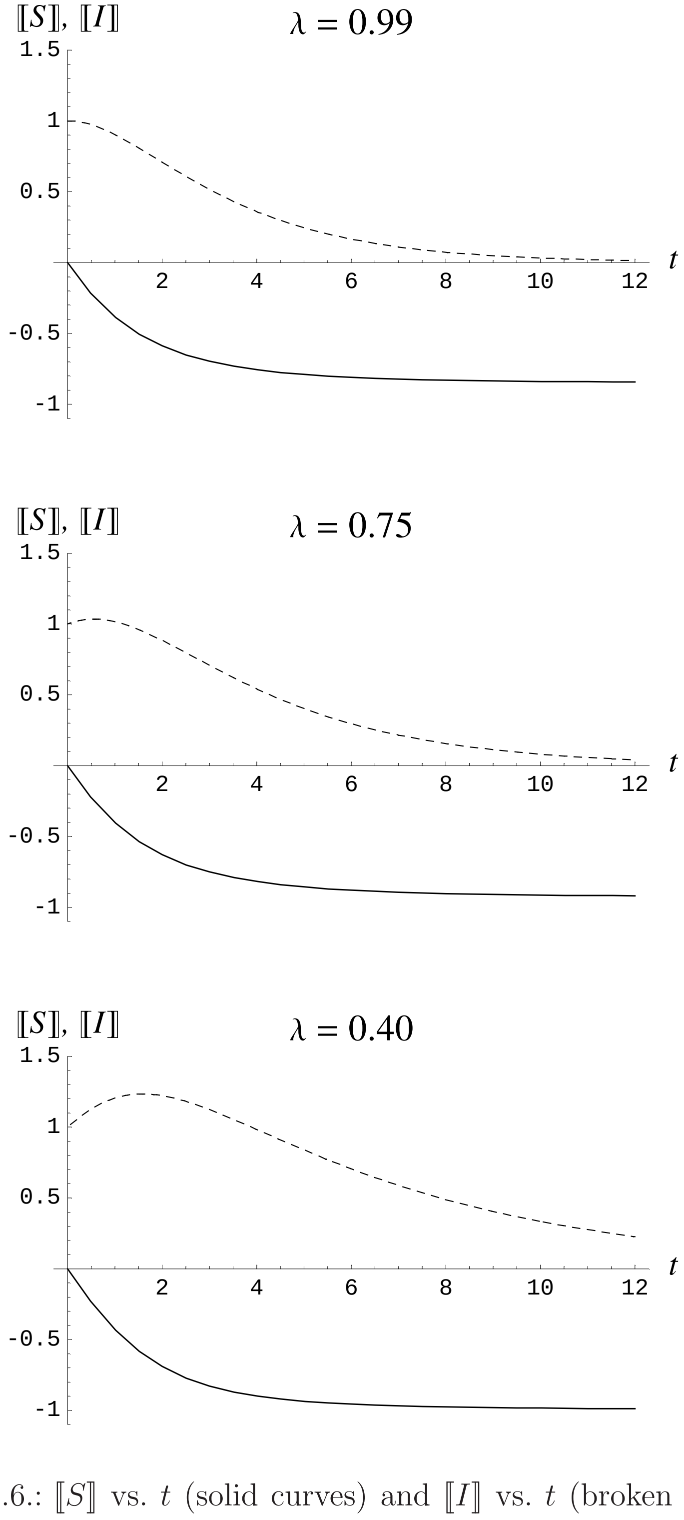

Figure 9.6.: $[\![S]\!]$ vs. t (solid curves) and $[\![I]\!]$ vs. t (broken curves) for $c_1 = c_2$, $[\![S]\!]_0 = 0$, and $[\![I]\!]_0 = 1$.

Remark: For the case $c_1 = c_2$, both the severity and duration of a high-diffusivity epidemic can be reduced by pushing λ as close as possible to unity, assuming (again) such a manipulation can be carried out.

9.3. Connection to other fields

In this section the conservation equation (9.1.4) with the type-II-flux law and varying nonlinear source terms is considered.

9.3.1. The Zel'dovich growth law and the cubic Rosen equation

Next, the following class of nonlinear wave equations is studied:

$$\rho_{tt} - c_\infty^2 \rho_{xx} = \gamma \rho_{\mathrm{s}}^{2-m}[\rho^{m-1}[1-\rho/\rho_{\mathrm{s}}]]_t, \qquad 0 \le \rho \le \rho_{\mathrm{s}} \quad \text{and} \quad m = 2, 3, \tag{9.3.1}$$

where the source term becomes the Zel'dovich [281] (resp. logistic) growth law for $m = 3$ (resp. $m = 2$), which have come to be known as equations of the Rosen[3] type. In general, for the order m it has to hold: $m \in \mathbb{N}$.

Recently, Jordan [150] investigated both traveling wave and singular surface phenomena for the case $m = 2$. In particular, he analyzed an exact traveling wave solution of, and investigated the evolution of shock and acceleration waves admitted by, this particular case of Eq. (9.3.1). In this section the case $m = 3$ is considered, i.e., the Zel'dovich growth law is assumed; and our intent is to compare/contrast traveling wave behavior for this case with that given in Jordan [150] for $m = 2$.

Traveling wave solutions

Now, we begin our search for traveling wave solutions with the following observation: Since Eq. (9.3.1) is invariant under the transformation $x \mapsto -x$, we need only consider, without loss of generality, right-traveling waves, i.e., solutions of the specific form

$$\rho(x,t) = \rho_{\mathrm{s}} f(\eta), \tag{9.3.2}$$

where $\eta = x - v_0 t$ is the wave variable, the propagation speed v_0 is a positive constant, and it is observed that $\eta \in \mathbb{R}$. Substituting Eq. (9.3.2) into Eq. (9.3.1) and then integrating once with respect to wave variable η yields, after simplifying, the following special case of Abel's [71, 132] equation:

$$[v_0^2 - c_\infty^2] f' + \gamma v_0 [f^2 - f^3] = \mathcal{K} \qquad \text{with } v_0 \neq c_\infty, \tag{9.3.3}$$

---

[3] G. Rosen [228] appears to have been the first to study partial differential equations of this type in the context of a physical application; specifically, he showed that they can arises in one-dimensional gas dynamics involving combustion.

where $\mathcal{K}$ is the constant of integration. In this section a prime denotes $\mathrm{d}/\mathrm{d}\eta$, and it is observed that $v_0 = c_\infty$ is a degenerate case. Let us assume that our wavefront is advancing from one constant state to another as the wave variable $\eta \to \infty$, where f_1, the value of f behind the front, is greater than f_2, the value ahead; in other words, we are seeking a traveling wave solution in the form of a diffusive soliton [225]. A diffusive soliton is any strictly monotonic, bounded traveling wave solution that approaches constant, but unequal, limits at $\pm\infty$. This means requiring that $\lim_{\eta\to\mp\infty} f(\eta) = f_{1,2}$, where $0 \leq f_2 < f_1 \leq 1$. Hence, it is readily shown that $f_{1,2}$ must then satisfy the propagation condition

$$f_1 + f_2 = f_1^2 + f_1 f_2 + f_2^2, \tag{9.3.4}$$

if the traveling wave solution we seek is to be in the form of a diffusive soliton.

Taking $f_2 = 0$ for simplicity, it is easy to see that Eq. (9.3.4) reduces to $f_1 = 1$. Noting that this implies that the constant of integration vanishes, i.e. $\mathcal{K} = 0$. It follows that the equilibrium solution $\bar{f} = 0$ is attracting from the right, and therefore stable[4] as far as we are concerned, only when the propagation speed exceeds the characteristic speed, i.e. $v_0 > c_\infty$. Thus, the propagation speed v_0 is supersonic. Imposing this restriction, we return to Eq. (9.3.3), separate variables, and then integrate once more. This yields the exact, but implicit, solution

$$\frac{1}{f} + \ln\left(\frac{1-f}{f}\right) = 2 + \frac{8\eta}{l_3}, \qquad \text{for} \quad (v_0 > c_\infty), \tag{9.3.5}$$

where the second constant of integration has been determined by requiring $f(0) = 1/2$ as initial condition. Here, the positive shock thickness[5] $l_m > 0$ is given by

$$l_m = 2^m L \qquad \text{with } m = 2, 3, \qquad \text{where} \qquad L = \frac{v_0}{\gamma}\left[1 - \frac{c_\infty^2}{v_0^2}\right], \tag{9.3.6}$$

and it is noted that l_2 is denoted as l_0 by Jordan [150]. Solving equation Eq. (9.3.5) for the traveling wave solution f in terms of the wave variable η (using [63, pp. 333–334]), the following exact solution is obtained:

$$f(\eta) = \frac{1}{1 + W_0(\exp(1)\exp(8\eta/l_3))}, \tag{9.3.7}$$

where $W_0(\cdot)$ denotes the principal branch of the Lambert W-function.

At this point it is instructive to compare/contrast the traveling wave solutions for the two cases of Eq. (9.3.1). Hence, in Figure 9.7 we have plotted the dimensionless density profiles based on Eq. (9.3.7) and

$$f_{m=2}(\eta) = \tfrac{1}{2}\left[1 - \tanh(2\eta/l_2)\right], \tag{9.3.8}$$

the corresponding exact solution for $m = 2$, see also Jordan [150], for two different values of L. From Figure 9.7(a) it is clear that (i) the $m = 3$ curve is asymmetric and (ii)

---

[4] Such an equilibrium solution, which is known as a saddle point, is said to be semi- or half-stable [231].

[5] The concept of shock thickness stems from classical compressible flow theory, see e.g. [214].

increasing the order m has decreased the rate at which the traveling wave solution $f \to 0$. These features stem from the fact that Eq. (9.3.7) behaves, asymptotically, like

$$f(\eta) \sim \begin{cases} \frac{1}{2(1+4\eta/l_3)}, & \eta \to \infty, \\ \\ 1 - \exp(1)\exp(8\eta/l_3), & \eta \to -\infty, \end{cases} \tag{9.3.9}$$

where it is made use of Eqs. (A.3.2). Thus, the traveling wave solution f tends to it limits at $\pm\infty$ algebraically and exponentially, respectively, when $m = 3$. This is in contrast to the strictly exponential asymptotic nature of Eq. (9.3.8), namely,

$$f(\eta) \sim H(-\eta) \mp \exp(\pm 4\eta/l_2), \qquad \eta \to \mp\infty, \tag{9.3.10}$$

where once again $H(\cdot)$ is used to denote the Heaviside unit step function. Also illustrated in Figure 3(a) is the fact that, for a given value of L, $l_3 > l_2$. Graphically, this means that the magnitude of the slope of the $m = 3$ curve is less than that of its counterpart at, and in the vicinity of, $\eta = 0$. Lastly, Figure 3(b) indicates that, just as in the $m = 2$ case, a shock of unit magnitude forms in the $m = 3$ traveling wave profile as the propagation speed $v_0 \to c_\infty+$, a result of the fact that $L \to 0$ as $v_0 \to c_\infty+$.

Remark: It should be noted that the Zel'dovich growth law also arises in mathematical biology; see, e.g., Newman [197] and Britton [46, p. 16]. Additionally, it is pointed out that under the Maxwell–Cattaneo-based model studied by Needham and King [194], which like the reaction-inertia one of the present section is a hyperbolic system, the Zel'dovich growth law corresponds to the special case $p = 2$ (p being the order in the notation given in Needham and King [194]).

Remark: Although a Green–Naghdi-type-II flux law is employed, the resulting partial differential equation involves damping and the traveling wave solution given in Eq. (9.3.8) (for $m = 2$) can be compared to the large time approximation of a Green–Naghdi-type-III rigid heat conductor with no heat source, see Bargmann et al. [34].

Shock amplitude analysis

Let $\mathcal{Z}(t) = \rho_{\mathrm{s}}^{-1}[\![\rho]\!]$ be the (dimensionless) shock amplitude and let $\mathcal{Z}(0)$ denote the value of $\mathcal{Z}$ at time $t = 0$. We now assume that $\mathcal{Z}(0) \neq 0$. It is a relatively straightforward process, using Hadamard's lemma (9.3.18) and the following formula for the jump of a product (cf. Lindsay and Straughan [177])

$$[\![AB]\!] = A^+[\![B]\!] + [\![A]\!]B^+ + [\![A]\!][\![B]\!] \tag{9.3.11}$$

to show that the ODE

$$\begin{aligned} \frac{\delta \mathcal{Z}}{\delta t} &= \gamma\rho_{\mathrm{s}}\mathcal{Z}\left[2\frac{\rho^+}{\rho_{\mathrm{s}}} + \mathcal{Z} - 3\left[\frac{\rho^+}{\rho_{\mathrm{s}}}\right]^2 - 3\left[\frac{\rho^+}{\rho_{\mathrm{s}}}\right]\mathcal{Z} - \mathcal{Z}^2\right] \\ \Leftrightarrow \frac{\delta \mathcal{Z}}{\delta t} - \alpha\mathcal{Z} - \beta\mathcal{Z}^2 + \gamma\rho_{\mathrm{s}}\mathcal{Z}^3 &= 0 \end{aligned} \tag{9.3.12}$$

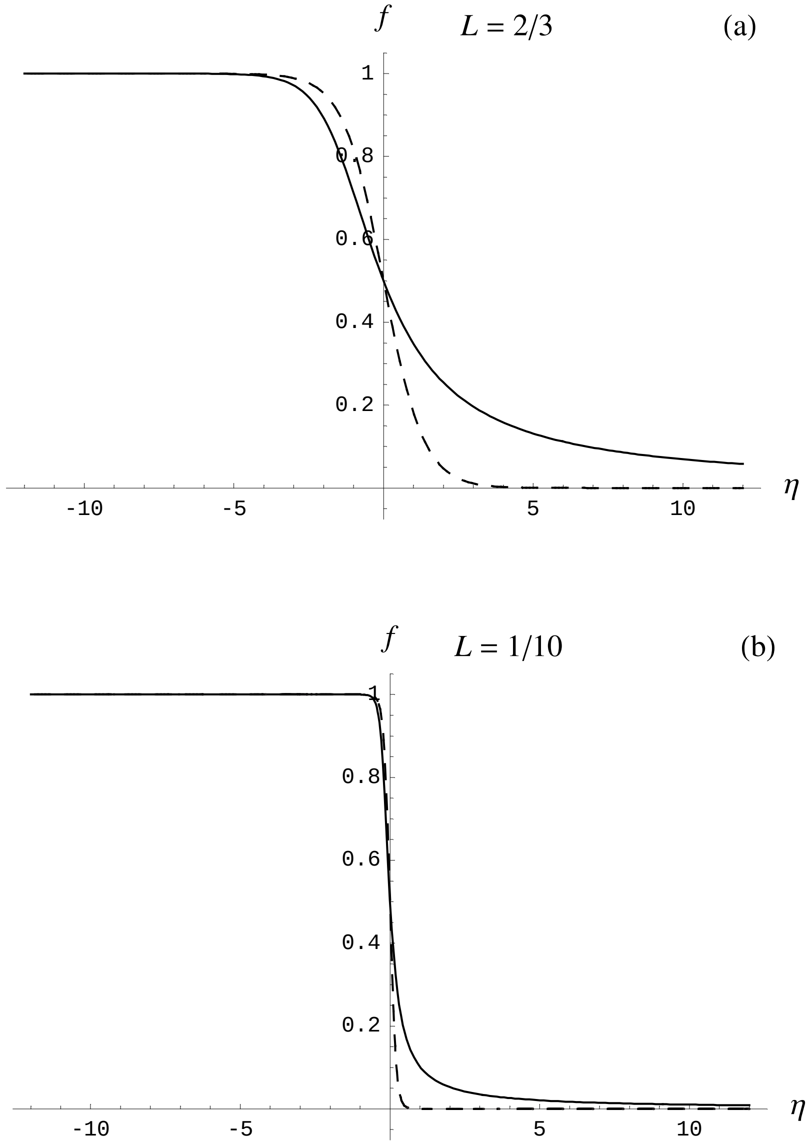

Figure 9.7.: Exact traveling wave solution under Zel'dovich growth law. Dimensionless density profiles based on Eq. (9.3.7), η is plotted vs. f. The broken line corresponds to the solution in case of $m = 2$, the solid line depicts the solution for $m = 3$. In Figure (a) the constant L, which is defined in Eq. (9.3.6), is chosen as $L = 2/3$ and in Figure (b) it is set $L = 1/10$. In both cases, the density profiles the Taylor shock behavior can clearly be seen.

governs the evolution of the shock amplitude $\mathcal{Z}(t)$ for the case of the Zel'dovich growth term. Here, $\alpha = \gamma\rho_\mathrm{s}\,[2\rho^+/\rho_\mathrm{s} - 3[\rho^+/\rho_\mathrm{s}]^2]$ and $\beta = \gamma\rho_\mathrm{s}[1 - 3\rho^+/\rho_\mathrm{s}]$. Since we are only interested in the special cases corresponding to constant ρ^+, which is denoted as ρ_c^+, in what follows we replace the former with the latter, where it is observed that $\rho_\mathrm{c}^+ \in [0, \rho_\mathrm{s})$.

In contrast to the logistic growth law $m = 2$ for which it is possible to derive the full solution for the shock amplitude (cf. Jordan [150]), here it is only possible to obtain the following two special case solutions of Eq. (9.3.12). We focus on the one which is physically relevant[6]:

$$\mathcal{Z}(t) = \frac{-1}{1 + W_\nu(-[1 + 1/\mathcal{Z}(0)]\exp(-[1 + 1/\mathcal{Z}(0)] - \gamma t))}, \quad \text{for } \rho_\mathrm{c}^+ = 0. \tag{9.3.13}$$

Here, W is again the Lambert W-function.

Mathematically, it is clear that then the temporal evolution of the shock amplitude $\mathcal{Z}$ as stated in Eq. (9.3.13) can occur in any one of the following two ways:

(i) If $\rho_\mathrm{c}^+ = 0$ and $\mathcal{Z}(0) = \sqrt{1/[\gamma\rho_\mathrm{s}]}$, then $\mathcal{Z}(t) = 1/\sqrt{3}$ for $t \geq 0$.

(ii) If $\rho_\mathrm{c}^+ = 0$ and $\mathcal{Z}(0) \in (0, \sqrt{1/[\gamma\rho_\mathrm{s}]})$, then $\mathcal{Z}(t) \in [\mathcal{Z}(0), 1)$, for $t \geq 0$, and $\mathcal{Z}(t) \to 1$ monotonically from below as $t \to \infty$.

9.3.2. Newman growth law

It should be noted here that in 1978 Aronson and Weinberger [15], some forty year after the pioneering studies of Fisher [95] and Kolmogorov–Petrovsky–Piskunov (KPP)[7] [161], considered the problem of the spread of a certain gene, via random mating, in a population of diploid individuals in N-spatial dimensions. Like Fisher, these authors considered a growth law of the form

$$R(\rho) = \rho\{[\tau_1 - \tau_2] - [2\tau_1 - 3\tau_2 + \tau_3][\rho/\rho_\mathrm{s}] + [\tau_1 - 2\tau_2 + \tau_3][\rho/\rho_\mathrm{s}]^2\}, \tag{9.3.15}$$

where τ_1, τ_2, and τ_3 are the constant death rates of the three possible genotypes. Note that for the death rates $\tau_1 = 2\tau_2 - \tau_3$ and $\tau_1 > \tau_2$, the growth term $R(\rho)$ reduces to the well-known Pearl–Verhulst (or logistic) growth law, namely $R(\rho) = [\tau_1 - \tau_2][\rho - \rho^2/\rho_\mathrm{s}]$. Besides biology, the logistic law also occurs in nuclear reactor engineering, where it serves as a model for the neutron flux and temperature in prompt feedback reactors (see Kastenberg and Chambré [158]). For death rates $\tau_3 = 3\tau_2 - 2\tau_1$ and $\tau_1 > \tau_2$, the growth R becomes $R(\rho) = [\tau_1 - \tau_2][\rho - \rho^3/\rho_\mathrm{s}^2]$. Under the classical parabolic theory, this

---

[6] The second analytical solution can be derived for $\rho_\mathrm{c}^+ = \frac{1}{3}\rho_\mathrm{s}$ and reads $\mathcal{Z}(t) = \frac{\sqrt{\alpha}\mathcal{Z}(0)\exp(\alpha t)}{\sqrt{1 + \mathcal{Z}^2(0)\gamma\rho_\mathrm{s}[\exp(2\alpha t) - 1]}}$.

[7] The classical one-dimensional Fisher–KPP equation reads

$$\rho_t - c_\infty^2\rho_{xx} = \gamma\rho\,[1 - \rho/\rho_\mathrm{s}] \tag{9.3.14}$$

where Fick's law of diffusion is used.

form of the source term exhibits the simplest type of front propagation, without induced pattern selection, into an unstable state (see van Saarloos [264]). This form of the growth R also occurs in Ginzburg–Landau theory, where it results from the Ginzburg–Landau free energy term (Murray [192]). Newman [197] extended the work of Fisher [95] and Kolmogorov, Petrovsky and Piskunov [161] by deriving traveling wave solutions for the case of a population density-dependent diffusion coefficient in the form of a power-law.

Traveling wave solutions

In this case our transport equation becomes

$$\rho_{tt} - c_\infty^2 \rho_{xx} = \gamma \rho_t [1 - 3(\rho/\rho_{\rm s})^2]. \tag{9.3.16}$$

On setting $\rho(x,t) = \rho_{\rm s} e(\xi)$, where $\xi = x - c_0 t$ is the wave variable and the real constant $c_0 > 0$ is the speed of the traveling wave, and then solving the resulting special case of Abel's equation using Jordan and Puri [151], we find the exact traveling wave solution for this case to be

$$e(\xi) = \frac{1}{\sqrt{1 + 3\exp(2c_0\gamma\xi/[c_0^2 - c_\infty^2])}} \qquad \text{with } c_0 > c_\infty, \tag{9.3.17}$$

where the condition $e(0) = 1/2$ is imposed. The restriction that the propagation speed must exceed the characteristic speed, i.e. $c_0 > c_\infty$, ensures that the equilibrium solution $\bar{\rho} = 0$ is stable. In Figure 9.9 we have plotted Eq. (9.3.17) for various values of the characteristic speed c_∞ and γ, keeping the speed of the traveling wave $c_0 = 1.0$ constant.

Shock amplitude analysis

Let $\mathcal{S}(t) = \rho_{\rm s}^{-1}[\![\rho]\!]$ be the (dimensionless) shock amplitude and let $\mathcal{S}(0)$ denote the value of $\mathcal{S}$ at time $t = 0$, where it is assumed that $\mathcal{S}(0) \neq 0$. It is a relatively straightforward process using Hadamard's lemma ([44, 54]), which in the present study assumes the form

$$\frac{\delta[\![\rho]\!]}{\delta t} = [\![\rho_t]\!] + c_\infty [\![\rho_x]\!], \tag{9.3.18}$$

and system (9.1.4), to show that the ODE

$$\frac{\delta \mathcal{S}}{\delta t} = \frac{\gamma}{2} \mathcal{S} \left[1 - 3[\rho^+/\rho_{\rm s}]^2 - 3[\rho^+/\rho_{\rm s}]\mathcal{S} - \mathcal{S}^2\right] \tag{9.3.19}$$

governs the evolution of the shock amplitude under the the growth law considered in this section. Here, $\rho^+ \in [0, \rho_{\rm s})$ is the value of the density ρ immediately ahead of the shock wave and $\delta/\delta t$ denotes the time-rate of change measured by an observer traveling with the shock wave.

A standard stability analysis reveals that Eq. (9.3.19) admits the equilibrium solutions $\bar{\mathcal{S}} = \{\mathcal{S}_2, 0, \mathcal{S}_1\}$, where the shock amplitudes $\mathcal{S}_2 \leq -1 < \mathcal{S}_1 \leq 1$ are given by

$$\mathcal{S}_{1,2} = \tfrac{1}{2}\left[-3[\rho_{\rm c}^{+}/\rho_{\rm s}] \pm \sqrt{4 - 3[\rho_{\rm c}^{+}/\rho_{\rm s}]^2}\right], \tag{9.3.20}$$

and it is noted that $\rho_{\rm c}^{+}/\rho_{\rm s} \in [0,1)$. The analysis also reveals that the shock amplitude $\mathcal{S}$ undergoes a transcritical bifurcation (e.g. Hale and Koçak [126]) at $\rho_{\rm c}^{+}/\rho_{\rm s} = 1/\sqrt{3}$. This means that as the ratio $\rho_{\rm c}^{+}/\rho_{\rm s}$ passes through the bifurcation value (i.e., $1/\sqrt{3}$), the two equilibrium show amplitude solutions $\bar{\mathcal{S}} = \{0, \mathcal{S}_1\}$ coalesce, and then switch their stability. The bifurcation diagram given in Figure 9.8 clearly illustrates the situation just described.

It is of interest to note that one can obtain an exact, explicit solution of Eq. (9.3.19) when $\rho^{+} = 0$. Restricting our attention to this special case, which is the one of greatest physical interest[8], and then separating variables and integrating, the corresponding exact solution is found to be

$$\mathcal{S}(t) = \frac{\mathcal{S}(0)\exp(\frac{1}{2}\gamma t)}{\sqrt{1 + \mathcal{S}^2(0)[\exp(\gamma t) - 1]}} \qquad \text{for } \rho^{+} = 0. \tag{9.3.21}$$

From Eq. (9.3.21) it is clear that the evolution of the shock amplitude $\mathcal{S}$ can occur in either of the following two ways:

(i) If $\rho^{+} = 0$ and $\mathcal{S}(0) = 1$, then $\mathcal{S}(t) = 1$ for $t \geq 0$.

(ii) If $\rho^{+} = 0$ and $\mathcal{S}(0) \in (0,1)$, then $\mathcal{S}(t) \in [\mathcal{S}(0), 1)$, for $t \geq 0$, and $\mathcal{S}(t) \to 1$ monotonically from below as $t \to \infty$.

In other words, when the value immediately ahead of the shock wave fulfills $\rho^{+} = 0$, the shock amplitude $\mathcal{S}$ is bounded for all $t \geq 0$ and, moreover, $\bar{\mathcal{S}} = 1$, where it is observed that $\mathcal{S}_1 = 1$ for $\epsilon = 0$, is a stable, nonzero equilibrium value of the shock amplitude.

9.4. Conclusions

The focus of this work was on the nature and behavior of traveling wave solutions and on the evolution of propagating shock waves in biological and physical reaction-diffusion cases. Fick's diffusion law was replaced with the Green–Naghdi type-II flux law, and applied to the SIR model of epidemic deseases and to the diffusion equation. In case of the latter, two different nonlinear growth laws were assumed and investigated. In all

---

[8] A second analytical solution can be derived for $\rho_{\rm c}^{+} = \frac{1}{\sqrt{3}}\rho_{\rm s}$: the shock wave then reads $\mathcal{S}(t) = \frac{-\sqrt{3}}{1+W_\nu(-\kappa_0\exp(-\kappa_0 - \frac{3}{2}\gamma t))}$. This is a mathematical valid solution, however of little physical relevance because it is in front of the bifurication value. Here, $\kappa_0 = 1 + \frac{\sqrt{3}}{\mathcal{S}(0)}$ and $\nu = \begin{cases} -1, & \mathcal{S}(0) \in (0, 1 - 3^{-1/2}], \\ 0, & \mathcal{S}(0) \in (-3^{-1/2}, 0). \end{cases}$ Moreover, W is the Lambert W-function, see Appendix for further details. Again, the shock amplitude $\mathcal{S}$ is bounded for all times $t > 0$.

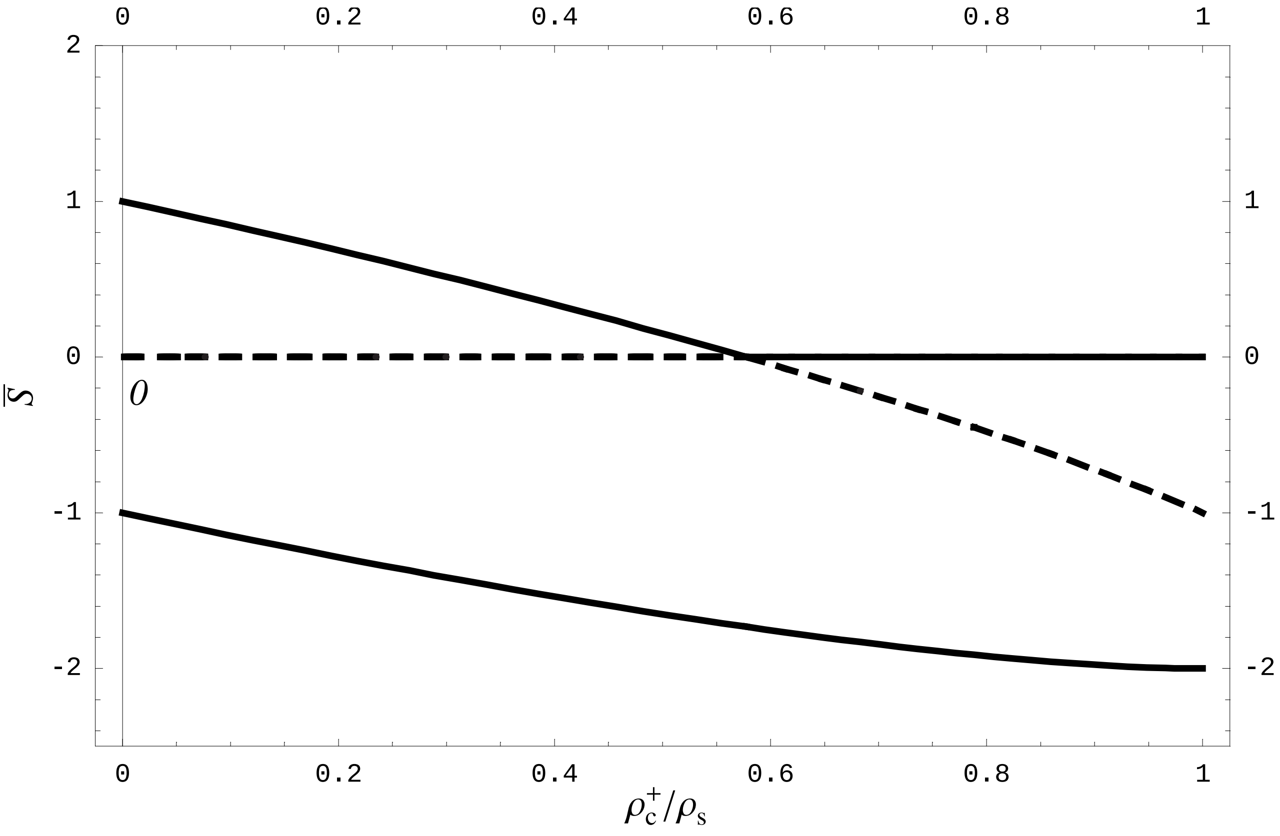

Figure 9.8.: Newman growth law. Bifurcation diagram showing transcritical bifurcation of the shock amplitude $\mathcal{S}$.

cases, we derived exact traveling wave solutions for the non-Fickian transport equations under the restriction that the propagation speeds are supersonic. In other words, the latter must exceed the characteristic speed c_∞.

What's more, in case of the SIR model for which the exact traveling wave solution is given by an implicit and complicated expression, we have been able to present approximated solutions which are easy manageable. For the non-classical diffusion equations, shock wave analyses were carried out and we obtained exact expressions for the shock wave amplitudes under the different nonlinear growth laws. It was shown that for a Zel'dovich growth law the traveling wave solution is in a form of a diffusive soliton. Both, the traveling wave solution and the shock amplitude are given in terms of the Lambert W-function. Thus, contrary to being associated with 'dissipationless diffusive transport', it has been shown that if the source term involved is density-/concentration-dependent, then the Green–Naghdi-II-flux law can give rise to a transport partial differential equation that exhibits positive attenuation (i.e. dissipation).

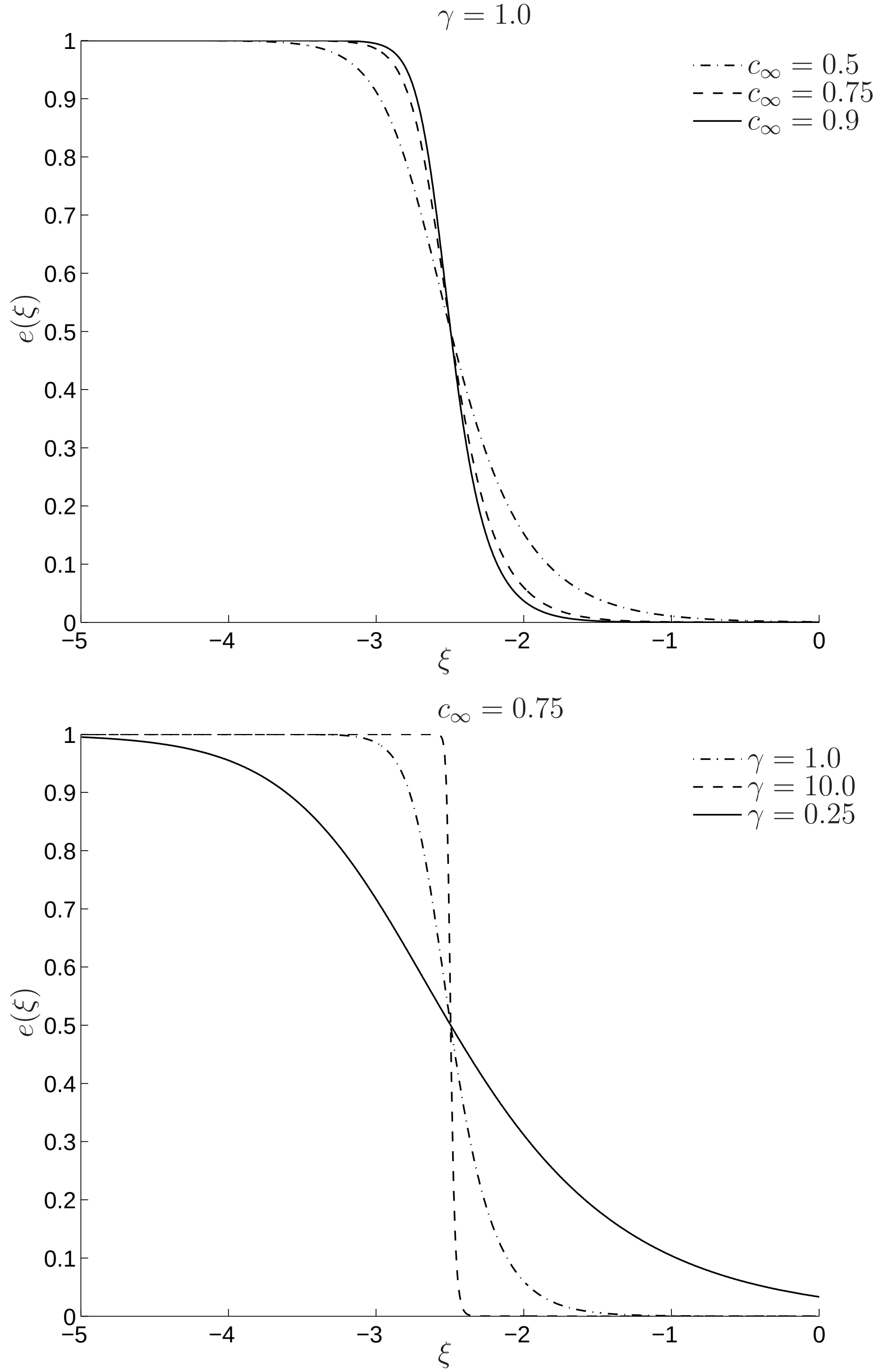

Figure 9.9.: Dimensionless density profile. Traveling wave solution under Newman law. The traveling wave solution e vs. the wave variable ξ generated from Eq. (9.3.17) for the constant traveling wave speed $c_0 = 1.0$. In the upper figure, the rate coefficient $\gamma = 1.0$ is kept constant and the characteristic speed c_∞ is varied. In the bottom figure, the density profile is depicted for constant characteristic speed $c_\infty = 0.75$ and various values of the rate coefficient γ.

10. Conclusions

In this thesis aspects of computational material modeling are presented. Different topics are studied such as crystal plasticity, polar ice, diffusion of polymers and further examples of diffusion in biological and physical sciences. In each case, as a first step, the underlying mathematical model is set up. Here, the difficulty lies in balancing the well-known objective to design the model "as easy as possible as complex as necessary". Usually, the emerging governing equations are too complex to solved analytically. Thus, computational methods are needed and, therefore, also part of this thesis.

Many engineering metals are polycrystalline with a well-defined crystallographic structure. Ordinary crystal plasticity theories cannot predict grain-size-dependent phenomena of second order in polycrystals. One of these effects is size-dependent hardening and an extended crystal plasticity models is required in order to overcome this drawback. In this thesis, the main focus is on the modeling of grain size-dependent effects in polycrystals.

Standard crystal plasticity accounts only for the effect of the history of crystallographic slip, i.e., of statistically stored dislocations, and not for geometrically necessary dislocations. First, in Chapter 2, models existing in the literature have been examined and analyzed from a computational modeling viewpoint. On that basis, a thermodynamically consistent extended continuum mechanics theory has been proposed in Chapter 5. It accounts for geometrically necessary dislocations and latent hardening. Geometrically necessary dislocations facilitate locally incompatible deformation which would otherwise take the form of (energetically less-favorable) local lattice deformation. Being in particular associated with interfaces and boundaries, GND accumulation leads to additional energy storage and kinematic-like hardening effects which exhibit a dependence on the size of the microstructure relative to the sample. Ordinary or standard crystal plasticity models do not predict these effects. The theory is set up in a thermodynamical framework and the free energy density is assumed to depend on the geometrically necessary dislocations. In turn, this leads to a non-local slip system flow rule representing an evolution field relation for the glide-system slips.

The theoretical part was accompanied by employing suitable discretization methods. For the spatial discretization it was resorted to a Bubnov–Galerkin finite element method in space. The primary unknowns are the displacement $\boldsymbol{u}$ and the geometrically necessary dislocation density $\boldsymbol{g}_\alpha$, whereas the plastic slip γ_α is regarded as a dependent quantity. This discretization approach is referred to as a dual mixed finite element method. In time, finite differences were applied. This procedure was applied to all numerical examples presented in Chapters 2–6, i.e. all examples of gradient crystal plasticity. The system of equations is highly coupled and nonlinear. Therefore, a Newton—Raphson strategy is applied. The performance of the proposed discretization methods is underlined by presenting various numerical examples.

An unresolved issue in gradient theory is the proper choice of grain boundary conditions. In the literature, there mainly exist two rather simple types for extended crystal plasticity continuum theories: micro-hard and micro-free boundary conditions, cf. [121] for the terminology. By micro-hard it is meant that the plastic slip is assumed to be zero at the grain boundaries. The other main choice of boundary condition for the plastic slip field is the so-called micro-free condition which assumes that a microstress vanishes on the grain boundary. In Chapter 4, a more general and more complex type of boundary conditions is suggested which incorporates the micro-hard and micro-free conditions as limiting cases. The main feature is that they take the crystallographic misorientation of adjacent grains into account: for a large misorientation the resistance against dislocation motion is large, whereas for a low misorientation the resistance is small.

However, there still exist some interesting open questions which are definitely worth having a look at in the future. In particular, the suggested models is to be used for more complex examples, such as simulating the multiscale deformation and failure behavior of strongly heterogeneous mesocrystalline sheet metal during milli- and microforming processes. Therefore, as part of this strategy, the extension to 3D in the computational code will be necessary.

Another important question which needs to be answered is how to better account for both individual grain behavior as well as grain interaction at grain boundaries. This still is a challenge in the current research directions.

Beyond the model development itself, there exist several challenges concerning the algorithmic formulation, the numerical implementation and solution of such models. The development of efficient and robust computational algorithm for the numerical implementation and solution of such models is state of the art and absolutely essential for their use in the numerical simulation of technological processes like microforming.

In this work, the material lengthscales which enter the extended crystal plasticity theories are regarded as constant. This simplifications can be changed to more realistic assumptions which will lead to a large increase in the model's complexity. For example, a possible dependence of lengthscales on the (dislocation) state of the material with the help of methods from statistical mechanics could be interesting (and challenging) to investigate. Summarizing, this thesis provides a deeper insight into different aspects of computational modeling of gradient crystal plasticity.

In Chapter 7 the anisotropic flow in polar ice is modeled in order to gain a better understanding for the underlying microstructure and its influence on the deformation process. In particular, a continuum mechanical, anisotropic flow model, which is based on an anisotropic flow enhancement factor, is applied. The polycrystalline ice is regarded as a mixture whose grains are characterized by their orientation. The approach is based on two distinct scales: the underlying microstructure influences the macroscopic material behavior and is taken into account phenomenologically. To achieve this the orientation mass density is introduced as a so called mesoscopic field, i.e. it depends on a mesoscopic variable (the orientation) in addition to position and time. The classical flow law of Glen is extended by a scalar enhancement factor. Moreover, four different effects (local rigid body rotation, grain rotation, rotation recrystallization, grain boundary migration) influencing the evolution of the grain orientations are taken into account. All modeling parameters are either measurable in or derivable from field observations or laboratory experiments. A finite volume method is chosen for the discretization procedure. Numerical results simulating the ice flow in the EPICA ice core EDML, Antarctica, are presented. The computed data agrees very well with the measured fabrics as well as the surface velocity. Additionally, in order to study the influence of the two existing deformation regimes of vertical compression and simple shear, both of them are studied separately. As suggested by the experimental findings, vertical compression predominates the deformation regime. The mathematical model is already set up for multiple dimensions. As a next step, an extension of the computational model (and the code) to the three-dimensional case and, thus, to large polar ice masses is desirable.

When a solvent penetrates the polymer near the glass transition temperature, three main phenomena occur: (1) The transport of the solvent, both within the glassy and within the plasticized portions of the material, follows a non-classical law until a characteristic time t_c. After t_c the usual Fickian behavior takes over and Fick's law is valid, although the values of the diffusion coefficients are different in the two regions. (2) A sharp moving front divides the polymer into two regions. Ahead of the front the polymer is still glassy due to a low solvent concentration. Behind the front, under the action of the solvent, the glassy state is undone and plasticization occurs. (3) Macroscopic elastic stresses between plasticized and glassy regions develop and eventually decay as the sample reaches equilibrium. In particular, the inner rigid glassy regions constrain the swelling of the outer plasticized portion. Case II diffusion is classified as traveling waves (or S-shape) form of the probability density (concentration) profiles with a straight line form of the isotherm sorption curve for early times of the process. Consequently, case II diffusion differs significantly from classical Fickian diffusion.

The classical Fickian theory of diffusion does not account for case II diffusion. The latter is generally observed when a low molecular weight solvent diffuses into a glassy polymer leading to a (spatially moving) rubber-glass phase transition. Typical industrial applications can be found in e.g. pharmaceutical, biological, environmental or automotive fields. Such possible applications include the removal of solvent from polymer solutions during dry spinning, microlithography, diffusional release of pollutants and additives from polymers into the environment, controlled release of agricultural chemicals, film casting and coating, development of photoresists, neurotransmitters' transport, or controlled-release drug delivery devices, for example. These experimental results led to much modeling effort. However, up to date no approach leads to an all-embracing theory. Chapter 8 represents a first step towards the computational modeling of case II diffusion in polymers. In this direction, a lot remains to be done, which is part of ongoing research.

There are several problems which must be discussed in the future. All models which exist in the literature at the moment have limitations as discussed in Chapter 8. None of it is capable of modeling all aspects of case II diffusion. Therefore, it is aimed at a theory which overcomes this drawback. Besides the necessity to prove its applicability with the help of benchmark problems (e.g. computational modeling of lab experiments of case II diffusion), the simulation of more complex example with emphasis on the examination of the swelling behavior is interesting task. Recall that swelling is an important property of polymers and part of the diffusion process. The solvent diffuses into the matrix until it reaches a constant saturated swelling. Here, computational simulations are a powerful tool, of course.

As mentioned above, usually the governing equations are too complex to be solved analytically. Few exceptions are presented in Chapter 9. For the non-classical diffusion equations, modeling non-Fickian reaction-diffusion in biological and physical sciences, presented in this chapter, analytical traveling wave solutions are determined and discussed. The analytical study of the partial differential equations has been of interest for many years (cf. Truesdell and Toupin [260]) and has been a topic of considerable interest. Here, the focus is on traveling wave solutions, being one example of singular surfaces. These exact expressions can provide valuable information on the existence and stability of solutions, the blow up of solutions or limitations of the models, for example. Moreover, they can lead to a more detailed understanding of the physics and serve as benchmarks for simple numerical simulations.

A. Mathematics

A.1. Notation

Throughout this thesis, scalar quantities are indicated by non-bold symbols, e.g. a, whereas vectors and tensors are denoted by bold symbols, e.g. $\boldsymbol{a}$. In order to distinguish spatial from material quantities, spatial quantities are denoted by lower case letters (e.g. $\boldsymbol{q}$) and material quantities by upper case letters (e.g. $\boldsymbol{Q}$). Furthermore, Einstein's summation convention is applied, i.e. it is summed over indices which appear twice. The following notation is used for the standard mathematical products: The simple contraction is denoted by "$\cdot$", e.g. $\{\boldsymbol{A} \cdot \boldsymbol{B}\}_{ik} = A_{ij}B_{jk}$, the double contraction by "$:$", e.g. $\boldsymbol{A} : \boldsymbol{B} = A_{ij}B_{ij}$ and the triple contraction by "$\vdots$", e.g. $\{\boldsymbol{C} \vdots \boldsymbol{D}\}_{lm} = C_{ijkl}D_{ijkm}$. The standard dyadic product is indicated by "$\otimes$", e.g. $\{\boldsymbol{A} \otimes \boldsymbol{B}\}_{ijkl} = A_{ij}B_{kl}$. The transpose of $\boldsymbol{A}$ is denoted by $\boldsymbol{A}^t$: $(A_{ij})^t = A_{ji}$.

Further, it is distinguished between the spatial and the material operations: The spatial and the material gradient are denoted by $\nabla_{\boldsymbol{x}}$ and ∇_{r}, respectively, whereas div and Div represent the corresponding divergences.

A.2. Definitions

alignment tensor: A good indicator for the fabric's degree of anisotropy are the so-called alignment or orientation tensors $\boldsymbol{a}^k$. They are macroscopic quantities and defined by

$$\boldsymbol{a}^k(\boldsymbol{x}, t) := \int_{S^2} f^*(\boldsymbol{x}, t, \boldsymbol{n})\, \underbrace{\boldsymbol{n} \otimes \ldots \otimes \ldots \otimes \boldsymbol{n}}_{k-\text{times}}\ \mathrm{d}^2 n. \tag{A.2.1}$$

They describe the distribution of intersections of the c-axis with the sphere of orientations and, thus, are well suited for comparing continuous fabrics which are described by the orientation distribution function. By definition, orientation tensors are symmetric and those of an odd order are zero. In this thesis, the focus is on the information given by $\boldsymbol{a}^2$. Note that, by definition, the trace of this orientation tensor equals unity

$$\mathrm{tr}(\boldsymbol{a}^2) = 1. \tag{A.2.2}$$

jump: A jump of a physical quantity $\{\bullet\}$ across a singular surface is the difference between its limiting values on either side of the singular surface and is denoted by $[\![\{\bullet\}]\!]$.

A.3. The Lambert W-function

The Lambert W-function is defined as the solution of the transcendental equation

$$W(z)\exp(W(z)) = z, \tag{A.3.1}$$

where z is a complex quantity and the roots of this equations correspond to the branches of W. By convention, the rth branch of the Lambert function W is denoted as W_r ($r \in \mathbb{Z}$) and W_0 is referred to as the principal branch, see also Figure A.1. Strictly speaking, W is not a function since there are two distinct real values of $W(x)$, which correspond to the branches $W_0(x)$ and $W_{-1}(x)$, for every $x \in (-\mathrm{e}^{-1}, 0)$ (i.e., W it is not injective on $-\mathrm{e}^{-1} < x < 0$); see Refs. [63, 67] and those therein. These two branches are the only ones to assume real values and coincide at the branch point $W_0(e^{-1}) = W_1(e^{-1}) = -1$. For $x < e^{-1}$, both $W_0(x)$ and $W_{-1}(x)$ are complex-valued.

In this thesis it is made use of the following large- and small-x asymptotic expressions of the principal branch of the Lambert W-function

$$\begin{aligned} W_0(x) &\approx x - x^2 + \ldots && \text{for } x \to 0, \\ W_0(x) &\approx \ln(x) - \ln(\ln(x)) + \mathcal{O}\left(\frac{\ln(x)}{\ln(\ln(x))}\right) && \text{for } x \to \infty. \end{aligned} \tag{A.3.2}$$

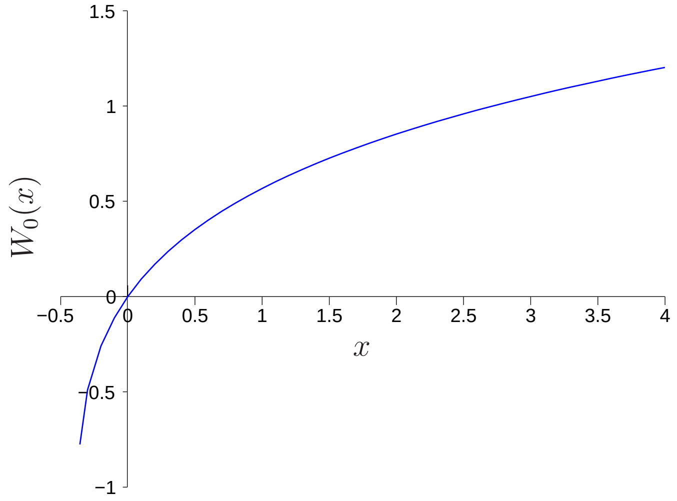

Figure A.1.: Lambert W-function, principal branch $W_0(x)$ for $-1/e < x < 4$.

Bibliography

[1] A. Acharya. Constitutive analysis of finite deformation field dislocation mechanics. *Journal of the Mechanics and Physics of Solids*, 52:301–316, 2004.

[2] A. Acharya and J. L. Bassani. Lattice incompatibility and a gradient theory of crystal plasticity. *Journal of the Mechanics and Physics of Solids*, 48:1565–1595, 2000.

[3] A. Acharya, J. L. Bassani, and A. Beaudoin. Geometrically necessary dislocations, hardening, and a simple gradient theory of crystal plasticity. *Scripta Materialia*, 48:167–172, 2003.

[4] A. Acharya, H. Tang, S. Saigal, and J. L. Bassani. On boundary conditions and plastic strain-gradient discontinuity in lower-order gradient plasticity. *Journal of the Mechanics and Physics of Solids*, 52:1793–1826, 2004.

[5] C. C. Ackermann, B. Bertram, H. A. Fairbank, and R. A. Guyer. Second sound in solid Helium. *Physical Review*, 18:789–791, 1966.

[6] C. C. Ackermann and W. C. Overton. Second sound in solid Helium-3. *Physical Review Letters*, 22(15):764–767, 1969.

[7] E. C. Aifantis. On the problem of diffusion in solids. *Acta Mechanica*, 37:265–296, 1980.

[8] E. C. Aifantis. On the microstructural origin of certain inelastic models. *Journal of Engineering Materials and Technology*, 106:326–330, 1984.

[9] F. Akasheh, H. Zbib, and T. Ohashi. Multiscale modelling of size effect in fcc crystals: discrete dislocation dynamics and dislocation-based gradient plasticity. *Philosophical Magazine*, 87:1307–1326, 2008.

[10] R. Al-Rub. Prediction of micro and nano-indentation size effect from conical or pyramidal indentation. *Mechanics of Materials*, 39:787–802, 2007.

[11] T. Alfrey, E. F. Gurnee, and W. G. Lloyd. Diffusion in glassy polymers. *Journal of Polymer Science Part C*, 12:249–261, 1966.

[12] R. B. Alley. Flow-law hypotheses for ice-sheet modeling. *Journal of Glaciology*, 38:245–256, 1992.

[13] L. Anand, M. E. Gurtin, S. P. Lele, and C. Gething. A one-dimensional theory of strain-gradient plasticity: Formulation, analysis, numerical results. *Journal of the Mechanics and Physics of Solids*, 53:1789–1826, 2005.

[14] R. Armstrong, I. Codd, R. M. Douthwaite, and N. J. Petch. The plastic deformation of polycrystalline aggregates. *Philosophical Magazine*, 8:45–58, 1962.

[15] D. Aronson and H. Weinberger. Multidimensional nonlinear diffusions arising in population genetics. *Advances in Mathematics*, 30:33–76, 1978.

[16] M. F. Ashby. The deformation of plastically non-homogeneous materials. *Philosophical Magazine*, 21:399–424, 1970.

[17] H. Askes, S. Bargmann, E. Kuhl, and P. Steinmann. Structural optimisation by simultaneous equilibration of spatial and material forces. *Communications in Numerical Methods in Engineering*, 21:433–442, 2005.

[18] G. Astarita and G. C. Sarti. A class of mathematical models for sorption of swelling solvents in glassy polymers. *Polymer Engineering and Science*, 18:388–395, 1978.

[19] N. Azuma. A flow law for anisotropic polycrystalline ice under uniaxial compressive deformation. *Cold Regions Science and Technology*, 23:137–147, 1995.

[20] N. Azuma and A. Higashi. Formation processes of ice fabric pattern in ice sheets. *Annals of Glaciology*, 6:130–134, 1985.

[21] J. L. Bamber and R. A. Bindschadler. An improved elevation dataset for climate and ice-sheet modelling: validation with satellite imagery. *Annals of Glaciology*, 25:439–444, 1997.

[22] S. Bargmann, M. Ekh, K. Runesson, and B. Svendsen. Modeling of polycrystals with gradient crystal plasticity: A comparison of strategies. *Philosophical Magazine*, 90:1263–1288, 2010.

[23] S. Bargmann, M. Ekh, B. Svendsen, and K. Runesson. Computational modeling of gradient hardening in polycrystals. *Technische Mechanik*, 30:316–323, 2010.

[24] S. Bargmann and P. M. Jordan. A second-sound based, hyperbolic SIR model for high-diffusivity spread. *Physics Letters A*, 375:898–907, 2011.

[25] S. Bargmann, A. McBride, and P. Steinmann. Models of Solvent Penetration in Glassy Polymers With an Emphasis on Case II Diffusion. A Comparative Review. *Applied Mechanics Reviews*, 64(1), 2011.

[26] S. Bargmann and D. Reddy. Modeling of polycrystals using a gradient crystal plasticity theory that includes dissipative microstresses. *European Journal of Mechanics - A/Solids*, 30:719–730, 2011.

[27] S. Bargmann, H. Seddik, and R. Greve. Computational modeling of the flow of anisotropic polar ice at the EDML deep-drilling site, Antarctica. *International Journal for Numerical and Analytical Methods in Geomechanics, accepted for publication*, 2011.

[28] S. Bargmann and P. Steinmann. Finite element approaches to non-classical heat conduction in solids. *Computer Modeling in Engineering & Science*, 9:133–150, 2005.

[29] S. Bargmann and P. Steinmann. Theoretical and computational aspects of non-classical thermoelasticity. *Computer Methods in Applied Mechanics and Engineering*, 196:516–527, 2006.

[30] S. Bargmann and P. Steinmann. Classical results for a non-classical theory: Remarks on thermo-dynamic relations in green-naghdi thermo-hyperelasticity. *Continuum Mechanics and Thermodynamics*, 19:59–66, 2007.

[31] S. Bargmann and P. Steinmann. An incremental variational formulation of coupled thermoelasticity for dissipative and non-dissipative solids. *Heat and Mass Transfer*, 45:107–116, 2008.

[32] S. Bargmann and P. Steinmann. Modeling of first and second sound. *International Journal of Solids and Structures*, 45:6067–6073, 2008.

[33] S. Bargmann, P. Steinmann, and R. Denzer. Material forces in non-classical thermo-hyperelasticity. *Journal of Thermal Stresses*, 32:361–393, 2009.

[34] S. Bargmann, P. Steinmann, and P. M. Jordan. On the propagation of second-sound in linear and nonlinear media: Results from Green–Naghdi theory. *Physics Letters A*, 372:4418–4424, 2008.

[35] S. Bargmann, B. Svendsen, and M. Ekh. An extended crystal plasticity model for latent hardening in polycrystals. *Computational Mechanics*, 48:631–645, 2011.

[36] J. L. Bassani. Incompatibility and a simple gradient theory of plasticity. *Journal of the Mechanics and Physics of Solids*, 49:1983–1996, 2001.

[37] C. Bayley, W. Brekelmans, and M. Geers. A comparison of dislocation induced back stress formulations in strain gradient crystal plasticity. *International Journal of Solids and Structures*, 43:7268–7286, 2006.

[38] C. J. Bayley, W. A. M. Brekelmans, and M. G. D. Geers. A three-dimensional dislocation field crystal plasticity approach applied to miniaturized structures. *Philosophical Magazine*, 87:1361–1378, 2007.

[39] A. N. Beris and B. J. Edwards. Thermodynamics of flowing systems: with internal microstructure. In *Oxford Engineering Science Series*, volume 36. Oxford University Press, 1994.

[40] T. R. Bieler, P. Eisenlohr, F. Roters, D. Kumar, D. E. Mason, M. A. Crimp, and D. Raabe. The role of heterogeneous deformation on damage nucleation at grain boundaries in single phase metals. *International Journal of Plasticity*, 25:1655–1683, 2009.

[41] R. B. Bird, R. C. Armstrong, and O. Hassager. *Dynamics of Polymeric Fluids*, volume 1: Fluid Mechanics. John Wiley & Sons, second edition, 1987.

[42] R. B. Bird, R. C. Armstrong, and O. Hassager. *Dynamics of Polymeric Fluids*, volume 2: Kinetic Theory. John Wiley & Sons, second edition, 1987.

[43] E. Bittencourt, A. Needleman, M. E. Gurtin, and E. Van der Giessen. A comparison of nonlocal continuum and discrete dislocation plasticity predictions. *Journal of the Mechanics and Physics of Solids*, 51:281–310, 2003.

[44] D. R. Bland. Wave theory and applications, sect. 6.9. *Oxford, UK: Oxford University Press*, 1988.

[45] U. Borg. A strain gradient crystal plasticity analysis of grain size effects in polycrystals. *European Journal of Mechanics A/Solids*, 26:313–324, 2007.

[46] N. F. Britton. Essential Mathematical Biology. *Springer*, 2003.

[47] L. Brown and R. Ham. Dislocationï¿½particle interactions. *In: A. Kelly and R.B. Nicholson (eds) Strengthening Methods in Crystals. Elsevier, Amsterdam*, pages 12–135, 1971.

[48] W. F. Budd and T. H. Jacka. A review of ice rheology for ice sheet modelling. *Cold Regions Science and Technology*, 16:107–144, 1989.

[49] P. J. Carreau and M. Grmela. Conformation tensor rheological models. In *Rheological Modelling: Thermodynamical and Statistical Approaches*, volume 381 of *Lecture Notes in Physics*, pages 126–157. Springer, 1991.

[50] C. Carstensen, K. Hackl, and A. Mielke. Nonconvex potentials and microstructures in finite-strain plasticity. *Proceedings of the Royal Society of London A*, 458:299–317, 2002.

[51] C. Cattaneo. Atti del seminario matematico e fisico della universita di modena. In *Atti del Seminario Matematico e Fisico della Universita di Modena*, volume 3, pages 3–21, 1948.

[52] P. Cermelli and M. E. Gurtin. On the characterization of the gemetrically necessary dislocations in finite plasticity. *Journal of the Mechanics and Physics of Solids*, 49:1539–1568, 2001.

[53] P. Cermelli and M. E. Gurtin. Geometrically necessary dislocations in viscoplastic single crystals and bicrystals undergoing small deformations. *International Journal of Solids and Structures*, 39:6281–6309, 2002.

[54] P. J. Chen. Growth and decay of waves in solids. *In Handbuch der physik, vol. VIa/3 (eds S. Flügge & C. Truesdell), pp. 303–402. Berlin, Germany: Springer*, 1973.

[55] P. G. Ciarlet. *Mathematical Elasticity. Volume I: Three-Dimensional Elasticity.* North-Holland Publishing Company, Amsterdam, 1988.

[56] J. Clayton, D. McDowell, and D. Bammann. A multiscale gradient theory for single crystalline elastoviscoplasticity. *International Journal of Engineering Science*, 42:427–457, 2004.

[57] H. Cleveringa, E. van der Giessen, and A. Needleman. Comparison of discrete dislocation and continuum plasticity predictions for a composite material. *Acta Materalia*, 45:3163–3179, 1997.

[58] D. S. Cohen. Theoretical models for diffusion in glassy polymers. *Journal of Polymer Science: Polymer Physics Edition*, 2:1001–1009, 1984.

[59] D. S. Cohen and A. B. White. Sharp fronts due to diffusion and stress at the glass transition in polymers. *Journal of Polymer Science: Part B: Polymer Physics*, 27:1731–1747, 1989.

[60] D. S. Cohen, A. B. White, and P. T. Witelski. Shock formation in a multidimensional viscoelastic diffusive system. *SIAM Journal on Applied Mathematics*, 55:348–368, 1995.

[61] B. D. Coleman and W. Noll. The thermodynamics of elastic materials with heat conduction and viscosity. *Archive for Rational Mechanics and Analysis*, 13:167–178, 1963.

[62] R. Collins. Mathematical modelling of controlled release from implanted drug-impregnated monoliths. *PSTT*, 1(6), 1998.

[63] R. M. Corless, G. H. Gonnet, D. E. G. Hare, D. J. Jeffrey, and D. E. Knuth. On the lambert w function. *Advances in Computational Mathematics*, 5:329–359, 1996.

[64] A. H. Cottrell. Effect of solute atoms on the behavior of dislocations. In H. H. Wills, editor, *Report of a Conference on Strength of Solids*, pages 30–36, University of Bristol, July 1948. The Physical Society, London.

[65] J. Crank. A theoretical investigation of the influence of molecular relaxation and internal stress on diffusion in polymers. *Journal of Polymer Science*, 6(2):1831–1855, 1953.

[66] J. Crank. *The Mathematics of Diffusion.* Oxford University Press, 1970.

[67] S. R. Cranmer. New views of the solar wind with the lambert w function. *American Journal of Physics*, 72:1397–1403, 2004.

[68] A. M. Cuitino and M. Ortiz. Computational modeling of single crystals. *Modelling and Simulation in Material Science and Engineering*, 1:225–263, 1992.

[69] Y. F. Dafalias. Orientation distribution function in non-affine rotations. *Journal of the Mechanics and Physics of Solids*, 49:2493–2516, 2001.

[70] H. Dai and D. M. Parks. Geometrically-necessary dislocation density and scale-dependent crystal plasticity. *Proceedings of Plasticity'97, A. S. Khan, editor*, pages 17–18, 1997.

[71] H. T. Davis. Introduction to nonlinear differential and integral equations. *Dover, New York*, 1962.

[72] R. de Borst and H.-S. Mühlhaus. Gradient-dependent plasticity: formulation and algorithmic aspects. *International Journal for Numerical Methods in Engineering*, pages 521–539, 1992.

[73] M. De Guzman, G. Neubauer, P. Flinn, and W. Nix. The role of indentation depth on the measured hardness of materials. *Materials Research Society Symposium Proceedings*, 308:613–618, 1993.

[74] D. De Kee, Q. Liu, and J. Hinestroza. Viscoelastic (non-Fickian) diffusion. *The Canadian Journal of Chemical Engineering*, 83:913–929, 2005.

[75] D. Dimiduk, M. Uchic, S. Rao, C. Woodward, and T. Parthasarathy. Overview of experiments on microcrystal plasticity in FCC-derivative materials: selected challenges for modelling and simulation of plasticity. *Modelling and Simulations in Materials Science and Engineering*, 15:135–146, 2007.

[76] J. K. Djoko, F. Ebobisse, A. T. McBride, and B. D. Reddy. A discontinuous Galerkin formulation for classical and gradient plasticity. Part 1: Formulation and analysis. *Computer Methods in Applied Mechanics and Engineering*, 196:3881–3897, 2007.

[77] J. K. Djoko, F. Ebobisse, A. T. McBride, and B. D. Reddy. A discontinuous Galerkin formulation for classical and gradient plasticity. Part 2: Algorithms and numerical analysis. *Computer Methods in Applied Mechanics and Engineering*, 197:1–21, 2007.

[78] M. Doi and A. Onuki. Dynamic coupling between stress and composition in polymer solutions and blends. *Journal de Physique II*, 2:1631–1656, 1992.

[79] C. J. Durning. Differential sorption in viscoelastic fluids. *Journal of Polymer Science: Polymer Physics Edition*, 23:1831–1855, 1985.

[80] C. J. Durning and M. Tabor. Mutual diffusion in concentrated polymer solutions under a small driving force. *Macromolecules*, 19:2220–2232, 1986.

[81] R. Ebeling and M. Ashby. Dispersion hardening of copper single crystals. *Philosophical Magazine*, 13:805–834, 1966.

[82] D. Edelen. On the existence of symmetry relations and dissipation potential. *Archive for Rational Mechanics and Analysis*, 51:218–227, 1973.

[83] O. Eisen, S. Kipfstuhl, D. Steinhage, and F. Wilhelms. Direct evidence for continuous radar reflector originating from changes in crystal-orientation fabric. *The Cryosphere*, 1:1–10, 2007.

[84] M. Ekh, S. Bargmann, and M. Grymer. Influence of grain boundary conditions on modeling of size-dependence in polycrystals. *Acta Mechanica*, 218:103–113, 2011.

[85] M. Ekh, M. Grymer, K. Runesson, and T. Svedberg. Gradient crystal plasticity as part of the computational modeling of polycrystals. *International Journal for Numerical Methods in Engineering*, 72:197–220, 2007.

[86] A. El Afif. *Diffusion de la matirière dans les polymeres.* PhD thesis, Ecole Polytechnique de Montréal, 2000.

[87] A. El Afif and M. Grmela. Non-fickian mass transport in polymers. *Journal of Rheology*, 46(3):591–628, 2002.

[88] A. El Afif, M. Grmela, and G. Lebon. Rheology and diffusion in simple and complex fluids. *Journal of Non-Newtonian Fluid Mechanics*, 86:253–275, 1999.

[89] I. Ertürk, J. A. W. van Dommelen, and M. G. D. Geers. Energetic dislocation interactions and thermodynamical aspects of strain gradient crystal plasticity theories. *Journal of the Mechanics and Physics of Solids*, 57:1801–1814, 2009.

[90] H. Espinosa, B. Prorok, and B. Peng. Plasticity size effects in free-standing submicron polycrystalline FCC films subjected to pure tension. *Journal of the Mechanics and Physics of Solids*, 52:667–689, 2004.

[91] U. Essmann and H. Mughrabi. Annihilation of dislocations during tensile and cyclic deformation and limits of dislocation densities. *Philosophical Magazine*, 40:731–756, 1979.

[92] L. P. Evers, W. A. M. Brekelmanns, and M. G. D. Geers. Non-local crystal plasticity model with intrinsic ssd and gnd effects. *Journal of the Mechanics and Physics of Solids*, 52:2379–2401, 2004.

[93] L. P. Evers, W. A. M. Brekelmans, and M. G. D. Geers. Scale dependent crystal plasticity framework with dislocation density and grain boundary effects. *International Journal of Solids and Structures*, 41:5209–5230, 2004.

[94] A. Fick. On liquid diffusion. *Philosophical Magazine*, 10:30–39, 1855.

[95] R. A. Fisher. The wave of advance of advantageous genes. *Annals of Eugenics*, 7:355–369, 1937.

[96] N. A. Fleck, G. M. Muller, M. F. Ashby, and J. W. Hutchinson. Strain gradient plasticity: theory and experiment. *Acta Metallurgica et Materialia*, 42:475–487, 1994.

[97] P. J. Flory. Thermodynamics of high polymer solutions. *Journal of Chemical Physics*, 9(8):66–661, 1941.

[98] S. Forest. Some links between Cosserat, strain gradient crystal plasticity and the statistical theory of dislocations. *Philosophical Magazine*, 88:3549–3563, 2008.

[99] S. Forest and R. Sedláček. Plastic slip distribution in two-phase laminate microstructures: dislocation-based versus generalized-continuum approaches. *Philosophical Magazine*, 83:245–276, 2003.

[100] P. Franciosi and A. Zaoui. Multislip in f.c.c. crystals a theoretical approach compared with experimental data. *Acta Metallurgica*, 30:1627–1637, 1982.

[101] P. Fredriksson and P. Gudmundson. Size-dependent yield strength of thin films. *International Journal of Plasticity*, 21:1834–1854, 2005.

[102] A. Friedman and G. Rossi. Phenomenological continuum equations to describe case II diffusion in polymeric materials. *Macromolecules*, 30:153–154, 1997.

[103] T. Z. Fu and C. J. Durning. Numerical simulation of Case II transport. *AIChE. Journal*, 39(6):1030–1044, 1993.

[104] H. Gao, Y. Huang, W. Nix, and J. Hutchinson. Mechanism based strain gradient plasticity - I. Theory. *Journal of the Mechanics and Physics of Solids*, 47:1239–1263, 1999.

[105] M. G. D. Geers, W. A. M. Brekelmans, and P. J. M. Janssen. Size effects in miniiaturized polycrystalline FCC samples: Strengthening versus weakening. *International Journal of Solids and Structures*, 43:7304–7321, 2008.

[106] J. W. Glen. The creep of polycrystalline ice. *Proceedings of the Royal Society London A*, 228:519–538, 1955.

[107] S. Govindjee and J. C. Simo. Coupled stress–diffusion: Case ii. *Journal of the Mechanics and Physics of Solids*, 41(5):863–887, 1993.

[108] A. J. Gow and T. Williamson. Rheological implications of the internal structure and crystal fabrics of the West Antarctic ice sheet as revealed by deep core drilling at Byrd Station. *CRREL Report*, 76:1665–1677, 1976.

[109] A. E. Green and P. M. Naghdi. A re-examination of the basic postulates of thermomechanics. *Proceedings of the Royal Society of London A*, 432:171–194, 1991.

[110] R. Greve and H. Blatter. *Dynamics of Ice Sheets and Glaciers.* Springer, Berlin etc., 2009.

[111] M. Grmela. Geometry of mesoscopic dynamics and thermodynamics. *Journal of Non-Newtonian Fluid Mechanics*, 120:137–147, 2004.

[112] M. Grmela. Why GENERIC? *Journal of Non-Newtonian Fluid Mechanics*, In press, 2010.

[113] M. Grmela and H. C. Öttinger. Dynamics and thermodynamics of complex fluids. I. Development of a general formalism. *Physical Review E*, 56(6):6620–6632, 1997.

[114] I. Groma, F. Csizor, and Z. M. Spatial correlation and higher-order gradient terms in a continuum description of dislocation dynamics. *Acta Materialia*, 51:1271–1281, 2003.

[115] I. Groma, G. Gyorgyi, and B. Kocsis. Dynamics of coarse grained dislocation densities from an effective free energy. *Philosophical Magazine*, 87:1185–1199, 2007.

[116] P. Gruber, J. Beohma, F. Onuseit, A. Wanner, R. Spolenak, and E. Arzt. Size effects on yield strength and strain hardening for ultra-thin Cu films with and without passivation: a study by synchrotron and bulge test techniques. *Philosophical Magazine*, 87:1185–1199, 2008.

[117] P. Gudmundson. A unified treatment of strain gradient plasticity. *Journal of the Mechanics and Physics of Solids*, 52:1379–1406, 2004.

[118] M. Gurtin. A finite-deformation, gradient theory of single-crystal plasticity with free energy dependent on densities of geometrically necessary dislocations. *International Journal of Plasticity*, 52:702–725, 2008.

[119] M. E. Gurtin. *An Introduction to Continuum Mechanics.* Academic Press, Orlando, 1981.

[120] M. E. Gurtin. On the plasticity of single crystals: free energy, microforces, plastic-strain gradients. *Journal of the Mechanics and Physics of Solids*, 48:989–1036, 2000.

[121] M. E. Gurtin. A theory of viscoplasticity that accounts for geometrically necessary dislocations. *Journal of the Mechanics and Physics of Solids*, 50:5–32, 2002.

[122] M. E. Gurtin. A gradient theory of small–deformation isotropic plasticity that accounts for the Burgers vector and for dissipation due to plastic spin. *Journal of the Mechanics and Physics of Solids*, 52:2545–2568, 2004.

[123] M. E. Gurtin. A theory of grain boundaries that accounts automatically for grain misorientation and grain-boundary orientation. *Journal of the Mechanics and Physics of Solids*, 56:640–662, 2008.

[124] M. E. Gurtin and L. Anand. A theory of strain-gradient plasticity for isotropic, plastically irrotational materials. Part I: Small deformations. *Journal of the Mechanics and Physics of Solids*, 53:1624–1649, 2005.

[125] M. E. Gurtin and A. Needleman. Boundary conditions in small-deformation, single-crystal plasticity that account for the Burgers vector. *Journal of the Mechanics and Physics of Solids*, 53:1–31, 2005.

[126] J. Hale and H. Koçak. Dynamics and bifurcations. *ch. 1,2. New York, NY: Springer*, 1991.

[127] E. O. Hall. The deformation and ageing of mild steel: III discussion of results. *Proceedings Physical Society London B*, 64:747–753, 1951.

[128] C.-S. Han, H. Gao, Y. Huang, and W. Nix. Mechanism-based strain gradient crystal plasticity-I. Theory. *Journal of the Mechanics and Physics of Solids*, 53:1188–1203, 2005.

[129] K. Hemker and W. Sharpe. Microscale characterization of mechanical properties. *Annual Review of Materials Research*, 37:93–126, 2007.

[130] M. Henning and H. Vehoff. Characterization of reference samples for continuum mechanics simulations - grain orientation, rotation and deformation as a function of the applied load. *Process Scaling, Strahltechnik; Eds. F. Vollertsen, F. Hollmann; BIAS-Verlag*, 24:185–192, 2003.

[131] J. H. Hildebrand. The entropy of solution of molecules of different size. *The Journal of Chemical Physics*, 15(5):225–228, 1947.

[132] J. M. Hill. Differential Equations and Group Methods for Scientist and Engineers. *CRC Press*, 1992.

[133] G. A. Holzapfel. *Nonlinear Solid Mechanics. A Continuum Approach for Engineering*. John Wiley & Sons, 2001.

[134] W. Hong, X. Zhao, and Z. Suo. Large deformation and electrochemistry of polyelectrolyte gels. *Journal of the Mechanics and Physics of Solids*, 58:558–577, 2010.

[135] W. Hong, X. Zhao, J. Zhou, and Z. Suo. A theory of coupled diffusion and large deformation in polymeric gels. *Journal of the Mechanics and Physics of Solids*, 56:1779–1793, 2008.

[136] R. L. Hooke. *Principles of Glacier Mechanics*. Cambridge University Press, Cambridge etc., 2nd edition, 2005.

[137] http://imechanica.org/node/2487, 2008.

[138] M. L. Huggins. Solutions of long chain compounds. *Journal of Chemical Physics*, 9:440, 1941.

[139] C.-Y. Hui and K.-C. Wu. Case-II diffusion in polymers, I. Transient swelling. *Journal of Applied Physics*, 61(11):5129–5136, 1987.

[140] C.-Y. Hui and K.-C. Wu. Case-ii diffusion in polymers, II. Steady-state front motion. *Journal of Applied Physics*, 61(11):5137–5149, 1987.

[141] F. J. Humphreys and M. Hatherly. Recrystallization and Related Annealing Phenomena. *Elsevier*, 2004.

[142] A. Hunter and M. Koslowski. Direct calculations of material parameters for gradient plasticity. *Journal of the Mechanics and Physics of Solids*, 56:3181–3190, 2008.

[143] J. Hutchinson. Plasticity at the micron scale. *International Journal of Solids and Structures*, 37:225–238, 2000.

[144] M. Hütter and T. A. Tervoort. Continuum damage mechanics: combining thermodynamics with a thoughtful characterization of the microstructure. *Acta Mechanica*, 201(1–4):297–312, 2008.

[145] M. Hütter and T. A. Tervoort. Coarse graining in elasto-viscoplasticity: bridging the gap from microscopic fluctuations to dissipation. *Advances in Applied Mechanics*, 42:253–317, 2009.

[146] H. E. Jackson, C. T. Walker, and T. F. McNelly. Second sound in NaF. *Physical Reviews*, 25(1):26–28, 1970.

[147] J. Jaisaardsuetrong and B. Straughan. Thermal waves in a rigid heat conductor. *Physics Letters A*, 366:433–436, 2007.

[148] P. Janssen, J. Hoefnagels, T. de Keijser, and M. Geers. Processing induced size effects in plastic yielding upon miniaturisation. *Journal of the Mechanics and Physics of Solids*, 56:2687–2706, 2008.

[149] P. M. Jordan. Growth and decay of shock and acceleration waves in a traffic flow model with relaxation. *Physica D*, 207:220–229, 2005.

[150] P. M. Jordan. Growth, decay and bifurcation of shock amplitudes under the type-II flux law. *Proceedings of the Royal Society London A*, 463:2783–2798, 2007.

[151] P. M. Jordan and P. Puri. Growth/decay of transverse acceleration waves in nonlinear elastic media. *Physics Letters A*, 335:150–156, 2005.

[152] D. D. Joseph and L. Preziosi. Heat waves. *Reviews of Modern Physics*, 61:41–73, 1989.

[153] D. Jou, J. Camacho, and M. Grmela. On the nonequilibrium thermodynamics of non-Fickian diffusion. *Macromolecules*, 24:3597–3602, 1991.

[154] N. S. Kalospiros, R. Ocone, G. Astarita, and J. H. Meldon. Analysis of anomalous diffusion and relaxation in solid polymers. *Industrial & Engineering Chemistry Research*, 30:851–864, 1991.

[155] T. A. Kals and R. Eckstein. Miniaturization in sheet metal working. *Journal of Materials Processing Technology*, 103:95–101, 2000.

[156] B. Kamb. Experimental recrystallization of ice under stress. *In: H. C. Heard, I. Y. Borg, N. L. Carter and C. B. Raileigh (Eds.), Flow and Fracture of Rocks, pp. 211–241. American Geophysical Union, Washington DC*, 1972.

[157] M. Kassner, S. Nemat-Nasser, Z. Suo, and G. Bao. New directions in mechanics. *Mechanics of Materials*, 37:231–259, 2005.

[158] W. Kastenberg and P. Chambre. On the stability of non-linearspace-dependent reacter kinetics. *Nuclear Sci. Eng.*, 31:67–79, 1968.

[159] W. O. Kermack and A. G. McKendrick. A Contribution to the Mathematical Theory of Epidemics. *Proceedings of the Royal Society London A*, 115:700–721, 1927.

[160] U. F. Kocks. The relation between polycrystal deformation and single crystal deformation. *Metallurgical Transactions*, 1:1121–1144, 1970.

[161] A. Kolmogoroff, I. Petrovsky, and N. Piscounoff. Etude de l'équations de la diffusion avec croissance de la quantite de matiere et son application a un probleme biologique. *Bulletin University of Moskow, Ser. International, Section A*, 1:1–25, 1937.

[162] K. Kondo. On the geometrical and physical foundations of the theory of yielding. *Proceedings of the Second Japan National Congress for Applied Mechanics, 1952, pp. 41–47, Science Council of Japan, Tokyo*, 1953.

[163] E. Kröner. Allgemeine Kontinuumstheorie der Versetzungen und Eigenspannungen. *Archive for Rational Mechanics and Analysis*, 4:273–334, 1960.

[164] E. Kuhl and D. W. Schmid. Computational modeling of mineral unmixing and growth - An application of the Cahn-Hilliard equation. *Computational Mechanics*, 39:439–451, 2007.

[165] M. Kuroda and V. Tvergaard. Studies of scale dependent crystal viscoplasticity models. *Journal of the Mechanics and Physics of Solids*, 54:1789–1810, 2006.

[166] M. Kuroda and V. Tvergaard. On the formulations of higher-order strain gradient crystal plasticity models. *Journal of the Mechanics and Physics of Solids*, 56:1591–1608, 2008.

[167] M. Kuroda and V. Tvergaard. A finite deformation theory of higher-order gradient crystal plasticity. *Journal of the Mechanics and Physics of Solids*, 56:2573–2584, 2008.

[168] E. H. Lee. Elastic-plastic deformation at finite strains. *Journal of Applied Mechanics*, 36:1–6, 1969.

[169] T. C. Lee, I. M. Robertson, and H. K. Birnbaum. An insitu transmission electronmicroscope deformation study of the slip transfer mechanisms in metals. *Metallurgical Transactions A: Physical Metallurgy and Materials Science*, 21:2437–2447, 1990.

[170] T. C. Lee, I. M. Robertson, and H. K. Birnbaum. TEM in situ deformation study of the interaction of lattice dislocations with grain-boundaries in metals. *Philosophical Magazine A: Physics of Condensed Matter Structure Defects and Mechanical Properties*, 62:131–153, 1990.

[171] S. P. Lele and L. Anand. A small-deformation strain-gradient theory for isotropic viscoplastic materials. *Philosophical Magazine*, 88:3655–3689, 2008.

[172] S. P. Lele and L. Anand. A large-deformation strain-gradient theory for isotropic viscoplastic materials. *International Journal of Plasticity*, 25:420–453, 2009.

[173] V. Levkovitch and B. Svendsen. On the large-deformation- and continuum-based formulation of models for extended crystal plasticity. *International Journal of Solids and Structures*, 43:7246–7267, 2006.

[174] T. Liebe and P. Steinmann. Theory and numerics of a thermodynamically consistent framework for geometrically linear gradient plasticity. *International Journal for Numerical Methods in Engineering*, 51:1437–1467, 2001.

[175] T. Liebe and P. Steinmann. Theory and numerics of a thermodynamically consistent framework for geometrically linear gradient plasticity. *International Journal for Numerical Methods in Engineering*, 51:1437–1467, 2001.

[176] S. Limkumnerd and E. van der Giessen. Statistical approach to dislocation dynamics: From dislocation correlations to a multiple-slip ontinuum theory of plasticity. *Physical Review B*, 77:184111–1841112, 2008.

[177] K. A. Lindsay and B. Straughan. Temperature waves in a rigid heat conductor. *Journal of Applied Mathematics and Physics (ZAMP)*, 27:653–662, 1976.

[178] J. D. Logan. An Introduction to Nonlinear Partial Differential Equations. *Wiley, New York*, 1994.

[179] V. Lubarda, J. Blume, and A. Needleman. An analysis of equilibrium dislocation distributions. *Acta Metallurgica et Materialia*, 41:625–642, 1993.

[180] S. R. Lustig, J. M. Caruthers, and N. A. Peppas. Continuum thermodynamics and transport theory of case II transport. *Chemical Engineering Science*, 47:3037–3057, 1992.

[181] Q. Ma and D. Clarke. Size dependent hardness of silver single crystals. *Journal of Materials Research*, 10:853–863, 1995.

[182] L. E. Malvern. *Introduction to the Mechanics of a Continuous Medium*. Prentice–Hall Inc, 1969.

[183] O. Manero and R. F. Rodríguez. A thermodynamic description of coupled flow and diffusion in a viscoelastic binary mixture. *Journal of Non-Equilibrium Thermodynamics*, 24(2):177–195, 1999.

[184] J. E. Marsden and T. J. R. Hughes. *Mathematical Foundations of Elasticity*. Dover Publications, Inc., 1994.

[185] J. C. Maxwell. On the dynamical theory of gases. *Philosophical Transactions of the Royal Society of London*, 157:49–88, 1867.

[186] A. Menzel and P. Steinmann. On the continuum formulation of higher gradient plasticity for single and polycrystals. *Journal of the Mechanics and Physics of Solids*, 48:1777–1796, 2000.

[187] C. Miehe. Strain-driven homogenization of inelastic microstructures and composites based on an incremental variational formulation. *International Journal for Numerical Methods in Engineering*, 55:1285–1322, 2002.

[188] A. Miyamoto. Mechanical properties and crystal textures of Greenland deep ice cores. *Doctoral thesis, Hokkaido University, Japan*, 1999.

[189] M. Montagnat and P. Duval. Rate controlling processes in the creep of polar ice: influence of grain boundary migration associated with recrystallization. *Earth and Planetary Science Letters*, 183:179–186, 2000.

[190] C. Motz, T. Schöberl, and R. Pippan. echanical properties of micro-sized copper bending beams machined by the focused ion beam technique. *Acta Materialia*, 53:4269–4279, 2005.

[191] T. Mura. Micromechanics of defects in solids. *Kluwer Publishers*, 1987.

[192] J. D. Murray. Mathematical biology, 2nd edn. *Berlin, Germany: Springer*, 1993.

[193] V. Narayanamurti and R. C. Dynes. Observation of second sound in Bismuth. *Physical Reviews*, 28:1461–1464, 1972.

[194] D. J. Needham and A. C. King. The evolution of travelling waves in the weakly hyperbolic generalized Fisher model. *Proceedings of the Royal Society London A*, 458:1055–1088, 2002.

[195] A. Needleman and J. G. Sevillano. Preface to the viewpoint set on: geometrically necessary dislocations and size dependent plasticity. *Scripta Materialia*, 48:109–111, 2003.

[196] A. C. Newell and J. A. Whitehead. Finite bandwidth, finite amplitude convection. *Journal of Fluid Mechanics*, 38:279–303, 1969.

[197] W. I. Newman. Some exact solutions to a non-linear diffusion problem in population genetics and combustion. *Journal of Theoretical Biology*, 85:325–334, 1980.

[198] L. Nicola, E. Van der Giessen, and M. E. Gurtin. Effect of defect energy on strain-gradient predictions of confined single-crystal plasticity. *Journal of the Mechanics and Physics of Solids*, 53:1280–1294, 2005.

[199] L. Nicola, Y. Xiang, J. Vlassak, E. van der Giessen, and A. Needleman. Plastic deformation of freestanding thin films: experiments and modeling. *Journal of the Mechanics and Physics of Solids*, 54:2089–2110, 2006.

[200] W. Nix, J. Greer, G. Feng, and E. Lilleodden. Deformation at the nanometer and micrometer length scales: effects of strain gradients and dislocation starvation. *Thin Solid Films*, 515:3152–3157, 2007.

[201] J. F. Nye. Some geometric relations in dislocated crystals. *Acta Metallurgica*, 1:153–162, 1953.

[202] R. W. Ogden. *Nonlinear Elastic Deformations*. Ellis Horwood Ltd., West Susex, England, 1982.

[203] N. Ohno and D. Okumura. Higher-order stress and grain size effects due to self-energy of geometrically necessary dislocations. *Journal of the Mechanics and Physics of Solids*, 55:1879–1898, 2007.

[204] M. Ortiz and E. A. Repetto. Non-convex energy minimization and dislocation structures in ductile single crystals. *Journal of the Mechanics and Physics of Solids*, 47:397–462, 1999.

[205] M. Ortiz and L. Stainier. The variational formulation of viscoplastic constitutive updates. *Computer Methods for Applied Mechanics and Engineering*, 171:419–444, 1999.

[206] H. C. Öttinger. *Beyond Equilibrium Thermodynamics*. Wiley, 2005.

[207] H. C. Öttinger and M. Grmela. Dynamics and thermodynamics of complex fluids. II. Illustrations of a general formalism. *Physical Review E*, 56:6633–6655, 1997.

[208] W. S. B. Paterson. The Physics of Glaciers. *Pergamon Press, Oxford etc., 3rd ed.*, 1994.

[209] J. R. Pellam. Investigations of pulsed second sound in liquid Helium. *Physical Review*, 75(8):1183–1194, 1948.

[210] P. Perzyna. Thermodynamic theory of viscoplasticity. *Advances in Applied Mechanics*, 11:313–354, 1971.

[211] V. Peshkov. Second Sound in Helium II. *Journal of Physics USSR*, 8:381, 1944.

[212] V. Peshkov. International conference on fundamental particles and low temperatures. In *Report*, Cambridge, July 22–27 1946.

[213] N. J. Petch. The cleavage strength of polycrystals. I. *Journal of Iron and Steel Institute*, 174:25–28, 1953.

[214] A. D. Pierce. Acoustics. *Acoustical Society of America, New York*, 1989.

[215] P. Pimienta, P. Duval, and V. Y. Lipenkov. Mechanical behaviour of anisotropic polar ice. *In: E. D. Waddington and J. S. Walder (Eds.), The Physical Basis of Ice Sheet Modelling, IAHS Publication No. 170, pp. 57–66. IAHS Press, Wallingford, UK*, 1987.

[216] L. Placidi. Thermodynamically consistent formulation of induced anisotropy in polar ice accounting for grain-rotation, grain-size evolution and recrystallization. *Doctoral thesis, Darmstadt University of Technology, Germany*, 2004.

[217] L. Placidi, R. Greve, H. Seddik, and S. H. Faria. A continuum-mechanical, anisotropic flow model for polar ice, based on an anisotropic flow enhancement factor. *Continuum Mechanics and Thermodynamics*, 22:221–237, 2010.

[218] L. Placidi and K. Hutter. Thermodynamics of polycrystalline materials treated by the theory of mixtures with continuous diversity. *Continuum Mechanics and Thermodynamics*, 17:409–451, 2006.

[219] J.-P. Poirier. Creep of crystals. *Cambridge University Press*, 1985.

[220] L. Preziosi. Cancer Modelling and Simulation. *Chapman & Hall/CRC*, 2003.

[221] S. Puri, A. Acharya, and A. Rollett. Controlling Plastic Flow across Grain Boundaries in a Continuum Model. *Metallurgical and Materials Transactions A*, DOI: 10.1007/s11661-010-0257-8, 2010.

[222] T. Qian and P. L. Taylor. From the thomas–windle model to a phenomenological description of case-ii diffusion in polymers. *Polymer*, 41(19):7159–7163, 2000.

[223] K. Rajagopal and L. Tao. Mechanics of mixtures. *World Scientific, Singapore, Appendix B*, 1995.

[224] I. Rao, J. Humphrey, and K. Rajagopal. Biological Growth and Remodeling: A Uniaxial Example with possible application to Tendons and Ligaments. *Computer Modeling in Engineering & Sciences*, 4:439–445, 2003.

[225] M. Remoissenet. Waves Called Solitons, third ed. *Springer, New York*, 1999.

[226] J. Rice. Inelastic constitutive relations for solids: an internal-variable theory and its application to metal plasticity. *Journal of the Mechanics and Physics of Solids*, 19:433–455, 1971.

[227] B. Riviére and S. Shaw. Discontinuous Galerkin finite element approximation of nonlinear non-Fickian diffusion in viscoelastic polymers. *SIAM Journal on Numerical Analysis*, 44(6):2650–2670, 2006.

[228] G. Rosen. Solutions of a certain nonlinear wave equation. *Journal of Mathematical Physics*, 45:235–265, 1966.

[229] G. Rossi, P. A. Pincus, and P. G. de Gennes. A phenomenological description of case–II diffusion in polymeric materials. *Europhysics Letters*, 32(5):391, 1995.

[230] D. S. Russell-Head and W. F. Budd. Ice sheet flow properties derived from borehole shear measurements combined with ice core studies . *Journal of Glaciology*, 24:117–130, 1979.

[231] G. Saccomandi. Acceleration waves in a thermo-microstretch fluid. *International Journal of Non-Linear Mechanics*, 29:809–817, 1994.

[232] H. Seddik. *A full-Stokes finite-element model for the vicinity of Dome Fuji with flow-induced anisotropy and fabric evolution.* Doctoral thesis, Graduate School of Environmental Science, Hokkaido University, Sapporo, Japan, 2008.

[233] H. Seddik, R. Greve, L. Placidi, I. Hamann, and O. Gagliardini. Application of a continuum-mechanical model for the flow of anisotropic polar ice to the EDML core, Antarctica. *Journal of Glaciology*, 45:631–642, 2008.

[234] H. Seddik, R. Greve, T. Zwinger, and L. Placidi. A full-Stokes ice flow model for the vicinity of Dome Fuji, Antarctica, with induced anisotropy and fabric evolution. *The Cryosphere Discussions*, 3:1–31, 2009.

[235] J. Shi and M. A. Zikry. Grain boundary interactions and orientation effects on crack behavior in polycrystalline aggregates. *International Journal of Solids and Structures*, 46:3914–3925, 2009.

[236] K. Shizawa and H. M. Zbib. A thermodynamical theory of gradient elastoplasticity with dislocation density tensor, I. Fundamentals. *International Journal of Plasticty*, 15:899–938, 1999.

[237] J. Y. Shu and N. A. Fleck. Strain gradient crystal plasticity: size-dependent deformation of bicrystals. *Journal of the Mechanics and Physics of Solids*, 47:297–324, 1999.

[238] J. Y. Shu, N. A. Fleck, E. van der Giessen, and A. Needleman. Boundary layers in constrained plastic flow: comparison of nonlocal and discrete dislocation plasticity. *Journal of the Mechanics and Physics of Solids*, 49:1361–1395, 2001.

[239] J. C. Simo. Topics on the numerical analysis and simulation of plasticity. In P. G. Ciarlet and J. L. Lions, editors, *Handbook of Numerical Analysis*, volume VI of *Handbook of numerical analysis*, pages 183–499. North-Holland, Amsterdam, 1998.

[240] J. C. Simo and T. J. R. Hughes. *Computational Inelasticity*, volume 7. Springer, 1998.

[241] P. Steinmann. Views on multiplicative elastoplasticity and the continuum theory on dislocations. *International Journal of Engineering and Science*, 34:1717–1735, 1996.

[242] N. A. Stelmashenko, M. G. Walls, L. M. Brown, and M. Y. V. Microindentations on W and Mo oriented single crystals: an STM study. *Acta Metallurgica et Materialia*, 41:2855–2865, 1993.

[243] J. S. Stölken and A. G. Evans. A microbend test method for measuring the plasticity length scale. *Acta Materialia*, 46:5109–5115, 1998.

[244] T. Svedberg and K. Runesson. A thermodynamically consistent theory of gradient-regularized plasticity coupled to damage. *International Journal of Plasticity*, 13:669–696, 1997.

[245] T. Svedberg and K. Runesson. An algorithm for gradient-regularized plasticity coupled to damage based on a dual mixed FE-formulation. *Computer Methods for Applied Mechanics and Engineering*, 161:49–65, 1998.

[246] B. Svendsen. Continuum thermodynamic extensions of crystal plasticity to include the effects of geometrically-necessary dislocations on the material behaviour. *Rendiconti del Seminario Matematico, Universita e Politecnico di Torino*, 58:209–235, 2000.

[247] B. Svendsen. Continuum thermodynamic models for crystal plasticity including the effects of geometrically-necessary dislocations. *Journal of the Mechanics and Physics of Solids*, 50:1297–1329, 2002.

[248] B. Svendsen. On thermodynamic and variational-based formulations of models for inelastic continua with internal lengthscales. *Computer Methods for Applied Mechanics and Engineering*, 193:5429–5452, 2004.

[249] B. Svendsen and S. Bargmann. On the continuum thermodynamic variational formulation of selected models for extended plasticity. *Journal of the Mechanics and Physics of Solids*, 58:1253–1271, 2010.

[250] B. Svendsen and K. Hutter. A continuum approach for modelling induced anisotropy in glaciers and ice sheets. *Annals of Glaciology*, 23:262–269, 1996.

[251] G. I. Taylor and C. F. Elam. The Plastic Extension and Fracture of Aluminium Crystals. *Proceedings of the Royal Society of London A*, 108:28–51, 1925.

[252] N. Thomas and A. H. Windle. Discontinuous shape changes associated with case ii transport of methanol in thin sheets of pmma. *Polymer*, 18(11):1195, 1977.

[253] N. Thomas and A. H. Windle. Transport of methanol in poly(methylmethacrylate). *Polymer*, 19:255–265, 1978.

[254] N. L. Thomas and A. H. Windle. A deformation model for case ii diffusion. *Polymer*, 21(6):613–619, 1980.

[255] N. L. Thomas and A. H. Windle. Diffusion mechanics of the system pmma-methanol. *Polymer*, 22(5):627–639, 1981.

[256] N. L. Thomas and A. H. Windle. A theory of case II diffusion. *Polymer*, 23:529–542, 1982.

[257] A. W. Thompson, M. I. Baskes, and W. F. Flanagan. The dependence of polycrystal work hardening on grain size. *Acta Metallurgica*, 21:1017–1032, 1973.

[258] H. E. Tresca. Mémoires sur l'Ecoulement des Corps Solides. *Mém. Sav. Acad. Sci., Paris, (Science Mathématiques et Physiques)*, 10:75–135, 1872.

[259] C. Truesdell and W. Noll. *The Non-Linear Field Theories of Mechanics*. Springer, New York, 3rd edition, 2004.

[260] C. Truesdell and R. A. Toupin. *The classical field theories. In: Handbuch der Physik.* Springer, New York, iii/1 edition, 1960.

[261] D. J. Unger and E. C. Aifantis. On the theory of stress-assisted diffusion, II. *Acta Mechanica*, 47:117–151, 1983.

[262] E. van der Giessen and A. Needleman. Discrete dislocation plasticity: a simple planar model. *Modelling and Simulation in Materials Science and Engineering*, 3:689–735, 1995.

[263] C. J. van der Veen. Fundamentals of Glacier Dynamics. *A. A. Balkema, Rotterdam, The Netherlands*, 1999.

[264] W. van Saarloos. Front propagation into unstable states. *Physics Reports*, 386:29–222, 2003.

[265] P. Vernotte. Les paradoxes de la théorie continue de léquation de la chaleur. *C. R. Acad. Sci.*, 246:3154–3155, 1958.

[266] D. Vesely. Diffusion of liquids in polymers. *International Materials Reviews*, 53(5):299–315, 2008.

[267] P. K. Vijalapura and S. Govindjee. Numerical simulation of coupled-stress case ii diffusion in one dimension. *Journal of Polymer Science: Part B: Polymer Physics*, 41:2091–2108, 2003.

[268] P. K. Vijalapura and S. Govindjee. An adaptive hybrid time-stepping scheme for highly non-linear strongly coupled problems. *International Journal for Numerical Methods In Engineering*, 64:819–848, 2005.

[269] P. K. Vijalapura, J. Strain, and S. Govindjee. Fractional step methods for index-1 differential-algebraic equations. *Journal of Computational Physics*, 203:305–320, 2005.

[270] G. Z. Voyiadjis and B. Beliktas. Mechanics of strain gradient plasticity with particular reference to decomposition of the state variables into energetic and dissipative components. *International Journal of Engineering Science*, 47:1405–1423, 2009.

[271] S. M. Vrech and G. Etse. FE approach for thermodynamically consistent gradient-dependent plasticity. *Latin American Applied Research*, 37:127–132, 2007.

[272] D. W. and S. J. Johnsen. A flow model and a time scale for the ice core from Camp Century, Greenland. *Journal of Glaciology*, 8:215–223, 1969.

[273] J. Weertman and J. R. Weertman. Elementary Dislocation Theory. *Oxford University Press*, 1992.

[274] R. B. Weertman. Creep of ice. *In: Physics and chemistry of ice. E. Whalley, S. J. Jones, L. W. Gold (Eds.)*, pages 320–337, 1973.

[275] I. Weikusat, S. Kipfstuhl, S. H. Faria, N. Azuma, and A. Miyamoto. Subgrain boundaries and related microstructural features in EDML (Antarctica) deep ice core. *Journal of Glaciology*, 55:461–472, 2009.

[276] C. Wesche, O. Eisen, H. Oerter, D. Schulte, and D. Steinhage. Surface topography and ice flow in the vicinity of the EDML deep-drilling site, Antarctica. *Journal of Glaciology*, 53:442–448, 2007.

[277] G. B. Whitham. Linear and Nonlinear Waves. *New York: John Wiley & Sons*, 1974.

[278] R. K. Wilson and E. C. Aifantis. On the theory of stress-assisted diffusion, I. *Acta Mechanica*, 45:273–296, 1982.

[279] J. C. Wu and N. A. Peppas. Modeling of penetrant diffusion in glassy polymers with an integral sorption Deborah number. *Journal of Polymer Science: Part B: Polymer Physics*, 31:1503–1518, 1993.

[280] Y. Xiang and J. J. Vlassak. Bauschinger and size effects in thin-film plasticity. *Acta Materialia*, 54:5449–5460, 2006.

[281] J. Xin. Front propagation in heterogeneous media. *SIAM Reviews*, 42:161–230, 2000.

[282] S. Yefimov and E. van der Giessen. Multiple slip in a strain-gradient plasticity model motivated by a statistical-mechanics description of dislocations. *International Journal of Solids and Structures*, 42:3375–3394, 2005.

[283] S. Yefimov and E. van der Giessen. Size effects in single crystal thin films: nonlocal crystal plasticity simulations. *European Journal of Mechanics A/Solids*, 24:183–193, 2005.

[284] T. I. Zohdi, K. Hutter, and P. Wriggers. A technique to describe the macroscopic pressure dependence of diffusive properties of solid materials containing heterogeneities. *Computational Materials Science*, 15:69–88, 1999.

[285] T. I. Zohdi and P. Wriggers. On the effects of microstress on macroscopic diffusion processes. *Acta Mechanica*, 136:91–107, 1999.